

Generically Orthogonal Decompositions of  
Collision Events and Measurement  
Combinations in Standard Model  $VH(b\bar{b})$   
Searches with the ATLAS Detector

A DISSERTATION PRESENTED  
BY  
STEPHEN K. CHAN  
TO  
THE DEPARTMENT OF PHYSICS

IN PARTIAL FULFILLMENT OF THE REQUIREMENTS  
FOR THE DEGREE OF  
DOCTOR OF PHILOSOPHY  
IN THE SUBJECT OF  
PHYSICS

HARVARD UNIVERSITY  
CAMBRIDGE, MASSACHUSETTS  
2018

©2018 – STEPHEN K. CHAN  
ALL RIGHTS RESERVED.

# Generically Orthogonal Decompositions of Collision Events and Measurement Combinations in Standard Model $VH(b\bar{b})$ Searches with the ATLAS Detector

## ABSTRACT

This thesis describes variations on the two lepton channel of the Run-2 search for the SM Higgs boson produced in association with a vector boson using different variable sets for multivariate analysis (MVA) training. The three variable sets in question are the set of variables from the fiducial analysis, a set based on the Lorentz Invariants (LI) concept, and a set based on a combination of masses and decay angles derived using the RestFrames (RF) package. Aside from the variable sets used for MVA training and discriminant distributions, the analysis is otherwise identical to the fiducial analysis. Both the LI and RF sets perform competitively on the basis of significances, with the RF set showing a  $\sim 3.5\%$  improvement in expected fits to Asimov and data, though neither set boosts observed significance. Both sets also reduce the observed error on  $\hat{\mu}$ , with the LI set reducing the error due to systematics by 7.5% and the RF set doing so by 16%.

The issue of combining multiple results from different channels and datasets is also examined through the combination of the fiducial Run 1 and Run 2 ATLAS  $VH(b\bar{b})$  results, which results in an observed signal strength of  $0.90^{+0.18}_{-0.18}(\text{stat.})^{+0.21}_{-0.19}(\text{syst.})$  and an observed (expected) significance of 3.6 (4.0) standard deviations, the first ever evidence of this process.

# Contents

o	INTRODUCTION	I
1	THE STANDARD MODEL HIGGS AND COLLIDER EVENT VARIABLES	4
1.1	The Standard Model Higgs Boson . . . . .	5
1.2	Higgs Boson Production and Decay at the Large Hadron Collider . . . . .	8
1.3	Collider Events and Event Level Variables . . . . .	12
1.4	Characterization with Event-Level Variables . . . . .	13
1.5	Lorentz Invariants . . . . .	16
1.6	RestFrames Variables . . . . .	18
1.7	Extensions to the $\ell$ and $\tau$ Lepton Channels . . . . .	20
2	THE LARGE HADRON COLLIDER AND THE ATLAS DETECTOR	24
2.1	The CERN Accelerator Complex . . . . .	25
2.2	The Large Hadron Collider . . . . .	25
2.3	ATLAS at a Glance . . . . .	30
2.4	The Inner Detector . . . . .	36
2.5	The ATLAS Calorimeters . . . . .	41
2.6	The Muon Spectrometer . . . . .	49
3	DATA AND SIMULATED SAMPLES	57
4	SIGNAL AND BACKGROUND MODELING	60
4.1	Event Generation In a Nutshell . . . . .	61
4.2	Description of Modeling Uncertainty Categories . . . . .	63
4.3	Process Specific Systematic Summaries . . . . .	74
5	OBJECT AND EVENT RECONSTRUCTION AND SELECTION	85
5.1	Triggers . . . . .	87
5.2	Electrons . . . . .	90
5.3	Muons . . . . .	92
5.4	Missing Transverse Energy . . . . .	94
5.5	Jets . . . . .	94
5.6	Flavor Tagging . . . . .	104
5.7	Miscellania and Systematics Summary . . . . .	114
5.8	Event Selection and Analysis Regions . . . . .	116

6	MULTIVARIATE ANALYSIS CONFIGURATION	118
6.1	Training Samples and Variable Selection . . . . .	119
6.2	MVA Training . . . . .	129
6.3	Statistics Only BDT Performance . . . . .	135
7	STATISTICAL FIT MODEL AND VALIDATION	144
7.1	The Fit Model . . . . .	145
7.2	Fit Inputs . . . . .	148
7.3	Systematic Uncertainties Review . . . . .	149
7.4	The VZ Validation Fit . . . . .	151
7.5	Nuisance Parameter Pulls . . . . .	154
7.6	Postfit Distributions . . . . .	164
7.7	VH Fit Model Validation . . . . .	166
8	FIT RESULTS	182
9	MEASUREMENT COMBINATIONS	188
9.1	Lepton Channel Combinations . . . . .	189
9.2	The Combined Fit Model . . . . .	194
9.3	Combined Fit Results . . . . .	207
10	CLOSING THOUGHTS	214
APPENDIX A MICROMEGAS TRIGGER PROCESSOR SIMULATION		217
A.1	Algorithm Overview . . . . .	218
A.2	Monte Carlo Samples . . . . .	222
A.3	Nominal Performance . . . . .	222
A.4	Fit Quantities . . . . .	223
A.5	Efficiencies . . . . .	228
A.6	Incoherent Background . . . . .	230
A.7	BCID . . . . .	236
A.8	Charge Threshold . . . . .	237
A.9	Misalignments and Corrections . . . . .	237
A.10	Individual Cases . . . . .	243
A.11	$ds \neq 0$ . . . . .	244
A.12	$dz \neq 0$ . . . . .	245
A.13	$dt \neq 0$ . . . . .	245
A.14	$\alpha \neq 0$ . . . . .	245
A.15	$\beta \neq 0$ . . . . .	245
A.16	$\gamma \neq 0$ . . . . .	246
A.17	Simulation Correction of the Algorithm Under Nominal Conditions . . . . .	247
A.18	Translation Misalignments Along the Horizontal Strip Direction ( $\Delta s$ ) . . . . .	251

A.19	Translation Misalignments Orthogonal to the Beamline and Horizontal Strip Direction $(\Delta z)$	252
A.20	Translation Misalignments Parallel to the Beamline ( $\Delta t$ )	254
A.21	Chamber Tilts Towards and Away from the IP ( $\gamma_s$ Rotation)	255
A.22	Rotation Misalignments Around the Wedge Vertical Axis ( $\beta_z$ )	256
A.23	Rotation Misalignments Around the Axis Parallel to the Beamline ( $\alpha_t$ )	257
A.24	Conclusion	259
<b>APPENDIX B TELESCOPING JETS</b>		<b>261</b>
B.1	Monte Carlo Simulation	262
B.2	Jet Reconstruction and Calibration	263
B.3	Event Reconstruction and Selection	264
B.4	Validation of Jet Calibration	267
B.5	Truth-Level Analysis	269
B.6	Errors on Telescoping Significances	271
B.7	Counting	271
B.8	Multiple Event Interpretations	272
B.9	$t(z) = z$	273
B.10	$t(z) = \rho_S(z) / \rho_B(z)$	274
B.11	Reconstructed-Level Analysis	278
B.12	Conclusions and Prospects	282
<b>APPENDIX C HISTORICAL ASIDE</b>		<b>283</b>
<b>REFERENCES</b>		<b>296</b>

# Listing of figures

1.1	The fundamental particles of the Standard Model. IC: [1] . . . . .	7
1.2	Dominant Higgs production modes. . . . .	9
1.3	Higgs decay mode branching fractions as a function of its mass; a line has been drawn at the observed Higgs mass of 125 GeV. . . . .	11
1.4	Reconstruction in a nutshell. You can (not) see the Higgs. . . . .	12
1.5	Summary of LI variables in the $ZH \rightarrow \ell\ell b\bar{b}$ topology. . . . .	16
1.6	The $ZH \rightarrow \ell\ell b\bar{b}$ decay tree. . . . .	18
1.7	The $ZH \rightarrow \nu\nu b\bar{b}$ decay tree. . . . .	23
2.1	The CERN Accelerator Complex [2] . . . . .	26
2.2	Schematic drawing of an LHC dipole magnet and cryogenics system. . . . .	27
2.3	Schematic and detailed views of the LHC ring. IC: [3], [4] . . . . .	28
2.3	The ATLAS coordinate system. "A" side is the airport, and "C" side is "Charlie's," a pub in Saint-Genis, France. . . . .	31
2.4	The ATLAS detector with principal subsystems shown. . . . .	36
2.5	The ATLAS inner detector. IC: [5] . . . . .	37
2.6	The ID material budget. IC: [6] . . . . .	37
2.7	Arrangement of pixels in the barrel. IC: [7] . . . . .	38
2.7	The ATLAS calorimeters. . . . .	41
2.8	Material depth of the ATLAS calorimeters. IC: [5] . . . . .	42
2.9	The accordion geometry of the LAr electromagnetic calorimeters is prominently shown in this illustration of an ECAL barrel module. IC: [5] . . . . .	44
2.9	The layout of the HEC in $r - \phi$ and $r - z$ ; dimensions are in millimeters. IC: [5] . .	47
2.10	The material layout for a typical section of the FCAL in the transverse plane. IC: [5]	47
2.11	The material layout for a typical section of the hadronic tile calorimeter. IC: [5] . .	48
2.12	The ATLAS muon spectrometer. Naming of the MDT stations obeys the following convention [BE] (barrel or end cap) [IEMo] (inner, inner extended (end cap only), middle, or outer layer) [1-6] (increasing in $z(r)$ for the barrel (end cap)), so EII is the station in the inner most end cap layer closest to the beam pipe. IC: [5] . . . . .	49
2.12	ATLAS MS detector performance. IC: [5] . . . . .	51
2.13	ATLAS MS trigger detector arrangement. IC: [5] . . . . .	54
4.1	The problem here is how to get from (a) to (b). . . . .	61
4.2	The $\delta_{EW}$ correction term for 2-lepton $qqZH$ . . . . .	69
4.3	The derivation of the 2-lepton $t\bar{t} m_{bb}$ shape systematic. . . . .	70

5.1	A clean ATLAS dijet event. . . . .	95
5.2	Infrared (a) and collinear (b) safety. . . . .	96
5.3	Different jet algorithms used on the same event. IC:[8]	97
5.4	A description of the 4-2-0 clustering algorithm. . . . .	100
5.5	An illustration of a secondary vertex in a $b$ -jet. Image credit: [9] . . . . .	105
5.6	An example of a pseudo-continous $b$ -tagging distribution . . . . .	110
5.7	Truth-tagging closure tests for 2 lepton, 2 jet mBB distributions in $\text{qqZllH}_{125}$ samples in three different $p_T^V$ regions. . . . .	III
5.8	Truth-tagging closure tests for 2 lepton, 2 jet dRBB distributions in $\text{qqZllH}_{125}$ samples in three different $p_T^V$ regions. . . . .	III
5.9	Truth-tagging closure tests for 2 lepton, 2 jet mBB distributions in $Z + \ell$ samples in three different $p_T^V$ regions. . . . .	II2
5.10	Truth-tagging closure tests for 2 lepton, 2 jet dRBB distributions in $Z + \ell$ samples in three different $p_T^V$ regions. . . . .	II2
5.11	Truth-tagging closure tests for 2 lepton, 2 jet mBB distributions in $t\bar{t}$ samples in three different $p_T^V$ regions. . . . .	II2
5.12	Truth-tagging closure tests for 2 lepton, 2 jet dRBB distributions in $t\bar{t}$ samples in three different $p_T^V$ regions. . . . .	II3
5.13	Truth-tagging closure tests for 2 lepton, 2 jet mBB distributions in $Z + bb$ samples in three different $p_T^V$ regions. . . . .	II3
5.14	Truth-tagging closure tests for 2 lepton, 2 jet dRBB distributions in $Z+bb$ samples in three different $p_T^V$ regions. . . . .	II3
6.1	Input variables in the 2 jet, low jet signal region for the standard variable set. Signal distributions are in red, and background distributions are in blue. . . . .	120
6.2	Input variables in the 2 jet, high jet signal region for the standard variable set. Signal distributions are in red, and background distributions are in blue. . . . .	120
6.3	Input variables in the 3+ jet, low jet signal region for the standard variable set. Signal distributions are in red, and background distributions are in blue. . . . .	120
6.4	Input variables in the 3+ jet, high jet signal region for the standard variable set. Signal distributions are in red, and background distributions are in blue. . . . .	121
6.5	Signal and background variable correlations for the standard variable set. . . . .	122
6.6	Input variables in the 2 jet, low jet signal region for the LI variable set. Signal distributions are in red, and background distributions are in blue. . . . .	122
6.7	Input variables in the 2 jet, high jet signal region for the LI variable set. Signal distributions are in red, and background distributions are in blue. . . . .	123
6.8	Input variables in the 3+ jet, low jet signal region for the LI variable set. Signal distributions are in red, and background distributions are in blue. . . . .	123
6.9	Input variables in the 3+ jet, high jet signal region for the LI variable set. Signal distributions are in red, and background distributions are in blue. . . . .	123
6.10	Signal and background variable correlations for the LI variable set. . . . .	124

6.11	Input variables in the 2 jet, low jet signal region for the RF variable set. Signal distributions are in red, and background distributions are in blue. . . . .	126
6.12	Input variables in the 2 jet, high jet signal region for the RF variable set. Signal distributions are in red, and background distributions are in blue. . . . .	126
6.13	Input variables in the 3+ jet, low jet signal region for the RF variable set. Signal distributions are in red, and background distributions are in blue. . . . .	127
6.14	Input variables in the 3+ jet, high jet signal region for the RF variable set. Signal distributions are in red, and background distributions are in blue. . . . .	127
6.15	Signal and background variable correlations for the RF variable set. . . . .	128
6.16	An example ranking, the RF variable set in the 2 jet, high $p_T^V$ region. . . . .	131
6.16	Rankings for the 2 jet standard variable set. . . . .	133
6.17	Rankings for the 3+ jet standard variable set. . . . .	133
6.18	Rankings for the 2 jet LI variable set. . . . .	133
6.19	Rankings for the 3+ jet LI variable set. . . . .	134
6.20	Rankings for the 2 jet RF variable set. . . . .	134
6.21	Rankings for the 3+ jet RF variable set. . . . .	134
6.22	Example output training (points) and testing (blocks) MVA discriminant distributions for the RF variable set in the 2 jet, high $p_T^V$ region. . . . .	136
6.22	Training (points) and testing (block histogram) in the 2 jet, low jet signal region for the standard variable set. Signal distributions are in red, and background distributions are in blue. . . . .	138
6.23	Training (points) and testing (block histogram) in the 2 jet, high jet signal region for the standard variable set. Signal distributions are in red, and background distributions are in blue. . . . .	138
6.24	Training (points) and testing (block histogram) in the 3+ jet, low jet signal region for the standard variable set. Signal distributions are in red, and background distributions are in blue. . . . .	139
6.25	Training (points) and testing (block histogram) in the 3+ jet, high jet signal region for the standard variable set. Signal distributions are in red, and background distributions are in blue. . . . .	139
6.26	Training (points) and testing (block histogram) in the 2 jet, low jet signal region for the RF variable set. Signal distributions are in red, and background distributions are in blue. . . . .	139
6.27	Training (points) and testing (block histogram) in the 2 jet, high jet signal region for the RF variable set. Signal distributions are in red, and background distributions are in blue. . . . .	140
6.28	Training (points) and testing (block histogram) in the 3+ jet, low jet signal region for the RF variable set. Signal distributions are in red, and background distributions are in blue. . . . .	140
6.29	Training (points) and testing (block histogram) in the 3+ jet, high jet signal region for the RF variable set. Signal distributions are in red, and background distributions are in blue. . . . .	140
6.30	Training (points) and testing (block histogram) in the 2 jet, low jet signal region for the LI variable set. Signal distributions are in red, and background distributions are in blue. . . . .	141

6.31	Training (points) and testing (block histogram) in the 2 jet, high jet signal region for the LI variable set. Signal distributions are in red, and background distributions are in blue.	141
6.32	Training (points) and testing (block histogram) in the 3+ jet, low jet signal region for the LI variable set. Signal distributions are in red, and background distributions are in blue.	141
6.33	Training (points) and testing (block histogram) in the 3+ jet, high jet signal region for the LI variable set. Signal distributions are in red, and background distributions are in blue.	142
6.34	Results of testing significances sorted by analysis region and variable set.	142
7.1	An example postfit distribution. The reason this looks different from postfit distributions later in this chapter is that this is a log plot. It shows rare samples ( $Z+cl$ , $Z+ll$ , $W+jets$ ), but obscures Data/MC agreement, which can only be seen via the ratio plot.	146
7.2	$\mu$ summary plots for the standard, LI, and RF variable sets. The Asimov case (with $\mu = 1$ by construction) is in (a), and $\hat{\mu}$ best fit values and error summary are in (b).	153
7.3	$\hat{\mu}$ summary plots with standalone fits for the different $n_{jet}$ regions for the standard, LI, and RF variable sets.	155
7.4	Pull comparison for signal process modeling NP's.	156
7.5	Pull comparison for all NP's but MC stats.	157
7.6	Pull comparison for jet NP's.	158
7.7	Pull comparison for MET NP's.	158
7.8	Pull comparison for Flavour Tagging NP's.	158
7.9	Pull comparison for $Z+jets$ NP's.	159
7.10	Pull comparison for diboson process modeling NP's.	159
7.11	NP correlations for standard variable fits.	159
7.12	NP correlations for LI variable fits.	160
7.13	NP correlations for RF variable fits.	160
7.14	Plots for the top 25 nuisance parameters according to their postfit impact on $\hat{\mu}$ for the standard (a), LI (b), and RF (c) variable sets.	161
7.14	Postfit $VZ$ plots in the 3+ jet, low pTV region for the RF variable set.	164
7.15	Postfit $VZ$ plots in the 2 jet, low pTV region for the RF variable set.	165
7.16	Postfit $VZ$ plots in the 2 jet, high pTV region for the RF variable set.	165
7.17	Postfit $VZ$ plots in the 3+ jet, high pTV region for the RF variable set.	166
7.18	Postfit $VZ$ plots in the 3+ jet, low pTV region for the LI variable set.	166
7.19	Postfit $VZ$ plots in the 2 jet, low pTV region for the LI variable set.	167
7.20	Postfit $VZ$ plots in the 2 jet, high pTV region for the LI variable set.	167
7.21	Postfit $VZ$ plots in the 3+ jet, high pTV region for the LI variable set.	168
7.22	Postfit $VZ$ plots in the 3+ jet, low pTV region for the standard variable set.	168
7.23	Postfit $VZ$ plots in the 2 jet, low pTV region for the standard variable set.	169
7.24	Postfit $VZ$ plots in the 2 jet, high pTV region for the standard variable set.	169
7.25	Postfit $VZ$ plots in the 3+ jet, high pTV region for the standard variable set.	170
7.26	Pull comparison for all NP's but MC stats.	170

7.27	Pull comparison for jet NP's. . . . .	171
7.28	Pull comparison for MET NP's. . . . .	171
7.29	Pull comparison for Flavour Tagging NP's. . . . .	171
7.30	Pull comparison for $Z+jets$ NP's. . . . .	172
7.31	Pull comparison for signal process modeling NP's. . . . .	172
7.32	NP correlations for standard variable fits. . . . .	172
7.33	NP correlations for LI variable fits. . . . .	173
7.34	NP correlations for RF variable fits. . . . .	173
7.35	Plots for the top 25 nuisance parameters according to their postfit impact on $\hat{\mu}$ for the standard (a), LI (b), and RF (c) variable sets. . . . .	174
7.36	Postfit $VH$ plots in the 3+ jet, low pTV region for the RF variable set. . . . .	176
7.37	Postfit $VH$ plots in the 2 jet, low pTV region for the RF variable set. . . . .	177
7.38	Postfit $VH$ plots in the 2 jet, high pTV region for the RF variable set. . . . .	177
7.39	Postfit $VH$ plots in the 3+ jet, high pTV region for the RF variable set. . . . .	178
7.40	Postfit $VH$ plots in the 3+ jet, low pTV region for the LI variable set. . . . .	178
7.41	Postfit $VH$ plots in the 2 jet, low pTV region for the LI variable set. . . . .	179
7.42	Postfit $VH$ plots in the 2 jet, high pTV region for the LI variable set. . . . .	179
7.43	Postfit $VH$ plots in the 3+ jet, high pTV region for the LI variable set. . . . .	180
7.44	Postfit $VH$ plots in the 3+ jet, low pTV region for the standard variable set. . . . .	180
7.45	Postfit $VH$ plots in the 2 jet, low pTV region for the standard variable set. . . . .	181
7.46	Binned S/B plots for the standard (a), LI (b), and RF (c) variable sets. Signal is weighted to $\mu = 1$ for comparison to the SM prediction. . . . .	181
8.1	$\mu$ summary plots for the standard, LI, and RF variable sets. The Asimov case (with $\mu = 1$ by construction) is in (a), and $\hat{\mu}$ best fit values and error summary are in (b). . . . .	185
9.1	Run 2 signal strength summary plots for 2 (WH/ZH, (a)) and 3 (o, 1, and 2 lepton, (b)) POI fits. . . . .	193
9.2	The raw and scaled coefficients for unfolding Run 1 (a and b) and Run 2 (c and d), respectively . . . . .	196
9.3	Ranks for the effective and unfolded JES NP Run1 combined workspaces. . . . .	199
9.4	Ranks for the effective and unfolded JES NP Run2 combined workspaces. . . . .	199
9.5	Ranks for the effective and unfolded JES NP Run1+Run2 combined workspaces. . . . .	200
9.6	Pull Comparisons: jesu—Jet Comb Unfold, <b>Comb Eff</b> , <b>Strong Unfold</b> , <b>Strong Eff</b> . . . . .	200
9.7	Pull Comparisons: jesu—JetMatched Comb Unfold, <b>Comb Eff</b> , <b>Strong Unfold</b> , <b>Strong Eff</b> . . . . .	201
9.8	Pull Comparisons: jesu—JetEff Comb Unfold, <b>Comb Eff</b> , <b>Strong Unfold</b> , <b>Strong Eff</b> . . . . .	201
9.9	Pull Comparisons: jesu—JetUnfold Comb Unfold, <b>Comb Eff</b> , <b>Strong Unfold</b> , <b>Strong Eff</b> . . . . .	202
9.10	Pull Comparisons: btag-b—BTagBo Comb Eff, <b>BTag Bo</b> . . . . .	204
9.11	Pull Comparisons: btag-b—BTagB Comb Eff, <b>BTag Bo</b> . . . . .	204

9.12	NP rankings for a combination featuring the weak JES scheme and a combination with the weak JES scheme + leading $b$ NP's correlated. . . . .	205
9.13	Ranked nuisance parameters for the Run1+Run2 combination. . . . .	208
9.14	$\hat{\mu}$ summary plot for a four parameter of interest fit. . . . .	210
9.15	$\hat{\mu}$ summary plot for a six parameter of interest fit. . . . .	211
9.16	$\hat{\mu}$ summary plot for a two parameter of interest (Run 1 and Run 2) values. . . . .	211
9.17	$\hat{\mu}$ summary plot for a two parameter of interest fit. . . . .	212
9.18	$\hat{\mu}$ summary plot for a three parameter of interest fit. . . . .	213
9.19	$\hat{\mu}$ summary plot for different $\sqrt{s}$ values. . . . .	213
A.1	Nominal residual plots; $\theta, \phi, \Delta\theta$ for $p_T = 100$ GeV muons . . . . .	224
A.2	The rms distributions of $\Delta\theta, \phi$ , and $\theta$ as a function of $\eta$ for $p_T = 100$ GeV; the final point in each plot is the rms obtained from a fit obtained from a fit to the fill distribution including all $\eta$ bins. . . . .	225
A.3	The rms distributions of $\Delta\theta, \phi$ , and $\theta$ as a function of $p_T$ . . . . .	226
A.4	The fitted rms of residual distributions for $\theta, \phi$ , and $\Delta\theta$ as a function of coincidence threshold for $p_T = 100$ GeV. . . . .	227
A.5	The raw rms of residual distributions for $\theta, \phi$ , and $\Delta\theta$ as a function of coincidence threshold for $p_T = 100$ GeV. . . . .	227
A.6	Nominal $\Delta\theta$ residual distribution for $p_T = 100$ GeV muons with coincidence thresholds $2X+1UV$ and $4X+4UV$ normalized to the same area and plotted together (top) as well as the ratio of the $2X+1UV$ distribution and the $4X+4UV$ per bin. . . . .	228
A.7	$\varepsilon_{alg}$ and as a function of coincidence threshold, $\eta$ (final point is $\varepsilon_{alg}$ integrated over all $\eta$ ), and $p_T$ . . . . .	229
A.8	$\varepsilon_{fit}$ and as a function of coincidence threshold, $\eta$ (final point is $\varepsilon_{fit}$ integrated over all $\eta$ ), and $p_T$ . . . . .	230
A.9	The distribution of highest slope-road coincidence thresholds in events; the o,o bin is the number of events passing selection requirements that fail to form the minimum $2X+1UV$ coincidence threshold necessary for a fit. . . . .	231
A.10	The algorithm and total efficiencies as a function of coincidence threshold for different background settings and slope-road sizes (standard and wide (one slope road as 1 VMM chip)). . . . .	233
A.11	The distribution of highest slope-road coincidence thresholds in events for the algorithm with wide slope-roads (width of 1 VMM) both without (a) and with (b) incoherent background; the o,o bin is the number of events passing selection requirements that fail to form the minimum $2X+1UV$ coincidence threshold necessary for a fit. . . . .	234
A.12	The three fit quantity residual rms values as a function of $p_T$ for different background settings and slope-road sizes (standard and wide (one slope road as 1 VMM chip)). . . . .	235
A.13	The rate of good BCID association based majority hit BCID as a function of $p_T$ and coincidence threshold. . . . .	236

A.14	The efficiencies as a function of coincidence threshold for charge thresholds of 0, 1, and 2.	238
A.15	The fit quantity residual rms values as a function of $p_T$ for charge thresholds of 0, 1, and 2.	238
A.16	The different misalignment cases as defined in the AMDB manual.	240
A.17	Nominal residual plots for the uncorrected cases; $\theta, \phi, \Delta\theta$ for $p_T = 100$ GeV muons	248
A.18	Nominal residual plots for the simulation corrected cases; $\theta, \phi, \Delta\theta$ for $p_T = 100$ GeV muons	248
A.19	Nominal residual plots as a function of $\eta$ with points as means and error bars as rms values in each $\eta$ bin for the angles $\theta, \phi, \Delta\theta$ for $p_T = 100$ GeV muons in the uncorrected case.	249
A.20	Nominal residual plots as a function of $\eta$ with points as means and error bars as rms values in each $\eta$ bin for the angles $\theta, \phi, \Delta\theta$ for $p_T = 100$ GeV muons in the corrected case.	250
A.21	The mean of the $\phi$ residual as a function of misalignment for the uncorrected case and the analytic and simulation correction cases.	252
A.22	The affected quantities of $\Delta z$ misalignments: $\theta$ bias, $\Delta\theta$ bias, and $\sigma_{\Delta\theta_{fit} - \Delta\theta_{tru}} / \sigma_{nominal}$ for both the misaligned and corrected cases.	253
A.23	The affected quantities of $\Delta t$ misalignments: $\theta$ bias, $\Delta\theta$ bias, and $\sigma_{\Delta\theta_{fit} - \Delta\theta_{tru}} / \sigma_{nominal}$ for both the misaligned and corrected cases.	254
A.24	The noticeable effects of rotations in the $s$ axis and the behavior of these quantities ( $\theta$ and $\Delta\theta$ bias shifts and $\sigma_{\Delta\theta_{fit} - \Delta\theta_{tru}} / \sigma_{nominal}$ ) with and without misalignment correction.	256
A.25	The effects of rotations in the $z$ axis on $\sigma_{\Delta\theta_{fit} - \Delta\theta_{tru}} / \sigma_{nominal}$ as a function of $\beta_z$ both with and without misalignment corrections.	257
A.26	The effects of rotation misalignments around the $t$ axis for $\phi$ bias and $\sigma_{\Delta\theta_{fit} - \Delta\theta_{tru}} / \sigma_{nominal}$ as a function of misalignment. The uncorrected and both the analytic and simulation correction cases are shown.	258
B.1	The mean and resolution of $p_T^{rec}/p_T^{tru}$ for the background $Z+jets$ sample for $ \eta  < 1.2$ and for $R = 0.4, 0.6, 1.0$ , and $1.5$ in 20 GeV bins of $p_T^{tru}$ for 20-200 GeV, one bin for 200-300 GeV, and one bin for 300-500 GeV, with bins chosen for purposes of statistics.	268
B.2	The $m_{bb}$ distribution for the telescoping jets with $R = 0.5, 1.0$ , and $1.5$ truth-level jets is shown for the signal and background samples in (a) and (b), respectively.	269
B.3	The 2D distribution of $m_{bb,R=0.9}$ vs. $m_{bb,R=0.4}$ is shown for signal and background truth-level samples in (a) and (b), respectively. The region chosen for the double $m_{bb}$ cut is outlined in orange.	270
B.4	Truth-level $\rho(z)$ distributions for the $m_{bb}$ window optimizing $(S/\delta B)_{t^*(z)}$ . $\rho_S(z)$ for the signal $ZH125$ sample is shown in (a), and $\rho_B(z)$ for the background $Z+jets$ sample is shown in (b). The distribution of $\rho_S(z) / \rho_B(z)$ for these samples is shown in (c).	276

B.5	A summary of the improvements for different truth-level telescoping jet cuts and weights is shown in bins of $p_T^Z$ . The final bin is the total improvement over all $p_T^Z$ . Shown are improvements for the 2D $m_{bb}$ cut (a), $t(z) = z$ (b), $t(z) = t^*(z)$ with 12 radii (c), and $t(z) = t^*(z)$ for various radii (d). . . . .	277
B.6	The $m_{bb}$ distribution for the telescoping jets with $R = 0.5$ , $R = 1.0$ , and $R = 1.5$ reconstructed-level jets is shown for the signal and background samples in (a) and (b), respectively. . . . .	278
B.7	The 2D distribution of $m_{bb,R=0.8}$ vs. $m_{bb,R=0.4}$ is shown for signal and background reconstructed-level samples in (a) and (b), respectively. The region chosen for the double $m_{bb}$ cut is outlined in orange. . . . .	279
B.8	Reconstructed-level $\rho(z)$ distributions for the $m_{bb}$ window optimizing $(S/\delta B)_{t^*(z)}$ . $\rho_S(z)$ for the signal $ZH125$ sample is shown in (a), and $\rho_B(z)$ for the background $Z+jets$ sample is shown in (b). The distribution of $\rho_S(z)/\rho_B(z)$ for these samples is shown in (c). . . . .	280
B.9	A summary of the improvements for different reconstructed-level telescoping jet cuts and weights is shown in bins of $p_T^Z$ . The final bin is the total improvement over all $p_T^Z$ . Shown are improvements for the 2D $m_{bb}$ cut (a), $t(z) = z$ (b), $t(z) = t^*(z)$ with 12 radii (c), and $t(z) = t^*(z)$ for various radii (d). . . . .	281

# Listing of tables

<p>1.1 Cross sections (in pb) for processes important to the SM <math>VH(b\bar{b})</math> analysis and the total Higgs cross section as a function of center of mass energy. Also given are the total number of Higgs bosons produced for given luminosities through both <math>WH</math> and <math>ZH</math> processes. Uncertainties are theoretical. . . . .</p> <p>1.2 Variables used to train the multivariate discriminant. Starred variables (<math>b</math>-tag scores) are not included in current versions of the standard discriminants, but have traditionally been included and most likely will be reintroduced as soon as their accompanying systematics are available. . . . .</p> <p>4.1 Summary of modeling systematic uncertainties, with background samples listed in order of importance. . . . .</p> <p>4.2 Summary of all systematic uncertainties on the <math>VH</math> cross section including their value, source and the corresponding nuisance parameter name. . . . .</p> <p>4.3 Summary of all systematic uncertainties on the <math>VH</math> acceptance and shapes originating from altering the PDF and <math>\alpha_S</math> uncertainties, including their corresponding nuisance parameter name. . . . .</p> <p>78table.caption.43</p> <p>4.5 The priors on the relative acceptance variations for <math>Z+hf</math>. The first column details the flavor components across which the acceptance variation is being considered, the second column lists the names of the corresponding nuisance parameter in the Profile Likelihood Fit, the third contains the value of the prior and the fourth column the processes and categories to which this nuisance parameter is applied. . . . .</p> <p>4.6 Effect of modeling systematics on <math>t\bar{t}</math> normalization in the 0 and 1-lepton analysis region. . . . .</p> <p>4.7 Effect of modeling systematics on <math>t\bar{t}</math> normalization in the 2lepton regions. The SysT-TbarPTV_L2_L2 systematic is implemented as a shape systematic over the full <math>VpT &gt; 75</math> GeV range, and as a result has different acceptance effects in the low and high <math>VpT</math> regions. Systematics are treated the same in both signal and control regions, and “lo” and “hi” refer to the <math>p_T^V</math> split in events. . . . .</p> <p>4.8 Summary of all shape uncertainties for the <math>t\bar{t}</math> process with short descriptions and the name of the corresponding nuisance parameters. . . . .</p> <p>4.9 Summary of all systematic uncertainties on the diboson cross section including their value, source and the corresponding nuisance parameter name. . . . .</p>	<p>II</p> <p>22</p> <p>74</p> <p>75</p> <p>76</p> <p>78</p> <p>79</p> <p>80</p> <p>80</p> <p>80</p> <p>81</p>
--	---

4.10	Summary of the systematic uncertainties on the VH acceptance in each analysis region and on the $p_T^V$ and $m_{b\bar{b}}$ shapes originating from altering the QCD scale, including their nuisance parameter name. . . . .	81
4.11	Summary of all uncertainties for the single top process with short descriptions and the name of the corresponding nuisance parameters, updated for the winter baseline analysis. . . . .	83
5.1	Summary table of triggers used in 2015 Data. . . . .	87
5.2	Summary table of triggers used in 2016 Data. . . . .	87
5.2	Electron selection requirements. . . . .	91
5.3	Muon selection requirements. . . . .	93
5.4	<code>AntiKt4EMTopoJets</code> selection requirements. The jet cleaning is applied via the JetCleaningTool, that removes events in regions corresponding to hot calorimeter cells. . . . .	101
5.5	$b$ -tagging working points available for MV2c10 for <code>AntiKt4EMTopoJets</code> . RR is the rejection rate (the inverse of efficiency). . . . .	107
5.6	Summary of the experimental systematic uncertainties considered. Details on the individual systematic uncertainties can be found in the given Sections of Ref. [10]. . . . .	114
5.6	Event selection requirements . . . . .	117
6.1	Full RF variable ranking study summary. Green (red) percentages represent gains (losses) in a validation significance at each step. . . . .	126
6.2	Variables used in MVA training. Variables in parentheses are only used in the $\geq 3$ jet regions. . . . .	129
7.1	Fit input segmentation. . . . .	149
7.2	Summary of modeling systematic uncertainties. . . . .	149
7.3	Summary of experimental systematic uncertainties. . . . .	150
7.4	Expected (for both data and Asimov) and observed $VZ \rightarrow \ell\ell b\bar{b}$ sensitivities for the standard, LI, and RF variable sets. . . . .	152
7.5	Summary of impact of various nuisance parameter categories on the error on $\mu$ for Asimov fits for the standard, LI, and RF variable sets. . . . .	162
7.6	Summary of impact of various nuisance parameter categories on the error on $\hat{\mu}$ for observed fits for the standard, LI, and RF variable sets. . . . .	162
7.7	Expected error breakdowns for the standard, LI, and RF variable sets . . . . .	175
7.8	Observed signal strengths, and error breakdowns for the standard, LI, and RF variable sets . . . . .	176
8.1	Expected (for both data and Asimov) and observed significances for the standard, LI, and RF variable sets. . . . .	183
8.2	Summary of error impacts on total $\mu$ error for principal categories in the Asimov standard, LI, and RF fits. . . . .	184

8.3	Summary of error impacts on total $\hat{\mu}$ error for principal categories in the observed standard, LI, and RF fits. . . . .	184
9.1	Summary of common signal event selections and the 2-lepton analysis. . . . .	190
9.2	Summary of event selections in the 0-lepton analyses. . . . .	190
9.3	Summary of event selections in the 1-lepton analyses. . . . .	191
9.4	Observed significance from an unconditional fit to the data corresponding to $36.1 \text{ fb}^{-1}$ and expected significances from a fit to an Asimov dataset and from a fit to the data. Expected significances from individual regions are estimated separately. . . . .	193
9.5	Expected and observed sensitivities for Run 1, Run 2, and combined workspaces with effective and unfolded JES NP's. . . . .	196
9.6	Error on signal strength breakdowns for Run 1 workspaces with effective and unfolded JES NP's. . . . .	197
9.7	Error on signal strength breakdowns for Run 2 workspaces with effective and unfolded JES NP's. . . . .	197
9.8	Error on signal strength breakdowns for combined workspaces with effective and unfolded JES NP's. . . . .	197
9.9	Expected sensitivities for both effective and unfolded combined workspaces using the strong and weak JES correlation schemes. . . . .	198
9.10	Error on signal strength breakdowns for both effective and unfolded combined workspaces using the strong and weak JES correlation schemes. . . . .	198
9.11	Expected and observed sensitivities for a combination featuring the weak JES scheme, combination with the weak JES scheme + leading $b$ NP's correlated, and the $b$ correlation with the 8 TeV NP with sign unflipped. . . . .	203
9.12	Run 1 + Run 2 W+jets modeling correlation projections . . . . .	203
9.13	$\chi^2$ extrapolation correlation tests for W+jets modeling and various levels of assumed correlation between Run 1 and Run 2. . . . .	206
9.14	The final Run 1+Run 2 NP correlation scheme. . . . .	207
9.15	Summary of the impact of different nuisance parameter categories on the total error on $\hat{\mu}$ for the combined Run1+Run2 fit. . . . .	209
9.16	Summary of multiple POI compatibilities. The well-known Run 1 7 TeV 0-lepton deficit is responsible for the low compatibility with the 6 and 3 POI fits. . . . .	209
9.17	A summary of main results for the Run 1, Run 2, and combined fits. . . . .	212
10.1	Summary of performance figures for the standard, LI, and RF variable sets. Uncertainties on $\hat{\mu}$ are quoted stat., syst. In the case of the latter two, % differences are given where relevant. Differences in errors on $\mu$ are on full systematics and total error, respectively. . . . .	216
A.1	The fitted (absolute) $\sigma$ of fit quantity residuals in mrad under different algorithm settings. . . . .	235

A.2	A summary of notation used in this section: note that non-AMDB notation is used in this section. . . . .	240
A.3	A summary of corrections with additional constants/operations (written as $n_{const}c/n_{ops}op$ ; $n_X$ is the number of X hits in a fit) necessary for analytic corrections. Yes means a correction exists but might not entirely remove misalignment effects, while yes+ means a quality of correction is only limited by knowledge of misalignment and memory . . . . .	246
A.4	A summary of levels of misalignment corresponding to a 10% degradation in any residual rms or, for biases shifts of, 0.01 mrad for $\theta$ , 1 mrad for $\phi$ , and 0.25 mrad for $\Delta\theta$ for both the uncorrected and corrected cases; $> 5$ mm and $> 1.5$ mrad mean that such a degradation does not occur for the range of misalignment studied. Most affected quantity in parentheses. . . . .	260
B.1	A summary of basic event selection requirements. Truth-level $b$ -tagging is done with truth-level information. . . . .	266
B.2	Topological requirements of the event selection. . . . .	266
B.3	$m_{bb}$ windows studied. These windows were chosen to optimize significances over all $p_T^Z$ . . . . .	275
B.4	A summary of significances for different weighting schemes and cuts and for reconstructed and truth jets for a luminosity of $20.3 \text{ fb}^{-1}$ . $\text{akt4}$ refers to the standard cut-based analysis using anti- $k_t$ with $R = 0.4$ jets. Column titles are $p_T^Z$ regions in GeV. . . . .	281

TO ALL OF MY TEACHERS AND MENTORS THROUGH THE YEARS.

# Acknowledgments

AN ENDEAVOR as ponderous as PhD is not possible without the support of many, and mine was no exception. First and foremost, I would like to thank my advisor, John Huth. Without John's support and wisdom in physics, primitive navigation, and so much else, the last six years would have neither been possible, and I can safely say the experience would not have been nearly so intellectually fulfilling. It has been an honor and a pleasure to have Matt Schwartz and Gary Feldman as my other two committee members, and their ideas and guidance certainly shaped the character of the research in these pages.

Doing research as a member of the ATLAS collaboration has certainly been an educational experience, and I have been very fortunate to have Harvard ATLAS members past and present as colleagues. Many thanks to Professors Melissa Franklin and Masahiro Morii for their sage counsel and genuine care for students on both sides of the Atlantic. A big thank you to David Lopez Mateos—I could not have done any of the research in this thesis without his guidance and watchful tutelage. It has also been a joy collaborating with Chris Rogan, whose RestFrames concept features prominently in this thesis. There are many other Harvard ATLAS members to whom I am indebted for their invaluable conversation, company, and companionship. Chief among these is Tony Tong, a most stolid roommate and friend. I would be remiss I did not also express heartfelt thanks to Karri,

Emma, Ann, Paolo Giromini (a conversationalist *par excellence*), William, Tomo, Tuna, Brian, Kevin, Andy, Julia, Jennifer, Stefano, Valerio, Larry, Pierluigi, Ben, Roger, and Joao. Not to be forgotten are the many fine folks in ATLAS at large and in HSG5, in particular Paolo Francavilla and Yuji Enari.

Even shuffling between continents, Harvard has felt like home. Sincere thanks to Lisa and Carol for being ready sources of candy, conversation, commiseration, and of course administrative support. Thank you as well to Angela, Korin, Felice, and all the other LPPC staff who made navigating bureaucracy in three countries and two timezones so much easier. To Erin and Sarah—we made it!

Finally, I would like to send love and thanks to my family, in particular to my mother, father, and my sister, Emily. I could not have done it without you.

吾生也有涯，而知也无涯。以有涯隨无涯，殆已；  
已而為知者，殆而已矣。

Zhuangzi, Book 3

# 0

## Introduction

SINCE THE DISCOVERY of a Standard Model (SM) like Higgs boson at the LHC in 2012[11][12], one of the main outstanding physics goals of the LHC has been to observe the primary SM Higgs decay mode,  $H \rightarrow b\bar{b}$ , with efforts primarily targeted at searching for Higgs bosons produced in association with a leptonically decaying vector ( $W$  or  $Z$ , denoted generically as  $V$ ) boson. This primary

Higgs decay mode also offers the best opportunity to observe direct Higgs coupling to quarks. As the integrated luminosity of data collected at the LHC increases,  $H \rightarrow b\bar{b}$  searches will increasingly become limited by the ability to constrain systematic uncertainties, with the latest result from ATLAS at  $\sqrt{s} = 13$  TeV using  $36.1\text{ fb}^{-1}$  of  $pp$  collision data already approaching this regime, having a  $VH(b\bar{b})$  signal strength of  $1.20^{+0.24}_{-0.23}(\text{stat.})^{+0.34}_{-0.28}(\text{syst.})$  at  $m_H = 125$  GeV [13].

While this effort will likely require a combination of several different methods at various different stages in the analysis chain, one possible avenue forward is to revise the multivariate analysis (MVA) discriminant input variables used, as various schemes offer the promise of reducing systematic uncertainties through more efficient use of both actual and simulated collision data. This thesis discusses two such alternate MVA schemes, the RestFrames (RF) and Lorentz Invariants (LI) variables, in the context of the 2-lepton channel of the Run 2 analysis in [13] and [14], henceforth referred to as the “fiducial analysis,” before a brief discussion of combinations across channels and datasets.

Electroweak symmetry breaking, Standard Model Higgs production and decay, and event level variables are treated in Chapter 1. The Large Hadron Collider and ATLAS detector are the subject of Chapter 2. Data and simulation samples used are described in Chapter 3. Signal and background modeling with accompanying systematics are defined in Chapter 4. Object and event reconstruction definitions and event selection requirements are outlined in Chapter 5. The multivariate analysis, including a description of the LI and RF variable sets and a summary of performance in the absence of systematic uncertainties, is described in Section 6. The statistical fit model and systematic uncertainties are described in Section 7, and the fit results may be found in Chapter 8. Combining channels

and datasets at different  $\sqrt{s}$  values is discussed in the context of the Run 1 + Run 2 SM  $VH(b\bar{b})$

combination in Chapter 9. Finally, conclusions and closing thoughts are presented in Chapter 10.

Editorial notes:

1. pdf will be *probability* distribution function
2. PDF will be *parton* distribution function
3. Unless otherwise stated, ATLAS and LHC/CERN images are from public available material from experiment webpages. Copyright terms may be found here <https://atlas.cern/copyright>.

*The relationship between theorists and experimentalists  
is like that between a truffle farmer and his pig*

Howard Georgi

# 1

## The Standard Model Higgs and Collider

### Event Variables

MUCH HAS BEEN SAID about the so-called Standard Model (SM) of particle physics, so only the bare essentials of electroweak symmetry breaking and Higgs production relevant to SM  $VH(b\bar{b})$  will

be addressed here. This discussion follows [15] Chapter 11 in both content and notation. We then move onto the treatment of kinematic variables in collider events, including the two novel schemes considered in this thesis, the Lorentz Invariants (LI) and RestFrames (RF) concepts.

### 1.1 THE STANDARD MODEL HIGGS BOSON

The generic scalar Lagrangian potential (the kinetic term will be addressed later) for a scalar in the SM is:

$$V(\Phi) = m^2 \Phi^\dagger \Phi + \lambda (\Phi^\dagger \Phi)^2 \quad (1.1)$$

where  $\Phi$  is a complex scalar doublet field under  $SU(2)$  from which the physical Higgs emerges after symmetry breaking. Its four degrees of freedom are typically decomposed as follows:

$$\Phi = \frac{1}{\sqrt{2}} \begin{pmatrix} \sqrt{2}\phi^+ \\ \phi^0 + i\alpha^0 \end{pmatrix} \quad (1.2)$$

$\phi^+$  is the complex charged component of the Higgs doublet, and  $\phi^0$  and  $\alpha^0$  are the CP-even and CP-odd neutral components, respectively.

If the sign of  $m^2 \Phi^\dagger \Phi$  is negative,  $\Phi$  acquires a *vacuum expectation value* or VEV:

$$\langle \Phi \rangle = \frac{1}{\sqrt{2}} \begin{pmatrix} 0 \\ \sqrt{\frac{2m^2}{\lambda}} \end{pmatrix} \quad (1.3)$$

with this value typically denoted  $v = \sqrt{2m^2/\lambda} = (\sqrt{2}G_F)^{-1/2} \approx 246$  GeV (with the coupling

of the 4-Fermi effective theory of weak interactions measured through experiments involving muon decay), and  $\phi^0$  is rewritten as  $\phi^0 = H + v$ .

This non-zero VEV induces spontaneous symmetry breaking in the SM's gauge (local) symmetry group of  $SU(3)_C \times SU(2)_L \times U(1)_Y$  since the VEV does not respect the  $SU(2)_L \times U(1)_Y$  symmetry of the Lagrangian (i.e.  $\langle \Phi \rangle$  is not invariant under a gauge transformation of this group). Three of the four generators of this subgroup are spontaneously broken, which implies the existence of three massless Goldstone bosons, which are in turn “eaten” by linear combinations of the  $W^a$  (with coupling strength  $g$ ) and  $B$  (with coupling strength  $g'$ ) bosons to form the longitudinal polarizations of the familiar  $W^\pm$  and  $Z$  bosons, with the last generator giving rise to the usual, unbroken  $U(1)_{EM}$  symmetry and its massless photon,  $A$ , as well as the scalar Higgs boson  $H$ . To see this, one starts with the full Higgs SM Lagrangian (kinetic minus potential only)

$$\mathcal{L}_{Higgs} = (D_\mu \Phi)^\dagger (D_\mu \Phi) - V(\Phi), \quad D_\mu \Phi = (\partial_\mu + ig\sigma^a W_\mu^a + ig' Y B_\mu / 2) \Phi \quad (1.4)$$

One simply plugs in the reparametrized  $\Phi$  with  $\phi^0 = H + v$ , collects the terms involving  $v$  together with the appropriate  $W$  and  $B$  kinetic terms to extract:

$$M_W^2 = \frac{g^2 v^2}{4}, \quad M_Z^2 = \frac{(g'^2 + g^2) v^2}{4} \quad (1.5)$$

This is left as an exercise for the reader; this exercise also makes manifest that the Higgs couples with the  $W^\pm$  and  $Z$  with strength quadratic in the gauge boson masses. Since the Higgs field also respects

the  $SU(3)_C$  color symmetry, the eight gluons are also left massless, and the  $H$  is left interacting with photons and gluons primarily through heavy quark loops (i.e. no tree-level interactions).

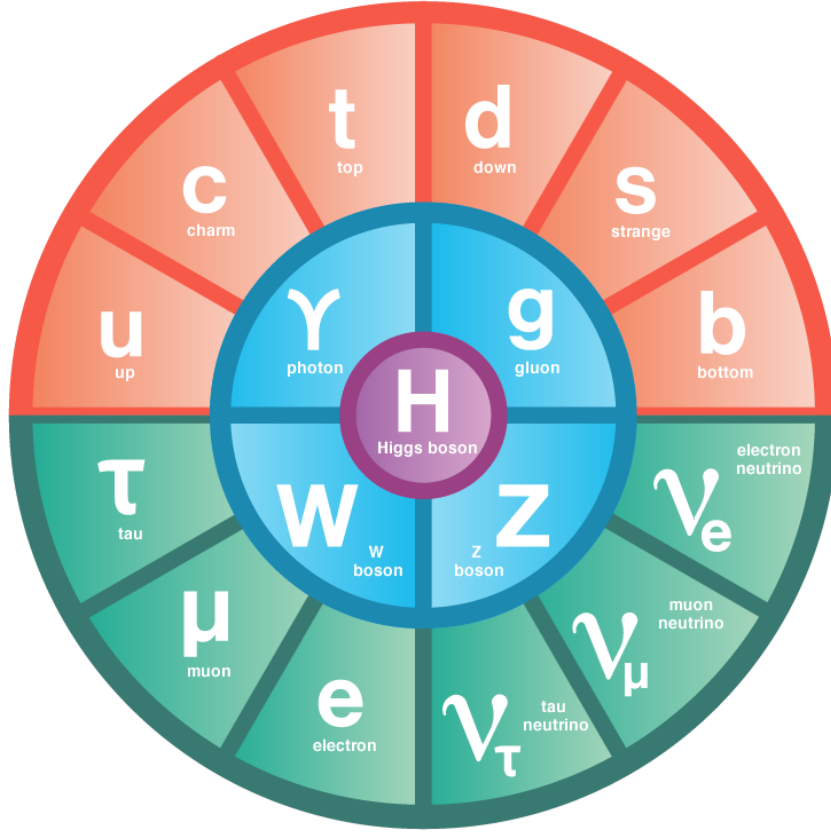


**Figure 1.1:** The fundamental particles of the Standard Model. IC: [1]

The Higgs is often introduced to the public at large as the mechanism through which fundamental fermions (enumerated in Figure 1.1) acquire mass—this is through the Yukawa interactions of the Higgs:

$$\mathcal{L}_{Yukawa} = -\hat{h}_{d_{ij}} \bar{q}_{L_i} \tilde{\Phi} d_{R_j} - \hat{h}_{u_{ij}} \bar{q}_{L_i} \tilde{\Phi} u_{R_j} - \hat{h}_{l_{ij}} \bar{l}_{L_i} \tilde{\Phi} e_{R_j} + h.c. \quad (1.6)$$

where  $\tilde{\Phi} = i\sigma_2 \Phi^*$ ,  $q_L$  ( $l_L$ ) and  $u_R$ ,  $d_R$  ( $e_R$ ) are the quark (lepton) left-handed doublets and right

handed singlets of the weak  $SU(2)_L$  group, with each term parametrized by a  $3 \times 3$  matrix in family space (also known as the fermion generations). The neutrinos have been purposely omitted since the mechanism that generates their mass is as of yet unknown, though these Yukawa interactions could have a non-zero contribution to neutrino masses. Once the Higgs VEV value is known and the Yukawa interaction matrices  $\hat{h}_{f_i j}$  (with  $i, j \in \{1, 2, 3\}$ ) are diagonalized, the fermion masses can simply be written as  $m_{f_i} = b_{f_i} v / \sqrt{2}$ . The SM has no motivation for any of these mass values, instead leaving them as empirically determined free parameters.

Note that from  $\mathcal{L}_{Yukawa}$ , it is easy to see that the Higgs couplings with fermions scale linearly with fermion mass. Higgs self-couplings and beyond the standard model (BSM) Higgs scenarios are beyond the scope of this thesis.

## 1.2 HIGGS BOSON PRODUCTION AND DECAY AT THE LARGE HADRON COLLIDER

The leading order Feynman diagrams for the four dominant modes of Higgs production at the LHC are shown in Figure 1.2, each described briefly in turn. The dominant process, accounting for some 87% of Higgs production at the nominal LHC center of mass energy of 14 TeV, is gluon-gluon fusion (ggF), shown at top left in Figure 1.2. At high center of mass energies, most of a proton's momentum is predominantly carried by gluons (as opposed to the constituent valence quarks associated with the hadron's identity). This, along with the difficulties associated with high luminosity antiproton beam production, is why the LHC was designed as a proton-proton collider instead of a proton-antiproton collider (like the Tevatron or SppS). As mentioned above, the Higgs does not couple directly to gluons but must instead be produced through the fermion loop shown in the fig-

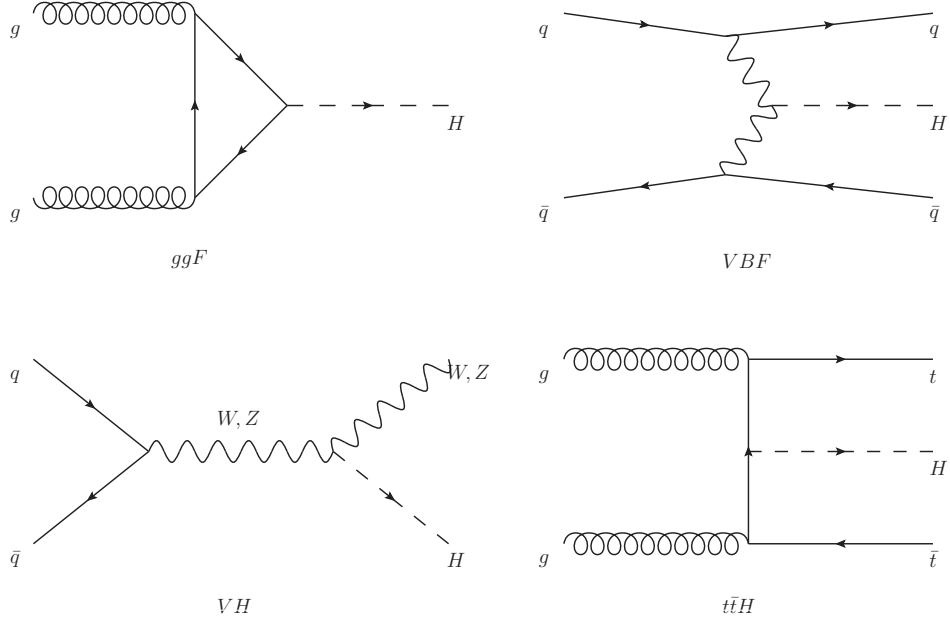


**Figure 1.2:** Dominant Higgs production modes.

ure. The heaviest fundamental fermion by far is the top quark, with  $m_t = 173$  GeV, so top loops dominate this process. While not particularly relevant for this thesis, about 14% of events in the 2-lepton channel of the  $H \rightarrow b\bar{b}$  analysis are ggF initiated.

The next most prevalent process is vector boson fusion (VBF), where vector bosons ( $W$  or  $Z$ , denoted generically as  $V$ ) from quarks in the colliding protons “fuse” to form a Higgs. These quarks typically form jets in the forward region, which provide a unique signature for this process. This process is not relevant for this thesis.

The third leading process is “Higgsstrahlung” or Higgs production in association with a vector boson, often simply  $VH$  production. In this process, a quark-antiquark pair in the colliding protons forms an energetic vector boson, which then radiates a Higgs (this is similar to photon emission of

accelerating electrons, called “Bremsstrahlung,” hence the name). Some fraction of the time (about 21% of the time for  $WH$  and 6.7% of the time for  $ZH$ ), the energetic  $V$  will decay leptonically (i.e. into a decay involving an electron or a muon), which provides a unique and triggerable signature for this process. Another 20% of the time for  $ZH$  production, the  $Z$  will decay to neutrinos, which are not absorbed by detectors and show up as missing transverse energy ( $\vec{E}_T^{\text{miss}}$ ), another triggerable signature. This ability to trigger on leptons and  $\vec{E}_T^{\text{miss}}$  and the requirement that this leptonic signature be consistent with a  $V$  allow one to significantly reduce the impact of multijet background (a very common generic processes at the LHC) on analysis. Hence, this is the process of primary importance to this thesis.

The final important Higgs production process is  $t\bar{t}H$  production, the box diagram in the lower right of Figure 1.2. Again, the top pair provides a useful signature for analysis. This, like VBF, is also not considered in this thesis.

Once the Higgs has been produced, it can decay in a number of ways, as shown in Figure 1.3. By far the most dominant decay mode of the Higgs is to  $b\bar{b}$  with a branching fraction of 58%. This  $b$ -quark pair then hadronizes into two  $b$ -jets (for a more thorough discussion of jets and  $b$ -jets in particular, see Section 5.5). However, many processes at the LHC create pairs of  $b$ -jets with invariant masses consistent with the Higgs and have much higher production rates ( $t\bar{t}$  production at the LHC is in the neighborhood of hundreds of pb, compared to Higgs cross sections of a few pb), so a clear process signature is necessary to study  $H \rightarrow b\bar{b}$  production at the LHC. This is why the bulk of search efforts have focused on  $VH$  production. A summary of Higgs production cross sections and simple extrapolations to raw numbers of Higgs bosons produced for  $VH$  for leptonically decaying  $V$

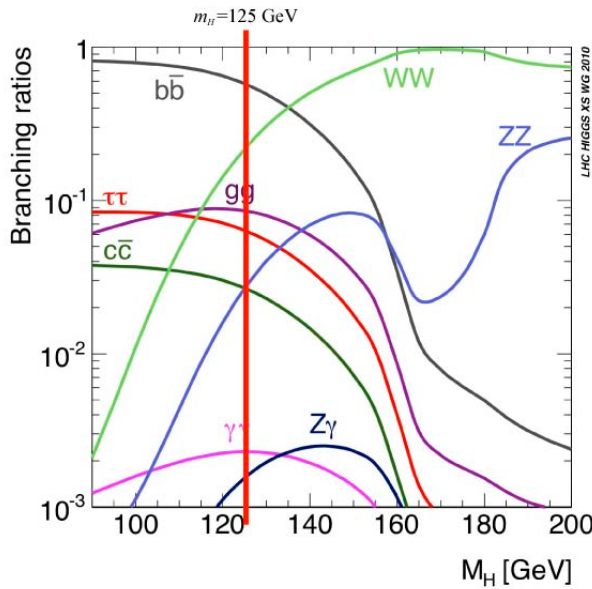


**Figure 1.3:** Higgs decay mode branching fractions as a function of its mass; a line has been drawn at the observed Higgs mass of 125 GeV.

is shown in Table 1.1

**Table 1.1:** Cross sections (in pb) for processes important to the SM  $VH (b\bar{b})$  analysis and the total Higgs cross section as a function of center of mass energy. Also given are the total number of Higgs bosons produced for given luminosities through both  $WH$  and  $ZH$  processes. Uncertainties are theoretical.

$\sqrt{s}$ (TeV)	ZH	WH	ggF	total $\sigma$	$N_{V \rightarrow \ell^+ \nu H}$
7	$0.34^{+4\%}_{-4\%}$	$0.58^{+3\%}_{-3\%}$	$15.3^{+10\%}_{-10\%}$	17.5	$4.7 \text{ fb}^{-1} \rightarrow 589$
8	$0.42^{+5\%}_{-5\%}$	$0.70^{+3\%}_{-3\%}$	$19.5^{+10\%}_{-11\%}$	22.3	$20.3 \text{ fb}^{-1} \rightarrow 3100$
13	$0.88^{+5\%}_{-5\%}$	$1.37^{+2\%}_{-2\%}$	$44.1^{+11\%}_{-11\%}$	50.6	$36.1 \text{ fb}^{-1} \rightarrow 11100$
14	$0.99^{+5\%}_{-5\%}$	$1.51^{+2\%}_{-2\%}$	$49.7^{+11\%}_{-11\%}$	57.1	$1000 \text{ fb}^{-1} \rightarrow 343000$

### 1.3 COLLIDER EVENTS AND EVENT LEVEL VARIABLES

Collision data in experiments like ATLAS is structured using what is known as the *event data model*.

In this model, one collision corresponds to one event. Since each bunch crossing contains more than one proton, there can be more than one collision per event and more than one hard scatter per collision. For each collision, tracks in an experiment's inner detector are used to identify the most energetic collision, which is taken to be the event. The raw data, the various tracks, energy deposits, and hits in the detector, undergo reconstruction (described at length in Chapter 5) both through automated, experiment-wide, standardized production and through analysis-specific level selections, corrections, and calibrations. The result of this considerable effort is a collection of labeled 4-vectors, representing the final state objects. This is shown in Figure 1.4.

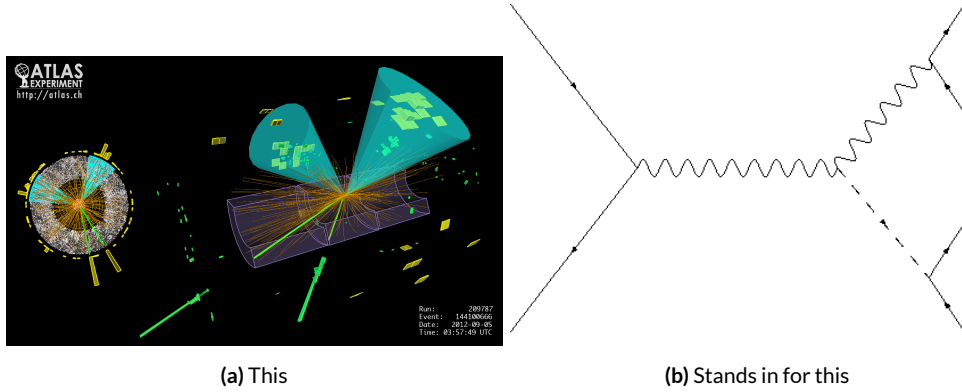


**Figure 1.4:** Reconstruction in a nutshell. You can (not) see the Higgs.

In the process that is the focus of this thesis, every event ultimately is condensed into a lepton pair (two electrons or two muons), two or three jets\*, all 4-vectors, and a  $\vec{E}_T^{\text{miss}}$  vector in the transverse

---

\*Sometimes more, though this is a small fraction of events, and the wisdom of this choice may be ques-

plane. Further selection then takes place to winnow down events into interesting regions of phase space hopefully more rich in signal-like events. Once events are selected in a search like the one in this thesis, one then analyzes the data to test its consistency with some background only hypothesis to produce the usual statistical results. This can be done in various ways, with principal approaches being: a simple counting experiment (often referred to as the “cut and count” approach), a functional fit for excesses over a falling background spectrum (the so-called “bump hunt” used in analyses like the  $H \rightarrow \gamma\gamma$  discovery channel), or the use of discriminant distributions as PDF’s in a likelihood fit (the approach of this analysis). These distributions can be simple counts (i.e. single bin distributions) in analysis regions, quantities of interest (the distribution of the invariant mass of the two  $b$ -jets in selected events with the greatest transverse momenta,  $m_{bb}$ , is used as a validation), or a multivariate analysis (MVA) discriminant.

#### 1.4 CHARACTERIZATION WITH EVENT-LEVEL VARIABLES

Traditionally, particle physicists have favored the approach of using distributions of physical variables since it is easier to develop physical intuition for what these distributions should look like during validation, so it is no surprise that as many LHC analyses have transitioned to using MVA techniques that these variables form the basis of many very robust physics results. These variables do quite well summarize many of the main physics features of an event for the signal topology, certainly much better than feeding all 18–22 4-vector components directly into a machine learning algorithm. In  $ZH \rightarrow \ell\ell b\bar{b}$  events, for example, one wishes to characterize the  $ZH$  system by using the

---

tioned

lepton pair as a stand-in for the  $Z$  and the  $b$ -jet pair as a stand-in for the  $H$ , and composite variables like  $m_{bb}$  and  $m_{\ell\ell}$  can be used to check whether events are consistent with these objects. There are also variables like  $p_T^V$  that characterize the momentum scale of the event, angles like  $\Delta R(b_1, b_2)$  and  $\Delta\phi(V, H)$  that can be further used to characterize the overall “shape” of these events, and variables like  $\vec{E}_T^{\text{miss}}$  that can discriminate against backgrounds like  $t\bar{t}$  that do not have a closed topology.

Nevertheless, the intuition based approach, with incremental addition of variables as they prove useful in the lifetime of an analysis’s iterations, does beg the question of whether there is a more systematic way to treat this information. There are clearly patterns to which variables are useful: these correspond to important information about the hypothesized physics objects and their relationships, and there have been many attempts to systematize the way these variables are found. Such systematic, top-down approaches often promise to increase performance in two ways. The first is by having higher descriptive power, often through some sophisticated treatment of the missing transverse energy in an event,  $\vec{E}_T^{\text{miss}}$ .  $\vec{E}_T^{\text{miss}}$  is just a single quantity, and if there is just one invisible object in a desired event topology, using  $\vec{E}_T^{\text{miss}}$  on its own often provides sufficient sensitivity. In more complicated topologies with multiple invisible particles in the final state, for example in many supersymmetry searches, a more careful treatment of the missing energy is often necessary.

The second means of improvement is through using a more orthogonal basis of description, which allows one to more efficiently use data and simulation samples. A more orthogonal basis implies that variables contain less overlapping information with each other and so allow for a more efficient exploration of parameter space. This means one can gain higher sensitivity from equivalent datasets using a more orthogonal basis. To see why this might be the case, take an MVA discrimi-

nant for  $ZH \rightarrow \ell\ell b\bar{b}$  formed using only the classic variables  $\Delta R(b_1, b_2)$  and  $p_T^V$ . In the  $ZH \rightarrow \ell\ell b\bar{b}$  topology, the transverse mass of the  $Z$  and  $H$  (and hence the lepton pair and jet pair) are equivalent. This means that at higher  $p_T^V$  the  $p_T$  of  $b$ -jets will also be higher, which in turn implies that they will have a smaller angle of separation and hence a smaller  $\Delta R(b_1, b_2)$ . This correlation is not unity—each variable still does have information the other does not—but is still very high. Hence, when training an MVA, which in principle knows nothing about these variables other than some set limits, an undue number of training events will be wasted converging upon relations that could be known *a priori*, and while this might be easy to hard code in for a two variable toy example, the dimensionality of any real discriminant makes this prohibitive. An MVA that uses data (both actual and simulated) more efficiently will also tend to be have lower variance, offering a potential avenue for reduction in the error on quantities of interest due to systematic uncertainties. Details of how this plays out in a likelihood fit will be deferred to the discussion of the fit model used in the  $VH(b\bar{b})$  search in Chapter 7.

Many of these novel schemes are designed to explicitly address the first issue of invisibles in the final state in channels where it is of paramount importance while having the second issue as something of a fringe benefit. However, as the amount of data taken at the LHC grows, analyses will increasingly become systematics limited, so an exploration to the veracity of the second claim has great potential for the high luminosity era of the LHC. The  $ZH \rightarrow \ell\ell b\bar{b}$  process offers a great setting for investigating this issue on its own since its closed topology largely mitigates any improvement from more sophisticated treatments of  $\vec{E}_T^{\text{miss}}$ . We introduce two of these more top-down approaches to event-level variables below: the “Lorentz Invariant” (LI) [[16](#)] and “RestFrames inspired” (RF) [[17](#)]

variable schemes. A broad overview of the concepts behind these schemes will be given here, with a more in-depth discussion of their implementation deferred until Chapter 6.

## 1.5 LORENTZ INVARIANTS

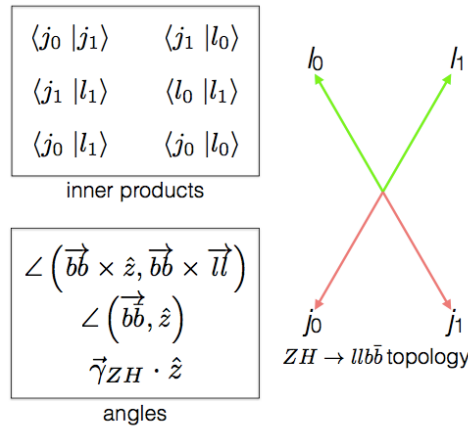


Figure 1.5: Summary of LI variables in the  $ZH \rightarrow \ell\ell b\bar{b}$  topology.

The LI variables, first put forth by S. Hagebeck and others [16], are based upon the concept that once the 4-vectors of an event are determined, all of the information in an event are encoded into their inner products (Lorentz invariant quantities, hence the name) and the angles between them. This makes for 16 quantities in all: the ten inner products of the 4-vectors, the three Euler angles, and the three parameters specifying the boost of the  $ZH$  system. The masses of the four final state objects are not considered very useful and so can be removed to leave six meaningful inner products (the  ${}_4C_2$  combinations<sup>†</sup> between distinct final state 4-vectors). Since these inner products can have

---

<sup>†</sup> ${}_nC_r = \frac{n!}{r!(n-r)!}$ , read “ $n$  choose  $r$ ” and known as the binomial coefficient, is the number of unique possible ways to choose combinations of  $r$  objects from a total set of  $n$  without regard to ordering within combinations.

an ill-defined physical interpretation and in order to help MVA training, each inner product is scaled by:

$$x \rightarrow \frac{x}{x + c} \quad (1.7)$$

where  $c$  is the mean of the distribution in the signal MC distribution. These inner products are denoted  $x_i_y_j$ , where  $x$  and  $y$  are either  $j$  (for jet) or  $l$  (for lepton) and the indices are either  $o$  ( $i$ ) for the leading (subleading) object by  $p_T$  in the event.

The number of useful angles can be reduced by recognizing some symmetries inherent in the final state. The symmetry around the beam axis eliminates one angle. Furthermore, the boost of the  $VH$  system is primarily in the beam direction ( $z$ ) direction, marginalizing the utility of the transverse boost angles. This leaves the boost in the  $z$  direction, denoted `gamma_ZHz`, and two angles chosen to be the angle between the  $b\bar{b}$  system and the beam (`angle_bb_z`) and the angle between  $(\vec{b}_1 + \vec{b}_2) \times \hat{z}$  and  $(\vec{b}_1 + \vec{b}_2) \times (\vec{l}_1 + \vec{l}_2)$  (`angle_bbz_bbll`).

These variables do contain a lot of information similar to the usual set: there are mass equivalents ( $j_0 \leftrightarrow m_{bb}$ , and  $l_0 \leftrightarrow m_{\ell\ell}$ ) and angles. Instead of individual final state object scales, there are the four jet/lepton inner products, though this correspondence (and indeed any physical interpretation) is far from clear. An important advantage of the LI variable set is that all of the variables are in it are orthogonal in the signal case by construction. A drawback of this framework in a completely closed final state is that there is no way to treat  $E_T^{miss}$  in a Lorentz invariant way.

There is also no prescription for any additional jets in the event beyond the two  $b$ -tagged jets.

They are simply ignored in these variable calculations since the fiducial analysis requirement of exactly two  $b$ -tagged jets eliminates any combinatoric ambiguity, and additional, untagged jets are assumed (not entirely rigorously) to be unrelated to the signal-like hard scatter.

## 1.6 RESTFRAMES VARIABLES

The RestFrames variables [17], calculated using the software package of the same name, is based upon the idea that the most natural frame in which to analyze objects of the signal decay tree is in their individual production (rest) frames. The signal decay tree for  $ZH \rightarrow \ell\ell b\bar{b}$  is show in Figure 1.6. Generally, one does not typically have enough information to determine exactly each of the in-

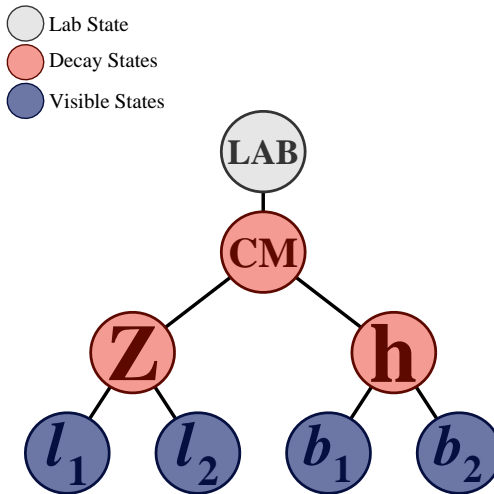


Figure 1.6: The  $ZH \rightarrow \ell\ell b\bar{b}$  decay tree.

termediate rest frames or the boosts between the frames, but in a completely closed final state like  $ZH \rightarrow \ell\ell b\bar{b}$ , this can be done in the usual way by adding the 4-vectors of the final state objects and solving the usual equations from special relativity (RestFrames does this automatically for each

event).

Each frame has associated with it the boost from its immediate parent and a mass scale; that mass (in this case the correspondence between RF mass variables and standard mass variables is exact) and the angles between the Euclidean three vector associated with boost and the axis of the decay products provide useful variables. In general, the polar angle (typically given as a cosine) is considered more useful than the azimuthal angle (typically just a  $\Delta\phi$ ), though this is dependent on the candidate decay tree. The  $Z$  frame, for example, has  $MZ$ , which is just the usual  $m_{\ell\ell}$ ,  $\cos Z$ , the cosine of the polar angle between the lepton momentum axis in their production frame and the boost from the  $ZH$  center of mass (CM) frame, and the angle  $d\phi_{CMZ}$ .

In addition to the masses and angles attached to individual object rest frames, energy scales associated with the CM frame can be used to contextualize other event level quantities. In particular, one can use the mass of the CM frame as a natural scale to evaluate the momentum of the CM frame, and the  $p_T$  of the CM frame as a natural scale for the event's  $E_T^{miss}$ , yielding the variables:

$$R_{p_T} = \frac{p_{T,CM}}{p_{T,CM} + M_{CM}}, \quad R_{p_z} = \frac{p_{z,CM}}{p_{z,CM} + M_{CM}}, \quad R_{met} = \frac{E_T^{miss}}{E_T^{miss} + p_{T,CM}} \quad (1.8)$$

denoted  $R_{pT}$ ,  $R_{pz}$ , and  $R_{met}$ . These can be thought of as behaving like significance based variables in particle physics, like METHT or impact parameter significances, or event level defined versions of the scalings applied to the LI inner products. These are used instead of the final state object scales and standard  $E_T^{miss}$  of the standard variable set.

Unlike the LI variables, the physical interpretation of RF variables is very clear. Everything has

physical units, and these are variables one might have introduced in the usual process of developing an MVA with the traditional mindset. The solution to the issue of additional jets in an event is not immediately clear. In order to keep the two non-standard MVA's on as equal footing as possible, the approach of simply ignoring additional jets is taken in this thesis. Nevertheless, it would be easy enough to redefine the  $H$  intermediate frame to have, for example, the two  $b$ -tagged jets and the highest  $p_T$  untagged jet for any subset of events. This flexibility is not a feature of the Lorentz Invariants framework. Of course, `RestFrames` cannot tell you what approach to take, but it is capable of handling more flexible topologies once optimization studies have been completed.

## 1.7 EXTENSIONS TO THE 1 AND 0 LEPTON CHANNELS

Both the LI and RF variable concepts are readily extendable to the 1-lepton channel. In this topology, one of the leptons in the  $ZH \rightarrow \ell\ell b\bar{b}$  diagram is replaced by a neutrino, the lone invisible particle in this final state. We can assume that the neutrino has zero mass and transverse momentum equal to the  $\vec{E}_T^{\text{miss}}$  in the event, leaving one undetermined degree of freedom, the longitudinal momentum of the neutrino,  $p_z^\nu$ .

The LI concept was in fact initially formulated to improve sensitivity in the 1-lepton channel, with the same orthogonality of variables described in the 2-lepton case being the main draw. The LI approach to estimating the neutrino longitudinal momentum is outlined in [16], which we reproduce here. We first guess the neutrino energy in its rest frame and then boost to the lab frame:

$$\langle E_\nu \rangle = \frac{1}{4}m_{WH} \implies \langle p_z^\nu \rangle = \beta\gamma \langle E_\nu \rangle = \frac{p_z^{WH}}{m_{WH}} \langle E_\nu \rangle = \frac{1}{4}p_z^{WH} \quad (1.9)$$

Finally, assuming energy and momentum in aggregate are equally shared among final state constituents, we arrive at

$$\langle p_z^\nu \rangle = \frac{1}{4} \times \frac{4}{3} \left( p_z^l + p_z^{j0} + p_z^{j1} \right) \quad (1.10)$$

The RF approach for the 1-lepton case amounts to replacing the  $Z \rightarrow \ell\ell$  in 1.6 with  $W \rightarrow \ell\nu$ . As alluded to in the 2-lepton discussion, when there is missing information in the final state from invisible particles and/or combinatoric ambiguities, recursive jigsaw reconstruction (RJR) offers a standard toolkit for deriving estimated boosts between rest frames by analytically minimizing on unknown quantities. While in more exotic final states with multiple invisible particles and combinatoric ambiguities the choice of jigsaw rule can be subjective, the case of  $W$  is well-studied and outlined in detail in Section V.A. of [17]. It reproduces the usual transverse mass of the  $W$  in place of MZ in the 2-lepton case. Not surprisingly, the underlying calculation is also much the same as the LI case (where rest frames and boost were explicitly invoked); again, information is the same, only its decomposition is different.

The 0-lepton channel would appear to present some difficulty as two neutrinos in the final state introduce extra degrees of freedom, but both concepts may be extended by treating the invisibly decaying  $Z$  as a single invisible particle and requiring the  $Z$  to be on-shell, as shown schematically in Figure 1.7. Both of these requirements may be folded into the 1-lepton framework to produce similar sets of variables.

While the precise variables that would be included in 0- and 1-lepton LI and RF MVA discriminants is beyond the scope of this thesis, looking at Table 9.1, we can see the dimensionality and in-

**Table 1.2:** Variables used to train the multivariate discriminant. Starred variables ( $b$ -tag scores) are not included in current versions of the standard discriminants, but have traditionally been included and most likely will be reintroduced as soon as their accompanying systematics are available.

Variable	Name	0-lepton	1-lepton	2-lepton
$p_T^V$	pTV		✓	✓
$\vec{E}_T^{\text{miss}}$	MET	✓	✓	✓
$p_T^{\text{jet1}}$	pTB <sub>1</sub>	✓	✓	✓
$p_T^{\text{jet2}}$	pTB <sub>2</sub>	✓	✓	✓
$\text{MV}_{2\text{C10}}(\text{jet}_1)^*$	$\text{MV}_{2\text{C10B1}}$	✓	✓	✓
$\text{MV}_{2\text{C10}}(\text{jet}_2)^*$	$\text{MV}_{2\text{C10B2}}$	✓	✓	✓
$m_{jj}$	mBB	✓	✓	✓
$\Delta R(\text{jet}_1, \text{jet}_2)$	dRBB	✓	✓	✓
$ \Delta\eta(\text{jet}_1, \text{jet}_2) $	dEtaBB	✓		
$\Delta\phi(V, H)$	dPhiVBB	✓	✓	✓
$\Delta\eta(V, H)$	dEtaVBB			✓
$M_{\text{eff}}(M_{\text{eff}3})$	HT	✓		
$\min(\Delta\phi(\ell, \text{jet}))$	dPhiLBmin		✓	
$m_T^W$	mTW		✓	
$m_{ll}$	mLL			✓
$\Delta Y(W, H)$	dYWH		✓	
$m_{\text{top}}$	mTop		✓	
Only in 3 Jet Events				
$p_T^{jet3}$	pTJ <sub>3</sub>	✓	✓	✓
$\text{MV}_{2\text{C10}}(\text{jet}_3)^*$	$\text{MV}_{2\text{C10B3}}$	✓	✓	✓
$m_{jjj}$	mBBJ	✓	✓	✓

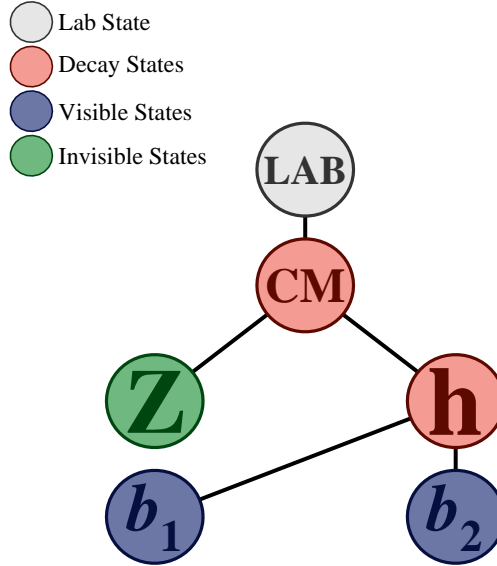


**Figure 1.7:** The  $ZH \rightarrow \nu\nu b\bar{b}$  decay tree.

puts of the discriminants of the fiducial analysis. The correspondence for LI/RF variables and standard variables extends nicely to the other lepton channels. The reduction in multiplicity of variables owing the lower number of degrees of freedom provided by treating the  $Z$  as a single invisible particle in the o-lepton channel would likely not be an issue, as one would just be able to use a greater fraction of available variables in the MVA discriminant.

*Noli turbare circulos meos*

Archimedes

# 2

## The Large Hadron Collider and the ATLAS Detector

THE CERN ACCELERATOR COMPLEX AND ITS EXPERIMENTS stand as a testament to human ingenuity and its commitment to the pursuit of fundamental knowledge. In this chapter, we give a

cursory overview of the CERN accelerator complex, including the Large Hadron Collider (LHC), before moving on to a more detailed review of the ATLAS detector.

## 2.1 THE CERN ACCELERATOR COMPLEX

The journey of protons from hydrogen canister to high energy collisions through the CERN accelerator complex, illustrated in Figure 2.1, is also one through the history of CERN’s accelerator program. After being ionized in an electric field, protons are first accelerated in a linear accelerator, LINAC 2<sup>\*</sup>, to a kinetic energy of 50 MeV. From there, they are fed into the Proton Synchotron Booster<sup>†</sup>, which further accelerates them to 1.4 GeV and, as its name implies, feeds them to the 628 m Proton Synchotron (PS, 1959[19]) and up to 25 GeV. The penultimate stage is the 7 km Super Proton Synchotron (SPS, 1976; responsible for the discovery of the  $W$  and  $Z$  bosons and the 1983 Nobel Prize [20]), which accelerates the protons to a kinetic energy of 450 GeV. Finally, these 450 GeV protons are injected into the LHC[21], a proton-proton collider housed in the 27 km circumference tunnel that housed the Large Electron Positron Collider (LEP) before its operations ceased in 2000.

## 2.2 THE LARGE HADRON COLLIDER

The LHC was designed to function primarily as a proton-proton collider with a center of mass energy  $\sqrt{s} = 14$  TeV and an instantaneous luminosity of  $1 \times 10^{34} \text{ cm}^{-2} \cdot \text{s}^{-1}$ , though it is also capable

---

\* 1978’s LINAC 2 is the successor to 1959’s LINAC 1; it will be replaced in 2020 by LINAC 4; LINAC 3 is responsible for ion production.

<sup>†</sup>Protons can be directly from a LINAC into the PS, but the higher injection energy allows for approximately 100 times more protons to be used at once[18], 1972.

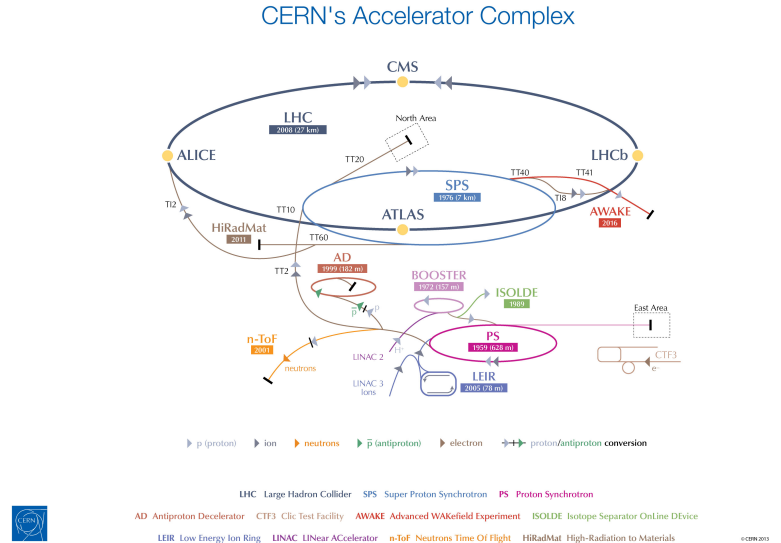


**Figure 2.1: The CERN Accelerator Complex [2]**

of producing heavy ion ( $\text{Pb-Pb}$ ) collisions, which it does for approximately one month in a typical year of physics collisions. Owing to an accident at the beginning of the LHC's initial run, the accelerator has operated at center of mass energies of 7, 8, and now 13 TeV.

One of the major cost-saving features of the he LHC is that, unlike the defunct Superconducting Supercollider (SSC), its construction did not call for a purpose built tunnel, with the LHC instead being housed in the old LEP tunnel. LEP, however, like the Tevatron, was a particle-antiparticle collider, which meant that both beams could circulate within the same beam pipe, so the LEP tunnel was never built to house two separate storage rings and magnet systems (as the SSC would have had). To accomplish the technically challenging task of housing two storage rings and sets of magnets in one system, the LHC magnets feature a “twin bore” design. The magnets themselves make use of superconducting NbTi cables and are cooled using superfluid helium to a temperature of 2

K, which allows for operational field strengths in excess of 8 T. A stable design is achieved by having the magnets share a common cold mass (a 27.5 ton iron yoke for each dipole kept at 1.9 K in which the magnets and beam pipes are embedded) and cryostat and by arranging the superconductor windings so that the magnetic fluxes of the two systems rotate in opposite directions. This results in an extremely complicated magnetic structure. The design layout of an LHC dipole magnet is shown in Figure 2.2. These dipole magnets are responsible for bending the LHC's proton beams, and their strength is the principal limiting factor in the center of mass energy achievable at a circular collider.

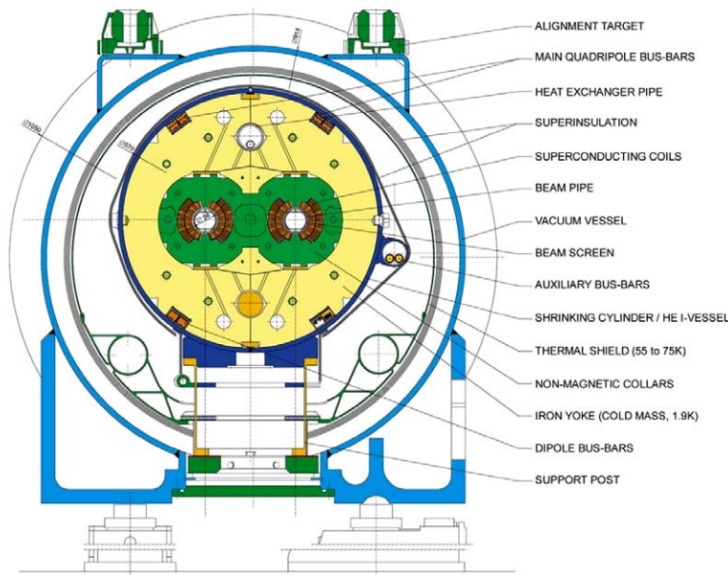


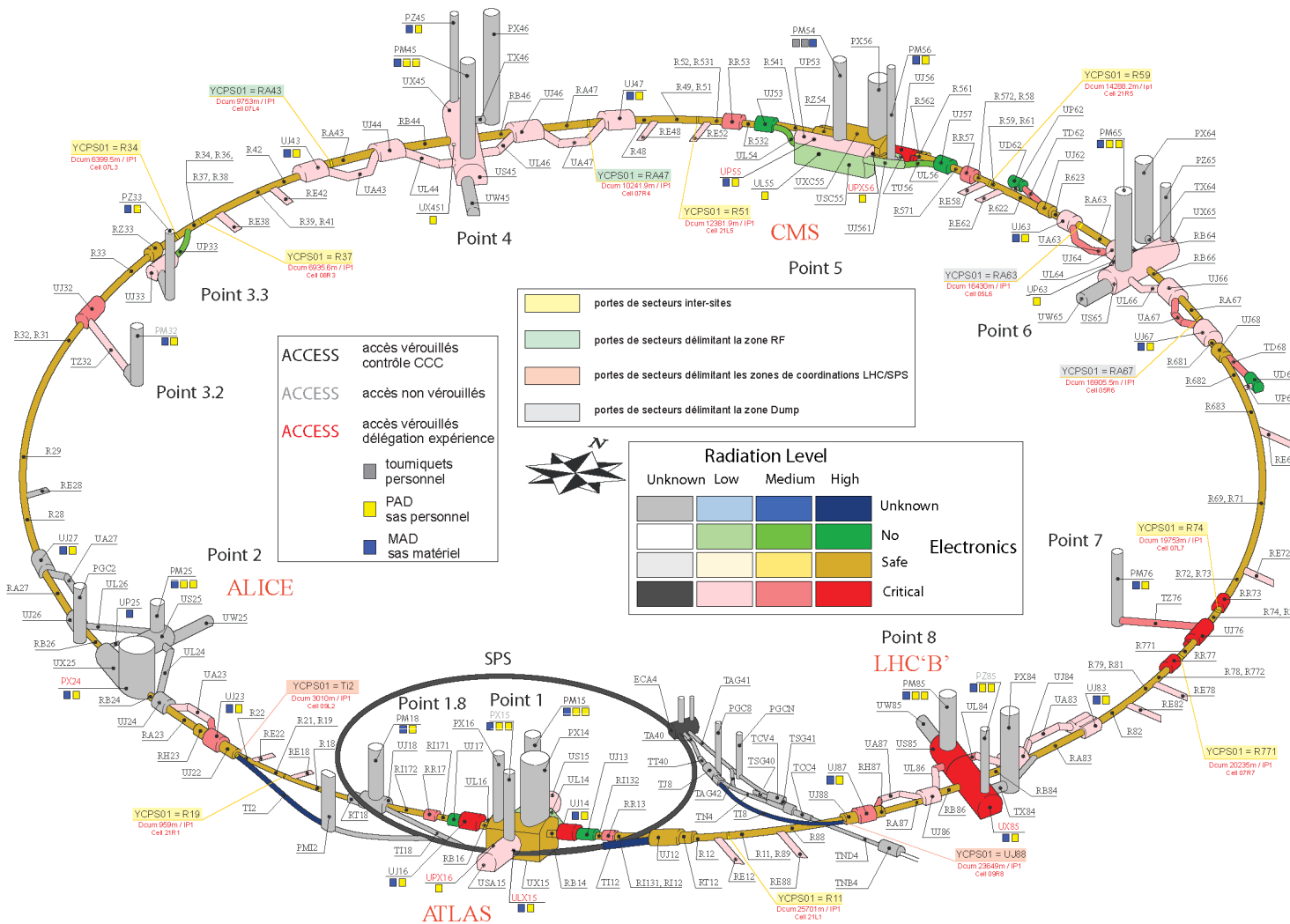
**Figure 2.2:** Schematic drawing of an LHC dipole magnet and cryogenics system.

The ideal version of a proton beam in the LHC consists of infinitely small bunches of protons of equal momentum equally spaced in the LHC ring (itself not a perfect circle). In reality, the protons in the beam deviate from each of these assumptions, with dispersion in both physical space

and momentum space. In general, charged particles in an accelerator ring will demonstrate pseudo-harmonic “betatron” oscillations about the ideal orbit, the amplitude of which gives a characteristic of the beam’s size. In order to get high energy protons to actually collide, different magnets are used to focus the beam and help nudge deviating particles back into more ideal behavior. There are quadrupole magnet assemblies in the short straight sections to accomplish this, as well as quadrupole, octupole, and sextupole magnets interspersed throughout the length of the LHC ring for beam stabilization and other higher order corrections. The interior of the LHC beam pipe operates at a nominal pressure of  $\sim 10^{-7}$  Pa, famously more rarefied than outer space.

The LHC ring itself is between 45 m and 170 m below ground and has a 1.4% incline towards Lac Léman with eight arcs and eight straight sections. In the middle of each of the eight straight sections, there are potential interaction points (each colloquially referred to by its number as “Point  $N$ ”), with each point housing either accelerator infrastructure or an experiment. A schematic of the contents of each component, as well as a more detailed view of the infrastructure in the LHC ring, can be found in Figure 2.3.

**Figure 2.3:** Schematic and detailed views of the LHC ring. IC: [3], [4]



Points 1, 2, 5, and 8 house the LHC’s experiments, ATLAS (*A Toroidal LHC ApparatuS*, one of the two general purpose detectors, discussed in detail below), ALICE (A Large Ion Collider Experiment, a dedicated heavy ion experiment), CMS (Compact Muon Solenoid, the other general purpose detector), and LHCb (LHC beauty, a *B* physics experiment), respectively. Point 3 houses a series of collimators that scatter and absorb particles in the beam with a large momentum deviation (which will have different orbital radii) from other particles in the beam (“momentum cleaning”), while Point 7 has a similar setup to remove particles with large betatron amplitudes (“betatron cleaning”). Both of these dedicated cleaning assemblies are in addition to the magnetic focusing assemblies discussed above and address the same issues. Point 4 contains the LHC’s RF (radio frequency; 400 MHz) acceleration system, responsible for taking protons from their injection energy of 450 GeV to their collision energy of 3.5, 4, 6.5, or 7 TeV. Point 6 is where the energetic ionizing radiation of circulating beams can be safely taken out of the collider into a block of absorbing material, either at the end of a data-taking run or in the event of an emergency (in the event of irregular behavior, it is essential to do this as quickly as possible to minimize damage to the accelerator and to experiments); this is known as a “beam dump.”

## 2.3 ATLAS AT A GLANCE

### 2.3.1 COORDINATES AND DISTANCES IN THE ATLAS DETECTOR

*A Toroidal LHC ApparatuS* is one of the two (the other being CMS) general purpose, high luminosity detectors at the LHC, located at Interaction Point 1, as described above. With a length of 44

m and a height of 25 m, it is the detector with largest physical dimensions at the LHC.<sup>‡</sup>. While primarily a high luminosity proton-proton collision detector, ATLAS does collect heavy ion collision data, typically for one month during a year of typical operation.

The ATLAS coordinate system is shown in Figure 2.3. It is a right-handed coordinate system centered at the nominal collision point, with the  $x$  axis pointing towards the center of the LHC ring, the  $z$  axis pointing up, and the  $y$  axis completing the right-handed coordinate system.

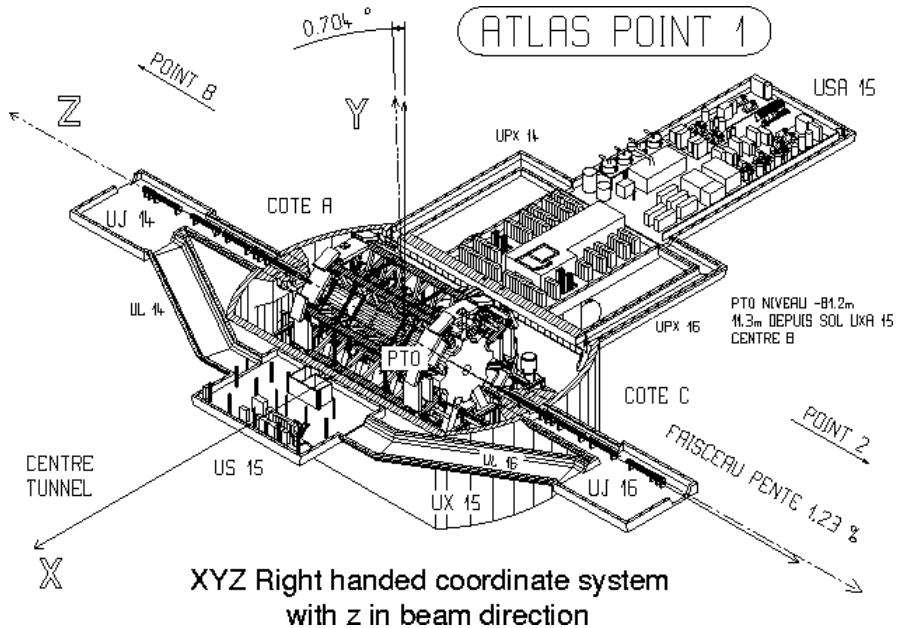


**Figure 2.3:** The ATLAS coordinate system. "A" side is the airport, and "C" side is "Charlie's," a pub in Saint-Genis, France.

While the Cartesian coordinates are useful for specifying the locations of things like detector components and activated calorimeter cells, cylindrical polar coordinates with the same origin,  $z$  axis, and handedness are often more suitable, with a point in 3-space expressed as  $(r, \phi, \eta)$ .  $r$  is the perpen-

---

<sup>‡</sup>This is the only reason CMS can call itself “compact.”

dicular distance from the beam axis. This differs from the usual spherical  $\rho$ , the distance of a point from the origin, because the ATLAS detector is cylindrical<sup>§</sup>, and so detector components are more easily located using  $r$  instead of  $\rho$ . In some contexts, the latter is used, though this is (or should be) made clear.  $\phi$  is the usual (right-handed) azimuthal angle around the beam axis, with  $o$  at the  $+x$  axis.

In a lepton collider where total momentum is conserved, a useful coordinate is the relativistic rapidity of a particle:

$$y = \frac{1}{2} \ln \left[ \frac{E + p_z}{E - p_z} \right] \quad (2.1)$$

with  $E$  and  $p_z$  as the energy and longitudinal momentum of the particle, respectively. The rapidity is the relativistic analog of a rotation angle; boosts can be added in a manner similar to rotations<sup>¶</sup>, and differences in rapidity are invariant under boosts. In a hadronic collider, where the participants in the hard scatter are partons inside of the proton of unknown momentum fraction, longitudinal momentum is not conserved. Nevertheless, since the incident momentum is entirely longitudinal, momentum is still conserved in the transverse plane, so quantities like transverse momentum  $\vec{p}_T$  or energy ( $E_T$ )<sup>||</sup> are often very useful in analysis. However, in the massless limit<sup>\*\*</sup>, we can take  $E =$

---

<sup>§</sup>“toroidal;” the hole is the beam pipe

<sup>¶</sup>Generally, one need only insert the appropriate factor of  $i$ , the square root of  $-1$ ; this introduces differences in sign and changes all of the trigonometric functions associated with rotations into hyperbolic trigonometric functions.

<sup>||</sup>Energy is not a vector quantity, but one can take the scalar or vectorial sum of vectors formed from energy deposits with their location as the direction and energy value as magnitude. In practice, primitives are almost always assumed to be massless, so transverse energy and momentum may loosely be thought of as equivalent, with  $E_T = |\vec{p}_T| = p_T$

<sup>\*\*</sup>not a terrible one for most particles depositing energy in the calorimeter; pions have masses of  $\sim 130$  MeV, and typical energies of calorimeter objects are  $\sim 10^3$  GeV, making for a boost of roughly 100.

$\sqrt{p_T^2 + p_z^2}$ . Hence, with  $\theta$  taken as the zenith angle and  $o$  corresponding to the  $+z$  direction, for a massless particle,  $p_z = E \cos \theta$ . Using the usual half angle formula  $\cos \theta = (1 - \tan^2 \theta) / (1 + \tan^2 \theta)$

$$\gamma = \frac{1}{2} \ln \left[ \frac{1 + \cos \theta}{1 - \cos \theta} \right] = \frac{1}{2} \ln \left[ \frac{(1 + \tan^2(\theta/2)) + (1 - \tan^2(\theta/2))}{(1 + \tan^2(\theta/2)) - (1 - \tan^2(\theta/2))} \right] = -\ln \left( \tan \frac{\theta}{2} \right) \quad (2.2)$$

This last expression, denoted  $\eta$ , is known as the pseudorapidity and is used instead of the polar angle as a coordinate in hadron colliders. Moreover, pion production (the most common hadronic process) is constant as a function of  $\eta$  in  $p\bar{p}$  collisions.

$$\eta = -\ln \left( \tan \frac{\theta}{2} \right) \quad (2.3)$$

Lower values of  $|\eta|$  ( $\lesssim 1.3$ ) correspond to more central areas of the detector known as the “barrel,” with the typical layout here being concentric, cylindrical layers. Larger values of  $|\eta|$  (to  $\sim 2.5$  for some systems and up to as much as  $\sim 4.5 - 5$  for others) are known as the “end caps,” where material is typically arranged as disks of equal radius centered on the beam pipe stacked to ever greater values of  $|z|$ . This terminology will be useful when discussing the various subsystems of the ATLAS detector. Since decay products from a collision propagate radially (in the calorimeter portions of the detector with no magnetic field), the radial coordinate is not so important for composite physics objects like electrons or jets, which are typically expressed as momentum 4-vectors. Hence,  $\eta$  and  $\phi$  are often the only useful spatial coordinates. Distances between objects are often expressed not as a

difference in solid angle, but as a distance,  $\Delta R$ , in the  $\eta - \phi$  plane, where

$$\Delta R_{12} = (\eta_1 - \eta_2)^2 + (\phi_1 - \phi_2)^2 \quad (2.4)$$

Two important concepts when discussing particles traveling through matter (e.g. particle detectors) are radiation lengths and (nuclear) interaction lengths, which characterize typical lengths for the energy loss of energetic particles traveling through materials. In general, the energy loss is modeled as an exponential

$$E = E_0 e^{-l/L} \quad (2.5)$$

where  $E_0$  is the initial energy, and  $L$  is a characteristic length. These lengths depend both on the incident particle and the material through which they pass. In the case of uniform, composite materials, the length may be found by calculating the reciprocal of the sum of mass fraction weighted reciprocal characteristic lengths of the components. This formula works quite well for modeling the very regular behavior of electromagnetic showers (energetic photons convert into electron/positron pairs, which emit photons...). In this case,  $L$  is denoted  $X_0$ ; this is the radiation length. Hadronic showers are far more complicated, with shower multiplicity and makeup being much more variable<sup>††</sup>. Nevertheless, a characteristic length can be tabulated for a standard particle type, typically pions, and is called the nuclear interaction length.

---

<sup>††</sup>Different initial hadrons will shower very differently, and hadronic showers will have phenomena like neutral pions converting to photons (which then shower electromagnetically), making them much trickier to deal with.

### 2.3.2 GENERAL LAYOUT OF ATLAS

The ATLAS detector and its main components are shown in Figure 2.4. ATLAS is designed as a largely hermetic detector, offering full coverage in  $\phi$  and coverage in  $|\eta|$  up to 4.7. The multiple subsystems allow for good characterization of the decay products from collisions in the LHC. The innermost system is the inner detector (ID); composed primarily of silicon pixels and strips immersed in a magnetic field, it is designed to reconstruct the curved trajectories of charged particles produced in collisions while taking up as little material as possible.

Surrounding the ID is the liquid argon based electromagnetic calorimeter (ECAL), which is designed to capture all of the energy of the electromagnetic showers produced by electrons and photons coming from particle collisions. The ECAL is in turn encapsulated by a scintillating tile and liquid argon based hadronic calorimeter (HCAL) that captures any remaining energy from the jets produced by hadronizing quarks and gluons.

The outermost layer of ATLAS is the muon spectrometer (MS), which has its own magnetic field produced by toroidal magnets. Muons are highly penetrating particles that escape the calorimeters with most of their initial momentum, so the MS and its magnets are designed to curve these charged particles and measure their trajectories to measure their outgoing momenta. Each of these detector systems has several principal subsystems and performance characteristics, which will be described in turn below.

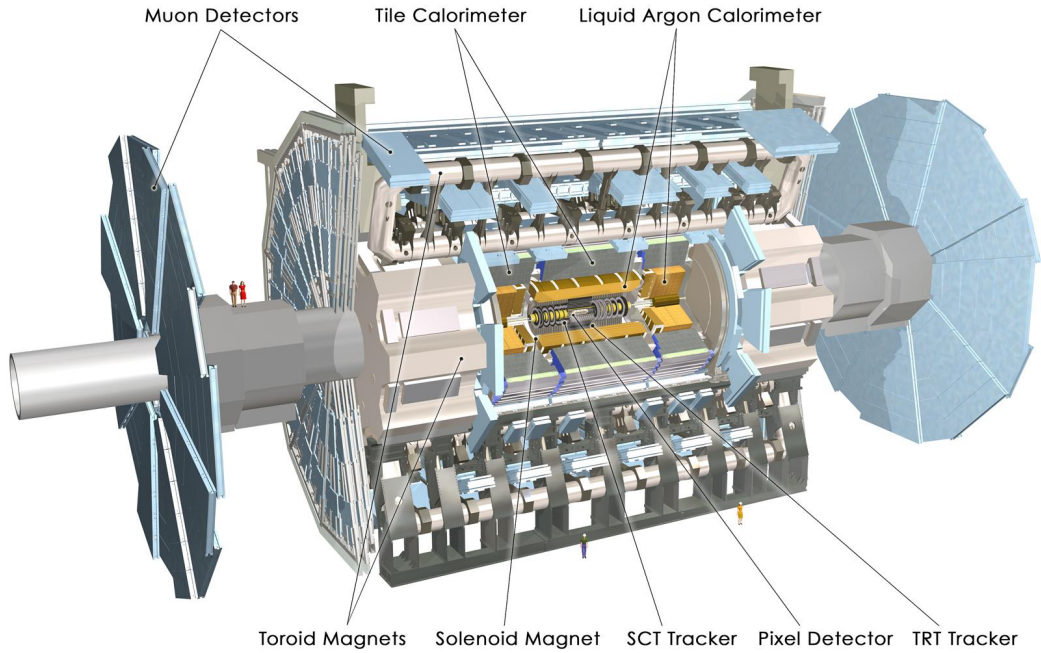


**Figure 2.4:** The ATLAS detector with principal subsystems shown.

## 2.4 THE INNER DETECTOR

ATLAS's inner detector (ID) is surrounded by a 2 T superconducting solenoid that is cryogenically cooled to a temperature of 4.5 K. The ID uses two silicon detector subsystems (the Pixel and Semiconductor (strip) Tracker (SCT)) to track the curved trajectories of charged particles emanating from particle collisions and a Transition Radiation Tracker (TRT) composed of gas straw detectors with filaments for  $e/\pi$  discrimination, as shown in Figure 2.5. The ID offers full coverage in  $\phi$  and extends to an  $|\eta|$  of 2.5.

Since the components of the ID do not provide an energy measurement, it is desirable for a tracking system to have as small a material budget as possible so that more accurate energy measurements

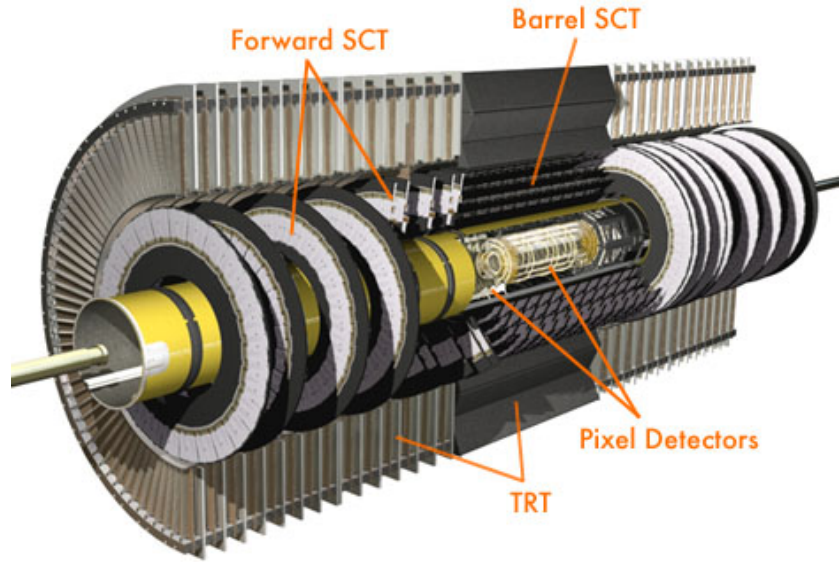


Figure 2.5: The ATLAS inner detector. IC: [5]

may be done in the calorimeters. Generally, there are two radiation lengths in the inner detector (the precise figure varies with  $\eta$ ); the full material budget, with the layout of the individual layers in each subsystem, can be seen in Figure 2.6.

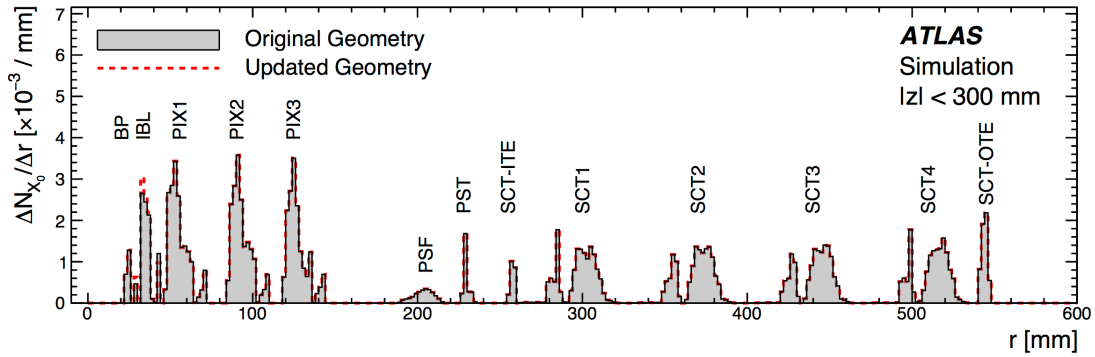


Figure 2.6: The ID material budget. IC: [6]

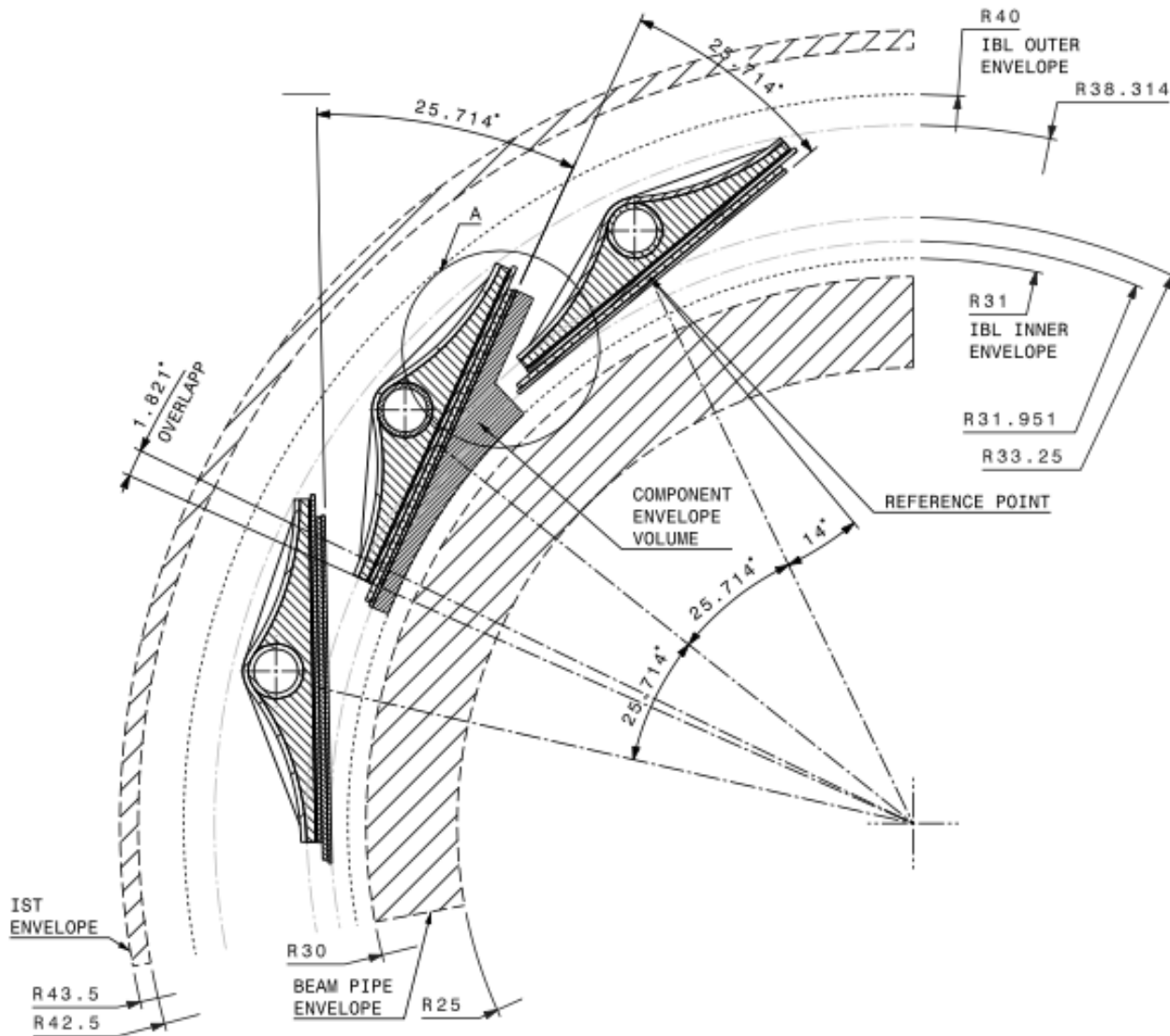
#### 2.4.1 THE PIXEL DETECTOR

The innermost part of ATLAS is the Pixel Detector, which, as the name suggests, is comprised of four layers of silicon pixels in the barrel at 32, 51, 89, and 123 mm from the beam pipe, and three layers in the end caps at 495, 580, and 650 mm from the beam pipe, with over 80 million channels total. The innermost layer of pixels, the insertable *B* layer (IBL) was installed during the 2013–14 LHC shutdown. The pixels are cooled to a temperature of  $\sim -5^\circ\text{C}$ , with  $N_2$  gas and operate at 150–600 V. The pixels themselves come in two sizes  $50 \times 400(600) \times 250 \mu\text{m}$ , with the larger pixels in the outer layers. They provide nominal resolution of  $10(115) \mu\text{m}$  resolution in  $r - \phi$  direction.

In order to improve total coverage in the detector and prevent any gaps, pixels are not installed flush with each other. Pixels in the barrel are tilted at about  $20^\circ$ , with an overlap in  $r - \phi$ , as shown in Figure 2.7. The disks of the ID end caps are rotated with respect to each other by  $3.75^\circ$ .

**Figure 2.7:** Arrangement of pixels in the barrel. IC: [7]

66



#### 2.4.2 THE SILICON MICROSTRIP DETECTOR (SCT)

The layout of the SCT is similar to that of the Pixel detector, except that, for cost considerations, the SCT uses silicon strips. These strips are also cooled to  $\sim -5^\circ\text{C}$  with  $\text{N}_2$  gas and operate from 150–350 V. Strip dimensions are  $80 \times 6000 \times 285 \mu\text{m}$ , and provide nominal  $17(580) \mu\text{m}$  resolution in  $r - \phi(z)$ . Barrel strips feature an  $11^\circ$  tilt and come in four layers at 299, 371, 443, and 514 mm. There are nine end cap disks on each side at  $z$  values varying from 934–2720 mm.

#### 2.4.3 TRANSITION RADIATION TRACKER (TRT)

The final and outermost subsystem in the ID is the Transition Radiation Tracker (TRT). It provides coverage for  $|\eta|$  up to 2.0 and is composed of straw detectors with a 4 mm diameter that run the length of the detector module. The straws provide  $130 \mu\text{m}$  resolution, are filled with a Xe-CO<sub>2</sub>-O<sub>2</sub> (70-27-3) gas combination, and operate at  $-1500$  V. The filaments and foil lining inside the straws induce X-ray emission in electrons and pions passing through the TRT as they move from a dielectric to a gas; this “transition radiation” is the source of the TRT’s name. Since the energy deposited due to transition radiation is proportional to the relativistic boost  $\gamma$ , for constant momentum, this is inversely proportional to mass. Thus, electrons will have  $\sim 130/0.5 = 260\times$  more transition radiation than pions, in principle enabling excellent electron/pion discrimination. The TRT will be replaced by silicon strips in the Phase II upgrade.

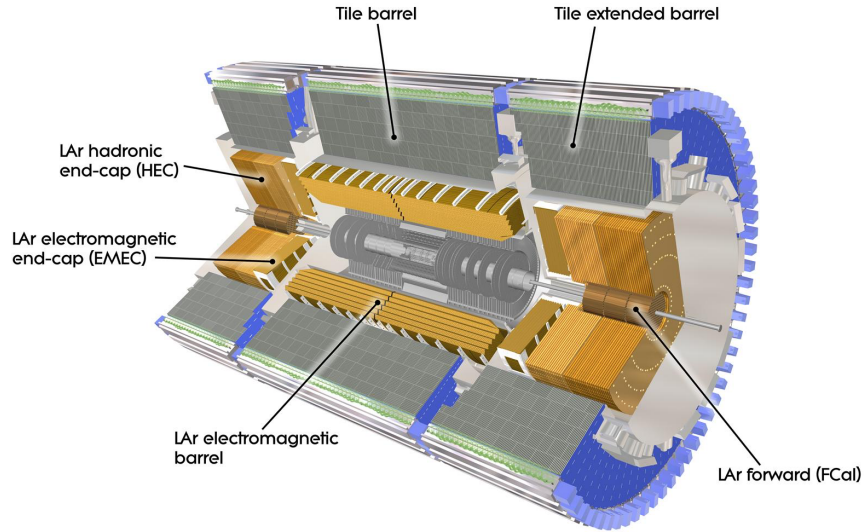


**Figure 2.7:** The ATLAS calorimeters.

## 2.5 THE ATLAS CALORIMETERS

ATLAS has four main calorimeter systems: the liquid argon based Electromagnetic Calorimeter (ECAL), the Hadronic End Cap (HEC), the Forward Calorimeters (FCAL), and the scintillating tile based hadronic Tile Calorimeter in the barrel. Their layout and material budget in interaction lengths can be seen in Figure 2.8.

### 2.5.1 CALORIMETER RESOLUTION

Before diving into the specifics of each of the ATLAS calorimeters, we review some aspects of calorimeter energy resolution performance. A calorimeter's relative energy resolution (a ratio) can be broken

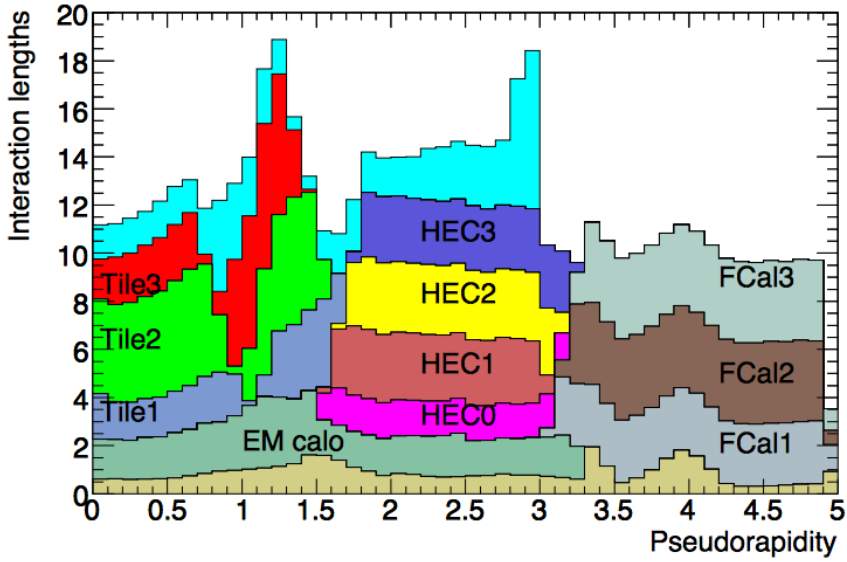


**Figure 2.8:** Material depth of the ATLAS calorimeters. IC: [5]

up into three orthogonal components, as shown in Equation 2.6.

$$\frac{\sigma_E}{E} = \frac{S}{\sqrt{E}} \oplus \frac{N}{E} \oplus C \quad (2.6)$$

$S$  is the photoelectron statistics or stochastic term and represents the coefficient to the usual counting term (assuming Gaussian statistics);  $N$  is a noise term, which is constant per channel (and hence comes in as  $1/E$  in the relative energy resolution); and  $C$  is a constant “calibration” term, which reflects how well one intrinsically understands a detector (i.e. mismodelling introduces an irreducible component to the energy resolution). If any detector were perfectly modeled/understood, it’s  $C$  term would be zero.  $N \sim 0.1 - 0.5$  GeV for a typical calorimeter regardless of type, so  $S$  and  $C$  are typically quoted.

A typical stochastic term scales as  $S \sim \text{few\%} \sqrt{d_{active} [\text{mm}] / f_{samp}}$ , where  $f_{samp}$  is the sampling fraction or the ratio of a calorimeter by mass is composed of an active material (i.e. one that registers energy deposits). The tile calorimeter, for example, has a sampling fraction of about 1/36. There are several reasons that this fraction is so low. First, many active volumes have insufficient stopping power; one wants to capture as much energy as possible from electromagnetic and hadronic showers inside the calorimeter, and this simply is not possible for most active media (one notable exception to this is the CMS crystal-based calorimeter; ATLAS is a more conservative design), so well-behaved absorbers like lead or iron are necessary to ensure all the energy is contained within a calorimeter. Another factor is cost; things like liquid argon are expensive. Finally, most active media are unsuitable for structural support, so sturdy absorbing materials help relieve engineering constraints.

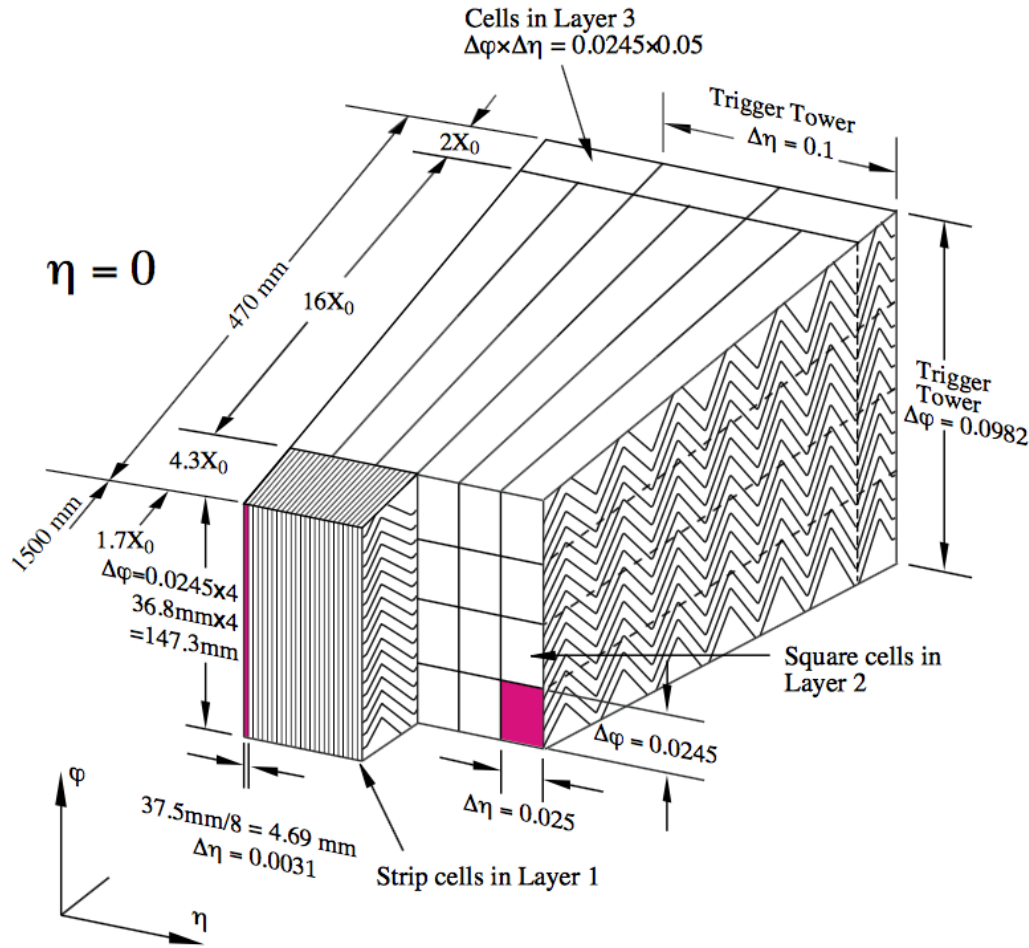
### 2.5.2 THE ELECTROMAGNETIC CALORIMETER (ECAL)

The ECAL has liquid argon (LAr) as an active material and lead as an absorber. The ECAL barrel extends to  $|\eta|$  of 1.475, with three layers at 1150, 1250, and 2050 mm, and its end cap, comprised of two wheels, covers  $1.375 < |\eta| < 2.5$ , (3.2) for the inner (outer) wheel, with 3 (2) layers out to 3100 mm. There is a 1.1 (0.5) cm thick layer of LAr pre-sampler up to  $|\eta|$  of 1.8 in the barrel (end cap) of the ECAL, which is designed to aid in correcting for electron and photon energy loss in the ID.

The LAr and lead absorber are arranged in alternating, beveled, sawtooth layers in what is known as an “accordion” geometry, shown in Figure 2.9, which shows the layout of a barrel module in the ECAL. The absorber thickness is 1.53 (1.13) mm for  $|\eta|$  less (more) than 0.8 to ensure a constant sampling fraction. This arrangement helps provide greater coverage in  $\phi$ .

**Figure 2.9:** The accordion geometry of the LAr electromagnetic calorimeters is prominently shown in this illustration of an ECAL barrel module. IC: [5]

45



The ECAL overall typically covers 2–4 interaction lengths or about 20–40 radiation lengths. Its performance corresponds to resolution coefficients  $S = 0.1 \text{ GeV}^{-1/2}$  and  $C = 0.002$  with a 450 ns drift time. In order to optimize the material budget and overall detector construction, the ECAL barrel infrastructure is integrated with that of the ID’s solenoid. The granularity of the ECAL barrel middle layer,  $\Delta\eta \times \Delta\phi$  cells of size  $0.025 \times 0.025$ , are used to define the granularity of calorimeter cluster reconstruction in ATLAS.

### 2.5.3 HADRONIC END CAPS (HEC)

The HEC covers an  $|\eta|$  range of 1.5 to 3.2. Like the ECAL end caps, the HEC consists of two identical wheels out to a distance from the beam axis of 2030 mm; its layout is shown in Figure 2.9. The HEC also has LAr as the active material, but instead has flat copper plates as absorbers for sampling fraction of 4.4% and 2.2% in the first and second wheels, respectively. Its granularity in  $\eta - \phi$  is  $0.1 \times 0.1$  for  $|\eta|$  up to 2.5 and  $0.2 \times 0.2$  in the more forward regions.

### 2.5.4 THE FORWARD CALORIMETER (FCAL)

The FCAL covers an  $|\eta|$  range from 3.1 to 4.9, again using LAr as the active material in gaps between rods and tubes in a copper-tungsten matrix, as shown in Figure 2.10. These system has characteristic performance corresponding to stochastic term of  $S \approx 1 \text{ GeV}^{-1/2}$ . There are three modules in the FCAL: one electromagnetic and two hadronic, with the latter two featuring a higher tungsten content for a larger absorption length.

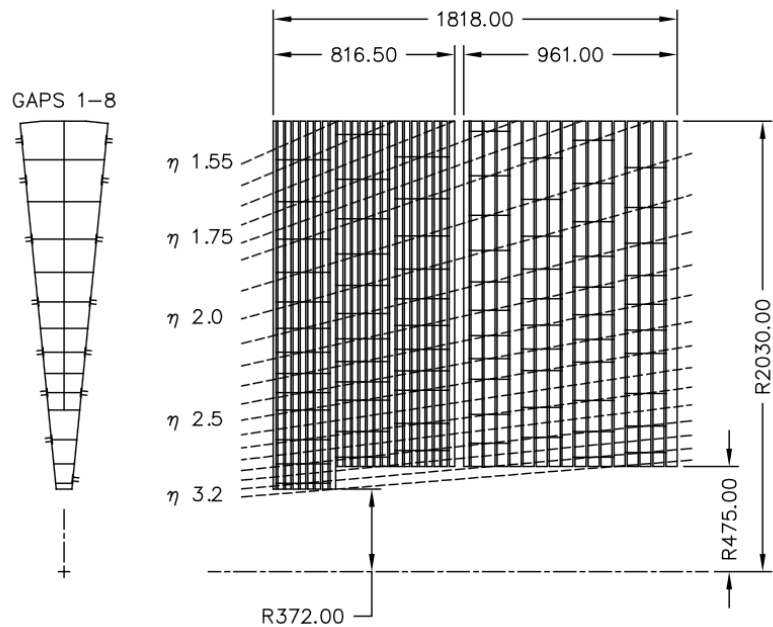


**Figure 2.9:** The layout of the HEC in  $r - \phi$  and  $r - z$ ; dimensions are in millimeters. IC: [5]

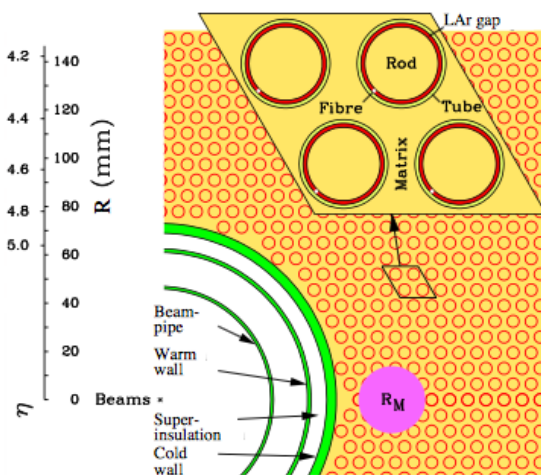


**Figure 2.10:** The material layout for a typical section of the FCAL in the transverse plane. IC: [5]

### 2.5.5 THE HADRONIC TILE CALORIMETER

The tile calorimeter, covering an  $|\eta|$  of up to 1.7 is made up of 64 modules in the barrel (each covering  $\Delta\phi$  of  $360/64 = 5.625^\circ$ ), each with a layout as in Figure 2.11. It is designed to be self-supporting

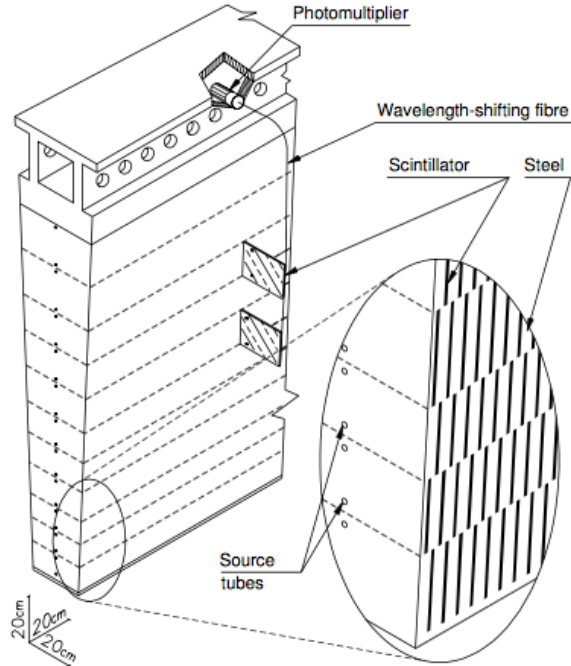


**Figure 2.11:** The material layout for a typical section of the hadronic tile calorimeter. IC: [5]

for structural reasons, and so is the only calorimeter without LAr as a an active medium, with a staggered matrix of active scintillating polystyrene and supporting steel. It operates at 1800 V with a 400 ns dead time and has a thickness corresponding to 10–20 interaction lengths (2.28–4.25 m). Its cells have a  $\Delta\eta \times \Delta\phi$  granularity of  $0.1 \times 0.1$  in the first two layers and  $0.2 \times 0.1$  in the last layer. Its performance corresponds to  $S = 0.5 \text{ GeV}^{-1/2}$  and  $C = 0.05$  (0.03 after calibration).

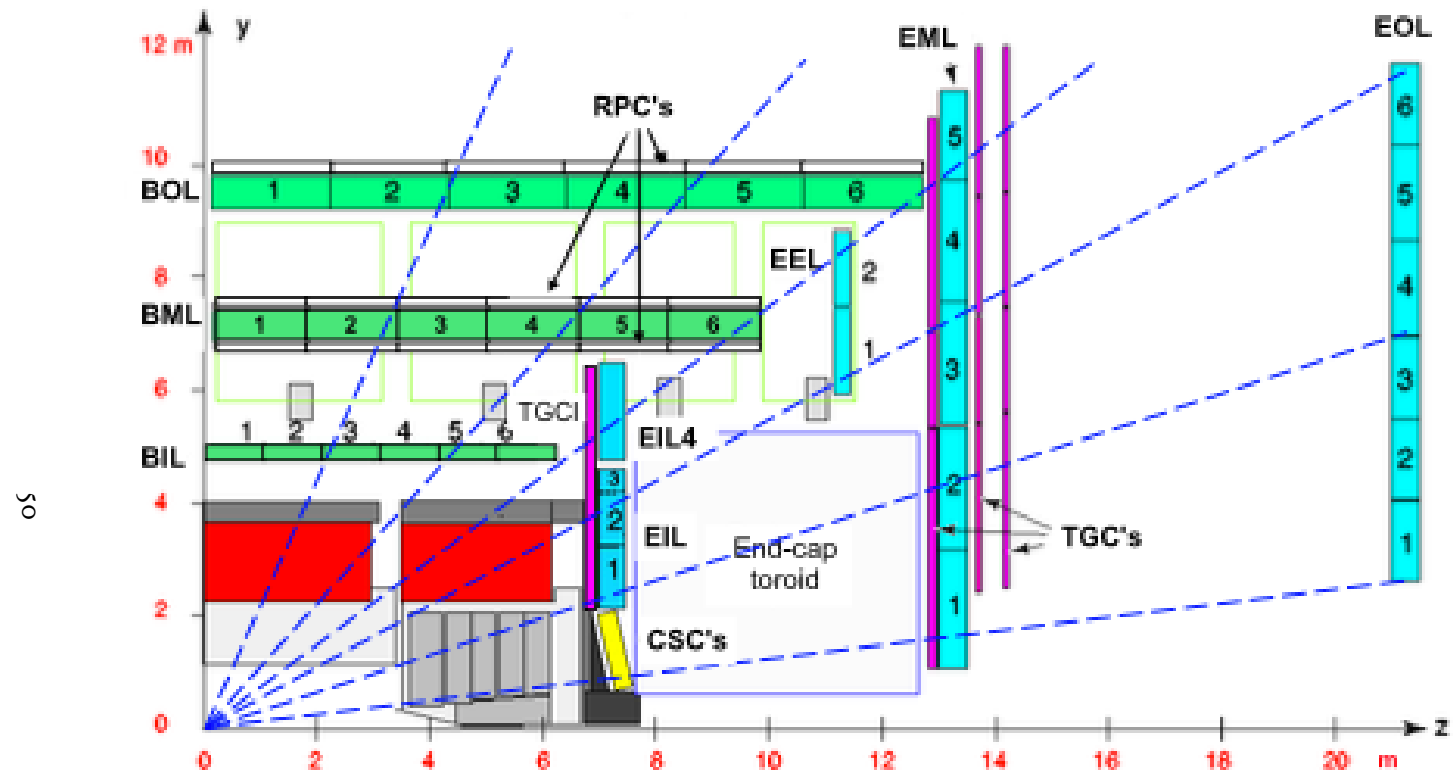
## 2.6 THE MUON SPECTROMETER

Since the energy of muons is not captured within the calorimeters, the stations of the ATLAS MS surround the entire detector and provide tracks of outgoing muons that can be matched to tracks in the ID. The ATLAS toroids, which provide field strengths of up to 2.5 (3.5) T in the barrel (end cap) with typical strengths of 0.5–1.0 T, bend the muons, which allows for a muon momentum measurement since the muon mass is known. The relative momentum resolution of a tracker (assuming, as in ATLAS, that bending primarily happens in the  $\phi$  direction) may be expressed as

$$\frac{\sigma_{p_T}}{p_T} = c_0 \oplus c_1 \cdot p_T \quad (2.7)$$

The  $c_0$  term represents a degradation in resolution due to multiple scattering, and is typically 0.5–2% [22]. The  $c_1$  term describes the phenomenon of, holding magnetic field constant, higher momentum muons curving less. This term has typical values of  $10^{-3} - 10^{-4}$  GeV $^{-1}$ . At very high  $p_T$  values, this is of particular concern since a very small curvature can result in charge misidentification.

**Figure 2.12:** The ATLAS muon spectrometer. Naming of the MDT stations obeys the following convention [BE] (barrel or end cap) [IEM0] (inner, inner extended (end cap only), middle, or outer layer) [1-6] (increasing in  $z(r)$  for the barrel (end cap)), so E11 is the station in the inner most end cap layer closest to the beam pipe. IC: [5]



A cross-sectional view (in  $r-z$ ) of the muon spectrometer with station names, detector types, and layouts is shown in Figure 2.12. There are three layers of muon detectors in both the barrel (at 5 000, 7 500, and 10 000 mm) and end cap (at 7 000 (11 000), 13 500, and 21 000 mm), with the innermost end cap layer split in two due to the end cap toroid. This corresponds to an  $|\eta|$  range up to 2.4 for both precision and trigger coverage, and up to 2.7 for precision detection only.<sup>##</sup>

The MS can reconstruct muons with transverse momenta from 5 GeV up to 3 TeV (with 10% resolution at 1 TeV (3% at 100 GeV)). Detectors in the MS fall into two broad headings, precision detectors and trigger detectors, both described below. Nominal performance of the current detector types in the MS is summarized in Figure 2.12, a table taken from [5]. It should be noted that  $|\eta|$  ranges quoted below, where applicable, do not include the range 0-0.1, where this a gap in the MS to allow for cabling and other services to the ATLAS detector; for a discussion of compensatory measures in muon reconstruction, see Chapter 5.

Type	Function	Chamber resolution (RMS) in			Measurements/track		Number of	
		$z/R$	$\phi$	time	barrel	end-cap	chambers	channels
MDT	tracking	35 $\mu\text{m}$ ( $z$ )	—	—	20	20	1088 (1150)	339k (354k)
CSC	tracking	40 $\mu\text{m}$ ( $R$ )	5 mm	7 ns	—	4	32	30.7k
RPC	trigger	10 mm ( $z$ )	10 mm	1.5 ns	6	—	544 (606)	359k (373k)
TGC	trigger	2–6 mm ( $R$ )	3–7 mm	4 ns	—	9	3588	318k

Figure 2.12: ATLAS MS detector performance. IC: [5]

---

<sup>##</sup>This will change with the New Small Wheel Phase I Upgrade. cf. Appendix A

### 2.6.1 PRECISION DETECTORS

The ATLAS MS has two types of precision detectors: Monitored Drift Tubes (MDT's) and Cathode Strip Chambers (CSC's). An MDT is a tube with a 3 cm diameter with length depending on the station in which the tube is located. The tube is filled with an Ar/CO<sub>2</sub> gas mixture and has a tungsten-rhenium wire at its center that is kept at 3 000 V when operational. The MDT's provide 35  $\mu\text{m}$  resolution (per chamber) in their cross-sectional dimension (there is no sensitivity along the axis of the wire). Resolution of this magnitude requires very precise knowledge of the location of the wires within the MDT's; this is generally true for detectors in the MS (trigger as well as precision); to this end, stations of the MS are aligned using an optical laser system. For a detailed description of how misalignment can affect performance, see Appendix A for a detailed discussion of misalignment's simulated effects on the performance of the proposed Micromegas trigger processor in the New Small Wheel (NSW) of the Phase I upgrade. Their 700 ns dead time, however, precludes their use as trigger detectors and also in the region of the small wheel (innermost endcap) closest to the beam pipe ( $|\eta|$  from 2.0 to 2.7), where rates are highest.

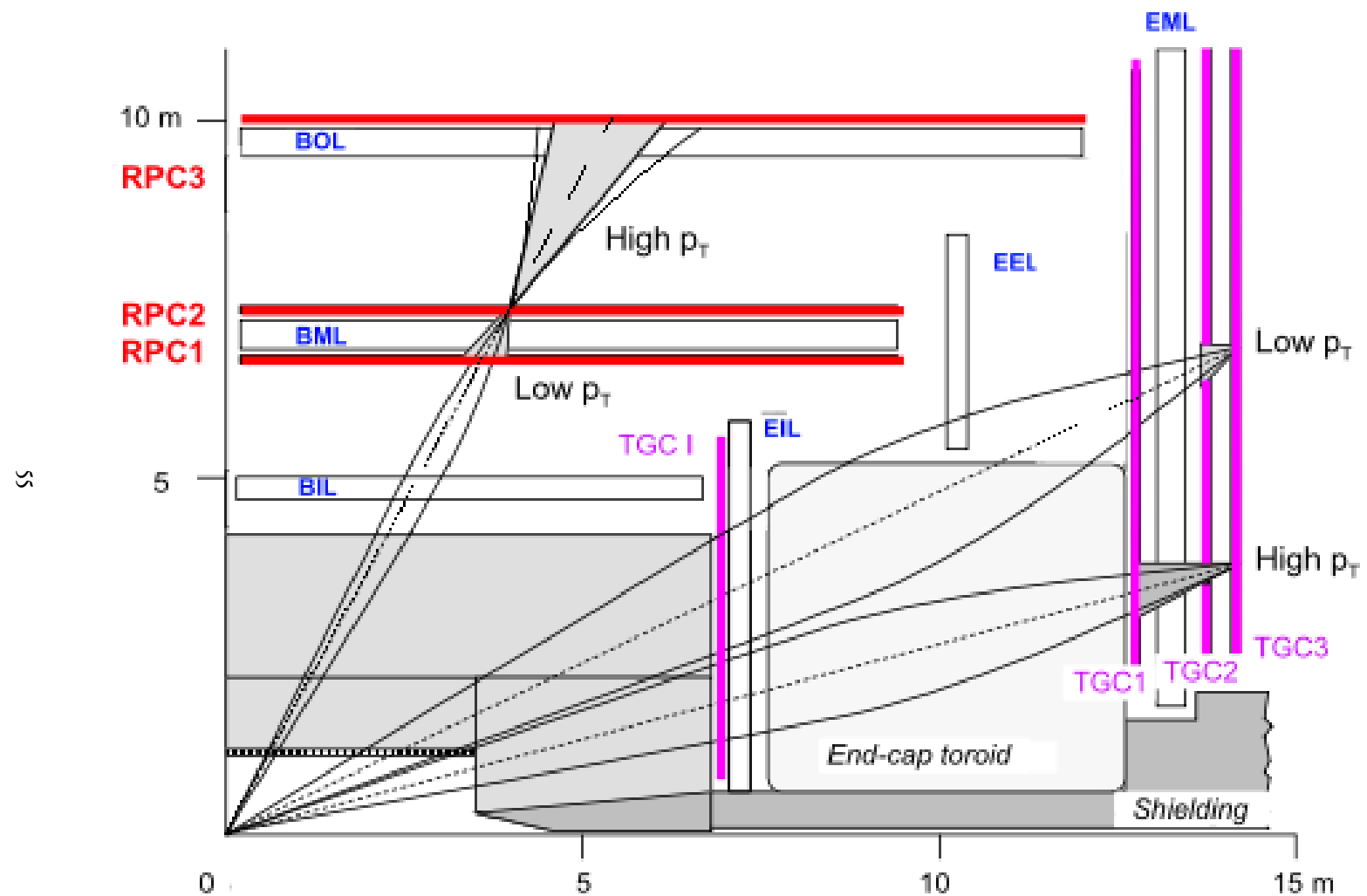
In this region, the precision detectors are the CSC's, which have a much lower dead time of  $\sim 40$  ns. These are multiwire proportional chambers with cathode planes that have orthogonal sets of strips, allowing for a measurement in both principal directions. CSC detector sizes also vary by station, coming in both small and large chambers. The CSC strip pitch is 5.31 (5.56) mm for the large (small) chambers, with position determined from the induced charge distribution in the strips. This corresponds to a nominal resolution of 60 (5 000)  $\mu\text{m}$  per plane in the bending (non-bending) direc-

tion. These are slated be replaced Micromegas detectors in the NSW.

## 2.6.2 TRIGGER DETECTORS

Trigger detectors have a fundamentally different role than the precision detectors, instead needing to deliver “good enough” approximate values of muon track positions and  $p_T$  values. The MS has two types of trigger detectors: Resistive Plate Chambers (RPC’s) in the barrel and Thin Gap Chambers (TGC’s) in the end caps. They collectively cover an  $|\eta|$  range to 2.4, and their arrangement is shown in Figure 2.13.

**Figure 2.13:** ATLAS MS trigger detector arrangement. IC: [5]



The RPC's are parallel plate detectors with a dead time of 5 ns and a thickness of 2 mm, kept at a potential of 9 800 V; they are deployed in three layers. RPC's, too, feature strips with orthogonal arrangements on the top and bottom planes, with a strip pitch of 23–35 mm.

The TGC's are multiwire proportional chambers with a dead time of 25 ns. Also, featuring orthogonal strips, the TGC's also provide a  $\phi$  measurement to compensate for the lack of MDT sensitivity in this direction. There are four layers of TGC's in the end cap. TGC's will be supplanted by sTGC's (small thin gap chambers) in the NSW.

For more details on how detector level trigger objects work in the ATLAS MS, see Appendix A for details on the Micromegas trigger processor algorithm.

*What do you read, my lord?*

*Words, words, words.*

Hamlet, 2:2

# 3

## Data and Simulated Samples

THE DATA AND Monte Carlo simulation (MC) samples used in this thesis are the same as in the fiducial analysis. The data corresponds to  $36.1 \text{ fb}^{-1}$  of  $pp$  collision data collected in 2015+16 at the ATLAS detector at  $\sqrt{s} = 13 \text{ TeV}$ . Details of the Run 1 analysis referenced in Chapter 9, may be found in [23]. Only events recorded with all systems in ATLAS in good working order and passing certain

quality requirements, according to a Good Run List (GRL), are analyzed.

Details about MC samples may be found in [24], and signal and background modeling are discussed in the next. The  $ZH \rightarrow \ell\ell b\bar{b}$  process is considered for both multivariate analysis (MVA) optimization and the final statistical analysis, while  $WH \rightarrow \ell\nu b\bar{b}$  and  $ZH \rightarrow \nu\nu b\bar{b}$  production are included in the final statistical analysis only. Signal MC samples were generated separately for  $qq$  and  $gg$  initiated  $VH$  processes.  $qqVH$  samples were generated with Powheg MiNLO + Pythia8 [25, 26] with the AZNLO [27] tune set and NNPDF3.0 PDF [28], with alternate samples generated using MadGraph5\_AMC@NLO [29] for the hard scatter generation and Pythia8 for the hardronization, parton shower (PS), underlying event (UE), and multiple parton interactions (MPI). Nominal  $ggZH$  samples were generated using Powheg for the matrix element (ME) and Pythia8 for the parton shower (PS), underlying event (UE), and multiple parton interactions (MPI), again applying the AZNLO tune and NNPDF3.0 PDF set. [30]

The background processes considered in these studies are  $Z+jets$ ,  $t\bar{t}$ , and diboson production for both MVA optimization and the final statistical analysis with single top production and  $W+jets$  only considered in the final statistical analysis.  $V+jets$  samples are generated using Sherpa 2.2.1 [31] for both the ME and PS. These samples are generated in different groups, according to the identity of the  $V$ , the max ( $H_T, p_T^V$ ) of events, with further subdivisions according to the flavor of the two leading jets in an event,  $b$ ,  $c$ , or  $l$ , for a total of six categories.  $t\bar{t}$  samples are generated using Powheg with the NNPDF3.0 PDF set interfaced with Pythia8 using the NNPDF2.3 PDF's and the A14 tune [32]. Single top samples use Powheg with the CT10 PDF's interfaced with Pythia6 using the CTEQ6L1 PDF's [33, 34]. Diboson samples are generated with Sherpa 2.2.1 interfaced with the

NNPDF<sub>3.0</sub> NNLO PDF set normalized to NLO cross sections [35].

*There are certain calculations one simply doesn't do in  
public.*

Alan Blaer

# 4

## Signal and Background Modeling

THIS CHAPTER summarizes the modeling of the dominant signal and background processes in this analysis, including corrections and systematic uncertainties (systematic uncertainty, also called nuisance parameter (NP), titles are set in `this` font) related to each process. Further details on the specifics of these topics, including in-depth studies for the derivation and definitions of some of the

quantities cited, may be found in [24]. We start with a general discussion of modeling and associated major categories of uncertainties before addressing each of the physics processes.

#### 4.1 EVENT GENERATION IN A NUTSHELL

Before diving into the specifics of modeling and systematic uncertainties associated with each major set of physics processes considered in this analysis, we review at a schematic level\* the problem of simulation event generation. Once a physics processes of interest has been determined, how one simulates an ensemble of particle collisions to model the process in question. This is illustrated in Figure 4.1. Note that the scope of this problem does not include how these generated collision products propagate through one's detector. This problem is left for Chapter 5.

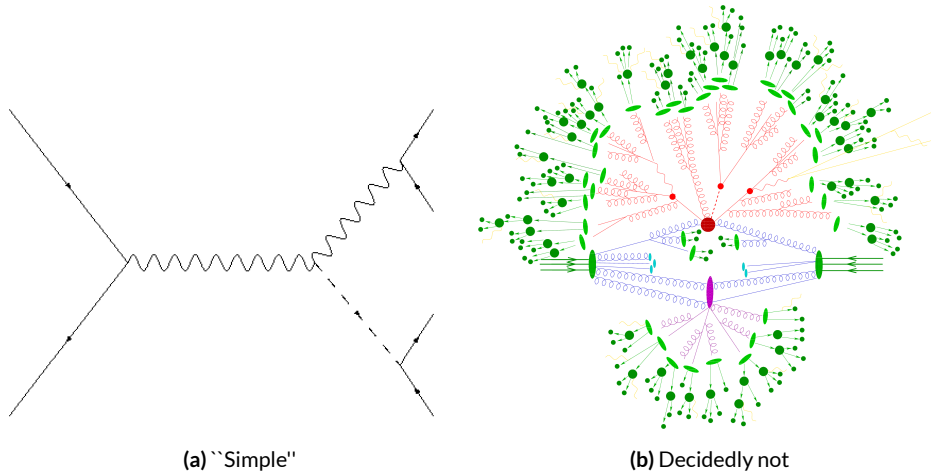


**Figure 4.1:** The problem here is how to get from (a) to (b).

The primary source of complication in event generation comes from dealing with hadronic ob-

---

\*i.e. this will not be a technically rigorous discussion. For a more thorough treatment, the reader is directed to the usual references.

jects both in the initial state (the lefthand side of Figure 4.1 (a); the LHC is a hadron collider) and the final state (this analysis searches for Higgs decays to  $b$ -jets, the lower righthand side of Figure 4.1). Common to all hadronic objects, by definition, are the many considerations that go into calculations in quantum chromodynamics (QCD). In calculating the hard scatter process itself, one must make a variety of choices, such as the parton distribution function (PDF) set to use and to what order in perturbation theory to do the calculation (common choices are leading order (LO), (next to) next to leading order ((N)NLO), and (next to) next to leading log (NNLL)) [36]. Similar considerations often need to be made for the electroweak parts of an event. These considerations and others in event generation (broadly called event generator “tuning”) will be discussed in more detail below.

The initial state includes not only the hard scatter partons that generate the physics process of interest, but also the rest of the partons in the colliding protons, known as the underlying event (UE). Moreover, the hard scatter partons may not be the only interacting partons in an event, further complicating matters; this phenomenon is known as multiple parton interactions (MPI). Specific to the final state are the kinematic distributions of the final state objects—what their energies and angular distributions will be—in addition to the overall cross section of the process that is measurable by the detector (acceptance effects). Furthermore, one has to model hadronization, the process by which any free (colored) partons in an event transform into colorless hadrons.

Typically, it takes several steps and tools to accomplish this. The hard scatter itself is often modelled with a dedicated event generator like PowHEG [25] or MADGRAPH [29], with events generated then interfaced with a tool like PYTHIA [26] for the PS, UE, and MPI, though there are exceptions (SHERPA [37], for example, can do both the hard scatter and hadronization/ for some pro-

cesses).

## 4.2 DESCRIPTION OF MODELING UNCERTAINTY CATEGORIES

Each of the steps in event generation described above has associated uncertainties. Some uncertainties are inherent in the calculations themselves. The choice of which order in perturbation theory to do a calculation, for example, comes with it an implicitly defined level of precision<sup>†</sup>. Extrapolating from one energy/momentum scale to another also introduces uncertainty. Furthermore, there is no *a priori* correct choice to make at each step in event generation, so each choice (the choice of generator, PDF set, parton shower calculator, all of their configurable parameters, etc.) implies an additional layer of uncertainty.

In order to quantify these choices, each source of systematic uncertainty is treated separately and given a unique name. To make this more concrete, take the specific example of the uncertainty associated with the  $H \rightarrow b\bar{b}$  branching ratio of 58%, called `ATLAS_BR_bb`, which encapsulates a number of effects (higher order terms, the mass of the  $b$  quark, and choice of  $\alpha_S$ ). The quoted (in principle asymmetric) uncertainty on the Higgs BR is not itself a direct input into the analysis model. Instead, the effect of varying the branching ratio up and down by one standard deviation is propagated to simulated collision events and recorded (i.e. the analysis is run with the Higgs branching ratio at  $\pm 1\sigma$ , and the results are recorded alongside the nominal result). The nominal and “up” and “down” variations are then typically taken to define a normally distributed, freely floating param-

---

<sup>†</sup>though this is less well-defined in QCD calculations than for electroweak calculations since they don’t converge

eter in the statistical fit model. Since these parameters associated with systematic uncertainties are not typically considered interesting quantities, they are often referred to as “nuisance parameters” (NP’s). The terms “systematic,” “systematic uncertainty,” and “nuisance parameter” are often used interchangeably.

The specifics of exactly how the effects of variations are saved and propagated to the full fit model are deferred to Chapter 7. The discussion here is confined to how systematic uncertainties for signal and background modeling and their accompanying variations are defined. Modeling systematics are derived separately for each physics process (simulation sample). Sometimes, all of the variation for a given process is encapsulated in a single systematic, but oftentimes the variations from multiple considerations are distinct enough to be treated separately. Furthermore, each of these separate systematics for a given sample/process may be treated in a number of ways (e.g. 0-lepton events may be treated differently from 2-lepton events). An additional subtlety is that a continuous parameter like a branching ratio lends itself quite naturally to defining Gaussian  $\pm 1\sigma$  variations, while for discrete variations, like choice of PDF set for parton showers, how to proceed is less obvious. This is addressed on a case-by-case basis, as described below.

Before enumerating each of the principal physics processes and their systematics, we begin by describing considerations and choices that must be addressed for every physics process in order to make the discussion of individual samples and systematics both clearer and less repetitive.

#### 4.2.1 PHYSICS CONSIDERATIONS

In general, evaluating the uncertainties arising from the many choices in event generation entails producing alternate samples of events, which practically means tuning parameters in the various software packages and/or using alternate packages/libraries to make new samples. Once these samples have been created, they are compared at truth-level (particle level) using a package called Rivet [38] instead of using the full ATLAS detector reconstruction for computational considerations. Given the nature of the problem and the tools, there are generally three main categories of physics issues, each described below.

#### UNDERLYING EVENT AND PARTON SHOWER

The modeling of the underlying event (UE) and parton shower (PS) are usually handled by the same package and so are usually treated together. The typical nominal choice in the fiducial analysis is PYTHIA8. One approach to modeling these uncertainties is simply to see what happens when a different model is used and then compare this alternate set of events to the nominal set, taking the difference as the (implicitly one standard deviation) scale of variation. Another approach is to vary some parameter within a given model, for example, using different tunes in the A14 set for PYTHIA8 with their accompanying variations, to characterize the scale of variation.

A natural question is how to treat these two approaches on the same footing. When examining a set of potential variations related to the same process or effect, oftentimes the largest single variation in a set is picked as defining the scale for the systematic uncertainty. Another approach is to use

the average over a set of variations.<sup>‡</sup> The `ATLAS_UEPS_VH_hbb` systematic, for example, uses the `Pythia8 + A14` tunes approach to determine the scale of UE variation and compares `Pythia8` with `Herwig7` to characterize the PS variation. Each of the `A14` tunes comes with an up and down variation, and the difference between each of these variations and a nominal setup may be expressed as a ratio,  $R$ , of total events.

As is often done when a physical argument can be made for combining related, but ultimately orthogonal categories/measurements/uncertainties/systematics, the combined UE+PS systematic is taken to be the sum in quadrature of these two effects:

$$\sum_{tunes} \max_{tune} (|R_{up} - R_{down}|) \oplus \sigma_{PS} \quad (4.1)$$

## QCD SCALE

The term “QCD scale” in the context of modeling uncertainties refers to the choice of renormalization ( $\mu_R$ ) and factorization ( $\mu_F$ ) scales used in QCD calculations. These are typically treated together. Usually, some multiplicative scale factor,  $f$ , is chosen, and each scale is varied in concert with the other scale by  $1, f$ , and  $1/f$  (nine total combinations), sometimes with a cap on how large the combined variation can be (so ignoring the  $(f, f)$  and  $(1/f, 1/f)$  cases). Just as in the UE+PS, the largest variation is usually taken as the systematic uncertainty.

Another important choice in the context of renormalization, to deal with infinities inherent in

---

<sup>‡</sup>Generally, the maximum is used if it is much larger than other variations, and the average is used if scales are comparable. In general, the historical preference is to be conservative.

quantum field theory calculations with loops, is the choice of regularization (to keep track of the infinities) and subtraction schemes (to eliminate them). A common combination is dimensional regularization (deforming the four dimensional integral to  $4 - \varepsilon$  dimensions and then taking  $\varepsilon \rightarrow 0$ ) with  $\overline{\text{MS}}$  (“MS-bar” (MS for “minimal subtraction”) subtracts off only the infinities plus some common factors that always appear in dimensional regularization). For more details, see, for example, [36]. While each scheme is internally consistent, each can yield different answers at a given order of calculation (and different subtraction schemes may be used for calculations at different orders).

## PARTON DISTRIBUTION FUNCTIONS AND $\alpha_s$

Finally, separate uncertainties are often made for the choice of parton distribution function (PDF) set and associated choice of strong coupling for QCD ( $\alpha_s$ ). Much as in the previous two cases, one can vary the parameter  $\alpha_s$  and study what samples of simulation events made using different PDF sets relative some nominal setup look like. Similarly, one can take the maximum, average, or sum in quadrature of different variations to characterize a systematic uncertainty.

### 4.2.2 MODELING SYSTEMATIC TYPES

With the concept of what type of effect is taken as a single systematic uncertainty and how its variations are generally evaluated, it is now time to turn to the issue of what exactly is being varied.

## ACCEPTANCE/NORMALIZATION

The most basic type of modeling uncertainty is a normalization uncertainty, often called an acceptance uncertainty. This simply denotes the uncertainty on the number of predicted events for a given process in a given region of phase space (usually delineated by the number of leptons in the final state and sometimes also by the number of and jets the  $p_T^V$ <sup>§</sup> of an event) and is usually expressed as a percent.

As an example, the uncertainty on the theoretical prediction of the  $H \rightarrow b\bar{b}$  branching ratio, denoted `ATLAS_BR_bb` (it is an ATLAS-wide systematic), is expressed as a normalization systematic with a value of 1.7%, affecting all  $VH$  processes. Now imagine we have an event in a  $VH$  sample with weight 1.0. The nominal histograms for this region gets filled with this event's relevant information with weight 1.0, while the `ATLAS_BR_bb__1up` (`_1do`) histograms get filled with weight 1.017 (0.983).

## SHAPE SYSTEMATICS

In addition to normalization systematics expressed as single numbers attached to different processes in different regions, there are also the so-called “shape systematics” and “shape corrections,” heuristically differences in distributions that exist in distributions even after correcting for normalizations, which gives distributions a different “shape” even if their integrals are the same (c.f. Figure 4.3).

---

<sup>§</sup>This is the transverse mass of the lepton pair for 2-lepton events, the vectorial sum of the single lepton and  $\vec{E}_T^{\text{miss}}$  for 1-lepton events, and the  $\vec{E}_T^{\text{miss}}$  for 0-lepton events.

These have the schematic form

$$w_{event} = \mathcal{A}_{region} \times f_{region}(event) \quad (4.2)$$

where  $w_{event}$  is the simulated event's weight,  $\mathcal{A}_{region}$  is the overall normalization (in principle including any systematics), and  $f_{region}(event)$  is some function of event-level variables, usually a single variable, like  $p_T^V$  or  $m_{bb}$ . The purpose of these systematics is to take into account (in the case of a systematic) or correct (in the case of a correction applied to the event weight) the non-trivial dependence of a normalization on one of these quantities. Some of these are taken from histograms while others are parametric functions (in this analysis, usually linear ones).

An example of the former case is the quantity  $\delta_{EW}$ , the difference between the nominal  $qqVH$  cross section and the differential cross section as a function of  $p_T^V$  at next to leading order (NLO). As a correction, this term is simply used as a correction factor  $k_{EW}^{NLO} = (1 + \delta_{EW})$ .

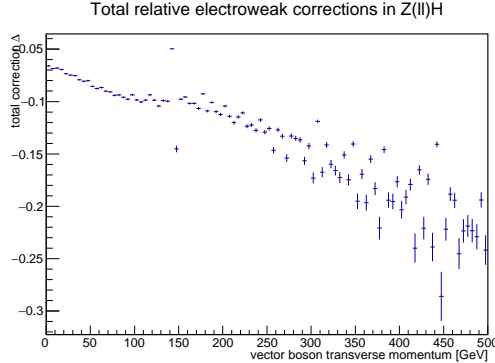


**Figure 4.2:** The  $\delta_{EW}$  correction term for 2-lepton  $qqZH$ .

An example of the latter case is the systematic associated with the  $m_{bb}$  dependence of the the

$t\bar{t}$  normalization for 2 jet,  $p_T^V \in [75, 150]$  GeV, 2 lepton events. In this case, a variety of effects are studied (ME, PS, UE), as shown in Figure 4.3. The top half of the plot is the  $m_{bb}$  plot for this region, with the black bars representing the nominal spectrum and spectra generated with different ME, PS, and UE choices. The ratio plot in the bottom half of the figure shows the scale of variation normalized to bin content. From this ratio plot, it is clear that the choice of ME (pink points) was seen to have the largest effect on normalization. The linear fit in the plot reasonably envelopes this maximum variation was done, and so is taken as the systematic variation. Hence, in this case,  $f_{region}(event)$  is a linear function of  $m_{bb}$ , with positive (negative) slope for the up (down) variation.

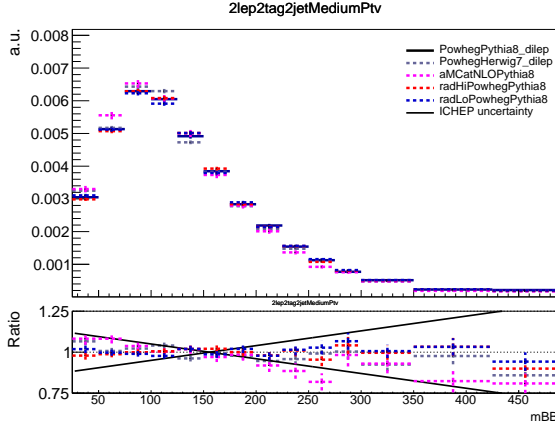


Figure 4.3: The derivation of the 2-lepton  $t\bar{t} m_{bb}$  shape systematic.

## DIVIDING MODELING UNCERTAINTIES: ACCEPTANCE RATIOS

In addition to uncertainties on absolute normalizations (both inclusive and region specific), modeling uncertainties are sometimes introduced for the ratio of normalizations between different regions. While these can be simple ratios, evaluating a systematic's effect between regions means eval-

uating nominal and alternate choices between regions, so the so-called “double ratio” is often taken as the scale of variation (plus one). The ATLAS\_UEPS\_VH\_hbb systematic mentioned above, for example, has associated with it, ATLAS\_UEPS\_VH\_hbb\_32JR. This systematic is evaluated by dividing the 3 jet to 2 jet ratio in the nominal setup by the same ratio in an alternate setup. These ratios generally look like:

$$\frac{\text{Acceptance}[\text{Category}_A(\text{nominalMC})]}{\text{Acceptance}[\text{Category}_B(\text{nominalMC})]} \Big/ \frac{\text{Acceptance}[\text{Category}_A(\text{alternativeMC})]}{\text{Acceptance}[\text{Category}_B(\text{alternativeMC})]} \quad (4.3)$$

Double ratio systematics are often included in addition to single systematics when a single systematic could potentially overestimate the total variation due to a single effect. In the above example, the choice of UE+PS in signal events may cause different overall variation in 2 jet events as compared to events with 3 or more jets due to QCD considerations. However, extrapolating between jet multiplicities can be a non-trivial exercise entirely regardless of the choice of generator for UE+PS (cf. the discussion of the Stewart-Tackman approach 4.2.2 below), so to include this variation in a single systematic would lead to overly conservative systematic uncertainties. Hence, using previous knowledge of this separate variation between jet multiplicity regions, one can define a double ratio systematic for a more accurate fit model.

The three main categories are ratios between different flavor regions, ratios between different lepton channels<sup>¶</sup>, and ratios between regions with different numbers of jets,  $n_{jet}$ . The first category is only relevant for  $V+jets$  systematics and will be treated in that process’s dedicated section below. As

---

<sup>¶</sup>e.g.  $Z+$ heavy flavor jets (at least one  $b$ -jet in the event; often denoted “hf” normalizations in 0- and 2-lepton events

this thesis is primarily concerned with the 2-lepton channel, the second category will not be treated in detail, though the treatment is much the same as other ratio systematics.<sup>||</sup> In order to discuss the  $n_{jet}$  ratios in systematics (e.g. the ratios in the double ratio example), we must first describe how exclusive  $n_{jet}$  cross section calculations are done.

**THEORETICAL ASIDE: STEWART-TACKMANN** A way to calculate uncertainties on processes in regions with different numbers of jets was developed by Stewart and Tackmann and is implicitly used for most  $n_{jet}$  ratio systematics [39]. The problem is how to calculate the cross section and associated uncertainty for a process with exclusively  $N$  jets in the final state. Generically:

$$\sigma_{\geq N} = \sigma_N + \sigma_{\geq N+1} \quad (4.4)$$

The physical interpretation of one parton to one jet is an idealized case. In order to demarcate between jets, one has some quantity that is used as a cutoff in an integral that defines the border between jet regions.

$$\sigma_{\geq N} = \int_0^{p_{cut}} \frac{d\sigma_N}{dp} + \int_{p_{cut}} \frac{d\sigma_{\geq N+1}}{dp} \quad (4.5)$$

Since these cutoffs (not necessarily constant, etc.) can make calculations more complicated, inclusive cross sections tend to be easier to calculate. Hence, it is usually much easier to evaluate the two inclusive cross sections and find the uncertainties on these by varying  $\alpha_S$  in the usual way (cf. Sec-

---

<sup>||</sup>Such ratios allow for information in one channel to help constrain other channels, particularly for hard to model processes like  $Z+\text{hf}$ . This helps to reduce final overall uncertainties in combined fits. For a discussion of the interplay of nuisance parameters in combined fits, cf. Chapter 9.

tion 4.2.1). One then assumes the inclusive uncertainties are uncorrelated, for a covariance matrix for  $\{\sigma_{\geq N}, \sigma_N, \sigma_{\geq N+1}\}$  of (with  $\Delta_x^2$  as the variance associated with  $x$ ):

$$\Sigma = \begin{pmatrix} \Delta_{\geq N}^2 & \Delta_{\geq N}^2 & 0 \\ \Delta_{\geq N}^2 & \Delta_{\geq N}^2 + \Delta_{\geq N+1}^2 & -\Delta_{\geq N+1}^2 \\ 0 & -\Delta_{\geq N+1}^2 & \Delta_{\geq N+1}^2 \end{pmatrix} \quad (4.6)$$

These calculations contain Sudakov double logs of  $\ln^2(p/Q)$ , where  $Q$  corresponds to the scale of the hard scatter process ( $m_H$ ), and  $p_{cut}$  is usually something like a  $p_T$  cutoff. When integrating over all of the phase space, these terms can come to dominate calculations when  $p \gg Q$ . The  $N+1$  term in the covariance matrix is an uncertainty associated with the cutoff, but the Sudakov double logs will dominate any higher order terms. Stewart and Tackmann give the following reasoning:

“In the limit  $\alpha_S^2 \approx 1$ , the fixed-order perturbative expansion breaks down and the logarithmic terms must be resummed to all orders in  $\alpha_S$  to obtain a meaningful result. For typical experimental values of  $p_{cut}$  fixed-order perturbation theory can still be considered, but the logarithms cause large corrections at each order and dominate the series. This means varying the scale in  $\alpha_S$  in Eq. (9) directly tracks the size of the large logarithms and therefore allows one to get some estimate of the size of missing higher-order terms caused by  $p_{cut}$ , that correspond to  $\Delta_{cut}$ . Therefore, we can approximate  $\Delta_{cut} = \Delta_{\geq 1}$ , where  $\Delta_{\geq 1}$  is obtained from the scale variation for  $\sigma_{\geq 1}$ .”

The above considerations are important for this analysis since phase space is separated into  $2$  and  $\geq 3$  jet regions, and the uncertainties for these regions are anti-correlated.

### 4.3 PROCESS SPECIFIC SYSTEMATIC SUMMARIES

Brief descriptions of modeling systematics, including recapitulations of nominal sample generation, are given in the following sections. The general approach here is to copy the relevant summary tables and describe any major deviations from the general procedures described in the previous section.

The dominant backgrounds for the 2-lepton channel are  $Z+hf$  and  $t\bar{t}$ , accounting for well over 90% of all background events. Diboson samples are the next-leading background and are an important validation sample; others are included for completeness. A summary of all the modeling systematics in this analysis are given in Table 4.1.

**Table 4.1:** Summary of modeling systematic uncertainties, with background samples listed in order of importance.

Process	Systematics
Signal	$H \rightarrow bb$ decay, QCD scale, PDF+ $\alpha_s$ scale, UE+PS (acc, $p_T^V$ , $m_{bb}$ , 3/2 jet ratio)
$Z+jets$	Acc, flavor composition, $p_T^V+m_{bb}$ shape
$t\bar{t}$	Acc, $p_T^V+m_{bb}$ shape
Diboson	Overall acc, UE+PS (acc, $p_T^V$ , $m_{bb}$ , 3/2 jet ratio), QCD scale (acc (2, 3 jet, jet veto), $p_T^V$ , $m_{bb}$ )
Single top	Acc, $p_T^V+m_{bb}$ shape

#### 4.3.1 SIGNAL PROCESSES

Nominal signal  $qqVH$  samples are generated using PowHEG with the `MinLO` (multiscale improved NLO) [40] procedure applied interfaced with PYTHIA8 using the AZNLO tune [27] and NNPDF3.0 PDF set [28]. For the 2-lepton case, gluon fusion initiated Higgs production is also considered (ac-

counting for  $\sim 14\%$  of the total cross section in this channel), with samples generated with Powheg interfaced with Pythia8 using the AZNLO tune. The NNPDF2.3 set [41] is used for both the ME and UE+PS.

Alternate samples  $qqVH$  samples are generated using MadGraph5\_aMC@NLO [42] for the ME and Pythia8 for the UE+PS, hadronization and MPI. The NNPDF2.3 5f FFN PDF sets and the Al4 tune [43]; the latter has variations included. Powheg+Minlo+Herwig7 were samples were also used for systematics.

The signal systematics categories are  $H \rightarrow bb$  decay cross section, QCD scale, PDF+ $\alpha_S$  scale, and UE+PS. Additionally, there is the NLOEWK correction described above. The correction scale factor is derived using the HAWK MC software. To encapsulate NNLOEW effects the maximum of 1%, the square of the correction factor, and the photon induced cross section is used as a systematic.

Table 4.2, reproduced from [24], summarizes the signal cross section systematics, which are applied uniformly across the analysis channels (as applicable).

**Table 4.2:** Summary of all systematic uncertainties on the  $VH$  cross section including their value, source and the corresponding nuisance parameter name.

Sys Name	source	Norm. effect	applied to
ATLAS_BR_bb	$H \rightarrow bb$ dec. unc, (HO effects, $m_b$ , $\alpha_S$ )	1.7%	all $VH$
ATLAS_QCDscale_VH	QCD scale uncertainty	0.7%	$qq \rightarrow VH$
ATLAS_QCDscale_ggZH	QCD scale uncertainty	27%	$gg \rightarrow ZH$
ATLAS_pdf_Higgs_VH	PDF+ $\alpha_S$ uncertainty	1.9% 1.6%	$qq \rightarrow WH$ $qq \rightarrow ZH$
ATLAS_pdf_Higgs_ggZH	PDF+ $\alpha_S$ uncertainty	5.0%	$gg \rightarrow ZH$

The remaining signal systematics are analysis channel specific and are summarized in Table 4.3. The methodologies match those described in Section 4.2. The UE+PS systematics were derived us-

ing the alternate samples mentioned above; QCD scale uncertainties were derived by varying scales by  $1/3$  and  $3$ ; and PDF uncertainties were derived by comparing the nominal set with the PDF4-LHC<sub>15\_30</sub> PDF set [44].

**Table 4.3:** Summary of all systematic uncertainties on the  $VH$  acceptance and shapes originating from altering the PDF and  $\alpha_S$  uncertainties, including their corresponding nuisance parameter name.

NP name	oL		1L		2L	
	2j	3j	2j	3j	2j	$\geq 3j$
ATLAS_UEPS_VH_hbb	10.0%	10.0%	12.1%	12.1%	13.9%	13.9%
ATLAS_UEPS_VH_hbb_32JR	–	13.0%	–	12.9%	–	13.4%
ATLAS_UEPS_VH_hbb_VPT	shape only		shape+norm			
ATLAS_UEPS_VH_hbb_MBB	shape only					
QCDscale_VH_ANA_hbb_J2	6.9%	–	8.8%	–	3.3%	–
QCDscale_VH_ANA_hbb_J3	-7%	+5%	-8.6%	+6.8%	-3.2%	+3.9%
QCDscale_VH_ANA_hbb_JVeto	–	-2.5%	–	3.8%	–	–
QCDscale_VH_ANA_hbb_VPT	shape only		shape+norm			
QCDscale_VH_ANA_hbb_MBB	shape only					
pdf_HIGGS_VH_ANA_hbb	1.1%	1.1%	1.3%	1.3%	0.5%	0.5%
pdf_VH_ANA_hbb_VPT	shape only		shape+norm			
pdf_VH_ANA_hbb_MBB	shape only					

### 4.3.2 $V + \text{jets}$

Nominal  $V + \text{jets}$  samples are generated using SHERPA 2.2.1@NLO<sup>\*\*</sup> [45] for both the ME and PS, interfaced with the NNPDF’s and using a five quark flavor scheme, and alternative samples are derived using MADGRAPH5 interfaced with PYTHIA8. In order to increase statistics in important regions of phase space, these samples were separated into kinematic slices based on  $p_T^V$  and into bins of jet flavor. The kinematic slices were in the quantity  $\max(H_T, P_T^V)$  and had the intervals [0–70, 70–

<sup>\*\*</sup>SHERPA 2.1 is used for some variations not available in SHERPA 2.2.1.

$140, 140-280, 280-500, 500-1000, > 1000]$  GeV. The jet flavor slices were made using flavor vetoes and filters:

- BFilter: at least 1 b-hadron with  $|\eta| < 4, p_T > 0$  GeV
- CFilterBVeto: at least 1 c-hadron with  $|\eta| < 3, p_T > 4$  GeV; veto events which pass the BFilter
- CVetoBVeto: veto events which pass the BFilter and/or the CFilterBVeto

These in turn are related to the main flavor regions used in the analysis, based on the flavor of the two leading jets in an event (based on  $p_T$ ). These five flavors (with up, down, and strange collectively known as “light”) yield six different flavor combinations:  $bb, bc, bl$  (these first three collectively known as “heavy flavor” or  $V+hf$ ),  $cc, cl, ll$  (or just “light” or  $l$ ). Ratio systematics are often made with respect to the acceptance in the  $bb$  region.

$V+jet$  systematics are derived in several steps. The first is to use double ratios of acceptances between analysis regions and nominal versus alternative MC’s (so  $(\text{Region1-nominal}/\text{Region2-nominal}) / (\text{Region1-alternate}/\text{Region2-alternate})$ ). The main region comparisons are 2 jet versus 3 jet ( $3+jet$  for 2-lepton) and then 0-lepton versus 2-lepton (1-lepton) for  $Z+hf$  ( $W+hf^{\dagger\dagger}$ ). The final uncertainty contains the sum in quadrature of four effects:

1. Variation of 0.5 and 2 of QCD scales in the **SHERPA** sample
2. Sum in quadrature of half the variation from different resummation and CKKW merging scales <sup>††</sup>
3. Maximal variation between nominal setup and **SHERPA** 2.2.1 with the MMHT2014nnlo68cl and CT14nnlo PDF sets

---

<sup>††</sup>The  $W+hf$  CR versus the SR is also considered for  $W+hf$

<sup>‡‡</sup>cf. [46], Section 2 for a summary of the CKKW method for different parton multiplicities used in **SHERPA**

#### 4. Difference between the **SHERPA** and **MADGRAPH<sub>5</sub>** sets

Summaries of the  $Z+jets$  uncertainties are provided here; the reader is referred to [24] for the  $W+jets$  systematics, as these events are virtually non-existent in the 2-lepton case with which this thesis is almost exclusively concerned. In Table ??, from [24] are the normalization systematics.

The flavor composition ratio systematics are in Table 4.5, also from [24].

**Table 4.5:** The priors on the relative acceptance variations for  $Z+hf$ . The first column details the flavor components across which the acceptance variation is being considered, the second column lists the names of the corresponding nuisance parameter in the Profile Likelihood Fit, the third contains the value of the prior and the fourth column the processes and categories to which this nuisance parameter is applied.

Category	Nuisance Parameter Name	Prior	Applied to
$Z+bc/Z+bb$	SysZbcZbbRatio	40%	$Z+bc$ events (0-Lepton)
		40%	$Z+bc$ events (2-Lepton 2jet)
		30%	$Z+bc$ events (2-Lepton $\geq 3$ jet)
$Z+bl/Z+bb$	SysZblZbbRatio	25%	$Z+bl$ events (0-Lepton)
		28%	$Z+bl$ events (2-Lepton 2jet)
		20%	$Z+bl$ events (2-Lepton $\geq 3$ jet)
$Z+cc/Z+bb$	SysZccZbbRatio	15%	$Z+cc$ events (0-Lepton)
		16%	$Z+cc$ events (2-Lepton 2jet)
		13%	$Z+cc$ events (2-Lepton $\geq 3$ jet)

Finally, the  $p_T^V$  and  $m_{bb}$  shape systematics are derived using control regions in data. The functional form for the  $p_T^V$  systematic is  $\pm 0.2 \log 10(p_T^V/50\text{GeV})$ , and that of the  $m_{bb}$  systematic is  $\pm 0.0005 \times (m_{jj} - 100\text{ GeV})$ .

---

These use the same selections as the signal regions except for  $b$ -tags (0, 1, and 2 tags are studied), with the added requirement in 2tag regions that  $m_{bb}$  not be in the range of 110–140GeV.

### 4.3.3 TOP-PAIR PRODUCTION

Nominal  $t\bar{t}$  samples are produced with PowHEG at NLO for the ME calculation using the NNPDF3.0 PDF set interfaced with PYTHIA8.210 using the A14 tune and the NNPDF2.3 PDF set at LO. The parameters `hdamp` (nominal value  $1.5m_{top}$ , a resummation damping factor for ME/PS matching that can heuristically thought of as tuning high  $p_T$  radiation) in PowHEG and `pThard` (nominal value 0) and `pTdef` (nominal value 2) in PYTHIA (both control merging with PowHEG) are varied to evaluate certain systematics. Alternative  $t\bar{t}$  samples use PowHEG+HERWIG7, MADGRAPH5\_aMC-@NLO+PYTHIA8.2, and the nominal setup with varied tunes and parameter values. Uncertainties are taken to cover the largest difference between the nominal and any of these alternate configurations.

The overall  $t\bar{t}$  normalization is a floating normalization, and further systematics attached to the ratio of acceptances between regions (3-to-2 jet, SR-to-WhfCR, and 1-to-0 lepton) are defined using double ratios; these are summarized in Tables 4.6 and 4.7, taken from [24].

**Table 4.6:** Effect of modeling systematics on  $t\bar{t}$  normalization in the 0 and 1-lepton analysis region.

Systematic	0-lepton		1-lepton			
	2j	3j	WCR 2j	SR 2j	WCR 3j	SR 3j
floating normalization						
SysttbarNorm_L0	8%	8%	–	–	–	–
SysttbarNorm_J2	9%	–	9%	9%	–	–
SysttbarNorm_DWhfCR_L1	–	–	25%	–	25%	–

---

The use of a top  $e - \mu$  control region helps constrain this.

**Table 4.7:** Effect of modeling systematics on  $t\bar{t}$  normalization in the 2lepton regions. The SysTTbarPTV\_L2\_L2 systematic is implemented as a shape systematic over the full  $VpT > 75$  GeV range, and as a result has different acceptance effects in the low and high  $VpT$  regions. Systematics are treated the same in both signal and control regions, and ``lo'' and ``hi'' refer to the  $p_T^V$  split in events.

	2jet		$\geq 3$ jets	
	lo	hi	lo	hi
norm_ttbar_J2_L2	floating normalization			-
norm_ttbar_J3_L2	-		floating normalization	
SysTTbarPTV_L2_L2	effect on each region obtained from shape rw			

Shape systematics for  $p_T^V$  and  $m_{bb}$  are linear and taken to cover the largest difference reasonably well, as described above in 4.2.2. These are summarized in Table 4.8, again taken from [24].

**Table 4.8:** Summary of all shape uncertainties for the  $t\bar{t}$  process with short descriptions and the name of the corresponding nuisance parameters.

Analysis region	Uncertainty	Value	Source	NP
0,1 lepton	$p_T^V$ shape	shape	fit through largest deviation (aMC@NLO + PYTHIA8)	TTbarPTV
2 lepton	$p_T^V$ shape	norm	fit through largest + shape & deviation (aMC@NLO + PYTHIA8)	TTbarPTV_L2
0,1 lepton	$m_{bb}$ shape	shape	fit through largest only & deviation (aMC@NLO + PYTHIA8)	TTbarMBB
2 lepton	$m_{bb}$ shape	shape	fit through largest only & deviation (aMC@NLO + PYTHIA8)	TTbarMBB_L2

#### 4.3.4 DIBOSON PRODUCTION

Three diboson production processes (collectively denoted  $VV$ ) are important for these analyses:  $ZZ$ ,  $WZ$ , and  $WW$ . Nominal samples are created using **SHERPA 2.2.1** using the NNPDF3.0 PDF set. Alternative samples use **POWHEG+PYTHIA8** and **POWHEG+HERWIG++**. The methodology here is similar to that of the  $t\bar{t}$  systematics, with both overall acceptance and lepton channel specific uncertainties, with the exception that UE+PS and QCD scale are treated separately (PDF+ $\alpha_s$  was found to be negligible).  $p_T^V$  shape systematics are described using linear fits, while  $m_{b\bar{b}}$  shape systematics are described using hyperbolic tangents (third degree polynomials) in the 2 jet (3 jet) regions. Once again, summary tables from [24] are reproduced here.

**Table 4.9:** Summary of all systematic uncertainties on the diboson cross section including their value, source and the corresponding nuisance parameter name.

Sys Name	source	Norm. effect	applied to
SysWWNorm	overall cross section uncertainty	25%	WW in all regions
SysWZNorm	overall cross section uncertainty	26%	WZ in all regions
SysZZNorm	overall cross section uncertainty	20%	ZZ in all regions

**Table 4.10:** Summary of the systematic uncertainties on the VH acceptance in each analysis region and on the  $p_T^V$  and  $m_{b\bar{b}}$  shapes originating from altering the QCD scale, including their nuisance parameter name.

NP name	0L: $ZZ \rightarrow \nu\bar{\nu}bb$		1L: $WZ \rightarrow \ell\nu bb$		2L: $ZZ \rightarrow \ell^+\ell^- bb$	
	2j	3j	2j	3j	2j	$\geq 3j$
SysVZ_UEPS_Acc	5.6%	5.6%	3.9%	3.9%	5.8%	5.8%
SysVZ_UEPS_32JR	-	7.3%	-	10.8%	-	3.1%
SysVZ_UEPS_VPT	shape+norm		shape only		shape+norm	
SysVZ_UEPS_MBB	shape only					
SysVZ_QCDscale_J2	10.3%	-	12.7%	-	11.9%	-
SysVZ_QCDscale_J3	-15.2%	+17.4%	-17.7%	+21.2%	-16.4%	+10.1%
SysVZ_QCDscale_JVeto	-	+18.2%	-	+19.0%	-	-
SysVZ_QCDscale_VPT	shape+norm		shape only		shape+norm	
SysVZ_QCDscale_MBB	shape only					

#### 4.3.5 SINGLE TOP PRODUCTION

Single top sample are generated separately for the different production channels ( $s$ ,  $t$ , and  $Wt$ ) using PowHEG with the CT10 NLO PDF's interfaced with PYTHIA6 using the PERUGIA2012 PS tune and the corresponding CTEQ6L1 LO PDF's and PHOTOS (TAUOLA) for QED final state ( $\tau$ ) decays. Just as with  $t\bar{t}$  samples, PowHEG and PYTHIA settings are varied for certain systematics. Alternative samples use PowHEG+PYTHIA6 with  $Wt$  diagram subtraction (DS) (instead of “diagram removal” for the ME calculation) and MADGRAPH5\_aMC@NLO+HERWIG++. Systematics are derived separately in each channel, and are well described in the summary Table 4.11 taken from [24].

**Table 4.11:** Summary of all uncertainties for the single top process with short descriptions and the name of the corresponding nuisance parameters, updated for the winter baseline analysis.

Production	Uncertainty	Value	Source	Nuisance Parameter
s-channel	overall normalization	4.6%	sum in quadrature of $\mu_R$ , $\mu_F$ , $\alpha_S$ and PDF uncertainties	<code>stopNorm</code>
t-channel	overall normalization	4.4%	sum in quadrature of $\mu_R$ , $\mu_F$ , $\alpha_S$ and PDF uncertainties	<code>stopTNorm</code> correlated with 2 jet and 3 jet case
t-channel	2 jet region acceptance of deviations in alternative generators	17%	sum in quadrature	<code>stopTAcc</code> correlated with overall and 3 jet case
t-channel	3 jet region acceptance	20%	sum in quadrature of deviations in alternative generators	<code>stopTAcc</code> correlated with overall and 2 jet case
$Wt$ channel	overall normalization	6.2%	sum in quadrature of $\mu_R$ , $\mu_F$ , $\alpha_S$ and PDF uncertainties	<code>stopWtNorm</code> correlated with 2 jet and 3 jet case
$Wt$ channel	2 jet region normalization	35%	sum in quadrature of deviations in alternative generators	<code>stopWtAcc</code> correlated with overall and 3 jet case
$Wt$ channel	3 jet region normalization	41%	sum in quadrature of deviations in alternative generators	<code>stopWtAcc</code> correlated with overall and 2 jet case
t-channel	$p_T^V$ shape	shape	fit through largest deviation ( <code>POWHEG+HERWIG++</code> ) $\pm 0.001 \times p_T^V \mp 0.17 + 1$	<code>StopPTV</code>
t-channel	$m_{b\bar{b}}$ shape	shape	fit through largest deviation ( <code>POWHEG+PYTHIA6 [radHi-radLo]</code> ) $\pm 0.0008 \times m_{b\bar{b}} \mp 0.12 + 1$	<code>StopMBB</code>
$Wt$ channel	$p_T^V$ shape	shape	fit through largest deviation ( <code>POWHEG+PYTHIA6</code> with diagram subtraction) $\pm 0.003 \times p_T^V \mp 0.69 + 1$	<code>StopWtPTV</code>
$Wt$ channel	$m_{b\bar{b}}$ shape	shape	fit through largest deviation ( <code>POWHEG+PYTHIA6</code> with diagram subtraction) $\pm 0.0036 \times m_{b\bar{b}} \mp 0.52 + 1$ ( $m_{b\bar{b}} < 275$ GeV) $\mp 0.47 + 1$ ( $m_{b\bar{b}} \geq 275$ GeV)	<code>StopWtMBB</code>

子路曰：衛君待子而為政，子將奚？

子曰：必也正名乎！

Confucius, *The Analects*

# 5

## Object and Event Reconstruction and Selection

IN BREAKING WITH THE STANDARD CONVENTION both object definitions and their associated experimental systematic uncertainties will be defined in this chapter: the hope is that the proximity

of these descriptions will allow them to elucidate each other. Summary tables are almost exclusively taken from [10] or [14]. This analysis, like most analyses in ATLAS, use central object definitions from collaboration combined performance (CP) groups<sup>\*</sup> using standard analysis tools and recommendations from these groups for the various objects and their accompanying systematic uncertainties.

Before proceeding to the objects used in this analysis, we begin with a few remarks on uncertainties associated with object reconstruction. Event-level variables and selections are discussed more in depth in Chapters 1 and 6. As described in Section 4.2, systematics quantify the uncertainty associated with certain effects, and are generally treated in an analysis by saving histograms of discriminating distributions corresponding to the nominal analysis except with the systematic in question varied by plus and minus one standard deviation each (one histogram each). While for modeling systematics this only corresponds to different event weights, for experimental systematics like those described in this chapter (with the exception of flavor tagging and certain trigger systematics), this is done by varying the parameter in question and re-running reconstruction with the systematic varied before recomputing all event level quantities and then saving discriminant values in their appropriate distributions. This is, in general, a much more computationally intensive process in the analysis, which is why an entire software framework, the `CxAODFramework`, was created for this analysis (see Section 3 of [10] for more details).

---

<sup>\*</sup>Teams of physicists within ATLAS dedicated to studying different aspects of reconstruction general to very many analyses. An example is the ATLAS Muon CP group, whose duties include providing definitions for how muons are reconstructed in ATLAS, different quality requirements and thresholds, and muon related systematic uncertainties, as well as software packages to make these definitions and guidelines easier to implement.

## 5.1 TRIGGERS

Tables of the triggers used with the 2015 and 2016 datasets are given in Tables 5.1 and 5.2.

**Table 5.1:** Summary table of triggers used in 2015 Data.

0 lep	1 lep	2 lep
HLT_xe70	HLT_xe70 HLT_e24_lhmedium_L1EM20VH OR HLT_e60_lhmedium OR HLT_e120_lhloose	HLT_mu20_iloose_L1MU15 OR HLT_mu40 HLT_e24_lhmedium_L1EM20VH OR HLT_e60_lhmedium OR HLT_e120_lhloose

**Table 5.2:** Summary table of triggers used in 2016 Data.

period	o lep	1 lep	2 lep
A	HLT_xe90_mht_L1XE50	HLT_xe90_mht_- L1XE50, HLT_e26_- lhtight_nod0_- ivarloose OR HLT_- e60_lhmedium_nod0 OR HLT_e60_medium OR HLT_e140_- lhloose_nod0	HLT_mu24_- ilosse(data), HLT_- mu24_ilosse_- L1MU15(MC) OR HLT_mu40,HLT_e26_- lhtight_nod0_- ivarloose OR HLT_- e60_lhmedium_nod0 OR HLT_e60_medium OR HLT_e140_- lhloose_nod0
B-D <sub>3</sub>	HLT_xe90_mht_L1XE50	HLT_xe90_mht_- L1XE50, HLT_e26_- lhtight_nod0_- ivarloose OR HLT_- e60_lhmedium_nod0 OR HLT_e60_medium OR HLT_e140_- lhloose_nod0	HLT_mu24_ivarmedium OR HLT_mu50, HLT_- e26_lhtight_nod0_- ivarloose OR HLT_- e60_lhmedium_nod0 OR HLT_e60_medium OR HLT_e140_- lhloose_nod0
D <sub>4</sub> -E <sub>3</sub>	HLT_xe110_mht_- L1XE50	HLT_xe110_mht_- L1XE50, HLT_e26_- lhtight_nod0_- ivarloose OR HLT_- e60_lhmedium_nod0 OR HLT_e60_medium OR HLT_e140_- lhloose_nod0	HLT_mu24_ivarmedium OR HLT_mu50, HLT_- e26_lhtight_nod0_- ivarloose OR HLT_- e60_lhmedium_nod0 OR HLT_e60_medium OR HLT_e140_- lhloose_nod0
$\geq F_1$	HLT_xe110_mht_- L1XE50	HLT_xe110_mht_- L1XE50, HLT_e26_- lhtight_nod0_- ivarloose OR HLT_- e60_lhmedium_nod0 OR HLT_e60_medium OR HLT_e140_- lhloose_nod0	HLT_mu26_ivarmedium OR HLT_mu50, HLT_- e26_lhtight_nod0_- ivarloose OR HLT_- e60_lhmedium_nod0 OR HLT_e60_medium OR HLT_e140_- lhloose_nod0

The 0-lepton channel uses a  $\vec{E}_T^{\text{miss}}$  trigger, while the 2-lepton channel uses single lepton triggers, with the 1-lepton analysis using both. Since the 0- and 1-lepton channels are largely beyond the scope of this thesis, the discussion here will be limited to the single lepton triggers; the interested reader is directed towards [10] and its cited sources for an in-depth discussion of the use of the  $\vec{E}_T^{\text{miss}}$  trigger.

The efficiency of triggers is in general different on simulated datasets than in actual data collected in ATLAS, so a scale factor to correct for this difference in efficiency must be applied to simulation events. This scale factor is given by the muon CP group for muons for both the 1- and 2-lepton cases and from the electron CP group for the 1-lepton case. For the two electron case, this was calculated by the analysis team as (details in [10]):

$$\frac{1 - (1 - \epsilon_{\text{MC}}^{e1} \times \text{SF}^{e1}) \times (1 - \epsilon_{\text{MC}}^{e2} \times \text{SF}^{e2})}{1 - (1 - \epsilon_{\text{MC}}^{e1}) \times (1 - \epsilon_{\text{MC}}^{e2})} \quad (5.1)$$

There are also systematic uncertainties associated with these trigger efficiencies. The single electron trigger efficiency systematic uncertainty is encapsulated in a single systematic, `EL_EFF_Trigger_Total_1NPCOR_PLUS_UNCOR`, while the single muon trigger efficiency has two components, one each for the sample statistics, `MUON_EFF_TrigStatUncertainty`, and systematic uncertainties `MUON_EFF_TrigSystUncertainty` associated with that efficiency's measurement.

While the momentum associated with the lowest un-prescaled single lepton triggers changes depending on data-taking conditions (the numbers associated with the triggers in the tables can be thought of as nominal  $p_T$  values for trigger level objects), the lowest typical value is  $\sim 25$  GeV. In order to maintain this triggering capability on low  $p_T$  muons in the higher luminosity environment

of the Run 3 LHC and beyond, trigger-capable detectors will be installed in upgraded New Small Wheels (NSW) of the ATLAS muon detector during the Phase I upgrade. Detailed studies in simulation of the trigger algorithm performance under nominal and misaligned conditions for the Micromegas detectors to be installed in the NSW may be found in Appendix A.

## 5.2 ELECTRONS

Electrons in ATLAS are reconstructed using a combination of the ATLAS electromagnetic calorimeter (ECAL) and inner detector (ID). Reconstruction begins by searching for so-called “seed clusters” in the ECAL. The ECAL is divided into a  $200 \times 256$  tower grid in the  $\eta - \phi$  plane, with each tower having a size of  $0.025$  square in  $\eta$  and  $\phi$ , corresponding to the granularity of the ECAL in its middle layer, with all energy in a tower summed longitudinally. A “sliding window” of  $3 \times 5$  cells in the  $\eta - \phi$  plane is then used to identify EM clusters associated with electrons based on criteria detailed in [47]. This comparatively simple algorithm (in contrast to jet reconstruction detailed below) is effective since electromagnetic showers have a well defined behavior and shape.

Once seed clusters have been formed, they are associated with tracks in the inner detector. Combined cluster-tracks pairs form electron candidates. In order for a electron candidate to be considered a suitable electron for analysis, it must pass certain quality requirements, based on a cut on the value of a likelihood-based (LH) discriminant (cf. [48] for details). This discriminant is given by:

$$d_{\mathcal{L}} = \frac{\mathcal{L}_S}{\mathcal{L}_S + \mathcal{L}_B}, \quad \mathcal{L}_S(\vec{x}) = \prod_{i=1}^n P_{s,i}(x_i) \quad (5.2)$$

where the  $s$  and  $S$  ( $b$  and  $B$ ) subscripts refer to distributions in fiducial signal (background) distributions in bins of  $|\eta|$  and  $E_T$ . The  $P(x_i)$  are probability distributions functions (pdf)'s for input variables. Several sets of input variables exist for increasingly stringent quality requirements on electrons; this analysis uses Loose LH electrons as the base for electron selection, with the input variables relating to leakage into the hadronic calorimeter (HCAL), shower and energy deposits in each of the ECAL layers, track quality requirements, TRT hits, and track-cluster matching. This analysis adds a LooseTrackOnly isolation requirement (the  $p_T$  sum of tracks within a certain  $\eta - \phi$  distance of the candidate track must be below a certain value), impact parameter significance cuts, and an explicit B-layer hit requirement. The  $ZH$ -signal electrons must further pass a  $27\text{ GeV}$   $p_T$  cut ( $1.05 \times p_T^{\text{trigger}}$ ). These requirements are summarized in Table 5.2.

**Table 5.2:** Electron selection requirements.

$e$ Selection	$p_T$	$\eta$	ID	$d_0^{\text{sig}}$	$ \Delta z_0^{\text{BL}} \sin \theta $	Isolation
$VH - \text{loose}$	$>7\text{ GeV}$	$ \eta  < 2.47$	LH Loose + B-layer cut	$< 5$	$< 0.5\text{ mm}$	LooseTrackOnly
$ZH - \text{signal}$	$>27\text{ GeV}$	$ \eta  < 2.47$	LH Loose + B-layer cut	$< 5$	$< 0.5\text{ mm}$	LooseTrackOnly
$WH - \text{signal}$	$>27\text{ GeV}$	$ \eta  < 2.47$	LH Tight	$< 5$	$< 0.5\text{ mm}$	FixedCutHighPtCaloOnly

### 5.2.1 ELECTRON SYSTEMATICS

The electron CP group has tabulated standard systematic uncertainties to be associated with the use of reconstructed electrons in ATLAS analyses in two main categories. The first category is related to efficiency corrections and is broken into three components: identification (`EL_EFF_ID_TotalCorrUncertainty`), reconstruction (`EL_EFF_Reco_TotalCorrUncertainty`), and isolation

(`EL_EFF_Iso_TotalCorrUncertainty`). The second category deals with electron energy scale (roughly, the uncertainty in taking the energy deposits in an EM cluster and turning them into an electron energy) and energy resolution (the width associated with this). This is in practice a very complicated procedure, with over 60 systematics associated, but this analysis is not at all sensitive to these effects and so a simplified model of two systematics, `EG_RESOLUTION_ALL` and `EG_SCALE_ALL`, is used.

### 5.3 MUONS

This analysis uses the standard CP muon collection in an event, though these muons in ATLAS are constructed in a variety of ways; for full details see [49] and [50]. Most muons are constructed using tracks in the chambers of the muon spectrometer (MS), with a variety of algorithms available. MS tracks are sufficient to reconstruct a muon (a fit on these tracks can be used to point back to an interaction point for vertex matching, for example) and, in the  $|\eta| \in (2.5, 2.7)$  interval where there is no tracking, these standalone (SA) muons are the default. The most common and robust form of muon reconstruction combines tracks in the MS with tracks in the ID (more precisely, a global refit with hits from both subsystems is typically done) to form combined (CB) muons. CB and SA muons automatically pass the loose reconstruction requirements for the Loose muons used in this analysis. Additionally, since there is a gap in the  $|\eta| < 0.1$  range in the MS to make room for cabling and other detector services, there are two further muon types used in this range: the segment tagged (ST) muons that match ID tracks to segments in the MDT or CSC chambers and the calorimeter tagged (CT) muons that match ID tracks to calorimeter clusters consistent with minimum ionizing

particles (which muons in ATLAS generally are).

Further quality requirements are imposed on Loose muons for the different muon categories used in this analysis. Isolation requirements similar to the electrons in corresponding categories are imposed, and impact parameter requirements are also imposed. The  $ZH$  signal muons also have a  $p_T$  cut at 27 GeV and a requirement that the muon fall within the  $|\eta|$  range of the ID.

**Table 5.3:** Muon selection requirements.

$\mu$ Selection	$p_T$	$\eta$	ID	$d_0^{\text{sig}}$	$ \Delta z_0^{\text{BL}} \sin \theta $	Isolation
$VH - \text{loose}$	$> 7 \text{ GeV}$	$ \eta  < 2.7$	Loose quality	$< 3$	$< 0.5 \text{ mm}$	LooseTrackOnly
$ZH - \text{signal}$	$> 27 \text{ GeV}$	$ \eta  < 2.5$	Loose quality	$< 3$	$< 0.5 \text{ mm}$	LooseTrackOnly
$WH - \text{signal}$	$> 25 \text{ GeV}$	$ \eta  < 2.5$	Medium quality	$< 3$	$< 0.5 \text{ mm}$	FixedCutHighPtTrackOnly

### 5.3.1 MUON SYSTEMATICS

Similar to the treatment of systematic uncertainties associated with the electrons, muons have CP defined systematics. The muon momentum scale and resolution systematics are divided into three categories associated one for uncertainties related to ID tracks (`MUONS_ID`), one for MS tracks (`MUONS_MS`), one for the overall scale (`MUONS_SCALE`), and two for charge dependent momentum scales (`MUON_SAGITTA_RHO` and `MUON_SAGITTA_RESBIAS`). The remaining systematics have a STAT and SYS component corresponding to the sample statistics and systematic uncertainties for their individual components. Efficiency scale factors use different standard candles in different  $p_T$  ranges ( $J/\psi$ 's ( $Z$ 's) below (above) 15 GeV), and so these systematics are broken up into two categories (`MUON_EFF_STAT` and `MUON_EFF_SYS`; `MUON_EFF_STAT_LOWPT` and `MUON_EFF_SYS_LOWPT`). There are also

isolation systematics (MUON\_ISO\_STAT, MUON\_ISO\_SYS) and track to vertex association systematics (MUON\_TTVA\_STAT, MUON\_TTVA\_SYS).

#### 5.4 MISSING TRANSVERSE ENERGY

High precision performance of  $\vec{E}_T^{\text{miss}}$  is not so crucial to the 2-lepton analysis (though it is very important to the other channels), so the interested reader is referred to [51].  $\vec{E}_T^{\text{miss}}$  in ATLAS is the negative vectoral sum of physics objects (in this analysis just jets and leptons, though in principle also including  $\tau$ 's and  $\gamma$ 's) and a so-called track based soft term (TST). The TST is comprised of valid ID tracks not associated with any physics objects in an event. These tracks must be associated to an event's primary vertex, have a  $p_T > 0.4$  GeV, and pass other quality requirements.

The  $\vec{E}_T^{\text{miss}}$  systematic uncertainties relevant to this analysis are related to track based energy scale and resolutions in both the soft term and in the jets and are: MET\_SoftTrk\_ResoPara, MET\_SoftTrk\_ResoPerp, MET\_SoftTrk\_ScaleDown, MET\_SoftTrk\_ScaleUp, MET\_JetTrk\_ScaleDown, and MET\_JetTrk\_ScaleUp.

#### 5.5 JETS

Unlike leptons, all analyses considered in this thesis are sensitive to factors regarding jet reconstruction and associated systematic uncertainties. A general discussion of jets precedes jet reconstruction in ATLAS and associated systematics relevant to this thesis.

### 5.5.1 JET ALGORITHMS

The hadronic nature of jets makes jet reconstruction a lot more complicated than electron or photon reconstruction, where a regular shower shape and track matching (or lack thereof in the case of the chargeless photon) provide a fairly straightforward and robust approach. The interested reader is referred to [8] for an excellent survey, from which this discussion is greatly abbreviated.

Looking at an event like the one in Figure 5.1, unambiguous individual jets are particularly easy to identify, more or less popping out of the  $\eta - \phi$  plane plot, but this is not always the case.

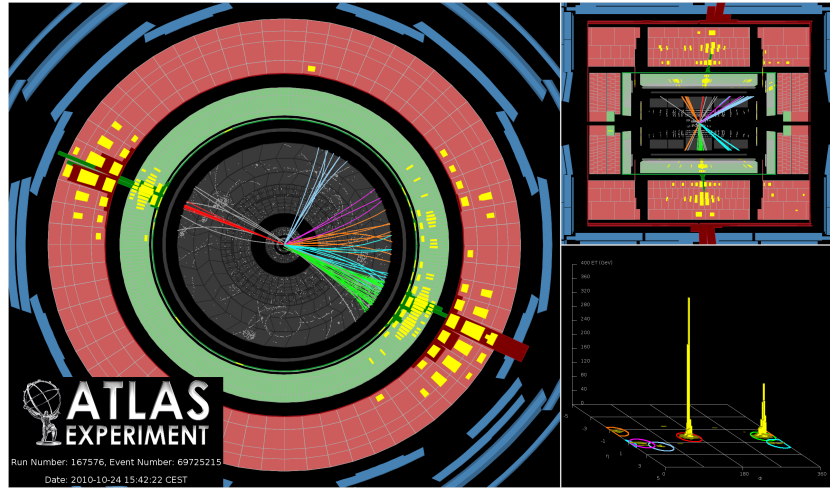


**Figure 5.1:** A clean ATLAS dijet event.

Two general methods of turning particles/calorimeter towers into jets exist: cone-based and sequential recombination. The general theme of the former is to find a hard (energetic) particle and draw a circle around it in the  $\eta - \phi$  plane in an intelligent manner, while the theme of the latter is to find some metric of distance between particles and then to cluster pairs based on this distance into jets in an intelligent way. Cone-based algorithms are simple (and therefore generally quite fast)

but generally lack some properties of the sequentially recombined jets (though there are notable exceptions like SISCone). Cone algorithm reconstructed jets are important for trigger level objects in ATLAS, though since no jet triggers are used in this analysis, they will not be discussed any further here.

The general drawback of cone-based algorithms is that they are not infrared and collinear (IRC) safe. That is, neither the emission of a soft (IR) quark or gluon during hadronization nor the collinear splitting of hard particles during hadronization should not change the final jet collection in an event. These are fairly common edge cases and can lead to certain pathologies in QCD calculations. Infrared and collinear safety are diagrammed schematically in Figures 5.2 (a) and (b), taken from [8].

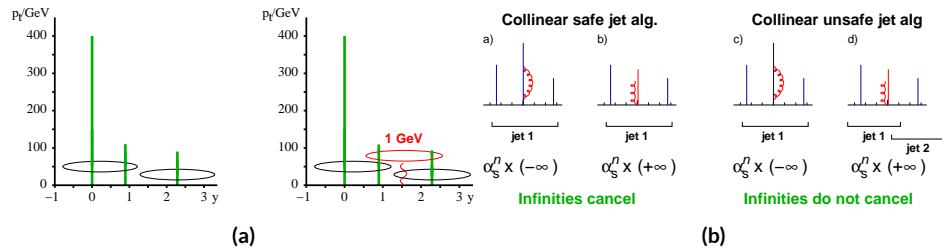


Figure 5.2: Infrared (a) and collinear (b) safety.

Sequential recombination algorithms are generally safe from these effects, as these edge cases are very “close” to each other by construction. A sequential recombination algorithm proceeds as follows

1. Evaluate the set of distances  $d_{ij}$  (for pairs of objects) and  $d_{iB}$  (the “beam distance” for each individual object)

$$d_{ij} = \min \left( p_{Ti}^{2p}, p_{Tj}^{2p} \right) \frac{\Delta R_{ij}^2}{R^2}, \quad d_{iB} = p_{Ti}^{2p} \quad (5.3)$$

2. Find the minimum distance

3. If the minimum distance is:

- A  $d_{ij}$ : cluster these objects together, and go to step 1
- A  $d_{iB}$ : call the  $i^{\text{th}}$  object a jet, remove it from the set of objects to be clustered, and go to step 1

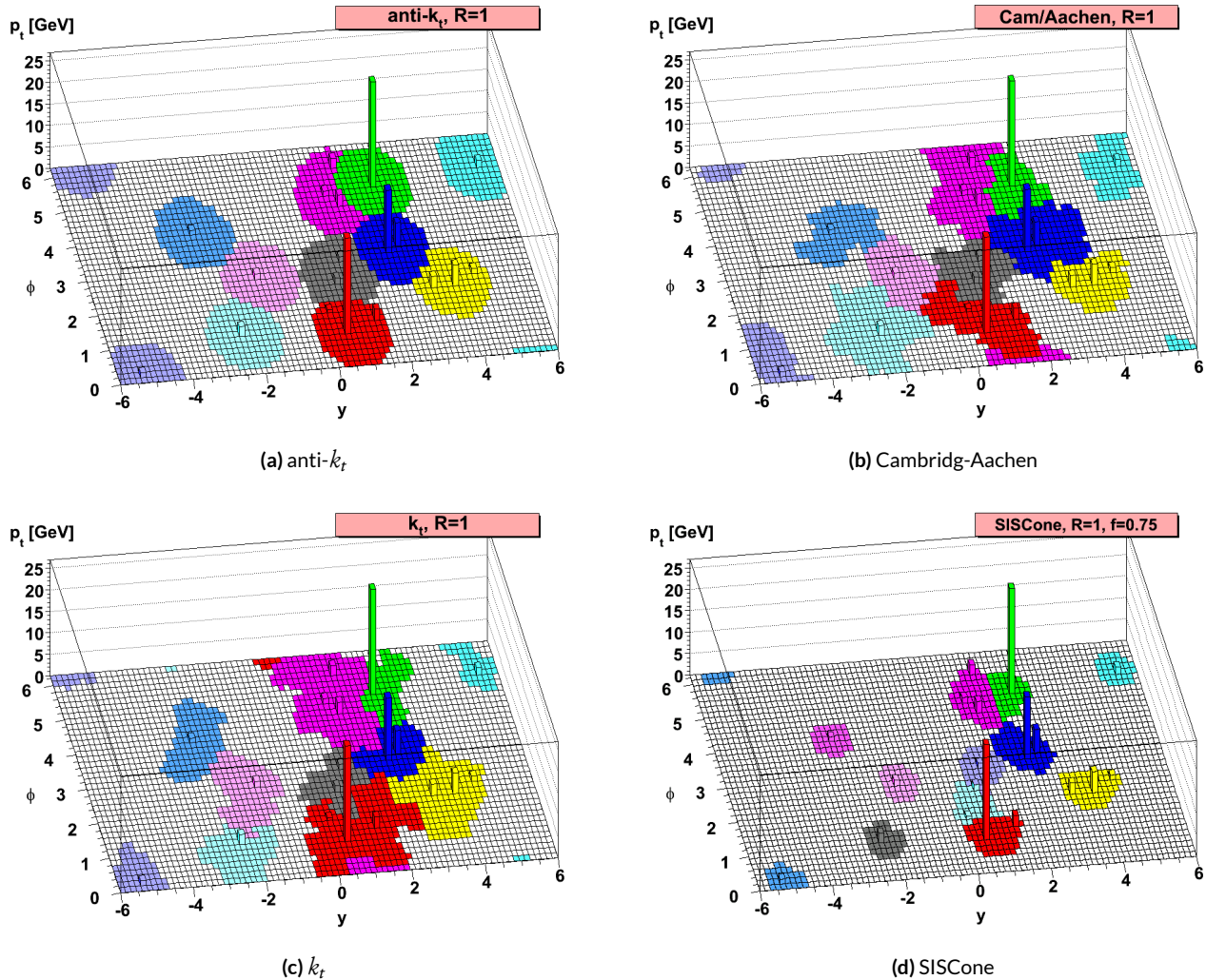
4. Repeat until all objects are clustered into jets

The choices one must make in sequential recombination are the size parameter  $R$ , akin to a cone radius in cone-based algorithms, and the momentum power  $p$ . Common choices and their trade-offs are:

- +1: the  $k_t$  algorithm; favors the softer particles in an event, so the cluster sequence gives a history of hadronization, but jet shapes are irregular (i.e. not circular in the  $\eta - \phi$  plane)
- 0: the Cambridge-Aachen algorithm: a pure distance metric; less substructure but jets tend to be more circular
- -1: the anti- $k_t$  algorithm: clustering begins with hardest particles in an event; regular, localized jet shapes, but virtually no substructure in clustering history

Jet reconstruction using all three algorithms on the same event, as well as SISCone, are shown in Figure 5.3.

**Figure 5.3:** Different jet algorithms used on the same event. IC:[8]



All three algorithms have uses for different applications in ATLAS, with anti- $k_t$   $R = 0.4$  jets being the default jet collection.<sup>†</sup> These are the jets used in this analysis.

If the choice of jet algorithm seems a little arbitrary, it is. There is no one-size-fits-all jet collection perfect for every application, and analyzers have to make these choices for themselves. One interesting choice is the jet size parameter,  $R$ . A large  $R$  jet will contain more of the radiation coming from a final state object, but its large size makes it susceptible to contamination from the underlying event and pileup (as well as other analysis objects if  $R$  is sufficiently large or objects sufficiently boosted), with small  $R$  jets having the opposite features.  $R = 0.4$  is a fairly middle-of-the-road choice. A natural question to ask is whether there needs to be just one jet collection in an analysis. Might there not be more information to be gained from looking at more jet sizes or clusterings? Preliminary studies point to this answer being yes and are addressed in Appendix B.

### 5.5.2 STANDARD ATLAS HBB JETS

There are a few considerations that arise with jets in physical detectors. The first is what type of object to use as the stand in for “particles” since ATLAS measures energy deposits, not pions. The approach ATLAS has settled upon are calorimeter topological clusters (or CaloTopoClusters for short) [52]. Unlike the sliding window algorithm used for electron clusters, CaloTopoClusters use a noise significance based approach in the “4-2-o” algorithm. Each cell in the electromagnetic and hadronic calorimeters (ECAL and HCAL, respectively) has associated with it a characteristic noise level ( $N$  in Equation 2.6), with this noise level in each channel, it is possible to construct a “significance” for the

---

<sup>†</sup>The other collections find their primary uses in jet substructure techniques. For an example, cf. the discussion of jet trimming in Appendix B.

registered energy deposit in a given channel for a given event by dividing the measured value by its characteristic noise. Groups of cells having a significance of 4 are taken as the centers of clusters in the  $\eta - \phi$  plane. The second layer in a cluster includes all neighboring cells to the central layer with significance of at least 2, and the final layer includes all the nearest neighbors to the second layer. This is described in Figure 5.4 from [53].

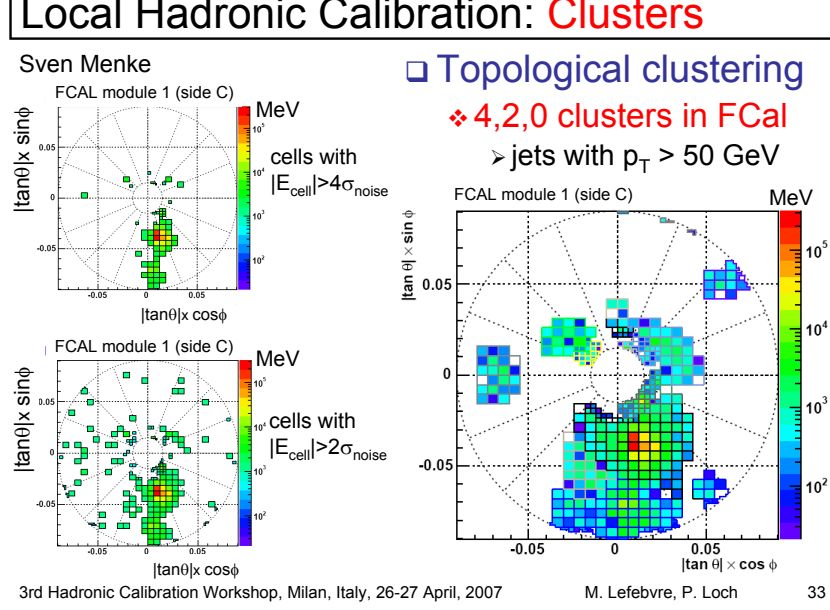


Figure 5.4: A description of the 4-2-0 clustering algorithm.

Once CaloTopoClusters have been formed and clustered into jets, they are calibrated using the electromagnetic (EM) scale (the scale for clusters coming from EM showers). Further details may be found in [54].

Jets in this analysis fall into two categories, “signal” and “forward” jets, and are required to pass certain quality requirements, described in Table 5.4. All jets must pass a series of jet cleaning require-

ments using calorimeter level variables to eliminate jets coming from problematic calorimeter cells and certain backgrounds. Some signal jet candidates also make use of a Jet Vertex Tagger (JVT) that uses primary vertex and jet and track  $p_T$  information to decide whether certain soft jets are likely to have come from the the primary (hard scatter) vertex in an event or are to be considered pileup. Further details on JVT may be found in [55]. Jets are further corrected using standard CP tools and a dedicated PtReco correction, all outlined in Section 7.3 of [10].

**Table 5.4:** AntiKt4EMTopoJets selection requirements. The jet cleaning is applied via the JetCleaningTool, that removes events in regions corresponding to hot calorimeter cells.

Jet Category	Selection Requirements
Forward Jets	jet cleaning $p_T > 30 \text{ GeV}$ $2.5 \leq  \eta  < 4.5$
Signal Jets	$p_T > 20 \text{ GeV}$ and $ \eta  < 2.5$ jet cleaning $\text{JVT} \geq 0.59$ if ( $p_T < 60 \text{ GeV}$ and $ \eta  < 2.4$ )

Overlap removal in this analysis is done according to the following precedence, taken from [10] with further steps only taken into account if an object survives previous steps:

- tau-electron: If  $\Delta R(\tau, e) < 0.2$ , the  $\tau$  lepton is removed.
- tau-muon: If  $\Delta R(\tau, \mu) < 0.2$ , the  $\tau$  lepton is removed, with the exception that if the  $\tau$  lepton has  $p_T > 50 \text{ GeV}$  and the muon is not a combined muon, then the  $\tau$  lepton is not removed.
- electron-muon: If a combined muon shares an ID track with an electron, the electron is removed.

If a calo-tagged muon shares an ID track with an electron, the muon is removed.

- electron-jet: If  $\Delta R(\text{jet}, e) < 0.2$  the jet is removed.

For any surviving jets, if  $\Delta R(\text{jet}, e) < \min(0.4, 0.04 + 10 \text{ GeV}/p_T^e)$ , the electron is removed.

- muon-jet If  $\Delta R(\text{jet}, \mu) < 0.2$  or the muon ID track is ghost associated to the jet, then the jet is removed if the jet has less than three associated tracks with  $p_T > 500 \text{ MeV}$  ( $\text{NumTrkPt} < 3$ ) or both of the following conditions are met: the  $p_T$  ratio of the muon and jet is larger than 0.5 ( $p_T^\mu/p_T^{\text{jet}} > 0.5$ ) and the ratio of the muon  $p_T$  to the sum of  $p_T$  of tracks with  $p_T > 500 \text{ MeV}$  associated to the jet is larger than 0.7 ( $p_T^{\mu\text{on}}/\text{SumPtTrkPt} > 0.7$ ).

For any surviving jets, if  $\Delta R(\text{jet}, \mu) < \min(0.4, 0.04 + 10 \text{ GeV}/p_T^\mu)$ , the muon is removed.

- tau-jet: If  $\Delta R(\tau, \text{jet}) < 0.2$ , the jet is removed.
- electron-fat jet: If  $\Delta R(e, \text{fat jet}) < 1.2$ , the fat jet is removed.

Jets are corrected using a muon-in-jet correction and then a kinematic fitter (Appendix D of [14]) for the 2-lepton case (PtReco correction for the 0- and 1- lepton case). The muon-in-jet correction is designed for  $b$ -jets. Since the decay of a  $b$ -quark to a  $c$ -quark and finally to a light quark (these are the multiple vertices for which JetFitter in Section 5.6.1 searches) involves two weak decays, there are two  $W$ -bosons involved in the decay. Some of these will decay semileptonically, and, while electron and  $\tau$  energy will be captured by the calorimeters, semileptonic  $\mu$ 's will only be registered in the MS, which occurs in some 44% of all decays from a theoretical standpoint, which amounts to about 12% in practice (due to track isolation requirements for the leptons). This value is about 1–2% for electrons, which deposit their energy in the calorimeter and so require no correction; any jet with a valid lepton associated to it is deemed semileptonic (all others are called hadronic). Any jet with muons associated with it has the closest muon's 4-vector (in the  $\eta - \phi$  plane) added to it.

The PtReco correction is a scale factor on the muon-in-jet corrected jet's 4-vector based on the jet's  $p_T$  and whether the jet is hadronic or semileptonic. This correction factor is based on particle level studies done on a TruthWZ sample. As the 0- and 1-lepton cases are not the focus of this thesis, the interested reader is directed to Section 7.3 of [10].

The kinematic fitter used in 2-lepton events with two or three jets takes as its input 12 fit parameters,

- energies of 2 electron or  $p_T$  of 2 muons
- energies of 2  $b$ -jets
- $\eta, \phi$  of 2 leptons and 2 jets
- $p_X$  and  $p_Y$  of  $\ell\ell b\bar{b}$  system.
- $m_{\ell\ell}$

and 3 constraints for the variation of these parameters,

- parameters : Gaussian ( $b$ -jet energy : Transfer Functions (TF); these are denoted  $L$ , with an  $L_{truth}$  as a prior) (the  $\phi$  parameters)
- $p_X$  and  $p_Y$  of  $\ell\ell b\bar{b}$  system : zero with a width of 9 GeV obtained from  $ZH$  signal MC.
- $m_{ll}$  : Breit-Wigner (BW) distribution of  $Z$  boson (final term, leptons denoted  $\Omega$ )

which leads to test statistic from the usual likelihood formalism to be minimized in each event:

$$\begin{aligned} -2 \ln \mathcal{L} = & \sum_{i=j} \left( \frac{(\phi_i^n - \phi_i^0)^2}{\sigma_\phi^2} \right) + \left( \frac{(\Omega_l^n - \Omega_l^0)^2}{\sigma_\Omega^2} \right) - 2 \ln (L^j) - 2 \ln (L_{truth}^j) \\ & + \sum_{i=x,y} \frac{(\sum p_i^n - \sum P_i)^2}{\sigma_{\sum p_i}^2} + 2 \ln \left( (m_{\ell\ell} - M_X^2)^2 + M_X^2 \Gamma^2 \right) \end{aligned} \quad (5.4)$$

### 5.5.3 JET SYSTEMATICS

As with the electron systematics, jet energy scale (JES) and resolution (JER) are the two principal considerations for systematic uncertainties, with even more standard. JER, as with the electron energy resolution, is a single systematic uncertainty, `JET_JER_SINGLE_NP`. There is also a single JVT efficiency `JET_JvtEfficiency` systematic uncertainty. There are 88 nominal JES systematics, and this analysis is sufficiently sensitive to these variations that a single systematic is grossly insufficient. Nevertheless, some simplification is possible, with the 75 of these nuisance parameters (mostly statistical uncertainties related to the  $Z$ +jet and  $\gamma$ +jet calibrations) being reduced to 8, and several explicitly named nuisance parameter. These remaining named NP's are: 3 NP's related to the  $\eta$  intercalibration used to extrapolate standard calibrations to other jet  $\eta$  regions, 4 NP's related to the flavor composition of principle background samples ( $W/Z$ +jets, top, and diboson), 4 pileup systematics, a single NP for the  $b$ -jet energy scale, a high  $p_T$  jet energy scale systematic, and one for jets that punch through the HCAL to leave energy deposits in the MS. These are listed explicitly in Table 5.6.

## 5.6 FLAVOR TAGGING

Given that the final state in this analysis involves pairs of jets originating from  $b$ -quarks, deploying effective flavor tagging algorithms is imperative. While flavor tagging in general can be used to isolate any flavor ( $b$ ,  $c$ , or light ( $u$ ,  $d$ ,  $s$ , or gluon-initiated jets)), this analysis exclusively looks for  $b$ -jets, so this disucssion will focus on  $b$ 's. At truth-level in sumlation, this is fairly straightforward: one need only look at the particles contained within a jet and seeing if any include a  $b$ -quark (sometimes a  $B$

hadron) in the decay chain.

### 5.6.1 DIRECT TAGGING

One of the most distinctive features of  $b$ -jets is the presence of secondary vertices, as illustrated in Figure 5.5. While most partons created in particle collisions will hadronize promptly,  $b$ -quarks will first hadronize into  $B$ -hadrons, which have lifetimes of about a picosecond. This small but finite lifetime means that these particles will travel about half a millimeter or so before decaying into a jet in much the usual way, and the tracks from this decay will point back to this displaced, secondary vertex.

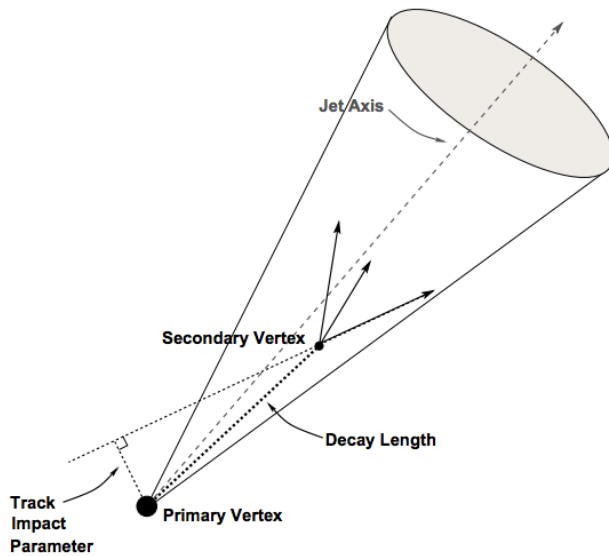


Figure 5.5: An illustration of a secondary vertex in a  $b$ -jet. Image credit: [9]

There are various secondary vertex algorithms used as inputs to the nominal  $b$ -tagging algorithm [56], with three main types of algorithms used as inputs

1. Track impact parameter based algorithms: I<sub>2</sub>PD (signed transverse only; more pileup robust), I<sub>3</sub>PD (signed transverse and longitudinal)
2. Inclusive secondary vertex reconstruction: SV1 (start with two track vertex pairs and construct a secondary vertex)
3. Multiple vertex reconstruction (decay chain): JetFitter (PV  $\rightarrow b \rightarrow c$  decay chain using Kalman filter)

All of these are combined into a boosted decision tree (BDT) and trained on five million  $t\bar{t}$  events with an 90%/10% light/ $c$  jet background to form the MV2c10 algorithm, with 10 referring to the percentage of charm events in the training background. The 10% charm ratio was found to be a good balance between increased charm rejection capability (as opposed to MV2c00, which has no charm in the background training samples) and loss in light jet rejection (compared to MV2c20, which has 20% charm events in background training samples).

**ANALYSIS SPECIFIC CONCERNS AND SYSTEMATIC UNCERTAINTIES** In addition to specifying the tagging algorithm, the working point efficiency must be specified. As with selection algorithms in general, there is a trade off between efficiency/recall (identifying all the  $b$ -jets, minimizing type II error) and purity/precision (making sure all jets positively identified are in fact  $b$ -jets, minimizing type I error). Nominal efficiency working points have been calibrated by the flavor tagging CP group and are outlined in Table 5.5.

These values are aggregate figures, as both the jet's  $p_T$  and  $\eta$  are inputs to the MV2c10 discriminant. The working point chosen for this analysis is the 70% `FixedCutBEff_70` working point, with “fixed cut” referring to the fact that this particular usage of the MV2c10 BDT value is a simple cut value.

**Table 5.5:**  $b$ -tagging working points available for MV2c10 for AntiKt4EMTopoJets. RR is the rejection rate (the inverse of efficiency).

name	MV2c10 weight cut	$b$ -tag eff, [%]	$c$ RR	light RR
FixedCutBEff_60	0.9349	60.03	34.54	1538.78
FixedCutBEff_70	0.8244	69.97	12.17	381.32
FixedCutBEff_77	0.6459	76.97	6.21	134.34
FixedCutBEff_85	0.1758	84.95	3.10	33.53

Just as with the trigger and lepton identification efficiencies, flavor tagging efficiencies differ from their nominal values somewhat depending on what simulation or data sample is being used. To account for this difference, just as in the other cases, scale factors are applied to simulation event weights. It is through these event weights, as with the modeling systematics, that the flavor tagging systematic uncertainties are applied. Given that there are 24 input variables to MV2c10 and that flavor tagging is in general a very difficult problem, it is not surprising that, as with the JES, there are very many systematic uncertainties associated with flavor tagging. However, as with JES, the CP group has compacted the full systematic set into a reduced set of 13 systematic uncertainties: 3 each associated with  $c$  and light jets, 5 for  $b$ -jets (with the naming convention `FT_EFF_Eigen-(B|C|Light)N`), one for the extrapolation of scale factors to different jet  $p_T$  regimes (`FT_EFF_Extrapolation`), and one for the charm to bottom extrapolation (`FT_EFF_Eigen_Extrapolation_from_charm`) [57]. This schematic is a middle-of-the-road “Medium” set of systematics.

### 5.6.2 TRUTH TAGGING

Since imposing a 2  $b$ -tag requirement overwhelmingly rejects events dominated by  $c$ - and light jets, statistics in such MC samples are very low. In order to circumvent this problem and restore full MC statistics, the tag rate function, or “truth-tagging” procedure (in contrast to the standard or “direct tagging” procedure) is applied, in which all events are kept but given a weight that preserves the overall shape and normalization of underlying distributions. Intuitively, this is done by giving events with real  $b$ -jets in MC a much higher weight than events having only  $c$ - or light jets. Truth-tagging is applied to all samples when conducting MVA training in order to maximize statistics and reduce the risk of overtraining. Truth-tagging is also used for data-MC comparison plots in 2-tag regions and for  $V + cc$ ,  $V + c\ell$ ,  $V + \ell$ , and  $WW$  samples used in the final likelihood fit. A detailed description of the truth-tagging process is provided below.

Each jet in a given event has associated with it a  $b$ -tagging efficiency, denoted  $\varepsilon$ , that is a function of its  $p_T$ ,  $\eta$ , and real flavor ( $b$ ,  $c$ , or light) from truth-level information in MC. Intuitively, this efficiency can be thought of as the likelihood that a given jet will be  $b$ -tagged. Hence,  $b$ -jets have a much higher  $b$ -tagging efficiency than  $c$ -jets, which in turn have a higher  $b$ -tagging efficiency than light jets. We define a truth-tag weight for a given combination of tagged and untagged jets as the product of the efficiencies of the tagged jets times the product of the complement of the efficiencies of the untagged jets. For example, for an event with three jets, labeled 1, 2, and 3, if jets 1 and 2 are tagged, and

jet 3 is untagged, the truth-tag weight associated with this combination is

$$\varepsilon_1 \varepsilon_2 (1 - \varepsilon_3) \quad (5.5)$$

In order to obtain a truth-tag weight for an event, one takes the sum of the weights for each possible tag combination. The current analysis requires that all events have exactly two  $b$ -tagged jets, so the truth-tag weight is the sum of all the weights of all possible pairs of tagged jets (events with fewer than two jets are discarded). Going back to the three jet example, one has the possible combinations: jets 1+2 as tagged and jet 3 as untagged; jets 1+3 as tagged and jet 2 as untagged; and finally jets 2+3 as tagged and jet 1 as untagged, which yields a total event weight of

$$w_{tot} = \varepsilon_1 \varepsilon_2 (1 - \varepsilon_3) + \varepsilon_1 \varepsilon_3 (1 - \varepsilon_2) + \varepsilon_2 \varepsilon_3 (1 - \varepsilon_1) \quad (5.6)$$

For some applications (e.g. in order to use variables like  $pT_{B1}$ , the  $p_T$  of the harder  $b$ -tagged jet in an event, in MVA training), it is necessary to choose a combination of jets in an event as “tagged.” This combination is chosen randomly, with the probability for a given combination to be chosen being proportional to its truth-tag weight. In the three jet example, the probability of tagging jets 1+2 is:

$$\frac{\varepsilon_1 \varepsilon_2 (1 - \varepsilon_3)}{w_{tot}} = \frac{\varepsilon_1 \varepsilon_2 (1 - \varepsilon_3)}{\varepsilon_1 \varepsilon_2 (1 - \varepsilon_3) + \varepsilon_1 \varepsilon_3 (1 - \varepsilon_2) + \varepsilon_2 \varepsilon_3 (1 - \varepsilon_1)} \quad (5.7)$$

Though not used in the current analysis, functionality exists for generic truth-tagging requirements (i.e. an arbitrary number of tags on an arbitrary number of jets) through the logical combina-

toric extension and for so-called “pseudo-continuous tagging,” where a  $b$ -tag score is generated for each jet in a given event. Since a random combination of jets is set by hand to pass the  $b$ -tagging cuts regardless of its  $b$ -tag score, a new score must be generated if this information is to be used in further analysis. Under current settings, jets that are tagged are assigned a random  $b$ -tag score that is sampled from the MV2c10 cumulative distribution above the 70% efficiency working point cut. All other jets in the event are assigned a random  $b$ -tag score below the 70% working point cut. Since these distributions are discrete, the scores are not truly continuous (cf. example distributions in Figure 5.6), hence the “pseudo-continuous” nomenclature.

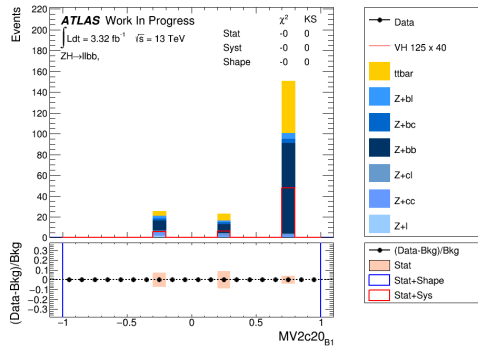


**Figure 5.6:** An example of a pseudo-continuous  $b$ -tagging distribution

A number of closure tests were performed on both the nominal and several systematics cases. In the plots that follow, truth (solid) and direct (dashed) tagging distributions for  $m_{bb}$  and  $\Delta R(b_1, b_2)$  in different  $p_T^V$  regimes for 2 lepton, 2 jet events. Agreement between the truth and direct tagging cases is generally very good, an example of which can be seen in Figures 5.7 and 5.8 for a signal  $q\bar{q}Z \rightarrow l\bar{l}H_{125}$  sample, and the overall benefit of truth-tagging can be somewhat dramatically seen in the corresponding plots  $Z + \ell$  samples in Figure 5.9 and 5.10. At high  $p_T^V$  ( $p_T^V > 200$  GeV), however, in

events with two real  $b$ -jets, there is a much greater likelihood that the  $b$ -jets will merge into a single jet, which render the naïve assumption that jets remain discrete invalid. While this does not appear to be a problem in most samples (cf.  $t\bar{t}$  in Figures 5.11 and 5.12), there is a mismodelling effect at low  $m_{bb}$  and low  $\Delta R(b_1, b_2)$  at  $p_T^V > 200$  GeV for  $W/Z + bb$  samples where truth-tagging overestimates the number of events in this merged regime, as can be seen in Figures 5.13 and 5.14.

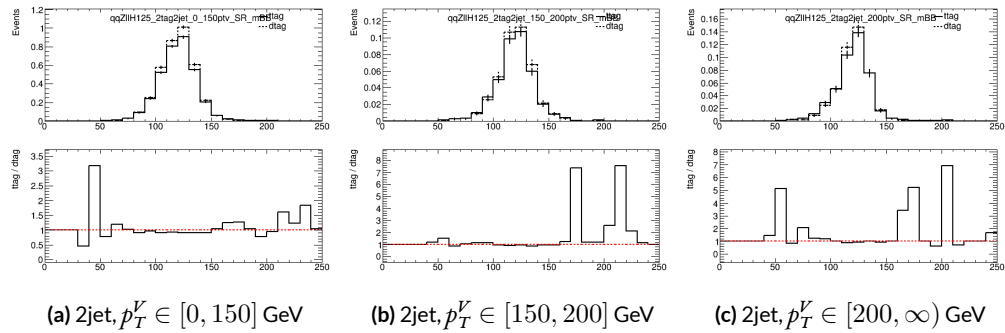


**Figure 5.7:** Truth-tagging closure tests for 2 lepton, 2 jet mBB distributions in qqZIIH125 samples in three different  $p_T^V$  regions.

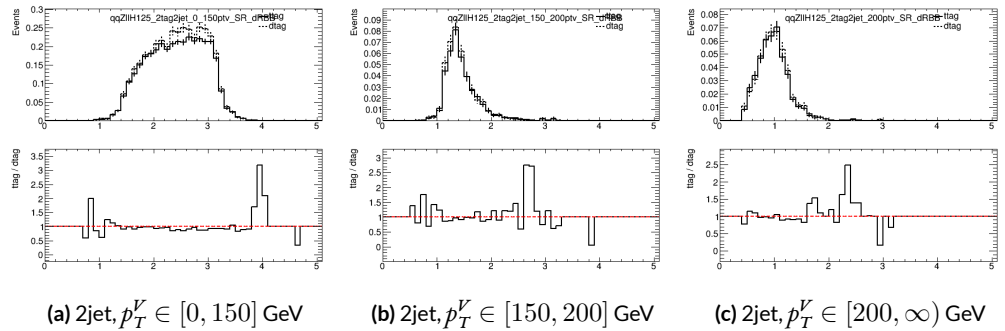


**Figure 5.8:** Truth-tagging closure tests for 2 lepton, 2 jet dRBB distributions in qqZIIH125 samples in three different  $p_T^V$  regions.

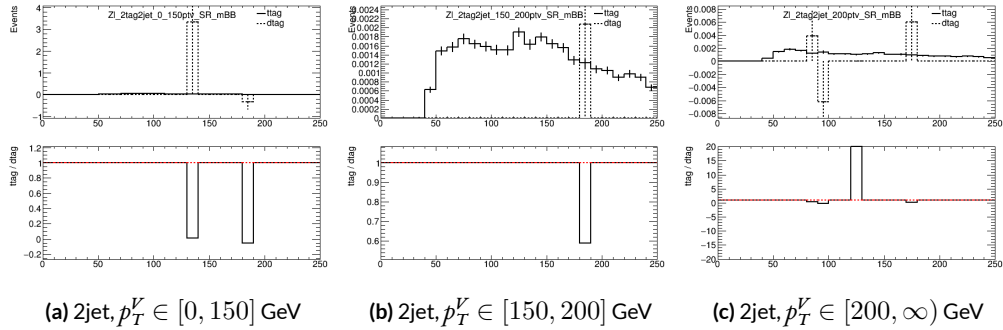


**Figure 5.9:** Truth-tagging closure tests for 2 lepton, 2 jet mBB distributions in  $Z + \ell$  samples in three different  $p_T^V$  regions.

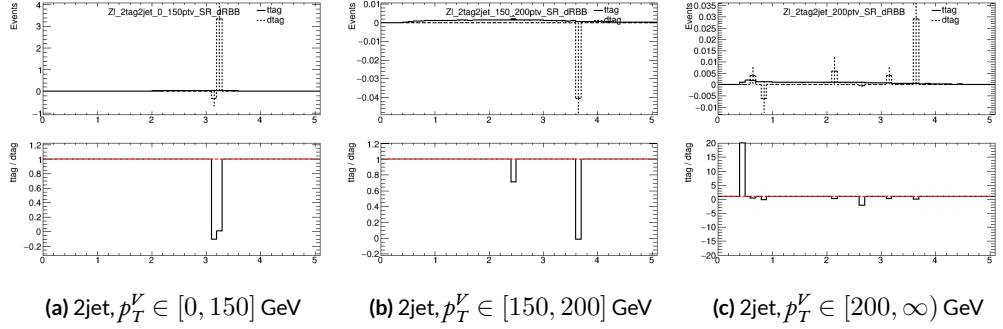


**Figure 5.10:** Truth-tagging closure tests for 2 lepton, 2 jet dRBB distributions in  $Z + \ell$  samples in three different  $p_T^V$  regions.

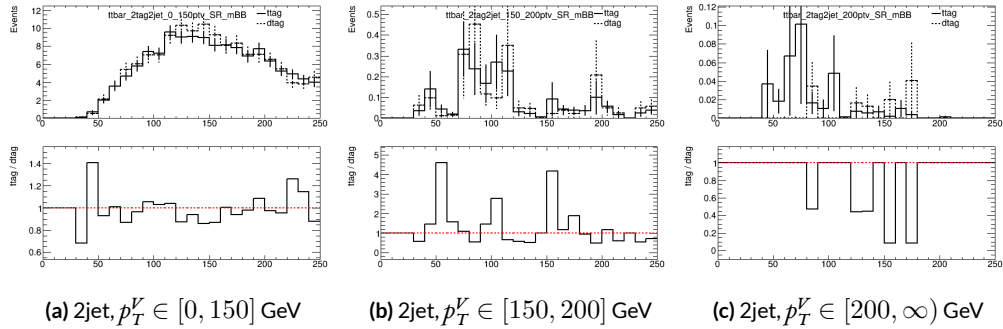


**Figure 5.11:** Truth-tagging closure tests for 2 lepton, 2 jet mBB distributions in  $t\bar{t}$  samples in three different  $p_T^V$  regions.

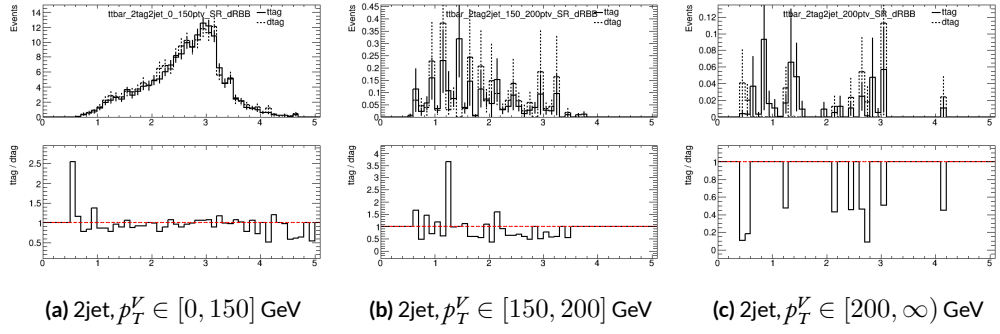


**Figure 5.12:** Truth-tagging closure tests for 2 lepton, 2 jet dRBB distributions in  $t\bar{t}$  samples in three different  $p_T^V$  regions.

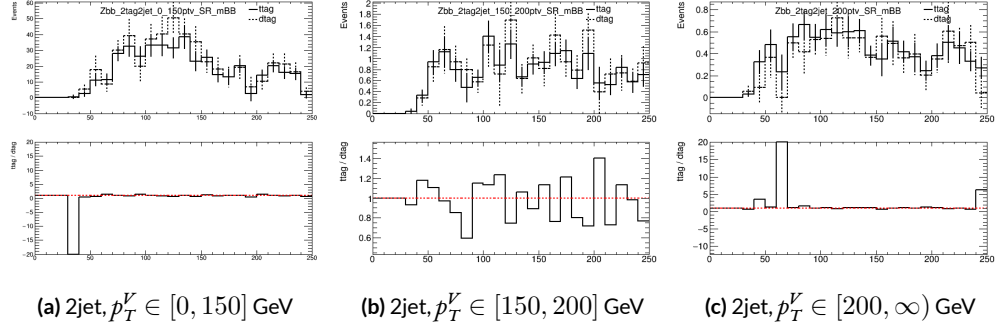


**Figure 5.13:** Truth-tagging closure tests for 2 lepton, 2 jet mBB distributions in  $Z + bb$  samples in three different  $p_T^V$  regions.

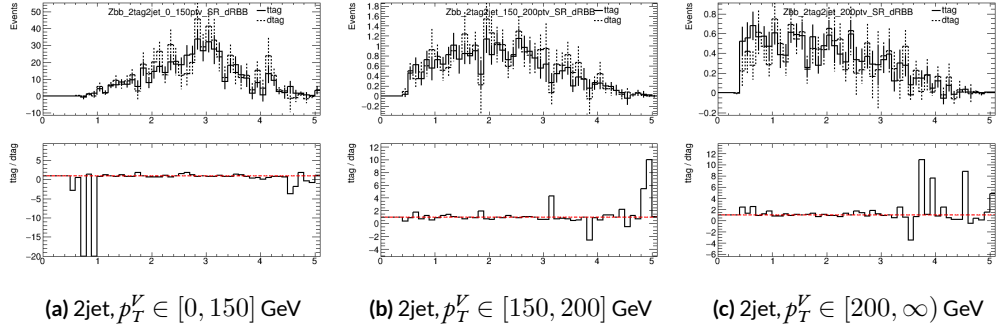


**Figure 5.14:** Truth-tagging closure tests for 2 lepton, 2 jet dRBB distributions in  $Z + bb$  samples in three different  $p_T^V$  regions.

## 5.7 MISCELLANIA AND SYSTEMATICS SUMMARY

A summary of all experimental systematics, taken from [14], may be found below. In addition to the systematics discussed above, there are also two further systematics, on the total integrated luminosity and on the event reweighting factor used to account for pileup, both included in Table 5.6.

**Table 5.6:** Summary of the experimental systematic uncertainties considered. Details on the individual systematic uncertainties can be found in the given Sections of Ref.[10].

Systematic uncertainty	Short description	Reference
Event		
Luminosity	uncertainty on total integrated luminosity	Section 11.1 in Ref. [10]
Pileup Reweighting	uncertainty on pileup reweighting	Section 11.1 in Ref. [10]
Electrons		
EL_EFF_Trigger_Total_1NPCOR_PLUS_UNCOR	trigger efficiency uncertainty	Section 11.2.2. in Ref. [10]
EL_EFF_Reco_Total_1NPCOR_PLUS_UNCOR	reconstruction efficiency uncertainty	Section 11.3.1. in Ref. [10]
EL_EFF_ID_Total_1NPCOR_PLUS_UNCOR	ID efficiency uncertainty	Section 11.3.1. in Ref. [10]
EL_EFF_Iso_Total_1NPCOR_PLUS_UNCOR	isolation efficiency uncertainty	Section 11.3.1. in Ref. [10]
EG_SCALE_ALL	energy scale uncertainty	Section 11.3.2. in Ref. [10]
EG_RESOLUTION_ALL	energy resolution uncertainty	Section 11.3.2. in Ref. [10]
Muons		
MUON_EFF_TrigStatUncertainty	trigger efficiency uncertainty	Section 11.2.2. in Ref. [10]
MUON_EFF_TrigSystUncertainty	reconstruction and ID efficiency uncertainty for muons with $p_T > 15$ GeV	Section 11.4.1. in Ref. [10]
MUON_EFF_STAT	reconstruction and ID efficiency uncertainty for muons with $p_T < 15$ GeV	Section 11.4.1. in Ref. [10]
MUON_EFF_SYS	isolation efficiency uncertainty	Section 11.4.1. in Ref. [10]
MUON_EFF_STAT_LOWPT	track-to-vertex association efficiency uncertainty	Section 11.4.1. in Ref. [10]
MUON_EFF_SYST_LOWPT	momentum resolution uncertainty from inner detector	Section 11.4.2. in Ref. [10]
MUON_ISO_STAT	momentum resolution uncertainty from muon system	Section 11.4.2. in Ref. [10]
MUON_ISO_SYS	momentum scale uncertainty	Section 11.4.2. in Ref. [10]
MUON_TTVA_STAT	charge dependent momentum scale uncertainty	Section 11.4.2. in Ref. [10]
MUON_TTVA_SYS		
MUON_ID		
MUON_MS		
MUON_SCALE		
MUON_SAGITTA_RHO		
MUON_SAGITTA_RESBIAS		
Jets		
JET_2iNP_JET_EffectiveNP_1	energy scale uncertainty from the in situ analyses splits into 8 components	Section 11.5.1. in Ref. [10]
JET_2iNP_JET_EffectiveNP_2	energy scale uncertainty from the in situ analyses splits into 8 components	Section 11.5.1. in Ref. [10]
JET_2iNP_JET_EffectiveNP_3	energy scale uncertainty from the in situ analyses splits into 8 components	Section 11.5.1. in Ref. [10]
JET_2iNP_JET_EffectiveNP_4	energy scale uncertainty from the in situ analyses splits into 8 components	Section 11.5.1. in Ref. [10]
JET_2iNP_JET_EffectiveNP_5	energy scale uncertainty from the in situ analyses splits into 8 components	Section 11.5.1. in Ref. [10]
JET_2iNP_JET_EffectiveNP_6	energy scale uncertainty from the in situ analyses splits into 8 components	Section 11.5.1. in Ref. [10]
JET_2iNP_JET_EffectiveNP_7	energy scale uncertainty from the in situ analyses splits into 8 components	Section 11.5.1. in Ref. [10]
JET_2iNP_JET_EffectiveNP_8restTerm	energy scale uncertainty from the in situ analyses splits into 8 components	Section 11.5.1. in Ref. [10]
JET_2iNP_JET_EtaIntercalibration_Modeling	energy scale uncertainty on eta-intercalibration (modeling)	Section 11.5.1. in Ref. [10]
JET_2iNP_JET_EtaIntercalibration_TotalStat	energy scale uncertainty on eta-intercalibrations (statistics/method)	Section 11.5.1. in Ref. [10]
JET_2iNP_JET_EtaIntercalibration_NonClosure	energy scale uncertainty on eta-intercalibrations (non-closure)	Section 11.5.1. in Ref. [10]
JET_2iNP_JET_Pileup_OffsetMu	energy scale uncertainty on pile-up (mu dependent)	Section 11.5.1. in Ref. [10]
JET_2iNP_JET_Pileup_OffsetNPV	energy scale uncertainty on pile-up (NPV dependent)	Section 11.5.1. in Ref. [10]
JET_2iNP_JET_Pileup_PtTerm	energy scale uncertainty on pile-up (pt term)	Section 11.5.1. in Ref. [10]
JET_2iNP_JET_Pileup_RhoTopology	energy scale uncertainty on pile-up (density $\rho$ )	Section 11.5.1. in Ref. [10]
JET_2iNP_JET_Flavor_Composition_Zjets	energy scale uncertainty on Z+jets sample's flavour composition	Section 11.5.1. in Ref. [10]
JET_2iNP_JET_Flavor_Composition_Wjets	energy scale uncertainty on W+jets sample's flavour composition	Section 11.5.1. in Ref. [10]
JET_2iNP_JET_Flavor_Composition_top	energy scale uncertainty on top sample's flavour composition	Section 11.5.1. in Ref. [10]
JET_2iNP_JET_Flavor_Composition	energy scale uncertainty on VV and VH sample's flavour composition	Section 11.5.1. in Ref. [10]
JET_2iNP_JET_Flavor_Response	energy scale uncertainty on samples' flavour response	Section 11.5.1. in Ref. [10]
JET_2iNP_JET_BJES_Response	energy scale uncertainty on b-jets	Section 11.5.1. in Ref. [10]
JET_2iNP_JET_PunchThrough_MC15	energy scale uncertainty for punch-through jets	Section 11.5.1. in Ref. [10]
JET_2iNP_JET_SingleParticle_HighPt	energy scale uncertainty from the behaviour of high-pT jets	Section 11.5.1. in Ref. [10]
JET_JER_SINGLE_NP	energy resolution uncertainty	Section 11.5.1. in Ref. [10]
JET_JvtEfficiency	JVT efficiency uncertainty	Section 11.5.1. in Ref. [10]
FT_EFF_Eigen_B	b-tagging efficiency uncertainties ("BTAG_MEDIUM"): 3 components for b jets, 3 for c jets and 5 for light jets	Section 11.7. in Ref. [10]
FT_EFF_Eigen_C		
FT_EFF_Eigen_L		
FT_EFF_Eigen_extrapolation	b-tagging efficiency uncertainty on the extrapolation to high- $p_T$ jets	Section 11.7. in Ref. [10]
FT_EFF_Eigen_extrapolation_from_charm	b-tagging efficiency uncertainty on tau jets	Section 11.7. in Ref. [10]
MET		
METTrigStat	trigger efficiency uncertainty	Section 11.2.1. in Ref. [10]
METTrigTop/Z	track-based soft term related longitudinal resolution uncertainty	Section 11.6. in Ref. [10]
MET_SoftTrk_ResoPara	track-based soft term related transverse resolution uncertainty	Section 11.6. in Ref. [10]
MET_SoftTrk_ResoPerp	track-based soft term related longitudinal scale uncertainty	Section 11.6. in Ref. [10]
MET_SoftTrk_Scale	track MET scale uncertainty due to tracks in jets	Section 11.6. in Ref. [10]

## 5.8 EVENT SELECTION AND ANALYSIS REGIONS

With object and event reconstruction described, it is now time to address which events are actually selected for use in analysis. This analysis focuses specifically on the 2-lepton channel of the fiducial analysis, with the event selection and analysis region definitions being identical. Common to all lepton channels in the fiducial analysis is the set of requirements on the jets in a given event. There must be at least two central jets and exactly two signal jets that have been “*b*-tagged” according to the MV2c10 algorithm [56], with at least one of these *b*-jets having  $p_T > 45$  GeV. For MVA training and certain background samples, a process known as “truth-tagging” is applied instead of the standard *b*-tagging to boost sample statistics and stabilize training/fits (cf. [14] Section 4.2 for details). After event selection, the *muon-in-jet* and *PtReco* corrections, described in [10] 6.3.3-4, are applied to the *b*-jets.

In addition to the common selections, there are 2-lepton specific selections. All events are required to pass an un-prescaled single lepton trigger, a full list of which may be found in Tables 5 and 6 of [10] with the requirement that one of the two selected leptons in the event must have fired the trigger. There must be 2 VH-loose leptons, and at least one of these must be a ZH-signal lepton (cf. Tables 5.2 and 5.3 for definitions). This lepton pair must have an invariant mass between 81 and 101 GeV. In addition to the jet corrections described above, a kinematic fitter is applied to the leptons and two leading corrected jets in an event with three or fewer jets<sup>‡</sup> to take advantage of the fact that the 2-lepton final state is closed (cf. [23]); these objects are only used for MVA training/fit inputs.

---

<sup>‡</sup>The gain from using the kinematic fitter is found to be smeared out in events with higher jet multiplicities.

In order to increase analysis sensitivity, the analysis is split into orthogonal regions based on the number of jets and the transverse momentum of the  $Z$  candidate (the vectoral sum of the lepton pair; this  $p_T$  is denoted  $p_T^V$ ): 2 and  $\geq 3$  jets;  $p_T^V$  in  $[75, 150), [150, \infty)$  GeV. In addition to the signal regions where the leptons are required to be the same flavor ( $e$  or  $\mu$ ), there are top  $e - \mu$  control regions used to constrain the top backgrounds.

All of these requirements are summarized in 5.6.

**Table 5.6:** Event selection requirements

Category	Requirement
Trigger	un-prescaled, single lepton
Jets	$\geq 2$ central jets; 2 $b$ -tagged signal jets, harder jet with $p_T > 45$ GeV
Leptons	2 VH-loose leptons ( $\geq 1$ ZH-signal lepton); same (opp) flavor for SR (CR)
$m_{\ell\ell}$	$m_{\ell\ell} \in (81, 101)$ GeV
$p_T^V$ regions (GeV)	$[75, 150), [150, \infty)$

It should be noted that the use of  $\geq 3$  jet events is a 2-lepton specific selection. These regions are exclusive 3 jet regions in the 0- and 1-lepton channels, but the fiducial 2-lepton analysis was found to see a  $\sim 4\%$  gain in sensitivity in studies by including  $\geq 4$  jet events [14].

猛き者も遂には滅びぬ、  
偏に風の前の塵に同じ。

Heike monogatari

# 6

## Multivariate Analysis Configuration

IN ORDER TO fully leverage the descriptive power of the 13 TeV dataset, this analysis makes use of a multivariate (MVA) discriminant. Where traditionally event counts or single discriminating variables per region of phase space have been fed to fits, MVA discriminants seek to integrate additional information not captured in the conventional phase space cuts plus dijet invariant mass distribu-

tions. Formulating the MVA discriminant is an exercise in supervised learning to construct a binary classifier, where one uses labeled “signal” and “background” MC events to optimize the parameters of a statistical model—in this case a boosted decision tree (BDT) with some set of physically motivated variables (or “factors”). The interested reader is directed to the standard references on machine learning for further details. Sample and variable selection, including variables derived using the RestFrames and Lorentz Invariants concepts introduced in Sections 1.5–1.7, are discussed in Section 6.1; MVA training is treated in Section 6.2; and the data statistics only (no systematics) performance of the three MVA discriminants is explored in Section 6.3.

## 6.1 TRAINING SAMPLES AND VARIABLE SELECTION

A subset of samples described in Chapter 3 is used for multivariate analysis training, with  $qqZH \rightarrow \ell\ell b\bar{b}$  and  $ggZH \rightarrow \ell\ell b\bar{b}$  used as signal samples and  $Z+jets$ ,  $t\bar{t}$ , and  $VV$  used as background samples. Truth-tagging (Section 5.6.2) is used on all samples in MVA training to improve training statistics and stability. All figures quoted in this section scale distributions to a luminosity of  $36.1 \text{ fb}^{-1}$ .

### 6.1.1 STANDARD VARIABLES

The standard set of variables taken as a baseline is the same as used in the fiducial analysis. The variables fall into several main categories: energy/momentum scales of composite objects ( $m_{bb}$ ,  $m_{bbb}$ ,  $p_T^V$ ,  $m_{\ell\ell}$ ), angles ( $\Delta R(b_1, b_2)$ ,  $\Delta\phi(V, H)$ ,  $\Delta\eta(V, H)$ ), transverse momenta of the jets in the event ( $p_T^{b_1}$ ,  $p_T^{b_2}$ ,  $p_T^{j_3}$ ), and  $E_T^{miss}$ . Input distributions for these variables in all the analysis signal regions may be found in Figures 6.1–6.4. The “kf” at the end of variable names denotes that these are derived using

4-vectors that are the result of the kinematic fitter.

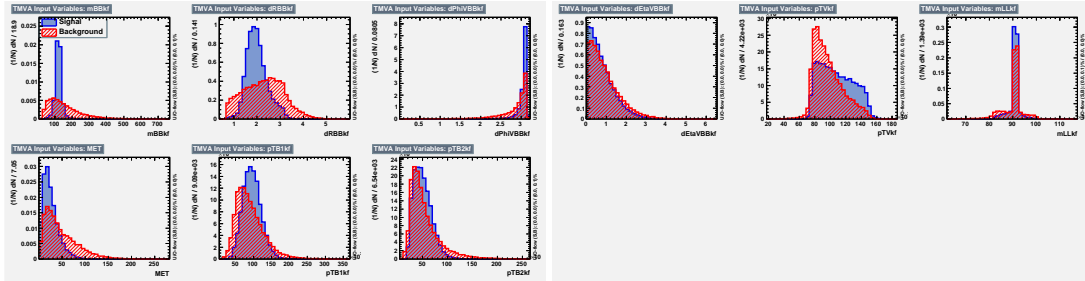


**Figure 6.1:** Input variables in the 2 jet, low jet signal region for the standard variable set. Signal distributions are in red, and background distributions are in blue.

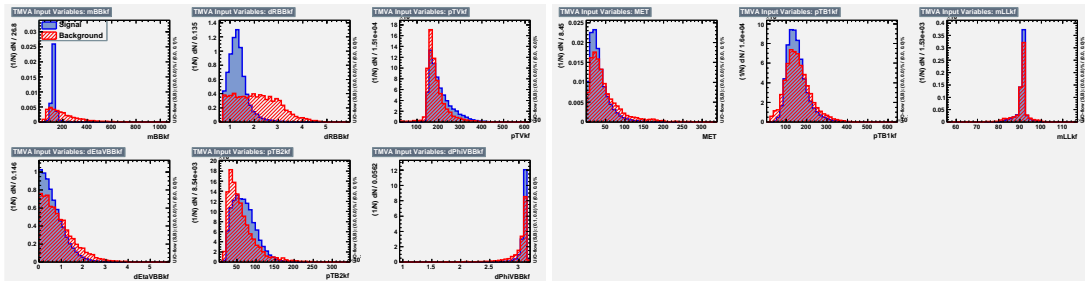


**Figure 6.2:** Input variables in the 2 jet, high jet signal region for the standard variable set. Signal distributions are in red, and background distributions are in blue.

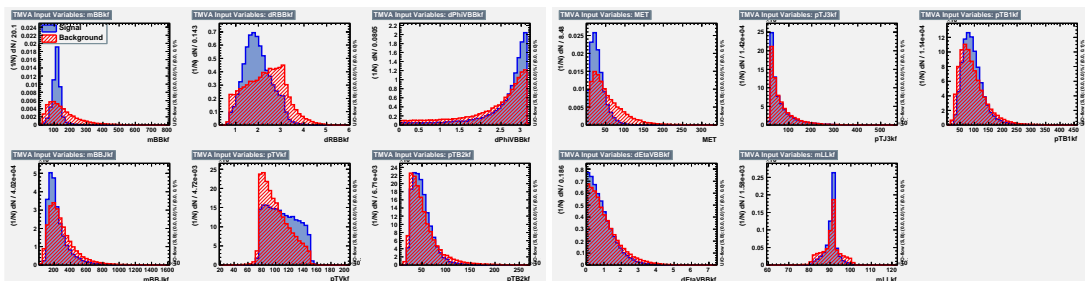


**Figure 6.3:** Input variables in the 3+ jet, low jet signal region for the standard variable set. Signal distributions are in red, and background distributions are in blue.

The distributions in the figure are used as inputs for one of the two k-folded final discriminants, and the order of the distributions is the hyperparameter optimized order for feeding into the BDT;

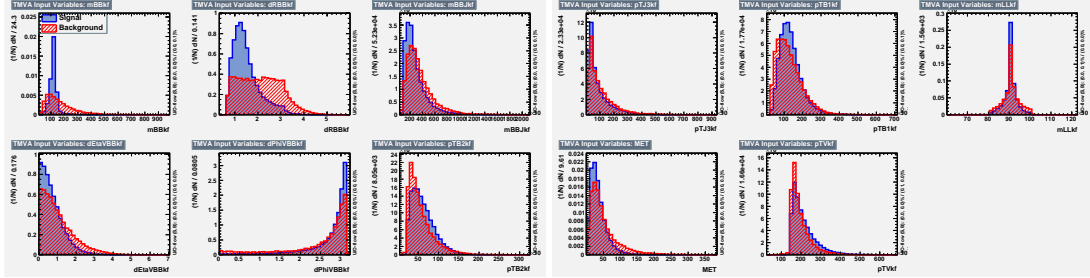


**Figure 6.4:** Input variables in the 3+ jet, high jet signal region for the standard variable set. Signal distributions are in red, and background distributions are in blue.

what precisely this means will be discussed in following sections. While variables in the analysis regions are generally similar, there are some notable exceptions.  $p_T^V$  and the correlated  $\Delta R(b_1, b_2)$  have different shapes, by construction for the former and by correlation for the latter, at low and high  $p_T^V$ . \* The  $\geq 3$  jet regions also have variables that are not applicable to the 2 jet regions; the inclusion of  $m_{BBJ}$  (the invariant mass of the two  $b$ -jets and leading untagged jet) in particular is of note and suggests a potential avenue forward for refinements of the non-standard variables.

Looking at the correlation matrices for the standard variables in Figure 6.5, it is easy to see that there are large number of non-trivial correlations (when looking at these correlation matrices, keep in mind that purple is perfect anti-correlation, red is perfect correlation (as with all variables with themselves—hence diagonals of red), and green is roughly zero correlation).

---

\*Recall that higher  $p_T^V$  means, in a balanced final state like  $ZH \rightarrow \ell\ell b\bar{b}$ , the  $b$ -jet pair will have higher  $p_T$  and hence be more collimated (lower  $\Delta R(b_1, b_2)$ ); this is not necessarily the case for background events, as the distributions show.

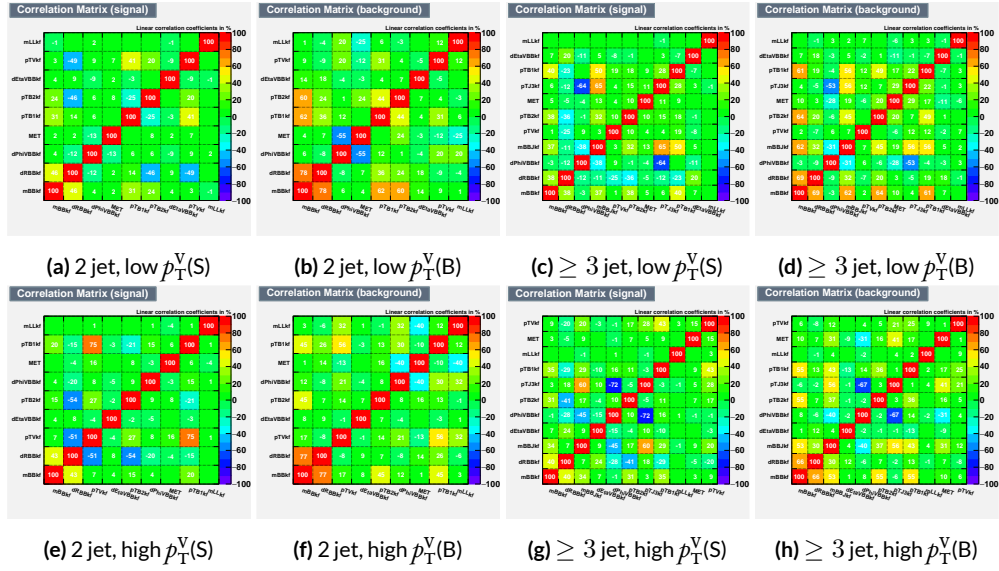


**Figure 6.5:** Signal and background variable correlations for the standard variable set.

### 6.1.2 LORENTZ INVARIANTS

In choosing the set of variables used for a set of Lorentz Invariants based discriminants, we decided to use S. Hagebeck's set from [16] and related studies. Distributions of these variables in the same arrangement as with the standard variables may be seen in Figures 6.6–??.

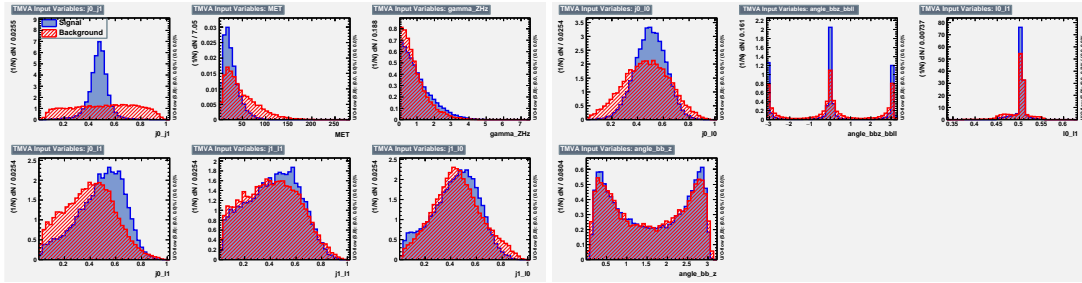


**Figure 6.6:** Input variables in the 2 jet, low jet signal region for the LI variable set. Signal distributions are in red, and background distributions are in blue.

One thing to note about the variable set chosen here is that  $\vec{E}_T^{\text{miss}}$  has been added to the standard

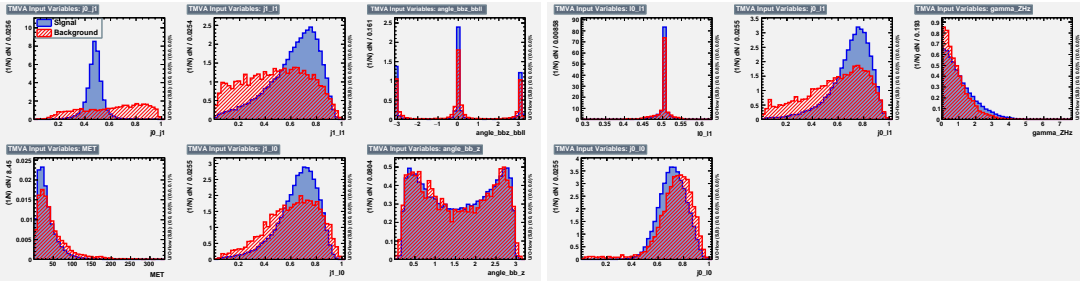


**Figure 6.7:** Input variables in the 2 jet, high jet signal region for the LI variable set. Signal distributions are in red, and background distributions are in blue.

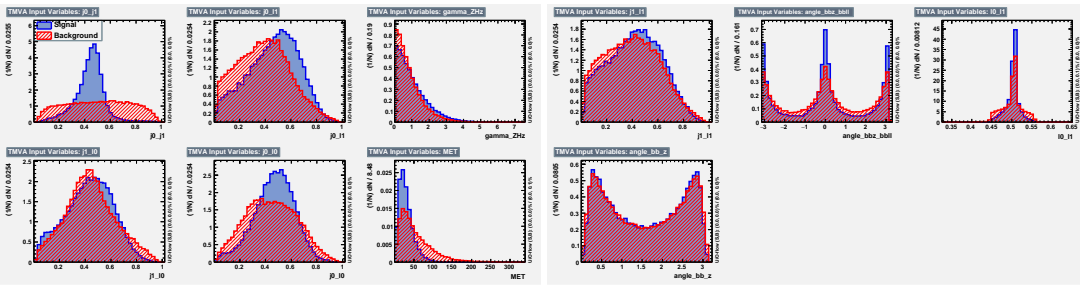


**Figure 6.8:** Input variables in the 3+ jet, low jet signal region for the LI variable set. Signal distributions are in red, and background distributions are in blue.

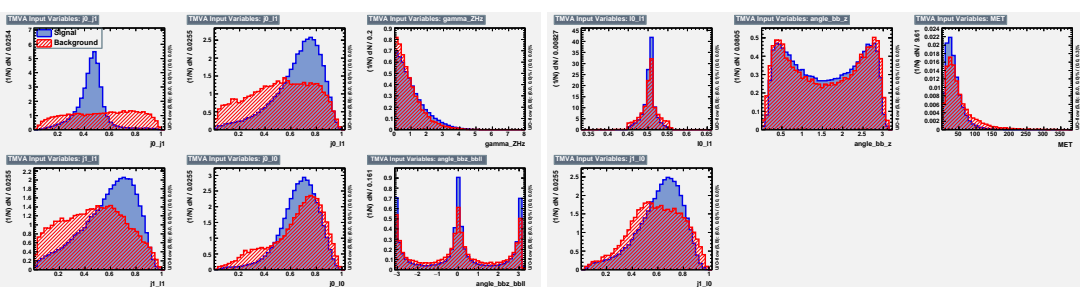


**Figure 6.9:** Input variables in the 3+ jet, high jet signal region for the LI variable set. Signal distributions are in red, and background distributions are in blue.

LI set. Since the LI construction assumes that this quantity is zero, there is no obvious way to include it. Nevertheless, as the correlation matrices for the LI variables show in Figure 6.10, there is actually very little correlation between  $\vec{E}_T^{\text{miss}}$  and the other variables (with this being slightly less the case for the background correlations, as to be expected since  $t\bar{t}$ , a principal background, is  $\vec{E}_T^{\text{miss}}$ -rich). Hence, if including  $\vec{E}_T^{\text{miss}}$  violates the spirit somewhat of the LI variables, it does not break terribly much with the aim of having a more orthogonal set.

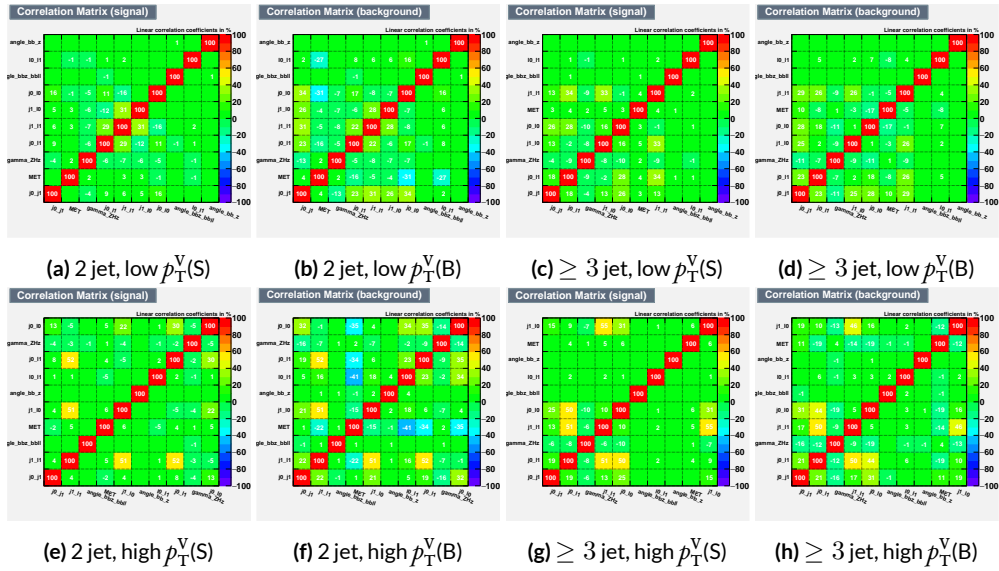


Figure 6.10: Signal and background variable correlations for the LI variable set.

### 6.1.3 RESTFRAMES VARIABLES

There is no precedent for using the RestFrames variables in the  $ZH \rightarrow \ell\ell b\bar{b}$  analysis, so a subset of possible RF variables had to be selected as the basis of a discriminant. The masses and cosines of boost angles from parent frames for the CM,  $Z$ , and  $H$  frames gives six variables, and it was decided that it would be good to match the LI in terms of variable number and treatment (i.e. no special treatment of the third jet), which leaves four more variables. In addition to the cosines, there are also the  $\Delta\phi$  angles. Furthermore, there are the event-by-event scaled momentum ratios, both longitudinal and transverse. There is also both a  $\Delta\phi$  and an CM-scaled ratio for the  $\vec{E}_T^{\text{miss}}$ . All of these variables were included in a ranking using slightly different training settings as the main hyperparameter optimization variable ranking described below. The goal of this study was not to develop a discriminant, as the number of variables is too high, but rather to see which ones are generally useful. Table 6.1 shows the results of this study. Percent gains (losses) at each step by adding the variable with biggest gain (smallest loss) are shown in green (red). The final row shows an aggregate ranking, calculated simply by adding up a variables ranks in all bins and ordering the variables smallest to greatest. This simple aggregation does not take into account which regions are potentially more sensitive and so where taken simply to give an idea of how variables generally performed. With this in mind, the RF variables were chosen to be the masses  $M_{CM}$ ,  $M_H$ , and  $M_Z$ , the angles  $\cos M_{CM}$ ,  $\cosh$ ,  $\cos Z$ ,  $d\phi M_{CMH}$ , and the ratios  $R_{pt}$ ,  $R_{pz}$ , and  $R_{met}$ . Their distributions may be seen in Figures ??–6.14.

Correlations for the chosen RF variables are shown in Figure 6.15. These correlations are much

**Table 6.1:** Full RF variable ranking study summary. Green (red) percentages represent gains (losses) in a validation significance at each step.

Region	Variable Chain
2jet pTVbin1	Rpt (65.8%), Rpz (29.0%), cosZ (11.4%), MZ (-1.75%), dphiCMH (7.26%), cosCM (3.95%), cosH (0.142%), MCM (2.18%), dphiCMZ (-2.3%), dphiCMMet (-0.236%), dphiLABCM (0.404%), Rmet (-4.04%)
3jet pTVbin1	Rpt (50.8%), Rpz (15.6%), MZ (14.8%), cosZ (3.08%), MCM (3.79%), dphiCMH (3.24%), cosH (0.75%), dphiCMMet (1.04%), Rmet (-1.03%), cosCM (5.31%), dphiCMZ (-1.27%), dphiLABCM (-2.88%), pTJ3 (-1.27%)
2jet pTVbin2	Rpt (52.0%), Rpz (13.8%), cosZ (16.9%), cosH (6.49%), MCM (1.71%), cosCM (6.21%), Rmet (4.25%), dphiCMMet (-1.53%), dphiLABCM (-0.757%), dphiCMH (0.213%), MZ (-0.788%), dphiCMZ (-2.39%)
3jet pTVbin2	Rpt (31.3%), Rpz (21.6%), cosH (8.97%), cosZ (1.42%), cosCM (11.3%), dphiCMZ (-2.84%), MCM (8.17%), dphiCMH (-0.841%), dphiLABCM (-0.00318%), dphiCMMet (-2.6%), pTJ3 (-3.21%), MZ (-1.8%), Rmet (-6.29%)
Aggregate	Rpt (o,o,o), Rpz (i,i,i,i), cosZ (2,3,2,3), cosH (6,6,3,2), MCM (7,4,4,6), MZ (3,2,10,n), dphiCMH (4,5,9,7), cosCM (5,9,5,4), dphiCMMet (9,7,7,9), dphiCMZ (8,10,11,5), Rmet (11,8,6,12), dphiLABCM (10,11,8,8)

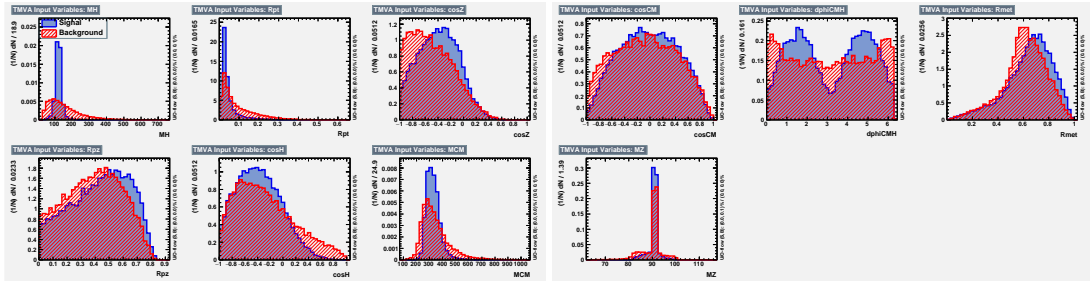


**Figure 6.11:** Input variables in the 2 jet, low jet signal region for the RF variable set. Signal distributions are in red, and background distributions are in blue.

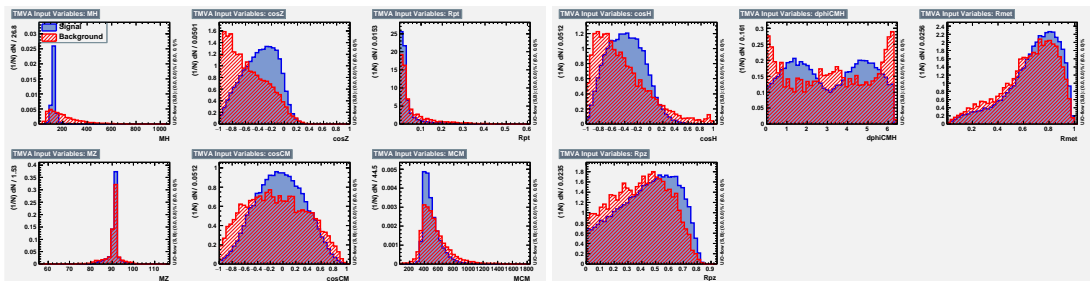


**Figure 6.12:** Input variables in the 2 jet, high jet signal region for the RF variable set. Signal distributions are in red, and background distributions are in blue.

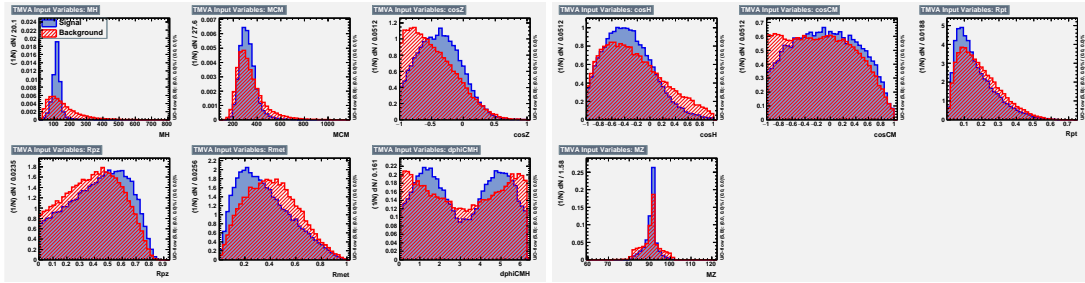


**Figure 6.13:** Input variables in the 3+ jet, low jet signal region for the RF variable set. Signal distributions are in red, and background distributions are in blue.

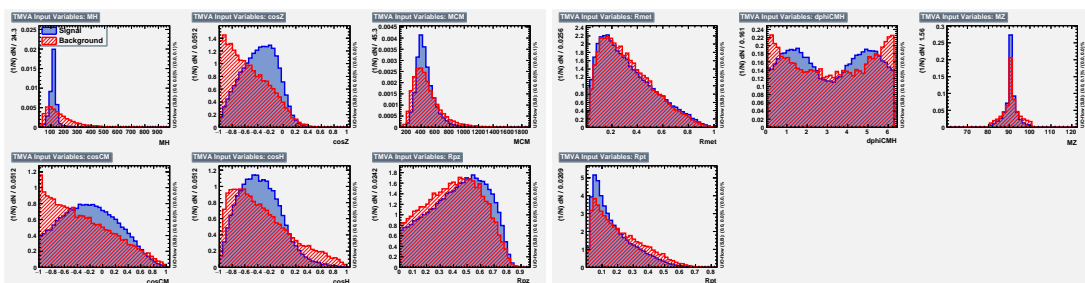


**Figure 6.14:** Input variables in the 3+ jet, high jet signal region for the RF variable set. Signal distributions are in red, and background distributions are in blue.

lower than for the standard case but still slightly higher than for the LI case. Notably, many strong correlations that exist for signal events do not exist in background events and vice versa, so what is lost in orthogonality may very well be recuperated in greater separation<sup>†</sup>. Given the generally better performance of the RF sets, as we shall see in following sections and chapters, this slight tradeoff is likely an aesthetic one, with the main benefits of a more orthogonal basis likely realized at this level of correlation.

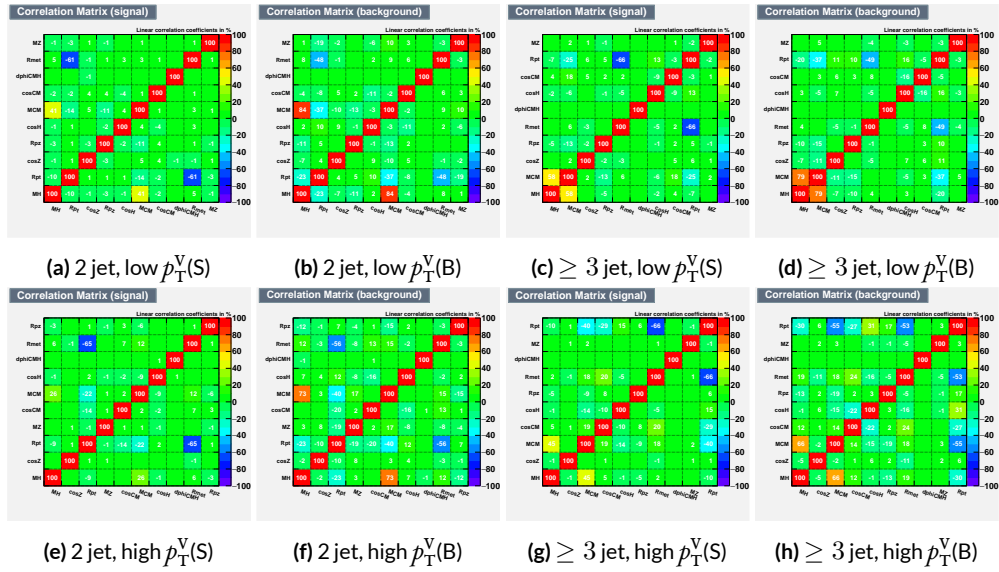


**Figure 6.15:** Signal and background variable correlations for the RF variable set.

A summary of the variables used in the three cases is given in 6.2.

<sup>†</sup>It is very hard to say for certain whether this is the case for MVA discriminants, and such dedicated studies might make worthwhile future studies.

**Table 6.2:** Variables used in MVA training. Variables in parentheses are only used in the  $\geq 3$  jet regions.

Variable Set	Variables
Standard	mBB, mLL, (mBBJ), pTV, pTB1, pTB2, (pTJ3), dRBB, dPhiVBB, dEtaVBB, MET 9 (11) vars
Lorentz Invariants	j0_j1, j0_l1, l0_l1, j1_l1, j0_l0, j1_l0, gamma_ZHz, angle_bbz_bbll angle_bb_z, MET 10 vars
RestFrames	MH, MCM, MZ, cosH, cosCM, cosZ, Rpz, Rpt, dphiCMH, Rmet 10 vars

## 6.2 MVA TRAINING

With variables chosen, the MVA discriminants must be trained and optimized. MVA training and hyperparameter optimization (in this case, just the order in which variables are fed into the MVA) is conducted using the “holdout” method. In this scheme, events are divided into three equal portions (in this case using `EventNumber%3`), with the first third (the “training” set) being used for the initial training, the second third (the “validation” set) being used for hyperparameter optimization, and the final third (the “testing” set) used to evaluate the performance of the final discriminants in each analysis region.

The MVA discriminant used is a boosted decision tree (BDT). Training is done in TMVA using the training settings of the fiducial analysis [14]<sup>‡</sup>. For the purposes of hyperparameterization and testing, transformation D with  $z_s = z_b = 10$  is applied to the BDT distributions, and the cumulative sum of the significance  $S/\sqrt{S + B}$  in each bin is calculated for each pair of distributions.

Transformation D is a histogram transformation, developed during the Run 1 SM  $VH(b\bar{b})$  search,

---

<sup>‡</sup>Namely, !H:!V:BoostType=AdaBoost:AdaBoostBeta=0.15:SeparationType=GiniIndex:-PruneMethod=NoPruning:NTrees=200:MaxDepth=4:nCuts=100:nEventsMin=5%

designed to reduce the number of bins in final BDT distributions and thereby mitigate the effect of statistical fluctuations in data while also maintaining sensitivity. Such an arbitrary transformation may be expressed as:

$$Z(I[k, l]) = Z(z_s, n_s(I[k, l]), N_s, z_b, n_b(I[k, l]), N_b) \quad (6.1)$$

where

- $I[k, l]$  is an interval of the histograms, containing the bins between bin  $k$  and bin  $l$ ;
- $N_s$  is the total number of signal events in the histogram;
- $N_b$  is the total number of background events in the histogram;
- $n_s(I[k, l])$  is the total number of signal events in the interval  $I[k, l]$ ;
- $n_b(I[k, l])$  is the total number of background events in the interval  $I[k, l]$ ;
- $z_s$  and  $z_b$  are parameters used to tune the algorithm.

Transformation D uses:

$$Z = z_s \frac{n_s}{N_s} + z_b \frac{n_b}{N_b} \quad (6.2)$$

Rebinning occurs as follow:

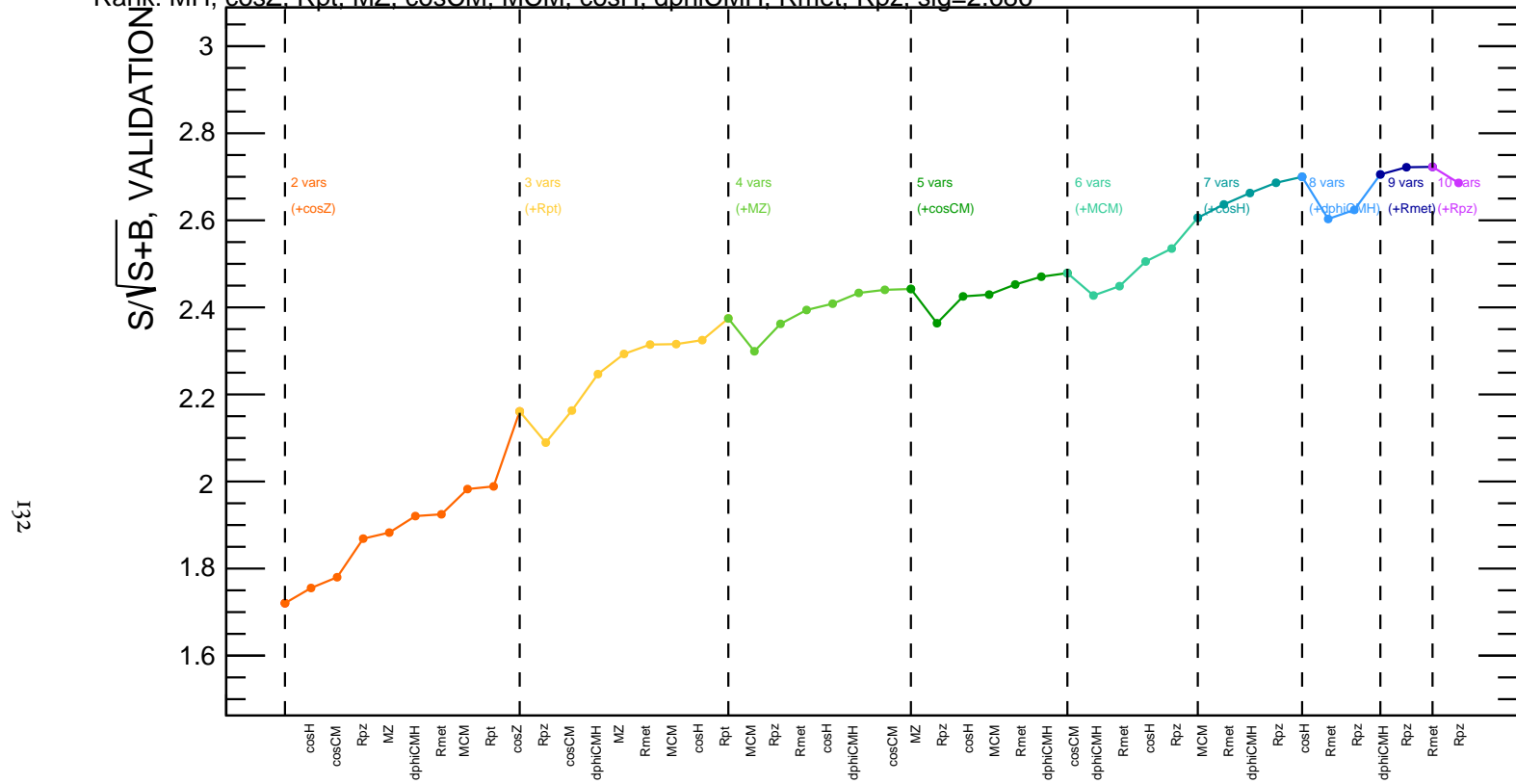
1. Begin with the highest valued bin in the original pair of distributions. Call this the “last” bin and use it as  $l$ , and have  $k$  be this bin as well.
2. Calculate  $Z(I[k, l])$
3. If  $Z \leq 1$ , set  $k \rightarrow k - 1$  and return to step 2. If not, rebin bins  $k-l$  into a single bin and name  $k-1$  the new “last” bin  $l$ .
4. Continue until all bins have been iterated through; if  $Z \leq 1$  for any remaining  $n$  of the lowest-valued bins (as is often the case), simply rebin these as a single bin.

Variable ranking is done iteratively (greedily) in each analysis region. In each set, the validation significance of a BDT using an initial subset of variables is calculated ( $dRBB$  and  $mBB$  for the standard set;  $j0\_j1$  for the LI set; and  $MH$  for the RF set). Each of the remaining unranked variables are then added separately, one at a time, to the BDT. The variable yielding the highest validation significance is then added to the set list of ranked variables and removed from the list of unranked variables. This process is repeated until no variables remain.

This training process is visualized using “ranking plots.” A prototypical example is given in Figure 6.16, the ranking for the RF variable set in the 2 jet, high  $p_T^V$  region. Each step is shown in a distinct color. In this example, the first step begins by training nine BDT’s with the variable  $MH$  and one of the other variables in this region. Graphically, we arrange the results ascending left to right based on their validation  $S/\sqrt{S+B}$ . At this step, this yields  $\cos H$ ,  $\cos CM$ ,  $Rpz$ ,  $MZ$ ,  $dphi CMH$ ,  $Rmet$ ,  $MCM$ ,  $Rpt$ , and the best performing  $\cos Z$ . Hence, this step is labeled “2 vars (+ $\cos Z$ )” to denote that the two variable  $MH-\cos Z$  BDT is used as the basis for the three variable step. Note that while each case is arranged left to right, each of these iteration is in practice computed in parallel. When examining a plot of this type, even though there are no errors given, one can use the smoothness of overall curve as an indicator for ranking stability (sometimes low statistics for certain samples can make jittery rankings inevitable, particularly near the end of rankings).

**Figure 6.16:** An example ranking, the RF variable set in the 2 jet, high  $p_T^V$  region.

Rank: MH, cosZ, Rpt, MZ, cosCM, MCM, cosH, dphiCMH, Rmet, Rpz, sig=2.686



These rankings are shown in Figures 6.16–6.21. Rankings tend to be fairly stable.

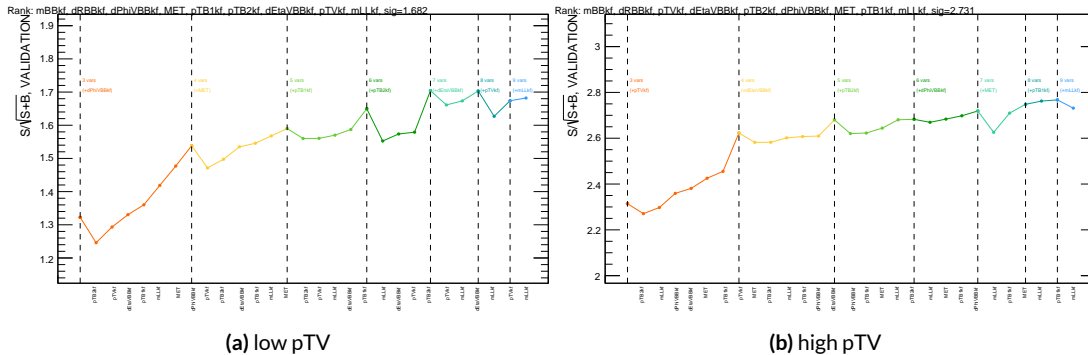


**Figure 6.16:** Rankings for the 2 jet standard variable set.

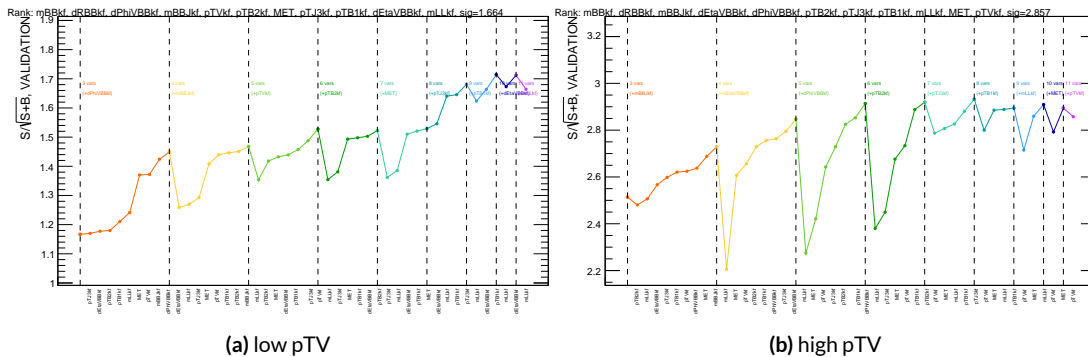


**Figure 6.17:** Rankings for the 3+ jet standard variable set.

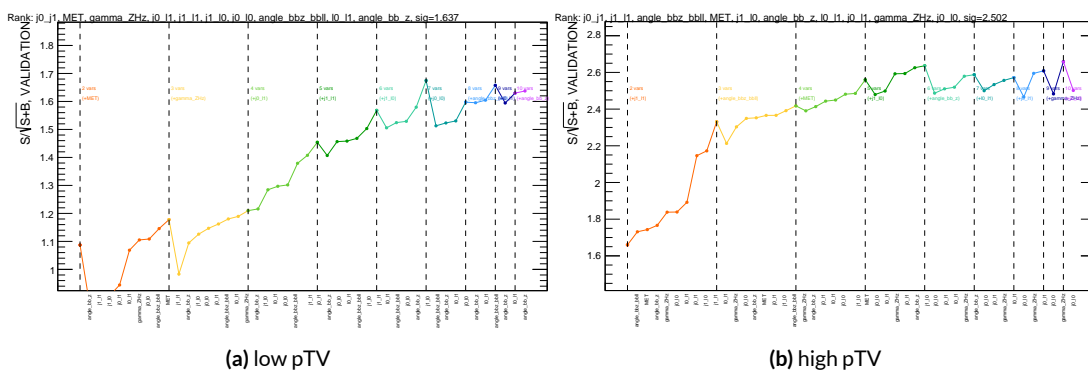


**Figure 6.18:** Rankings for the 2 jet LI variable set.

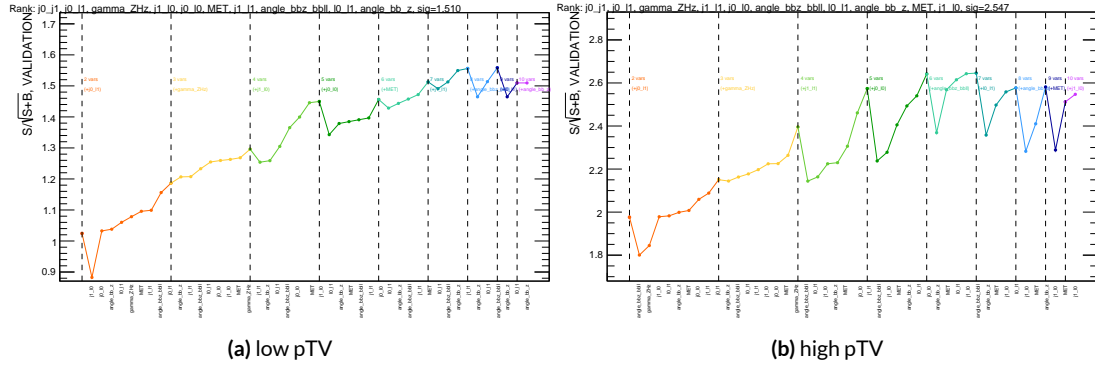


Figure 6.19: Rankings for the 3+ jet LI variable set.

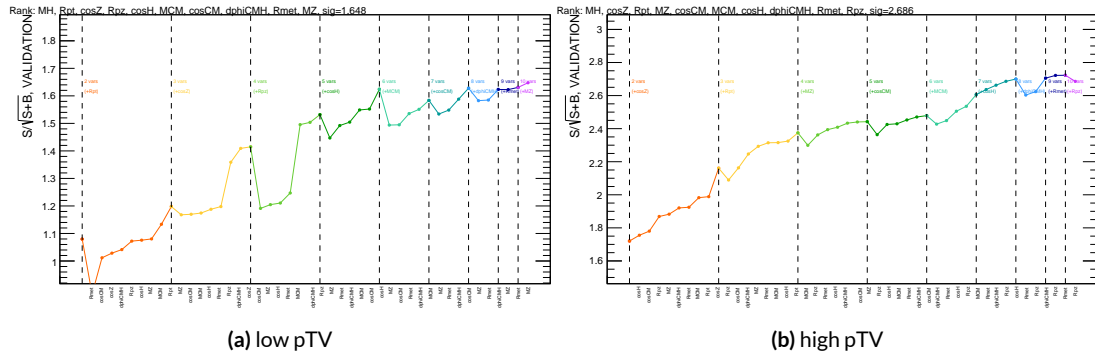


Figure 6.20: Rankings for the 2 jet RF variable set.

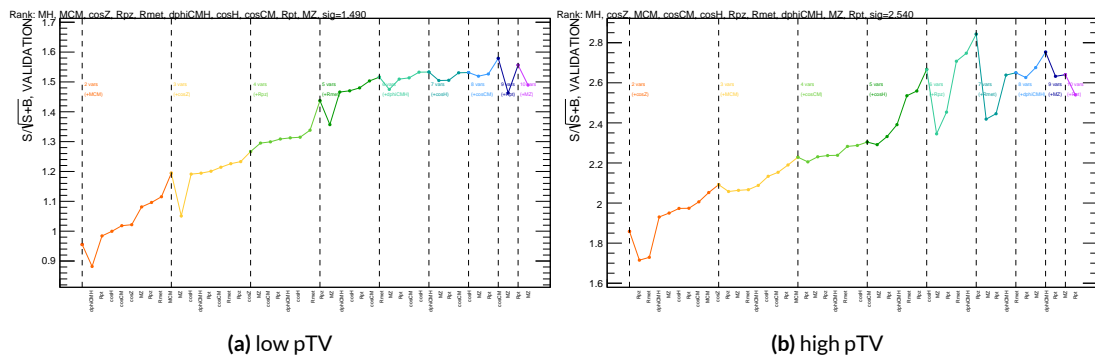


Figure 6.21: Rankings for the 3+ jet RF variable set.

Once variables have been ranked, the BDT may be used both to evaluate performance in a simplified analysis scenario in the absence of systematic uncertainties (described below in Section 6.3) and to create xml files for the production of fit inputs for an analysis including systematics. Following the approach taken in the fiducial analysis, BDT discriminants using two “k-folds” are produced to prevent overtraining, since the samples used for training are the same as those used to produce inputs for the full profile likelihood fit. In this scheme, a BDT trained on events with an even (odd) `EventNumber` are used to evaluate events with an odd (even) `EventNumber`.

### 6.3 STATISTICS ONLY BDT PERFORMANCE

As described above, cumulative significances can be extracted from pairs of signal and background BDT output distributions in a given region. In order to evaluate performance of variable sets in the absence of systematic uncertainties, such pairs can be constructed by evaluating BDT score on the testing set of events using the optimal variable rankings in each region. We show two versions of each testing distribution for each variable set in each signal region in Figures ??–???. The training distribution is always shown as points. The plots with block histograms with numbers of bins that match (do not match) the training distribution do not (do) have transformation D applied. Transformation D histograms are included to show the distributions actually used for significance evaluation, while the untransformed histograms are included to illustrate that the level of overtraining is not too terrible<sup>§</sup>. For better comparison of the distributions, all histograms have been scaled to have the same normalization.

---

<sup>§</sup>The raw distributions include a K-S test statistic for signal (background) distributions.

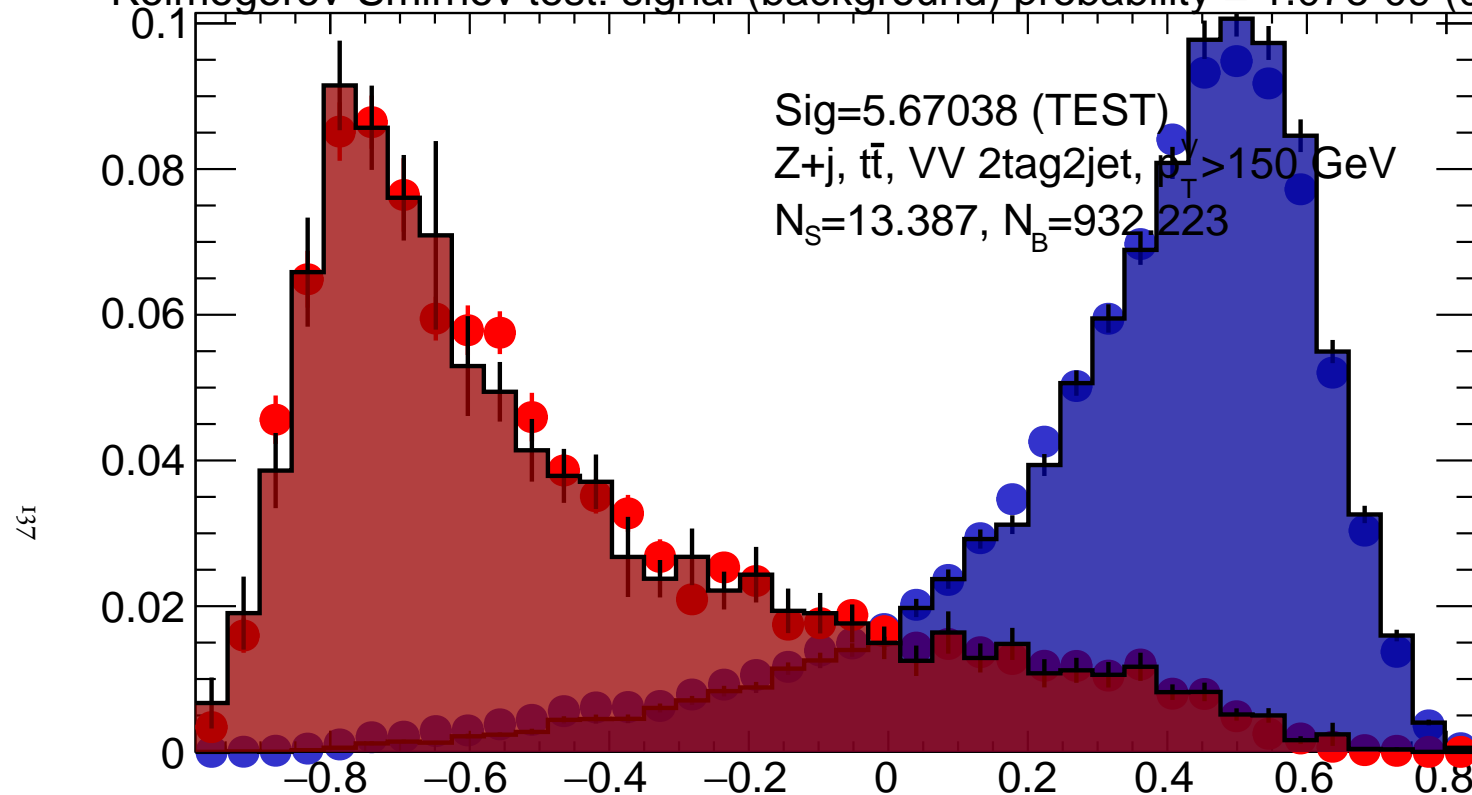
An example of training/(untransformed) testing distributions is given in 6.22. Visually, one expects the training and testing distributions to look similar, but not too similar (an indication of over-training). This qualitative intuition can be quantified via the two sample Kolmogorov-Smirnov test, which uses the maximum difference in distribution CDF's to obtain an “overtraining probability” given by:

$$D_{n,m} = \sup_x |F_{1,n}(x) - F_{2,m}(x)| = \sqrt{\frac{n+m}{nm} \times \left( -\frac{1}{2} \ln \left( \frac{\alpha}{2} \right) \right)} \quad (6.3)$$

In the  $n = m$  case,  $\alpha = 2e^{-nD_n^2}$ , which is the usual null hypothesis (same distribution) probability. Generally, the background probabilities are higher because the background distributions rely on some relatively low statistics MC samples (e.g.  $VV$ , which has low yields with analysis event selection requirements). The signal distribution, on the other hand, only relies on high statistics signal MC samples (with most events passing selection requirements and making it into the discriminants by design).

**Figure 6.22:** Example output training (points) and testing (blocks) MVA discriminant distributions for the RF variable set in the 2 jet, high  $p_T^V$  region.

Kolmogorov-Smirnov test: signal (background) probability = 1.07e-09 (0.879)



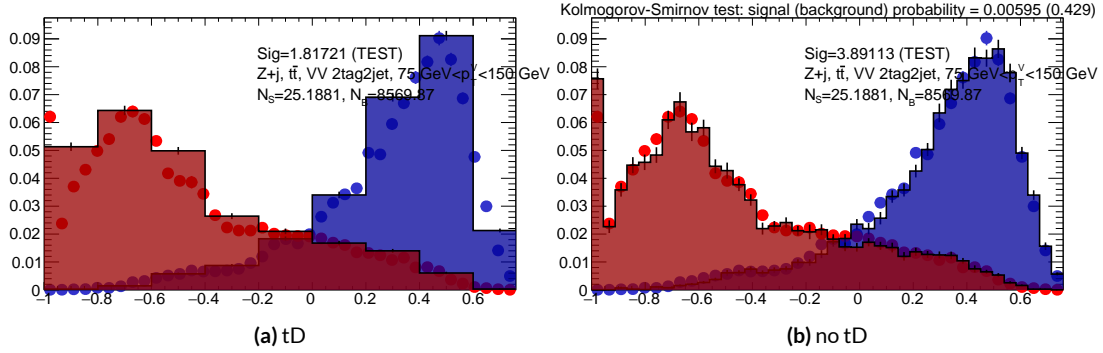


**Figure 6.22:** Training (points) and testing (block histogram) in the 2 jet, low jet signal region for the standard variable set. Signal distributions are in red, and background distributions are in blue.

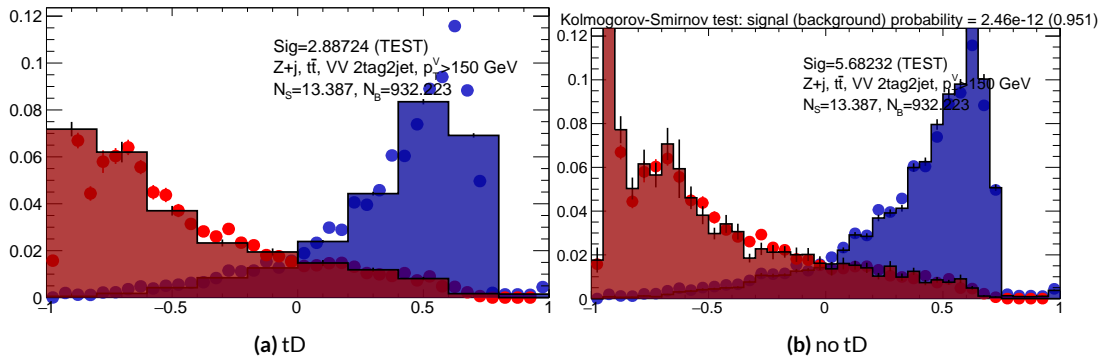


**Figure 6.23:** Training (points) and testing (block histogram) in the 2 jet, high jet signal region for the standard variable set. Signal distributions are in red, and background distributions are in blue.

As can be seen in the summary of cumulative significances for each of these analysis regions and variable sets in Figure 6.34, the performance of each of the variable sets is quite similar. The standard set performs best, with the LI (RF) set having a cumulative significance that is 7.9% (6.9%) lower. This suggests that the LI and RF variables, in the  $ZH \rightarrow \ell\ell b\bar{b}$  closed final state, have no more intrinsic descriptive power than the standard set. That these figures are all relatively high ( $\sim 4.5$ ) is due largely to the absence of systematics and possibly in part due to the fact that many of the most significant bins occur at high values of the BDT output, which, as can be seen in any of the testing

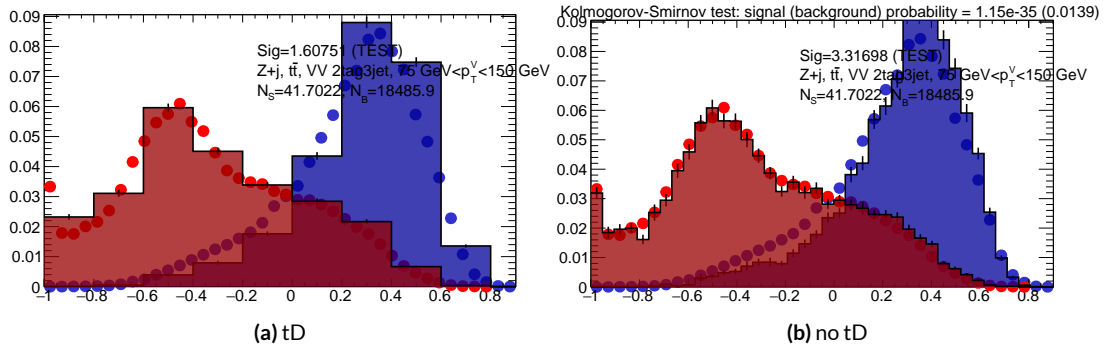


**Figure 6.24:** Training (points) and testing (block histogram) in the 3+ jet, low jet signal region for the standard variable set. Signal distributions are in red, and background distributions are in blue.

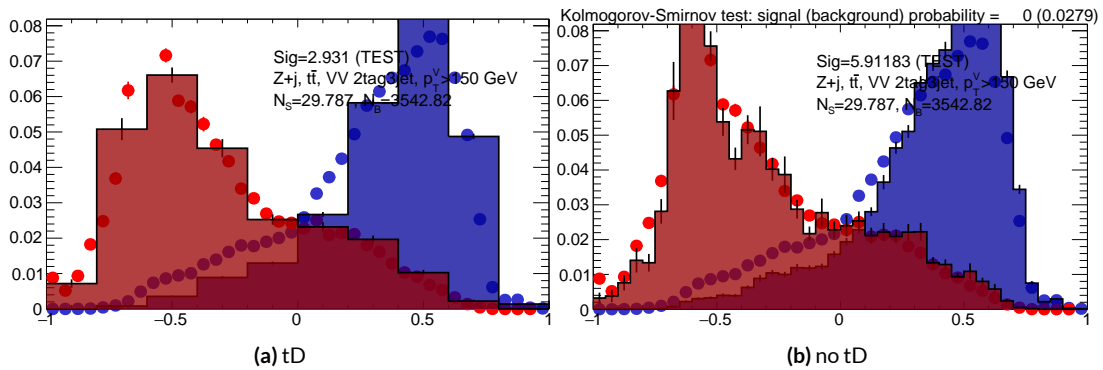


**Figure 6.25:** Training (points) and testing (block histogram) in the 3+ jet, high jet signal region for the standard variable set. Signal distributions are in red, and background distributions are in blue.

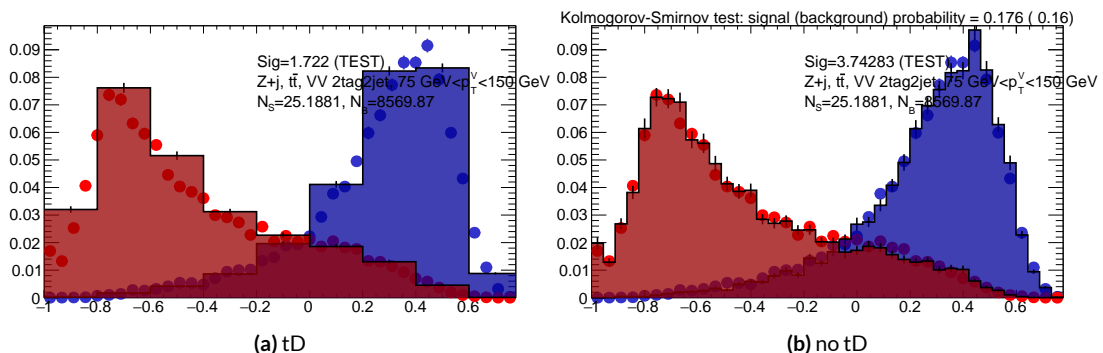


**Figure 6.26:** Training (points) and testing (block histogram) in the 2 jet, low jet signal region for the RF variable set. Signal distributions are in red, and background distributions are in blue.

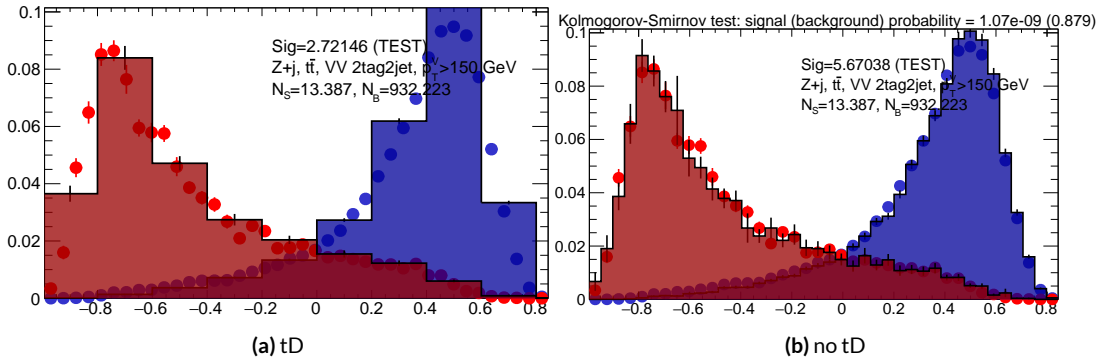


**Figure 6.27:** Training (points) and testing (block histogram) in the 2 jet, high jet signal region for the RF variable set.  
Signal distributions are in red, and background distributions are in blue.

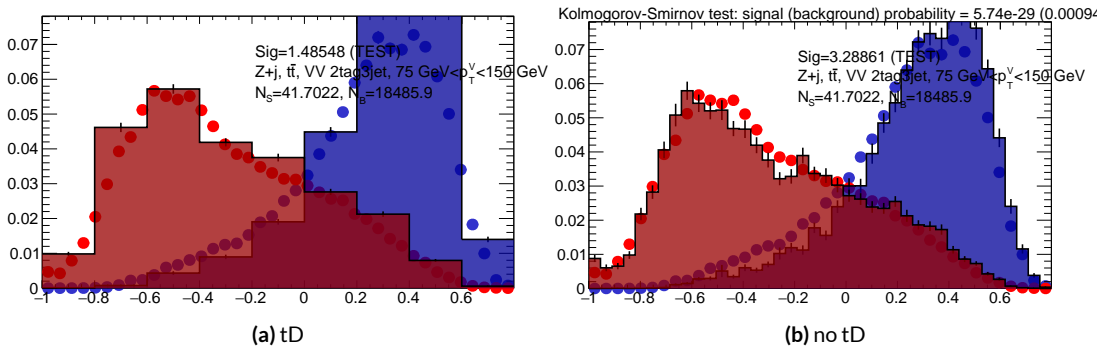


**Figure 6.28:** Training (points) and testing (block histogram) in the 3+ jet, low jet signal region for the RF variable set.  
Signal distributions are in red, and background distributions are in blue.

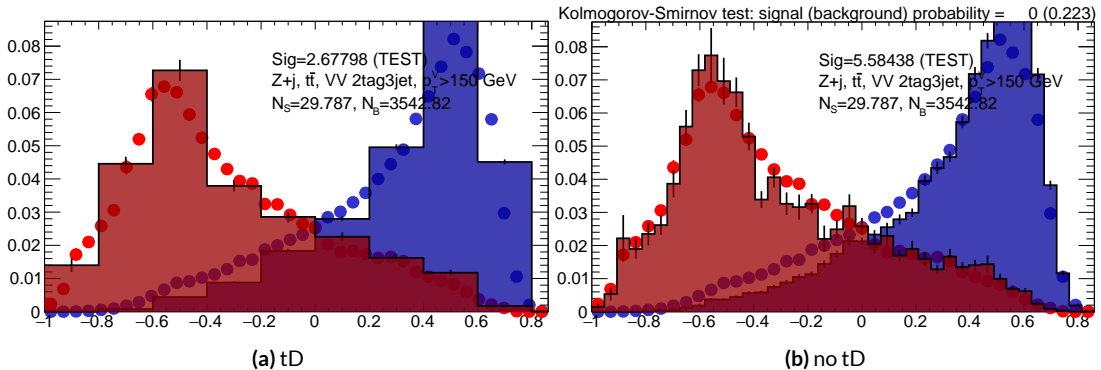


**Figure 6.29:** Training (points) and testing (block histogram) in the 3+ jet, high jet signal region for the RF variable set.  
Signal distributions are in red, and background distributions are in blue.

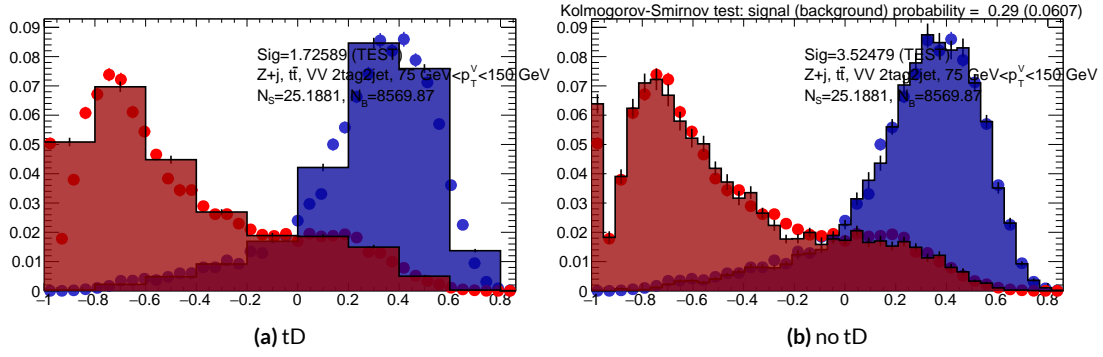


**Figure 6.30:** Training (points) and testing (block histogram) in the 2 jet, low jet signal region for the LI variable set.  
Signal distributions are in red, and background distributions are in blue.

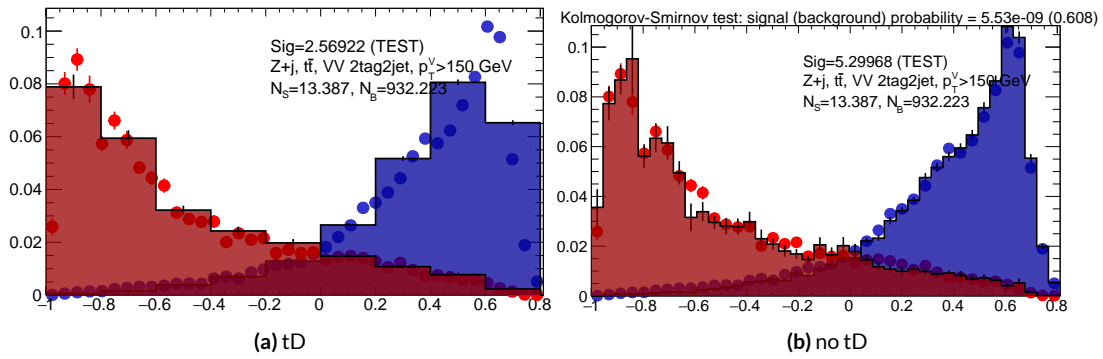


**Figure 6.31:** Training (points) and testing (block histogram) in the 2 jet, high jet signal region for the LI variable set.  
Signal distributions are in red, and background distributions are in blue.

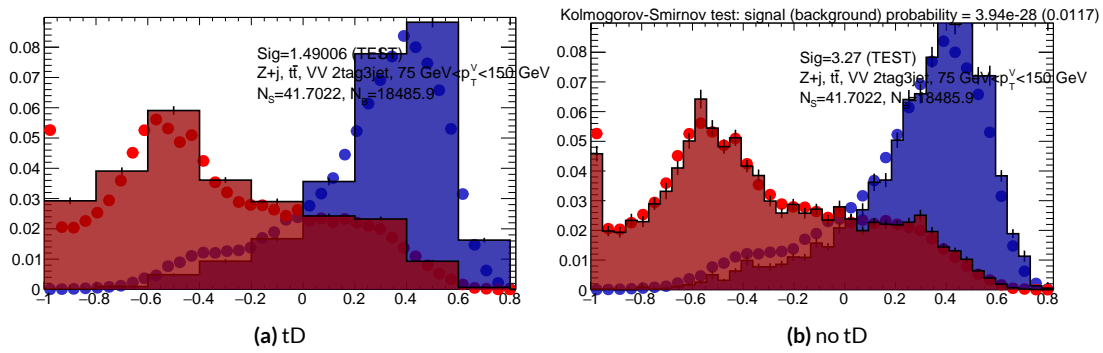


**Figure 6.32:** Training (points) and testing (block histogram) in the 3+ jet, low jet signal region for the LI variable set.  
Signal distributions are in red, and background distributions are in blue.

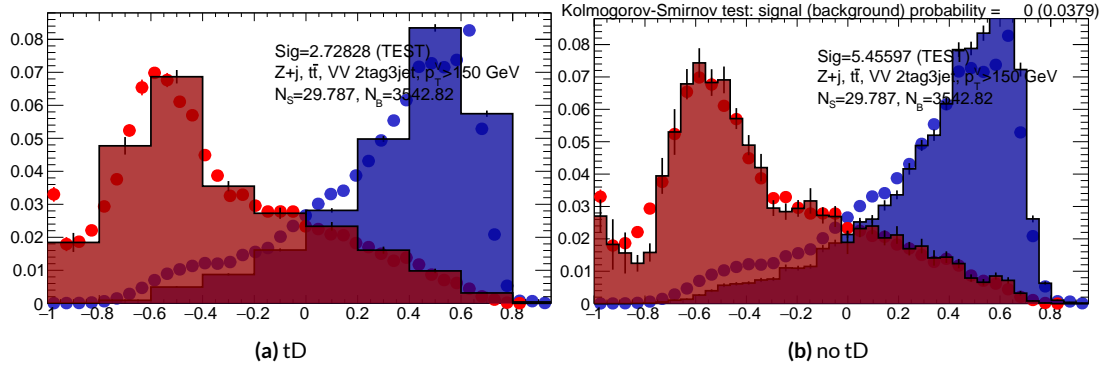


**Figure 6.33:** Training (points) and testing (block histogram) in the 3+ jet, high jet signal region for the LI variable set. Signal distributions are in red, and background distributions are in blue.

distributions, contain a small fraction of background events. An interesting feature to note in Fig-

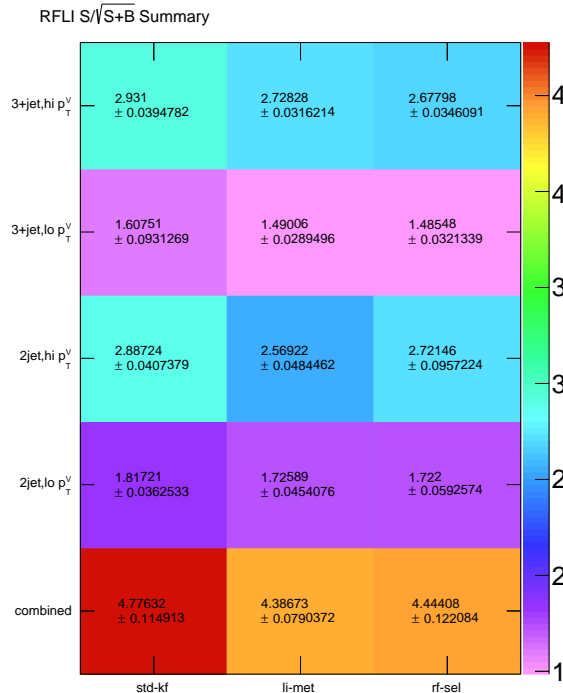


**Figure 6.34:** Results of testing significances sorted by analysis region and variable set.

ure 6.34 is that while the standard set does perform better in all regions, the gap is larger in the  $\geq 3$

jet regions, suggesting that further optimization in the  $\geq 3$  jet case could be useful. Moreover, as discussed at the end of Chapter 5, the choice of  $\geq 3$  jet and not exclusive 3 jet regions is a 2-lepton specific choice and may not be justified for the non-standard variable sets.

*Multivac picked you as most representative this year.*

*Not the smartest, or the strongest, or the luckiest, but*

*just the most representative. Now we don't question*

*Multivac, do we?*

Isaac Asimov, “Franchise”

# 7

## Statistical Fit Model and Validation

THE ULTIMATE GOAL of an analysis like the search for SM  $VH(b\bar{b})$  decay is to say with as much justified precision as possible with the ATLAS collision data whether or not the SM-like Higgs observed in other decay modes also decays to  $b$ -quarks and, if so, whether this rate is consistent with the SM prediction. In the limit of perfect modeling of both background processes and detector/reconstruction,

the only free parameter is this production rate, referred to typically as a “signal strength,” denoted  $\mu$ , with  $\mu = 1$  corresponding to the SM prediction and  $\mu = 0$  corresponding to the SM with no Higgs.

To get a better sense of what this might look like, take a look at the example discriminant distribution in Figure 7.1. The black points are data (with statistical error bars), and the colored block histograms have size corresponding to the number of predicted events for each process in each bin of the final BDT. In the limit of perfect understanding, a fit would correspond to a constant scale factor on the red, signal histogram, where one would choose a best fit  $\mu$  value, denoted  $\hat{\mu}$ , that would minimize the sum in quadrature of differences between the number of observed data events and  $\mu s_i + b_i$ , where  $s_i$  and  $b_i$  are the predicted number of signal and background events in each bin.

The only source of uncertainty would be due to data statistics, so for an infinitely large dataset with perfect understanding,  $\mu$  could be fitted to arbitrary precision. This, of course, is not the case since there is a finite amount of data and very many sources of systematic uncertainty, discussed in previous chapters. This chapter will first describe how systematic uncertainties are integrated into the statistical fit of this analysis before describing two sets of cross checks on both a validation  $VZ$  fit and on the fit for the  $VH$  fit of interest.

## 7.1 THE FIT MODEL

In order to derive the strength of the signal process  $ZH \rightarrow \ell\ell b\bar{b}$  and other quantities of interest while taking into account systematic uncertainties or nuisance parameters (NP’s, collectively denoted  $\theta$ ), a binned likelihood function is constructed as the product over bins of Poisson distribu-

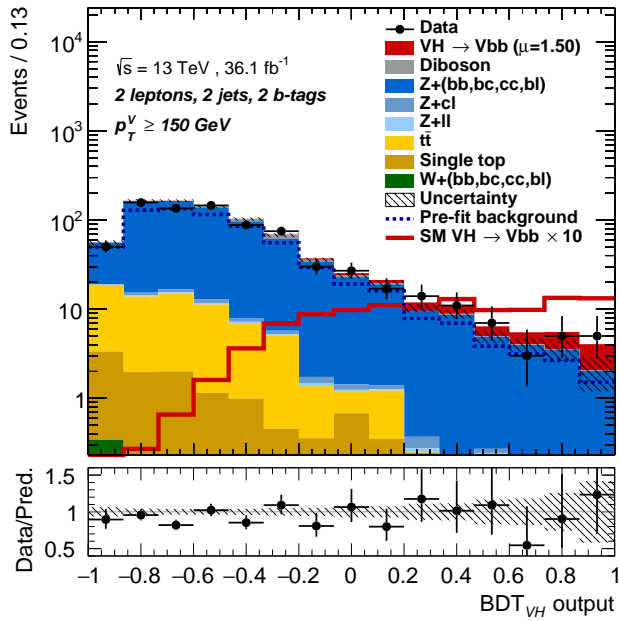


**Figure 7.1:** An example postfit distribution. The reason this looks different from postfit distributions later in this chapter is that this is a log plot. It shows rare samples ( $Z+cl$ ,  $Z+ll$ ,  $W+jets$ ), but obscures Data/MC agreement, which can only be seen via the ratio plot.

tions:

$$\mathcal{L}(\mu, \theta) = \text{Pois}(n | \mu S + B) \left[ \prod_{i \in \text{bins}} \frac{\mu s_i + b_i}{\mu S + B} \right] \prod_{j \in \text{NP's}} \mathcal{N}_{\theta_j}(\theta_j, \sigma_j^2 | 0, 1) \quad (7.1)$$

where  $n$  is the total number of events observed,  $s_i$  and  $b_i$  are the number of expected signal and background events in each bin, and  $S$  and  $B$  are the total expected signal and background events. The signal and background expectations generally are functions of the NP's  $\theta$ . NP's related to the normalization of signal and background processes fall into two categories. The first set is left to float freely like  $\mu$  while the second set are parametrized as log-normally distributed to prevent negative predicted values. All other NP's are parametrized with Gaussian priors. This results in a “penalty” on the NLL discussed below of  $(\hat{\alpha} - \mu_\alpha)^2 / \sigma_\alpha^2$ , for NP  $\alpha$ , normally parametrized with mean  $\mu_\alpha$

(corresponding to the nominal prediction) and variance  $\sigma_\alpha^2$  (derived as discussed in Chapters 4 and 5) for an MLE of  $\hat{\alpha}$ .

One can maximize<sup>\*</sup> the likelihood in Equation 7.1 for a fixed value of  $\mu$  to derive estimators for the NP's  $\theta$ ; values of  $\theta$  so derived are denoted  $\hat{\theta}_\mu$  to emphasize that these are likelihood maximizing for a given  $\mu$ . The profile likelihood technique finds the likelihood function's maximum by comparing the values of the likelihood over all possible values of  $\mu$  using these "profiles" and picking the one with the greatest  $\mathcal{L}(\mu, \hat{\theta}_\mu)$  value; these values of  $\mu$  and  $\theta$  are denoted  $\hat{\mu}$  and  $\hat{\theta}$ . The profile likelihood can further be used to construct a test statistic<sup>†</sup>

$$q_\mu = -2 \left( \log \mathcal{L}(\mu, \hat{\theta}_\mu) - \log \mathcal{L}(\hat{\mu}, \hat{\theta}) \right) \quad (7.2)$$

This statistic can be used to derive the usual significance ( $p$  value), by setting  $\mu = 0$  to find the compatibility with the background-only hypothesis [58]. If there is insufficient evidence for the signal hypothesis, the  $CL_s$  method can be used to set limits [59].

In order to both validate the fit model and study the behavior of fits independent of a given dataset, a so-called "Asimov"<sup>‡</sup> dataset can be constructed for a given fit model; this dataset has each bin equal to its expectation value for assumed values of the NP's and a given  $\mu$  value (in this case,  $\mu = 1$ , the SM prediction).

---

<sup>\*</sup>Maximization is mathematically identical to finding the minimum of the negative logarithm of the likelihood, which is numerically an easier problem.

<sup>†</sup>The factor of -2 is added so that this statistic gives, in the asymptotic limit of large  $N$ , a  $\chi^2$  distribution.

<sup>‡</sup>A reference to the short story quoted at the beginning of this chapter in which a computer picks a single voter to stand in for the views of the entire American electorate.

## 7.2 FIT INPUTS

Inputs to the binned likelihood are distributions of the BDT outputs described in Chapter 6 for the signal regions and of  $m_{bb}$  for the top  $e - \mu$  control regions. These regions split events according to their  $p_T^V$  and number of jets. All events are required to have two  $b$ -tagged jets, as well as pass the other event selection requirements summarized in Table 5.6; the only difference between the signal and control region selections is that the same flavor requirement (i.e. leptons both be electrons or muons) is flipped so that events in the control region have exactly one electron and one muon. The BDT outputs are binned using transformation D, while the  $m_{bb}$  distributions have 50 GeV bins, with the exception of the 2 jet, high  $p_T^V$  region, where a single bin is used due to low statistics.

Input distributions in MC are further divided according to their physics process. The signal processes are divided based on both the identity of associated  $V$  and the number of leptons in the final state;  $ZH \rightarrow \ell\ell b\bar{b}$  events are further separated into distributions for  $qq$  and  $gg$  initiated processes.  $V+jets$  events are split according to  $V$  identity and into the jet flavor bins described in Chapter 3. Due to the effectiveness of the 2  $b$ -tag requirement suppressing the presence of both  $c$  and  $l$  jets, truth-tagging is used to boost MC statistics in the  $cc$ ,  $cl$ , and  $ll$  distributions.<sup>§</sup> For top backgrounds, single top production is split according to production mode ( $s$ ,  $t$ , and  $Wt$ ), with  $t\bar{t}$  as single category. Diboson background distributions are also split according to the identity of the  $V$ 's ( $ZZ$ ,  $WZ$ , and  $WW$ ). Fit input segmentation is summarized in Table 7.1.

---

<sup>§</sup>Since  $WW$  is not an important contribution to the already small total diboson background, no truth-tagging was applied here, in contrast to the fiducial analysis.

**Table 7.1:** Fit input segmentation.

Category	Bins
# of Jets	2, 3+
$p_T^V$ Regions (GeV)	$[75, 150], [150, \infty)$
Sample	data, signal $[(W, qqZ, ggZ)] \times n_{lep}$ , $V+jets [(W, Z) \times (bb, bc, bl, cc, cl, l)]$ , $t\bar{t}$ , diboson ( $ZZ, WW, WZ$ ), single top ( $s, t, Wt$ )

### 7.3 SYSTEMATIC UNCERTAINTIES REVIEW

Tables 7.2 and 7.3 summarize modeling (Chapter 4) and experimental (Chapter 5) systematic uncertainties considered in this analysis, respectively. In addition to these, simulation statistics uncertainties (“MC stat errors”) are also included in the fit model. There is one distribution per systematic (one each for up and down) per sample per region. The  $\pm 1\sigma$  variation for a systematic is calculated as the difference in the integrals between the nominal and up/down varied distributions.

**Table 7.2:** Summary of modeling systematic uncertainties.

Process	Systematics
Signal	$H \rightarrow bb$ decay, QCD scale, PDF+ $\alpha_S$ scale, UE+PS (acc, $p_T^V, m_{bb}, 3/2$ jet ratio)
$Z+jets$	Acc, flavor composition, $p_T^V+m_{bb}$ shape
$t\bar{t}$	Acc, $p_T^V+m_{bb}$ shape
Single top	Acc, $p_T^V+m_{bb}$ shape
Diboson	Overall acc, UE+PS (acc, $p_T^V, m_{bb}, 3/2$ jet ratio), QCD scale (acc (2, 3 jet, jet veto), $p_T^V, m_{bb}$ )

The systematics distributions undergo processes known as “smoothing” and “pruning” before being combined into the final likelihood used in minimization.

The difference between systematics varied distributions and nominal distributions approaches

**Table 7.3:** Summary of experimental systematic uncertainties.

Process	Systematics
Jets	21 NP scheme for JES, JER as single NP
$E_T^{\text{miss}}$	trigger efficiency, track-based soft terms, scale uncertainty due to jet tracks
Flavor Tagging	Eigen parameter scheme (CDI File: 2016-20_7-13TeV-MC15-CDI-2017-06-07_v2)
Electrons	trigger eff, reco/ID eff, isolation eff, energy scale/resolution
Muons	trigger eff, reco/ID eff, isolation eff, track to vertex association, momentum resolution/scale
Event	total luminosity, pileup reweighting

some stable value in the limit of large simulation statistics, but if the fluctuations due to simulation statistics in a distribution are large compared to the actual physical effect (whether this is because the actual effect is small or if the actual distribution is derived from a small number of simulation events), then systematic uncertainty will be overestimated by, in effect, counting the MC stat error multiple times. Smoothing is designed to mitigate these effects by merging adjacent bins in some input distributions. Smoothing happens in two steps (the full details of smoothing algorithms may be found in [14] and in the `WSMaker` code):

1. Merge bins iteratively where bin differences are smallest in input distributions until no local extrema remain (obviously, a single peak or valley is allowed to remain)
2. Sequentially merge bins (highest to lowest, like transformation D) until the statistical uncertainty in a given bin is smaller than 5% of merged bin content

Not all systematic uncertainties defined are included in the final fit. Systematics are subject to “pruning” (individually in each region/sample: there are two histograms per systematic (up/down) per region per sample, so pruning just consists of removing the histograms from the set of distribu-

tions included in the likelihood) if they are do not have a significant impact, defined as follows:

- Normalization/acceptance systematics are pruned away if either:
  - The variation is less than 0.5%
  - Both up and down variations have the same sign
- Shape systematics pruned away if either:
  - Not one single bin has a deviation over 0.5% after the overall normalization is removed
  - If only the up or the down variation is non-zero
- Shape+Normalization systematics are pruned away if the associated sample is less than 2% of the total background and either:
  - If the predicted signal is  $< 2\%$  of the total background in all bins and the shape and normalization error are each  $< 0.5\%$  of the total background
  - If instead at least one bin has a signal contribution  $> 2\%$  of the total background, and only in each of these bins, the shape and normalization error are each  $< 2\%$  of the signal yield

## 7.4 THE VZ VALIDATION FIT

One of the primary validation cross-checks for the fiducial analysis was a  $VZ$  fit—that is, conducting the entire analysis but looking for  $Z \rightarrow b\bar{b}$  decays instead of the Higgs. The idea here is that the  $Z$  is very well understood and so “rediscovering”  $Z$  decay to  $b$ ’s is taken as a benchmark of analysis reliability since the complexity of the fit model precludes the use of orthogonal control regions for

validation as is done in other analyses (generally, if there is a good control region, one prefers to use it to constrain backgrounds and improve the fit model). To do this, a new MVA discriminant is made by keeping all hyperparameter configurations the same (e.g. variable ranking) but using diboson samples as signal. For the 2-lepton case, this means using  $ZZ \rightarrow \ell\ell b\bar{b}$  as the signal sample. This new MVA is used to make the inputs described in Section 7.2, and the fit is then run as for the  $VH$  fit (again, with  $ZZ$  as signal).  $VH$  samples are considered background in these diboson fits.

The  $VZ$  fit sensitivities for the standard, LI, and RF fits are summarized in Table 7.4. The expected significances are all fairly comparable and about what was the case in the fiducial analysis. The observed significance for the standard set matches fairly well with the expected value on data, but the LI and RF observed significances are quite a bit lower.

**Table 7.4:** Expected (for both data and Asimov) and observed  $VZ \rightarrow \ell\ell b\bar{b}$  sensitivities for the standard, LI, and RF variable sets.

	Standard	LI	RF
Expected (Asimov)	3.83	3.67	3.72
Expected (data)	3.00	2.95	3.11
Observed (data)	3.17	1.80	2.09

These values, however, are consistent with the observed signal strength values, which can be seen in Figure 7.2 (b), with both the LI and RF fits showing a deficit of signal events with respect to the SM expectation, though not by much more than one standard deviation (a possible explanation is explored in the following section). Just as in the  $VH$  fits, errors arising systematic uncertainties are lower in the fits to the observed dataset. That the effect is not noticeable in Asimov fits is not too

surprising, since this analysis (and these variable configurations in particular), is not optimized for  $VZ$ .

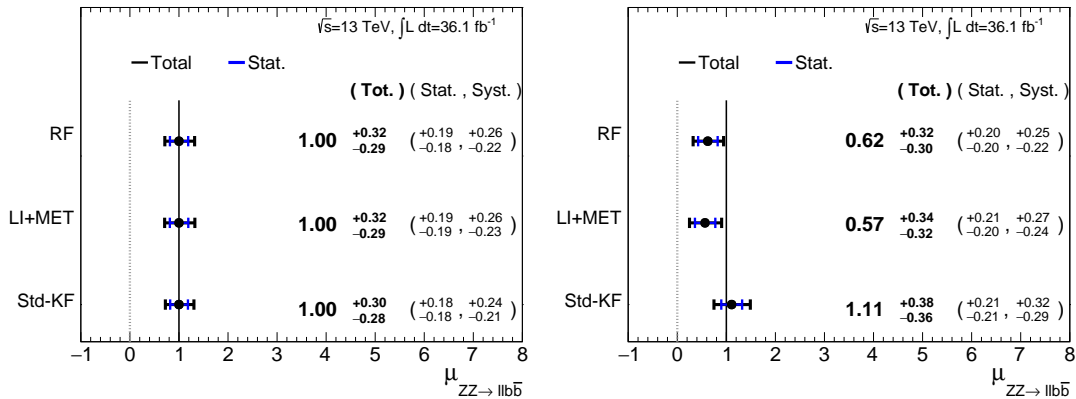


**Figure 7.2:**  $\mu$  summary plots for the standard, LI, and RF variable sets. The Asimov case (with  $\mu = 1$  by construction) is in (a), and  $\hat{\mu}$  best fit values and error summary are in (b).

#### 7.4.I 2 AND $\geq 3$ JET FITS

While the treatment of simply ignoring any additional jets in the event seems adequate for the  $VH$  analysis (discussed below), the potential shortcoming of this treatment appears in the  $VZ$  analysis when the 2 and  $\geq 3$  jet cases are fit separately<sup>¶</sup>, as can be seen in Figure 7.3. Compared to the standard fit, the LI and RF fits have lower  $\hat{\mu}_{\geq 3 \text{ jet}}$  values, consistent with the interpretation that the additional information from the third jet in the  $\geq 3$  jet regions for the standard case is important for characterizing events in these regions for  $VZ$  fits.

A natural question to ask is why this would be an issue for the  $VZ$  but not the  $VH$  case. One potential answer is that at high transverse boosts, there is a greater probability for final state

<sup>¶</sup>standalone fits, with half the regions each, not 2 POI fits

radiation in the hadronically decaying  $Z$ , so there are more events where the third jet should be included in the calculation of variables like  $m_{b\bar{b}}$  or for angles involving the  $b\bar{b}$  system (e.g.  $\cosh$  in the RF case). While the absolute scale at which the low and high  $p_T^V$  regions are separated remains the same does not change from the  $VH$  to the  $VZ$  analysis, 150 GeV, the implicit cutoff on the transverse boost of the hadronically decaying boson does. For the Higgs, with a mass of 125 GeV, the  $p_T^V$  cutoff corresponds to  $\gamma \sim 1.56 - 6.74$ , but for the  $Z$ , with a mass of 91 GeV, this is  $\gamma \sim 1.93 - 9.21$ , about 23–37% higher.

If either the LI or RF schemes were to be used in a mainstream analysis, these validation fits suggest that the third jet ought to be included in variable schemes (e.g. by adding the third jet to the Higgs in the high  $p_T^V$  case). On the issue of whether or not  $\geq 4$  jet events should be included, the RF set shows very little sensitivity to this change (a 2 jet and 3 jet only fit moves  $\hat{\mu}$  to 0.64, while doing so for the LI set moves it to 0.40), so this, like the addition of the third jet into the variable sets, would have to be addressed individually. Nevertheless, this optimization is beyond the scope of this thesis, which aims to preserve as much of the fiducial analysis as possible for as straightforward a comparison as possible.

For completeness, we include the full set of fit validation results for the  $VZ$  fit, explaining them in turn.

## 7.5 NUISANCE PARAMETER PULLS

The first set of plots statistical fit experts will want to look at are the “pulls” and “pull comparisons.” In these plots, the best fit (nominal) values and one standard deviation error bars are shown for ob-

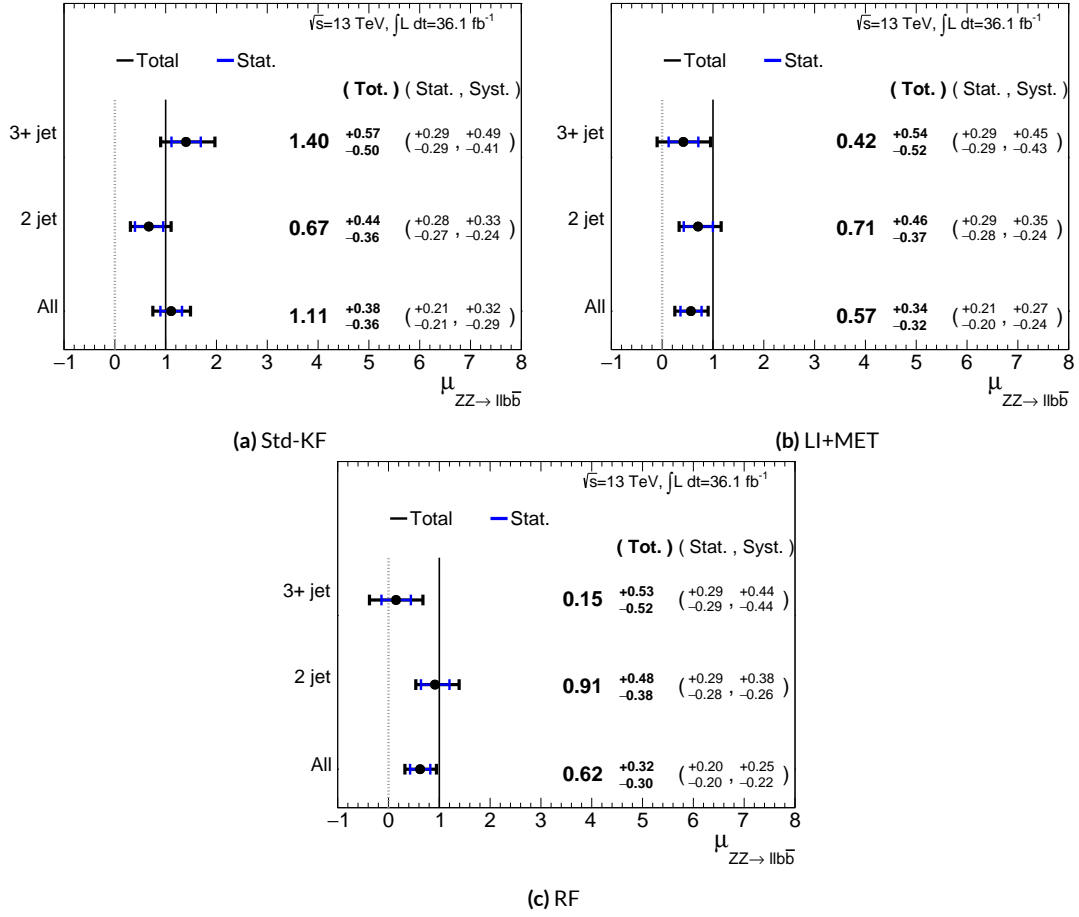


**Figure 7.3:**  $\hat{\mu}$  summary plots with standalone fits for the different  $n_{jet}$  regions for the standard, LI, and RF variable sets.

served (Asimov) pull plots, with the green and yellow bands corresponding to  $\pm 1, 2\sigma$ , respectively.

These plots are divided by NP category for readability. <sup>¶</sup> In pull comparisons, these pulls are overlaid and color-coded. Pull comparisons here have the following color code: black is the standard variable set, red is the LI set, and blue is the RF set.

We give an example in Figure 7.4, which shows the  $Z+jets$  modeling systematics. The green (yel-

---

<sup>¶</sup>Over 100 non-MC stat NP's survive pruning in these 2-lepton only Run 2 fits; well over 500 survive in the Run 1+Run 2 combined fit.

low) band represents  $\pm 1$  ( $2$ )  $\sigma$ . NP's with norm are the freely floating parameters mentioned above initialized to  $1 \pm 0$ , while all other NP's are the Gaussian (or log-normal for non-freely floating normalizations) are initialized\*\* in the fit to  $0 \pm 1$ . Both types of NP's can be seen in the figure. Generally, some deviation is expected in a fit, but several “strongly pulled” (i.e. the absolute value of an NP central value divided by the error bar size is greater than one) NP's is a sign of a “bad” fit. Here, ZPtV is strongly pulled for all three fits, and ZMb is strongly pulled for the LI fits; this is unsurprising since  $Z+jets$  modeling has traditionally been hard. Such plots let the analyzer look for problems in fit models and compare different analyses and are the first fit diagnostic plot used in the fit workflow.

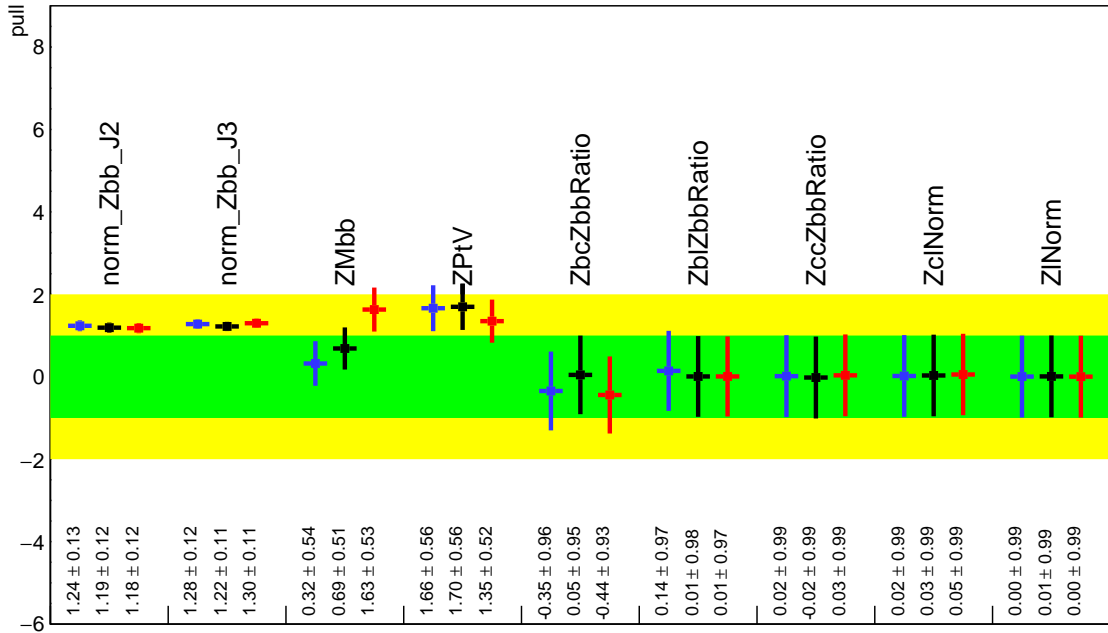
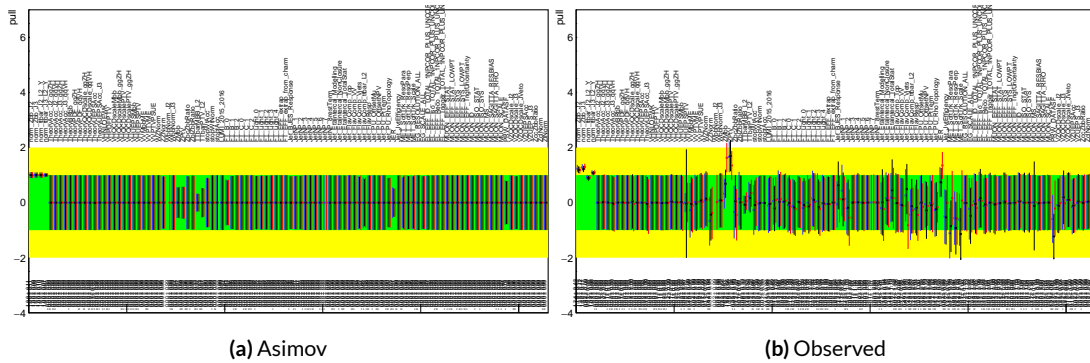


Figure 7.4: Pull comparison for signal process modeling NP's.

\*\*with the usual mean subtraction/standard deviation division applied

A well-behaved fit has pulls close to nominal values (“closeness” should be interpreted in the context of pull value divided by pull error). As can be seen in Figures 7.5–7.9, the fits for the three different variable sets are fairly similar from a NP pull perspective, though the  $Z$ +jets  $m_{bb}$  and  $p_T^V$  NP’s and the jet energy resolution NP are heavily pulled (a handful of poorly behaved pulls is not uncommon, though typically warrants further investigation). As a general note, these pull plots calculate pulls using a simultaneous **HESSE** matrix inversion, which is fine for relatively small fits, but the more reliable **MINOS** result, which calculates the impact of each NP on its own, should be cross-checked for significant pulls<sup>††</sup>. The ranking plots below do this.



**Figure 7.5:** Pull comparison for all NP’s but MC stats.

Nuisance parameter correlation matrices (for correlations with magnitude at least 0.25) for all three variable set fits can be found in Figures 7.11–7.13. These are useful for seeing which NP’s move together (if there is no physical argument for them to do so, this is a potential indicator that further investigation is warranted). These are similar to the correlation matrices in e.g. Figure 6.15 except with ordering inverted (so the diagonal is oriented the other way).

---

<sup>††</sup>This becomes more of an issue for very large fits, like the full Run 1 + Run 2 combined fits in Chapter 9.

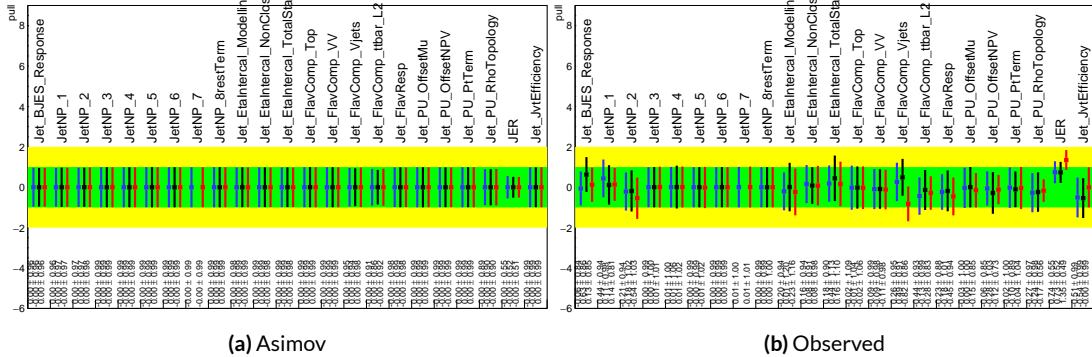


**Figure 7.6:** Pull comparison for jet NP's.

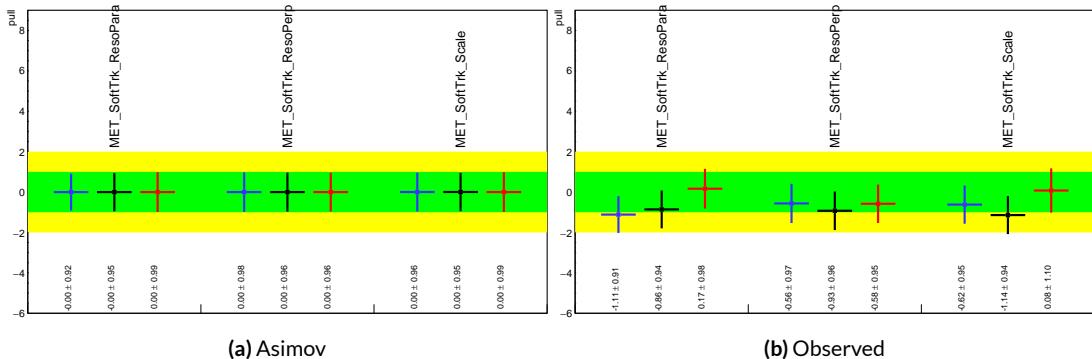


**Figure 7.7:** Pull comparison for MET NP's.

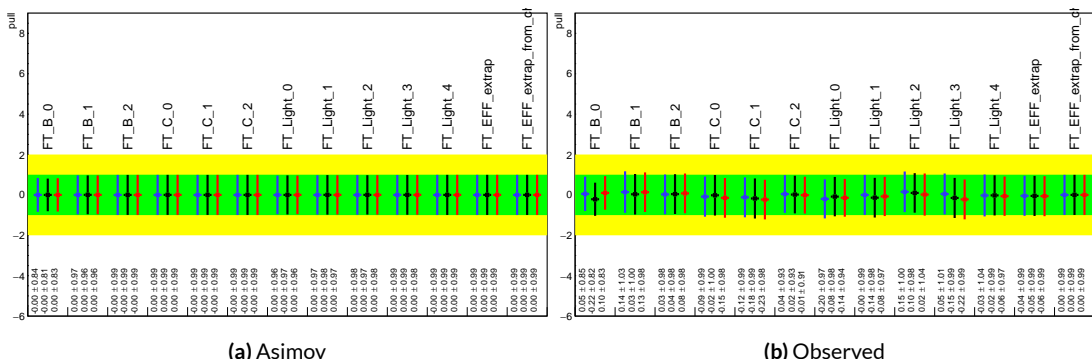


**Figure 7.8:** Pull comparison for Flavour Tagging NP's.

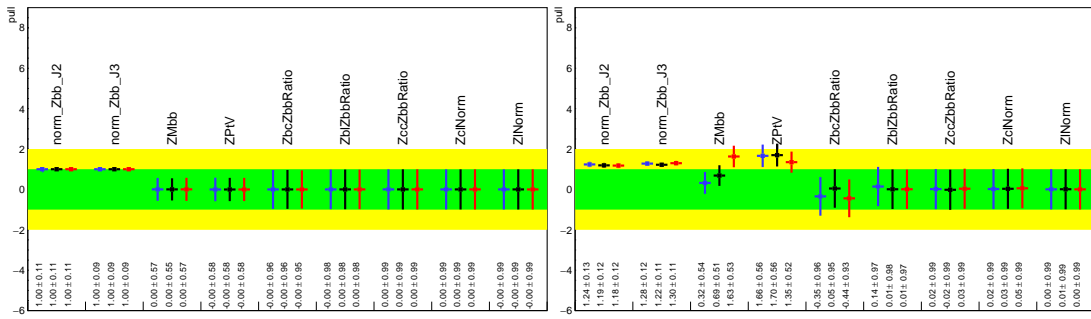


Figure 7.9: Pull comparison for  $Z + \text{jets}$  NP's.

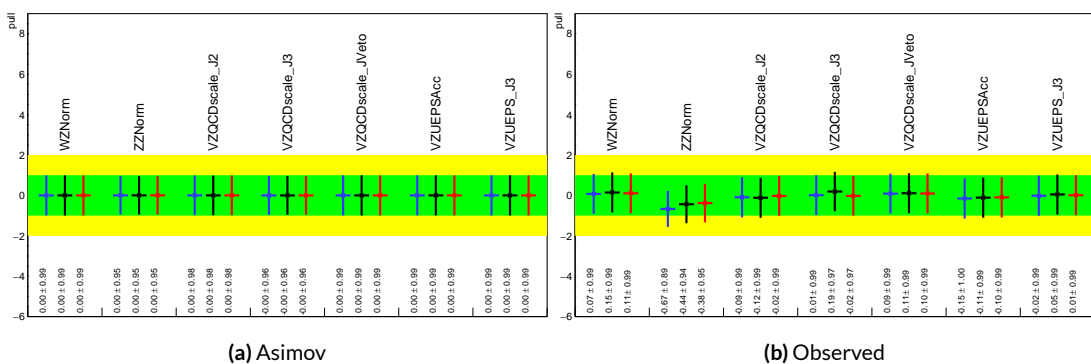


Figure 7.10: Pull comparison for diboson process modeling NP's.

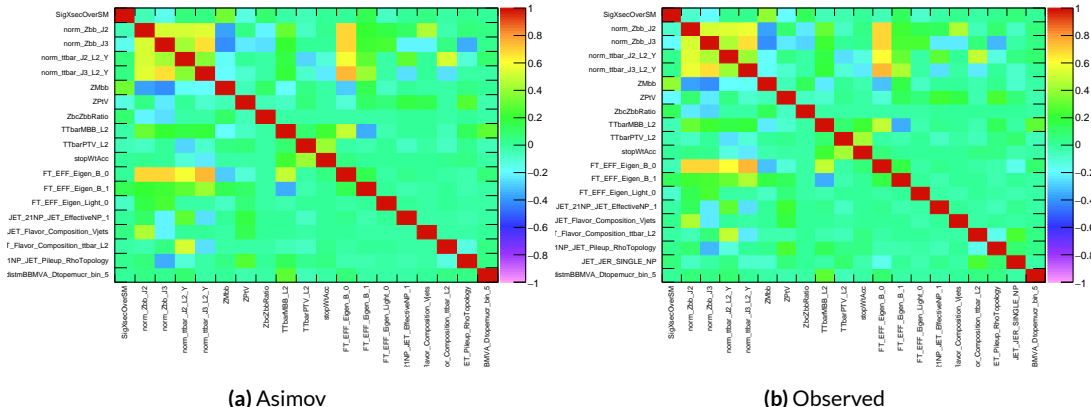
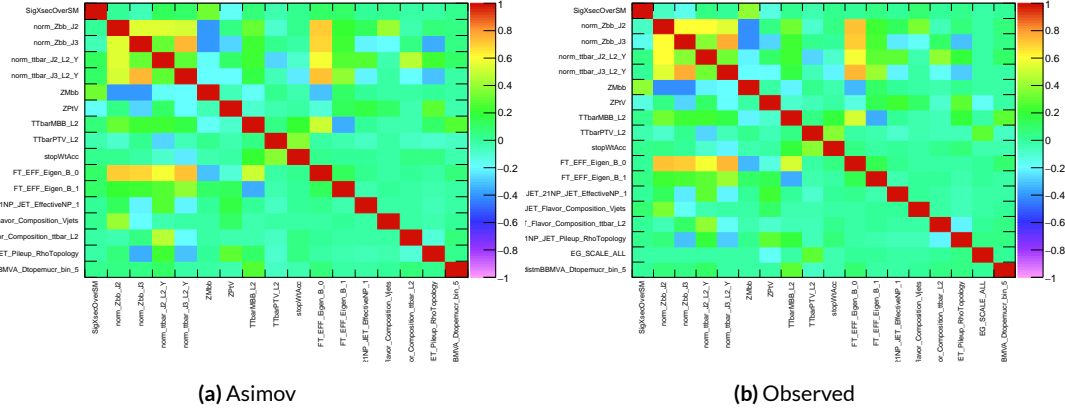
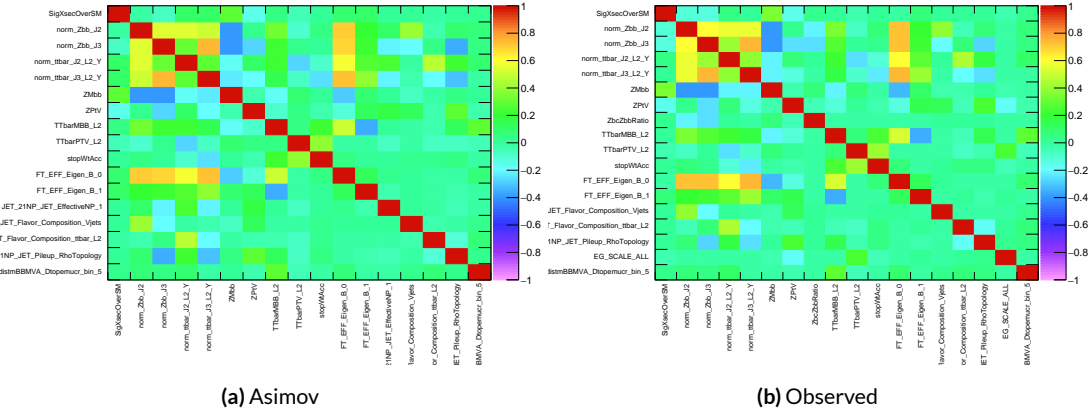


Figure 7.11: NP correlations for standard variable fits.



**Figure 7.12:** NP correlations for LI variable fits.



**Figure 7.13:** NP correlations for RF variable fits.

## 7.5.1 NUISANCE PARAMETER RANKING PLOTS AND BREAKDOWNS

The next set of fit results that is used to diagnose the quality of a fit is the impact of different nuisance parameters on the total error on  $\mu$ , both individually and as categories. Figure 7.14 shows the top 25 nuisance parameters ranked by their postfit impact on  $\hat{\mu}$ ; these plots use the aforementioned, more reliable MINOS approach. This set of rankings is fairly similar, with  $Z+jets$  systematics being particularly prominent. The advantage of seeing individual nuisance parameter rankings, as opposed to impacts of categories in aggregate, is that particularly pathological NP's are easier to see; in particular, jet energy resolution and  $Z+jets p_T^V$  systematic from the pull comparison plots show up with high rankings. Blue (Yellow) bands are post-(pre-) fit impact on  $\mu$ , and the black (red) points with error bars are the same as for the standard (floating normalization) NP's in the pull comparison plots.

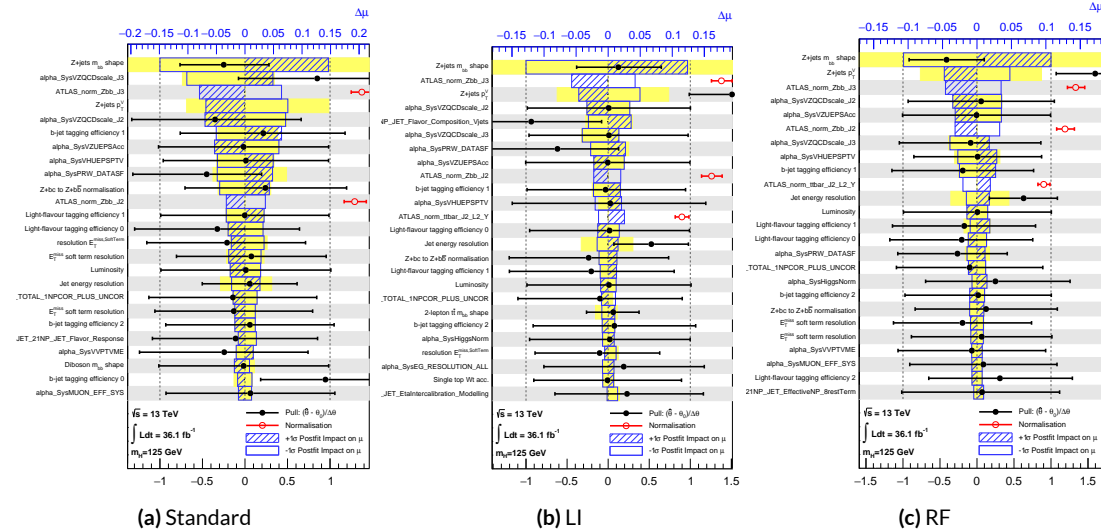


**Figure 7.14:** Plots for the top 25 nuisance parameters according to their postfit impact on  $\hat{\mu}$  for the standard (a), LI (b), and RF (c) variable sets.

This is consistent with the picture of NP’s taken in aggregate categories in Tables 7.5 and 7.6, known as “breakdowns,” with  $Z$ +jets in particular featuring prominently. In all of these tables, there is a 10% cutoff of full systematics impact (FullSyst) for displaying a given NP category. Of particular interest is also the lower impact of MC stats in the observed fit.

**Table 7.5:** Summary of impact of various nuisance parameter categories on the error on  $\mu$  for Asimov fits for the standard, LI, and RF variable sets.

	Std-KF	LI+MET	RF
Total	+0.305 / -0.277	+0.324 / -0.292	+0.319 / -0.288
DataStat	+0.183 / -0.179	+0.190 / -0.186	+0.188 / -0.184
FullSyst	+0.244 / -0.212	+0.262 / -0.226	+0.258 / -0.221
All normalizations	+0.093 / -0.084	+0.098 / -0.079	+0.094 / -0.076
Jets	+0.034 / -0.029	+0.033 / -0.028	+0.032 / -0.026
MET	+0.035 / -0.027	+0.015 / -0.012	+0.020 / -0.016
BTag	+0.064 / -0.051	+0.063 / -0.031	+0.059 / -0.032
BTag b	+0.053 / -0.041	+0.061 / -0.028	+0.055 / -0.025
BTag light	+0.030 / -0.027	+0.016 / -0.013	+0.022 / -0.019
Luminosity	+0.039 / -0.022	+0.039 / -0.022	+0.040 / -0.022
Diboson	+0.049 / -0.028	+0.047 / -0.026	+0.047 / -0.026
Model Zjets	+0.106 / -0.105	+0.113 / -0.110	+0.102 / -0.099
Zjets flt. norm.	+0.039 / -0.053	+0.024 / -0.029	+0.021 / -0.031
Model ttbar	+0.015 / -0.013	+0.032 / -0.017	+0.030 / -0.016
MC stat	+0.097 / -0.094	+0.108 / -0.103	+0.107 / -0.104

**Table 7.6:** Summary of impact of various nuisance parameter categories on the error on  $\hat{\mu}$  for observed fits for the standard, LI, and RF variable sets.

	Std-KF	LI+MET	RF
$\hat{\mu}$	1.1079	0.5651	0.6218
Total	+0.381 / -0.360	+0.339 / -0.316	+0.322 / -0.299
DataStat	+0.214 / -0.211	+0.210 / -0.205	+0.201 / -0.197
FullSyst	+0.315 / -0.292	+0.267 / -0.241	+0.252 / -0.225
All normalizations	+0.121 / -0.123	+0.095 / -0.090	+0.082 / -0.079
Jets	+0.047 / -0.040	+0.044 / -0.041	+0.027 / -0.024
MET	+0.055 / -0.046	+0.015 / -0.015	+0.012 / -0.010
BTag	+0.083 / -0.079	+0.041 / -0.031	+0.041 / -0.035
BTag b	+0.063 / -0.059	+0.032 / -0.022	+0.031 / -0.026
BTag light	+0.051 / -0.046	+0.024 / -0.021	+0.025 / -0.022
Luminosity	+0.044 / -0.022	+0.026 / -0.006	+0.027 / -0.008
Diboson	+0.049 / -0.026	+0.025 / -0.013	+0.027 / -0.017
Model Zjets	+0.156 / -0.162	+0.133 / -0.133	+0.115 / -0.117
Zjets flt. norm.	+0.061 / -0.089	+0.041 / -0.064	+0.028 / -0.056
Model ttbar	+0.015 / -0.024	+0.018 / -0.005	+0.017 / -0.009
MC stat	+0.140 / -0.143	+0.132 / -0.131	+0.128 / -0.129

## 7.6 POSTFIT DISTRIBUTIONS

Finally, postfit distributions for the MVA discriminant ( $m_{bb}$ ) distribution in the signal (top  $e - \mu$  control) region for the standard, Lorentz Invariant, and RestFrames variable sets are shown. It is generally considered good practice to check the actual postfit distributions of discriminating quantities used to make sure there is good agreement. <sup>##</sup> It should be noted that agreement is not always great when “eyeballing” a distribution, as fits are messy and  $V+hf$  modeling is notoriously hard. This is particularly true in the  $VZ$  fit since normalizations for  $Z+hf$  in particular are derived using  $VH$  optimized sidebands. This is also why a lot of these plots are presented as log plots (which hide disagreement better; the general argument goes that one has the ratio plots on the bottom and log plots allow one to see rare backgrounds in plots).

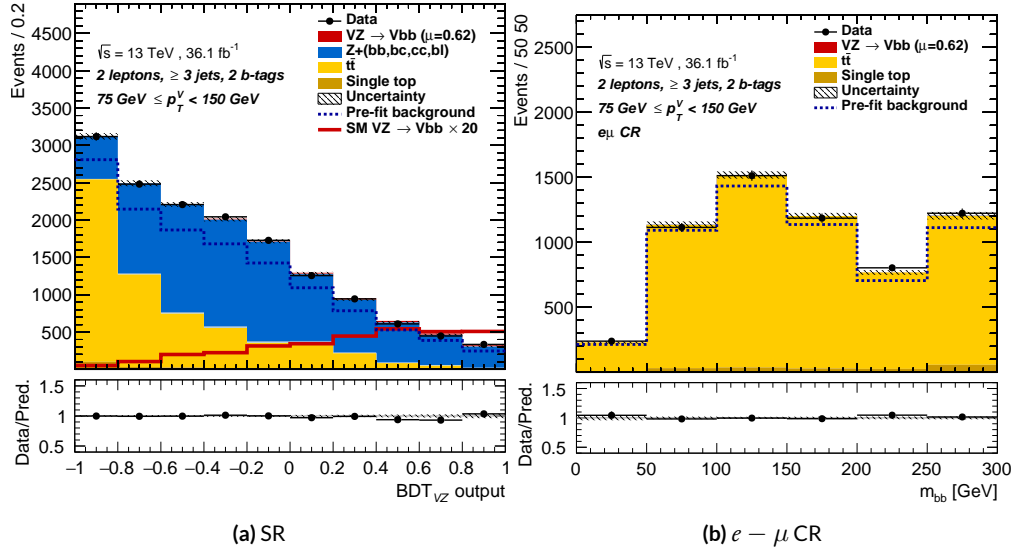


**Figure 7.14:** Postfit  $VZ$  plots in the 3+ jet, low pTV region for the RF variable set.

<sup>##</sup>Sometimes distributions of input variables (MC histograms scaled by their postfit normalizations) are also used.

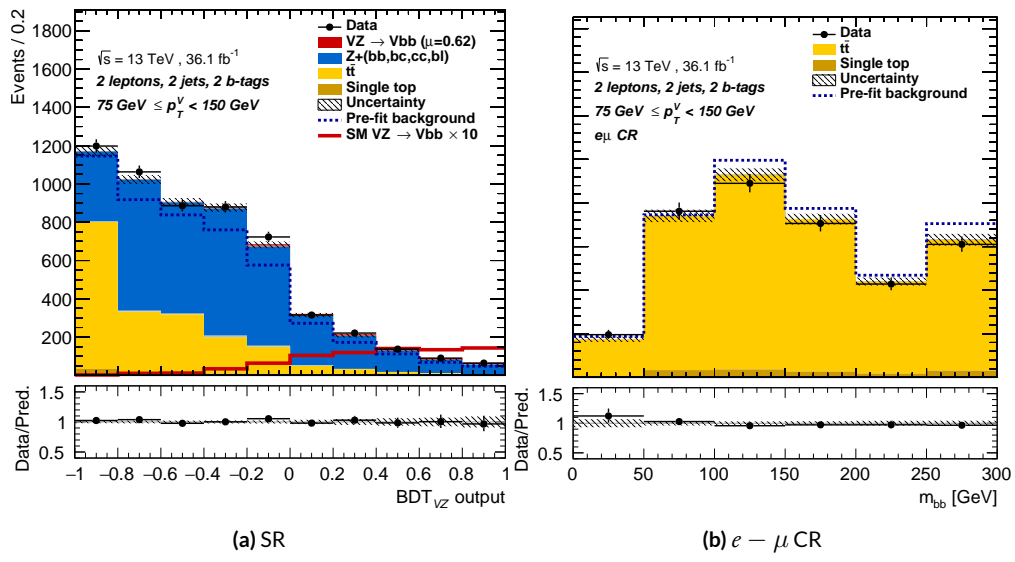


Figure 7.15: Postfit  $VZ$  plots in the 2 jet, low pTV region for the RF variable set.

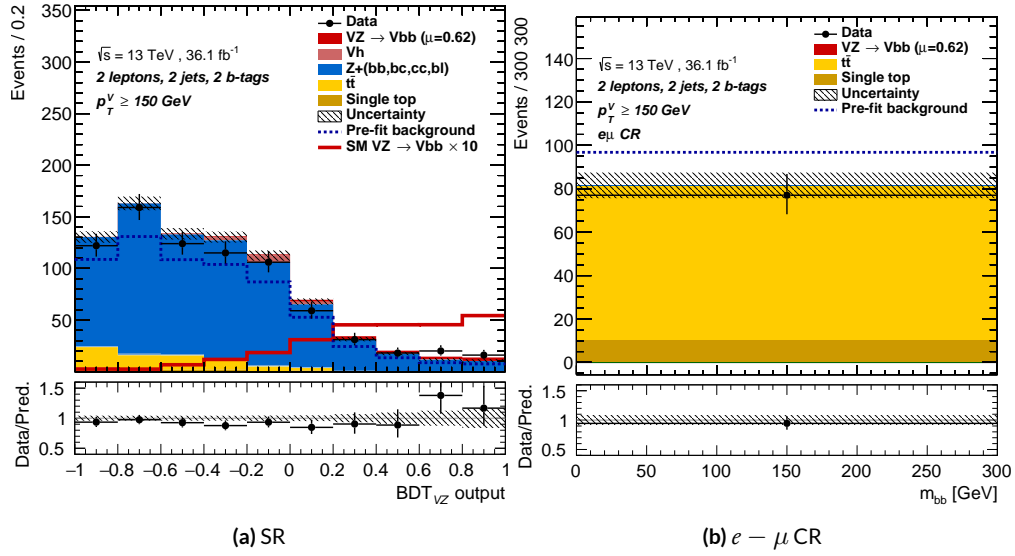


Figure 7.16: Postfit  $VZ$  plots in the 2 jet, high pTV region for the RF variable set.

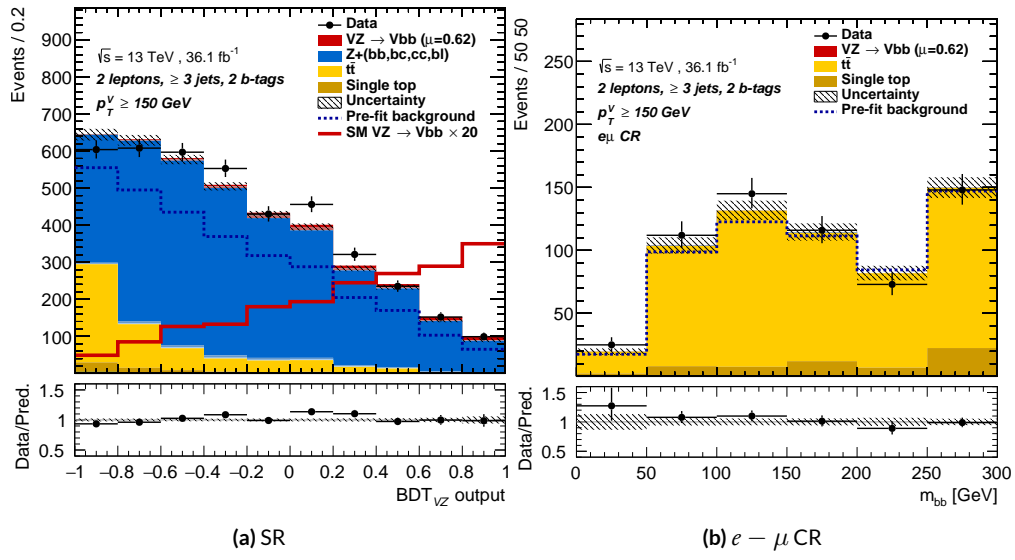


Figure 7.17: Postfit  $VZ$  plots in the 3+ jet, high pTV region for the RF variable set.

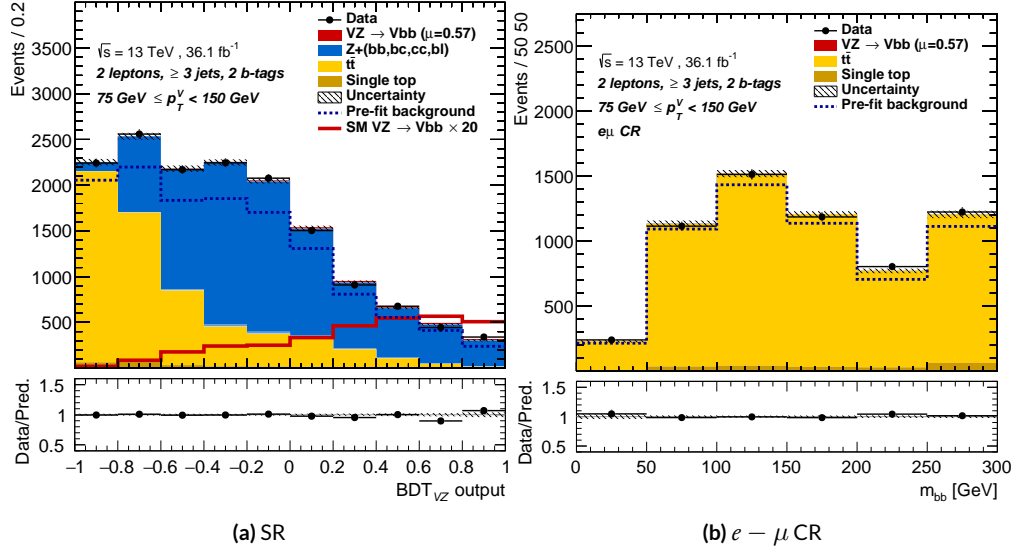
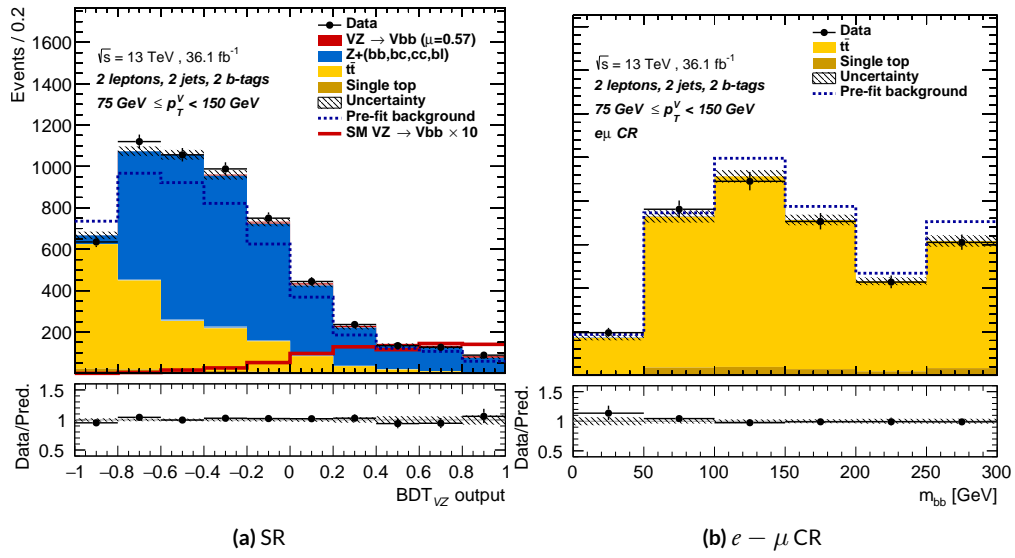


Figure 7.18: Postfit  $VZ$  plots in the 3+ jet, low pTV region for the LI variable set.

## 7.7 VH Fit Model Validation

We now move onto the fit validation distributions and numbers for the  $VH$  fit of interest.



**Figure 7.19:** Postfit  $VZ$  plots in the 2 jet, low pTV region for the LI variable set.

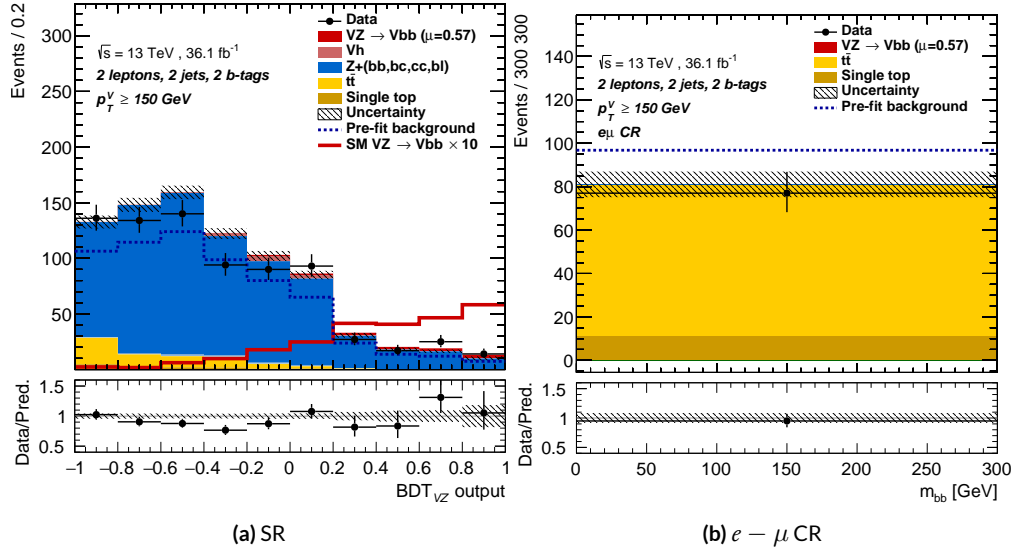


**Figure 7.20:** Postfit  $VZ$  plots in the 2 jet, high pTV region for the LI variable set.

### 7.7.1 NUISANCE PARAMETER PULLS

As can be seen in Figures 7.26–7.30, the fits for the three different variable sets are fairly similar from a NP pull perspective. Again, black is the standard variable set, red is the LI set, and blue is the RF

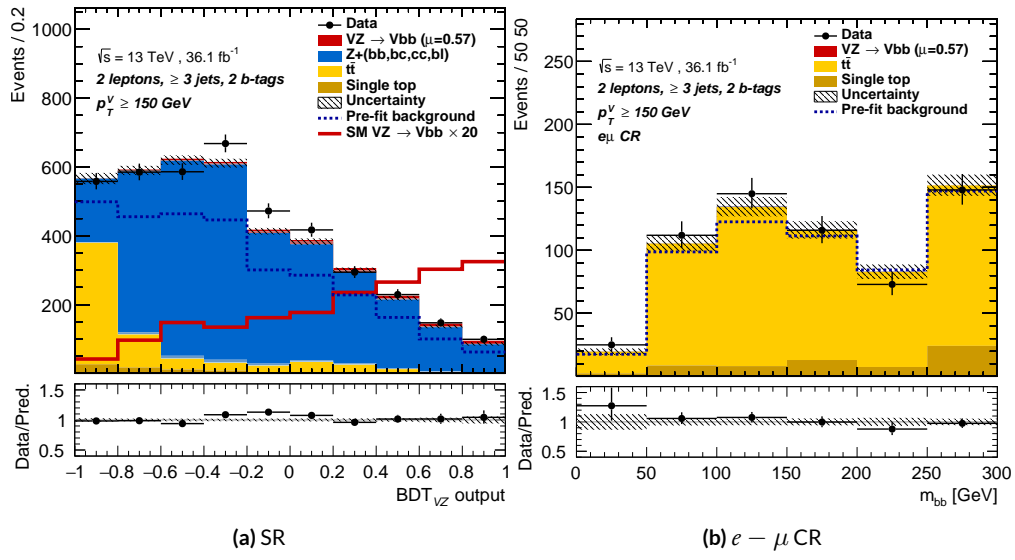


**Figure 7.21:** Postfit  $VZ$  plots in the 3+ jet, high pTV region for the LI variable set.

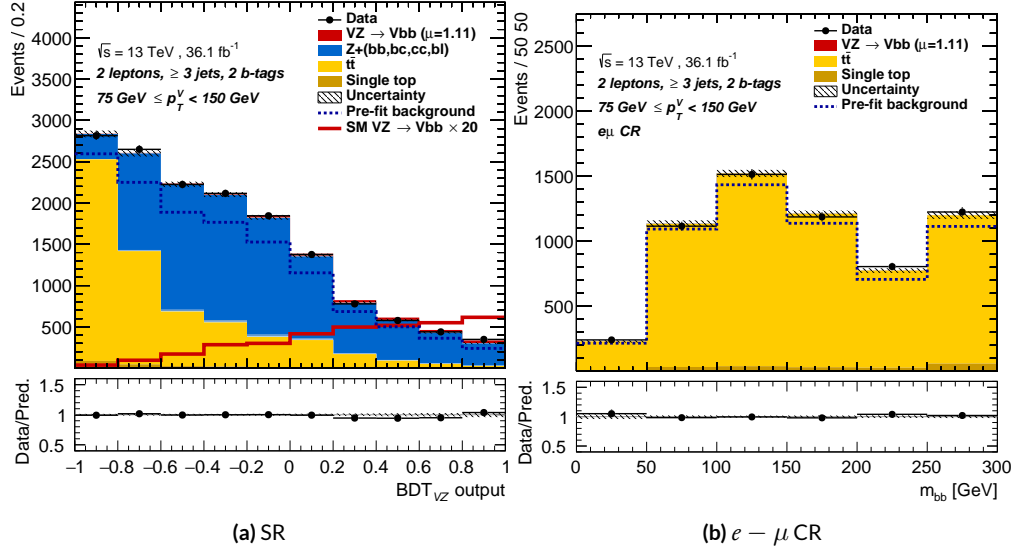


**Figure 7.22:** Postfit  $VZ$  plots in the 3+ jet, low pTV region for the standard variable set.

set. The possible exception is the signal UE+PS  $p_T^V$  systematic, which looks very different for all three cases (underconstrained for the standard, but overconstrained for the novel variable cases), though this difference goes away in the ranking plot, meaning this is almost certainly an unphysical artifice

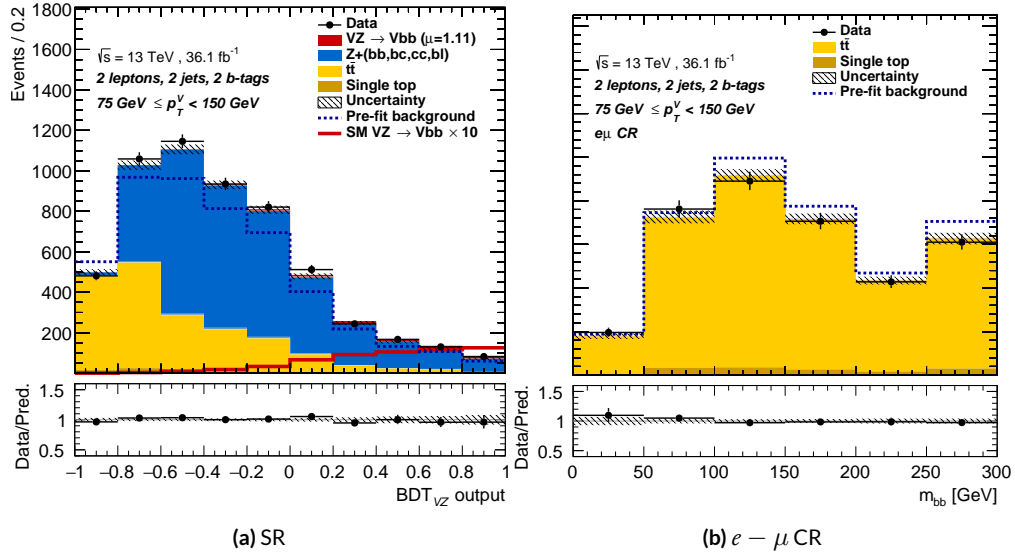


**Figure 7.23:** Postfit  $VZ$  plots in the 2 jet, low pTV region for the standard variable set.

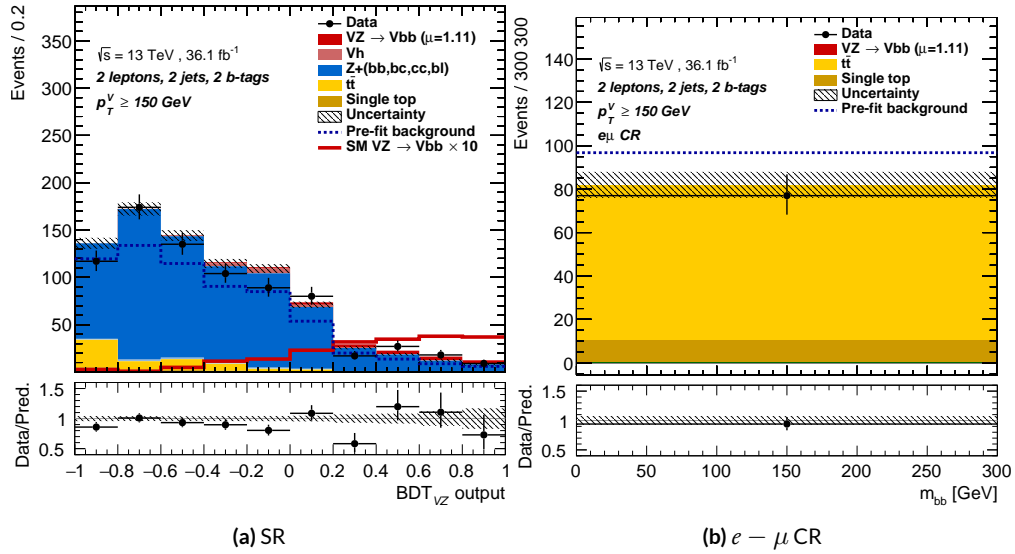


**Figure 7.24:** Postfit  $VZ$  plots in the 2 jet, high pTV region for the standard variable set.

of the faster HESSE inversion used to produce the pull comparison plots.

Nuisance parameter correlation matrices (for correlations with magnitude at least 0.25) for all

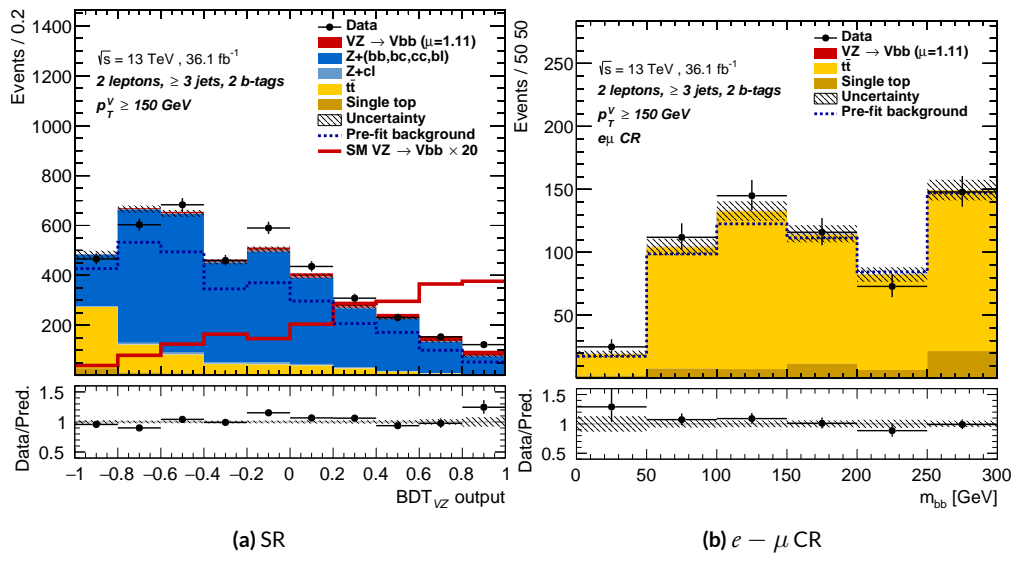


**Figure 7.25:** Postfit  $VZ$  plots in the 3+ jet, high  $p_{T^V}$  region for the standard variable set.

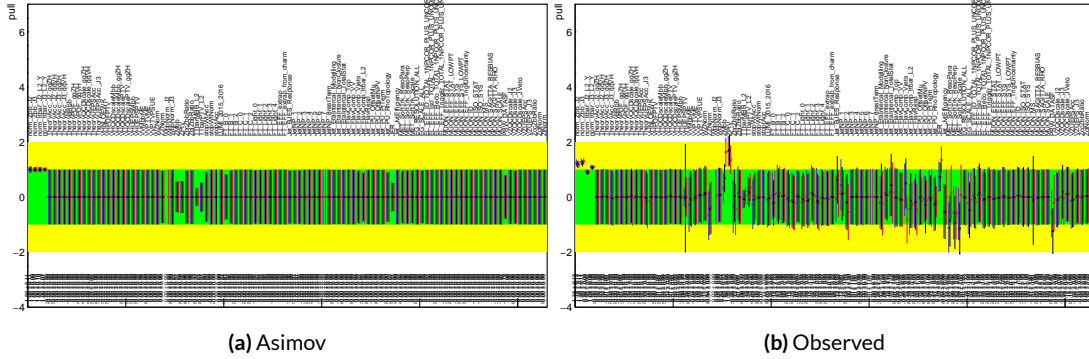


**Figure 7.26:** Pull comparison for all NP's but MC stats.

three variable set fits can be found in Figures 7.32–7.34.

### 7.7.2 FULL BREAKDOWN OF ERRORS

A postfit ranking of nuisance parameters according to their impact on  $\hat{\mu}$  for the different variable sets may be found in Figure 7.35, with rankings being fairly similar. In particular, the signal UE+PS

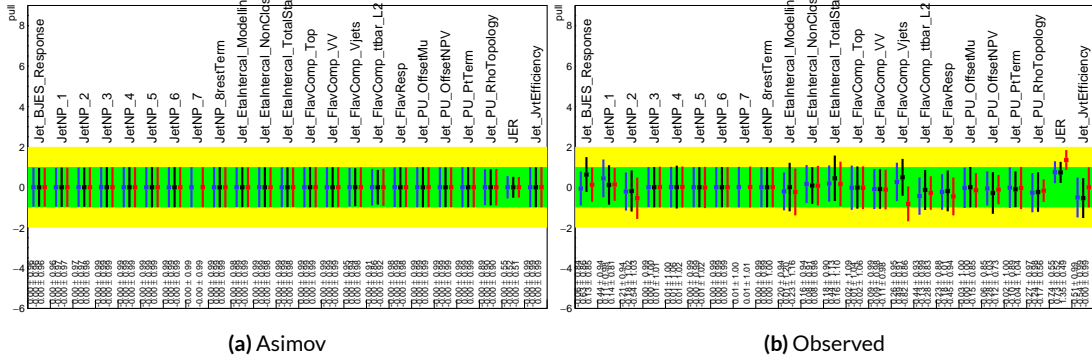


**Figure 7.27:** Pull comparison for jet NP's.

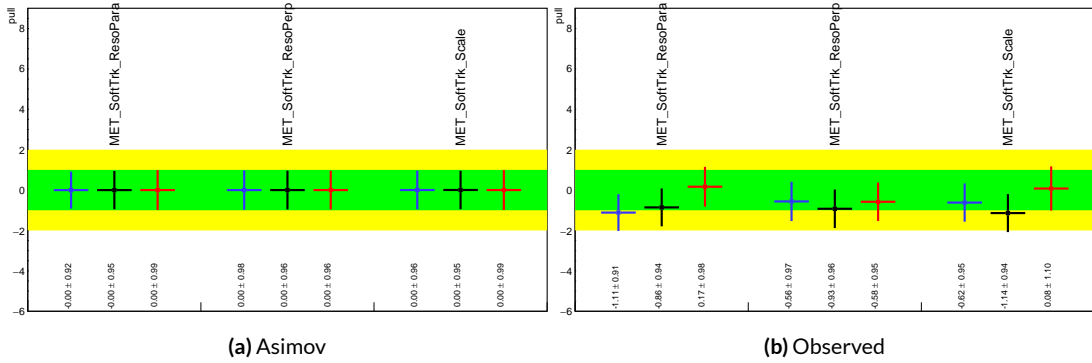


**Figure 7.28:** Pull comparison for MET NP's.

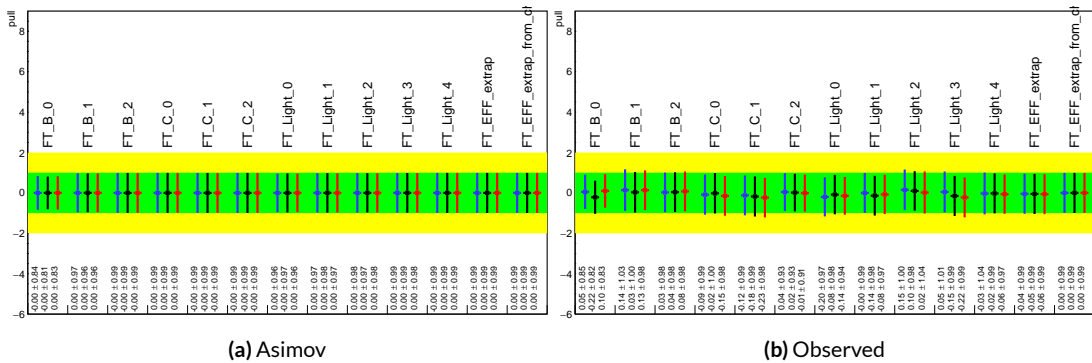


**Figure 7.29:** Pull comparison for Flavour Tagging NP's.

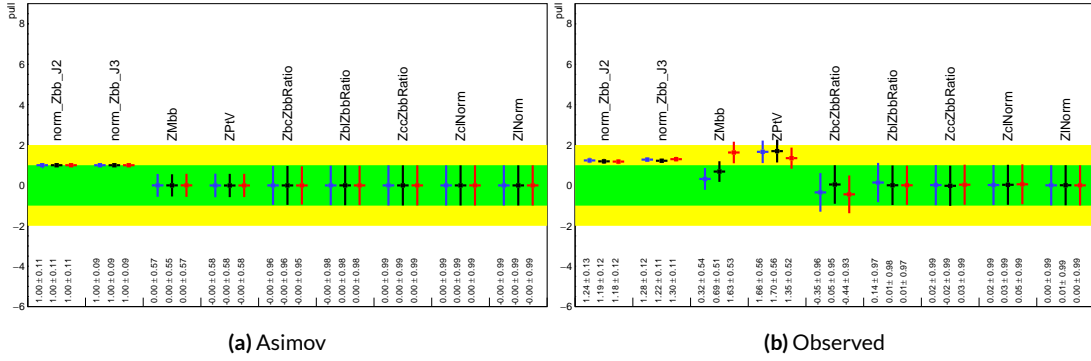


**Figure 7.30:** Pull comparison for  $Z + \text{jets}$  NP's.

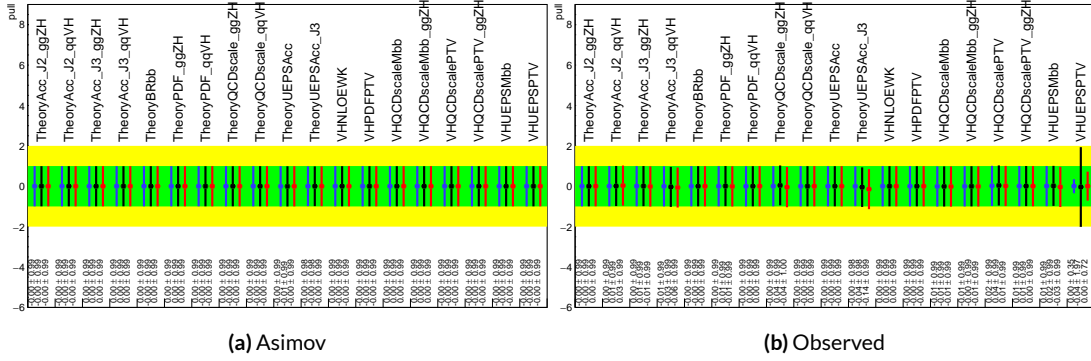


**Figure 7.31:** Pull comparison for signal process modeling NP's.

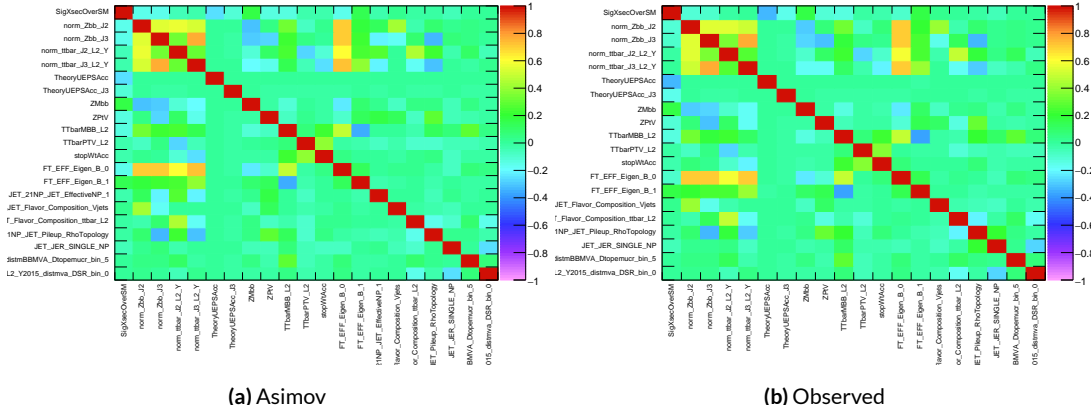


**Figure 7.32:** NP correlations for standard variable fits.

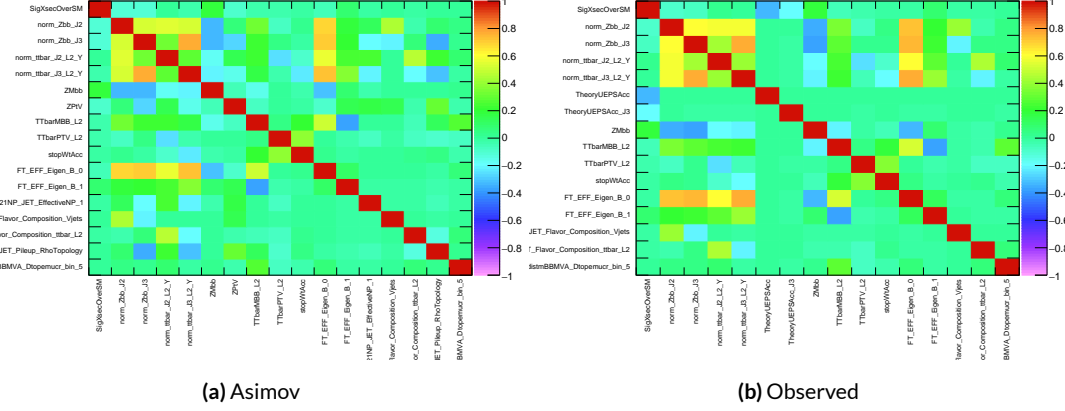


Figure 7.33: NP correlations for LI variable fits.

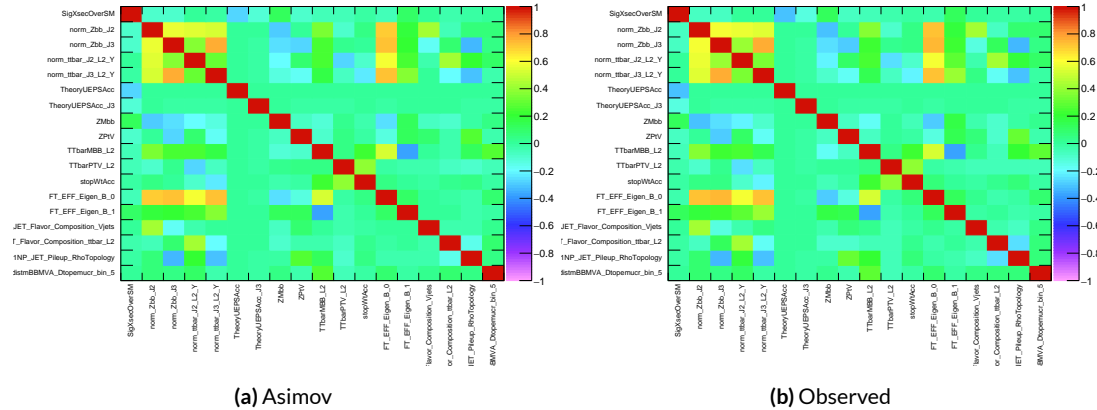
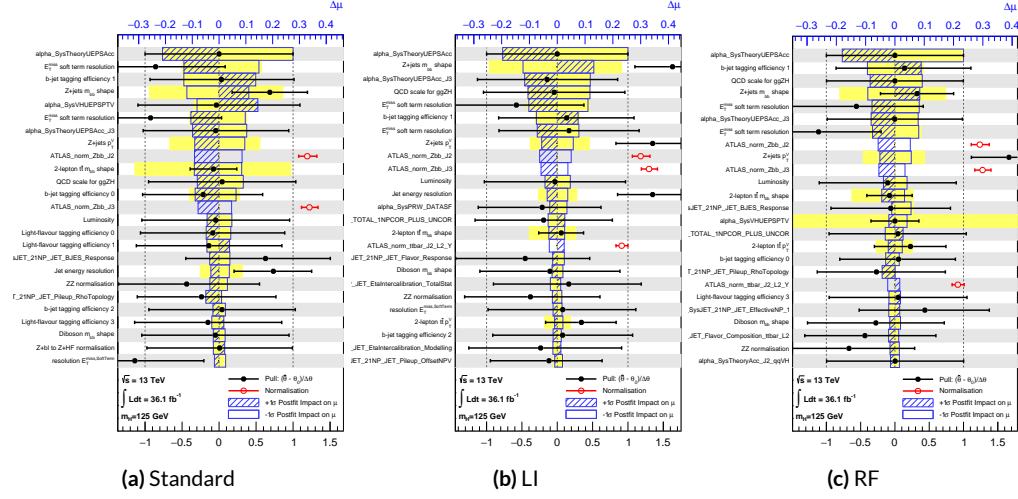


Figure 7.34: NP correlations for RF variable fits.

$p_T^V$  systematic is top-ranked for all three variable sets and also looks very similar, unlike in the pull comparison plot, reiterating the importance of evaluating individually the impact of highly ranked NP's. The  $Z+jets p_T^V$  is highly pulled in all three cases, though this is less severe for the non-standard set (it is off the scale for the standard variable ranking). The RF discriminant mitigates the effect of poorly modeled jet energy resolution better than the other sets.

The Asimov (Table 7.7) and observed (Table 7.8) breakdowns both consistently suggest that the



**Figure 7.35:** Plots for the top 25 nuisance parameters according to their postfit impact on  $\hat{\mu}$  for the standard (a), LI (b), and RF (c) variable sets.

LI variable set does a better job of constraining systematic uncertainties than the standard set and that the RF set does better still. It is also not surprising that the gain is more substantial in the observed fit than in the Asimov fits, as in the latter there are the “penalty” terms from pulls in addition to the overall broadening in the likelihood.

### 7.7.3 POSTFIT DISTRIBUTIONS AND S/B PLOTS

Postfit distributions for the MVA discriminant ( $m_{bb}$ ) distribution in the signal (top  $e - \mu$  control)

region for the standard, Lorentz Invariant, and RestFrames variable sets are found in Figures ??–??.

Here, as in the  $VZ$  fit, agreement is reasonable. In a combined fit with all three channels,  $Z+hf$  normalizations in particular would be correlated across the o- and z-lepton channels, which might help to better constrain this mismodeling (and perhaps as a result some of the  $Z+jets$  systematics as well).

**Table 7.7:** Expected error breakdowns for the standard, LI, and RF variable sets

	Std-KF	LI+MET	RF
Total	+0.608 / -0.511	+0.632 / -0.539	+0.600 / -0.494
DataStat	+0.420 / -0.401	+0.453 / -0.434	+0.424 / -0.404
FullSyst	+0.440 / -0.318	+0.441 / -0.319	+0.425 / -0.284
All normalizations	+0.128 / -0.129	+0.112 / -0.112	+0.099 / -0.092
Jets	+0.051 / -0.030	+0.044 / -0.035	+0.025 / -0.042
MET	+0.173 / -0.091	+0.140 / -0.074	+0.117 / -0.063
BTag	+0.138 / -0.136	+0.069 / -0.071	+0.076 / -0.078
BTag b	+0.125 / -0.125	+0.067 / -0.070	+0.073 / -0.075
BTag light	+0.057 / -0.051	+0.020 / -0.014	+0.009 / -0.018
Luminosity	+0.052 / -0.020	+0.050 / -0.016	+0.050 / -0.019
Diboson	+0.043 / -0.039	+0.035 / -0.031	+0.038 / -0.029
Model Zjets	+0.119 / -0.117	+0.124 / -0.127	+0.095 / -0.086
Zjets flt. norm.	+0.080 / -0.106	+0.052 / -0.092	+0.026 / -0.072
Model ttbar	+0.076 / -0.080	+0.025 / -0.035	+0.025 / -0.040
Signal Systematics	+0.262 / -0.087	+0.272 / -0.082	+0.290 / -0.088
MC stat	+0.149 / -0.136	+0.168 / -0.154	+0.153 / -0.136

One final type of plot presented as a result is the binned  $\log_{10} (S/B)$  in signal regions distributions may be found in Figure 7.46. For these plots, one fills a histogram with the  $\log_{10} (S/B)$  ratio in each postfit distribution bin weighted by the total number of events. In this case, a log plot is helpful because the highest bins would be invisible on a linear plot. These distributions are allegedly useful for seeing where most of one's sensitivity lies. Practically, it is problematic if the pull (from the null hypothesis) is higher at lower  $S/B$  values, which may indicate a poorly optimized discriminant.

**Table 7.8:** Observed signal strengths, and error breakdowns for the standard, LI, and RF variable sets

	Std-KF	LI+MET	RF
$\hat{\mu}$	1.7458	1.6467	1.5019
Total	+0.811 / -0.662	+0.778 / -0.641	+0.731 / -0.612
DataStat	+0.502 / -0.484	+0.507 / -0.489	+0.500 / -0.481
FullSyst	+0.637 / -0.451	+0.591 / -0.415	+0.533 / -0.378
All normalizations	+0.158 / -0.147	+0.130 / -0.119	+0.112 / -0.110
Jets	+0.071 / -0.059	+0.065 / -0.047	+0.036 / -0.051
MET	+0.209 / -0.130	+0.190 / -0.102	+0.152 / -0.077
BTag	+0.162 / -0.166	+0.093 / -0.070	+0.115 / -0.099
BTag b	+0.142 / -0.147	+0.090 / -0.066	+0.110 / -0.094
BTag light	+0.074 / -0.072	+0.025 / -0.022	+0.031 / -0.029
Luminosity	+0.079 / -0.039	+0.073 / -0.034	+0.069 / -0.032
Model Zjets	+0.164 / -0.152	+0.141 / -0.143	+0.101 / -0.105
Zjets flt. norm.	+0.070 / -0.109	+0.041 / -0.086	+0.033 / -0.083
Model ttbar	+0.067 / -0.102	+0.029 / -0.040	+0.040 / -0.048
Signal Systematics	+0.434 / -0.183	+0.418 / -0.190	+0.364 / -0.152
MC stat	+0.226 / -0.201	+0.221 / -0.200	+0.212 / -0.189

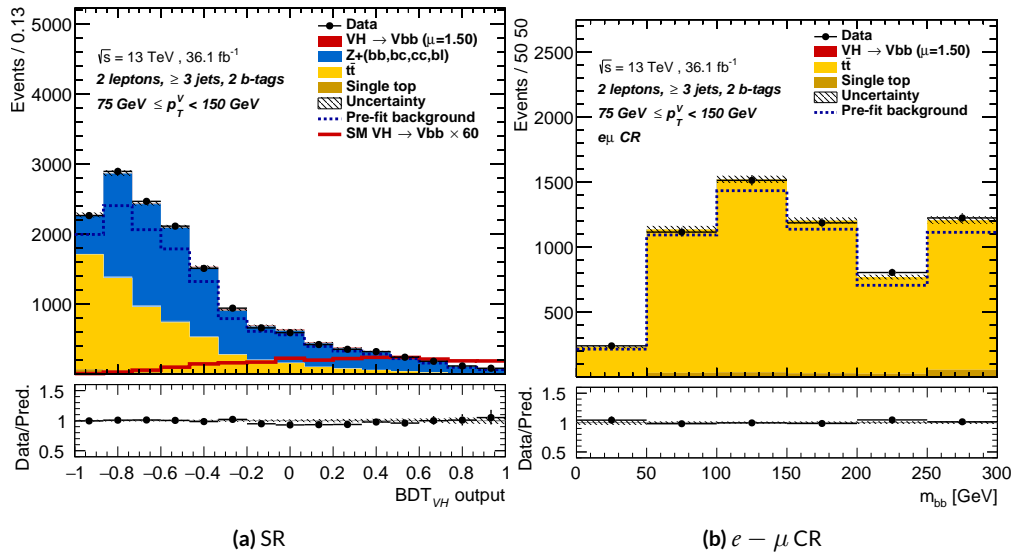


**Figure 7.36:** Postfit  $VH$  plots in the 3+ jet, low pTV region for the RF variable set.

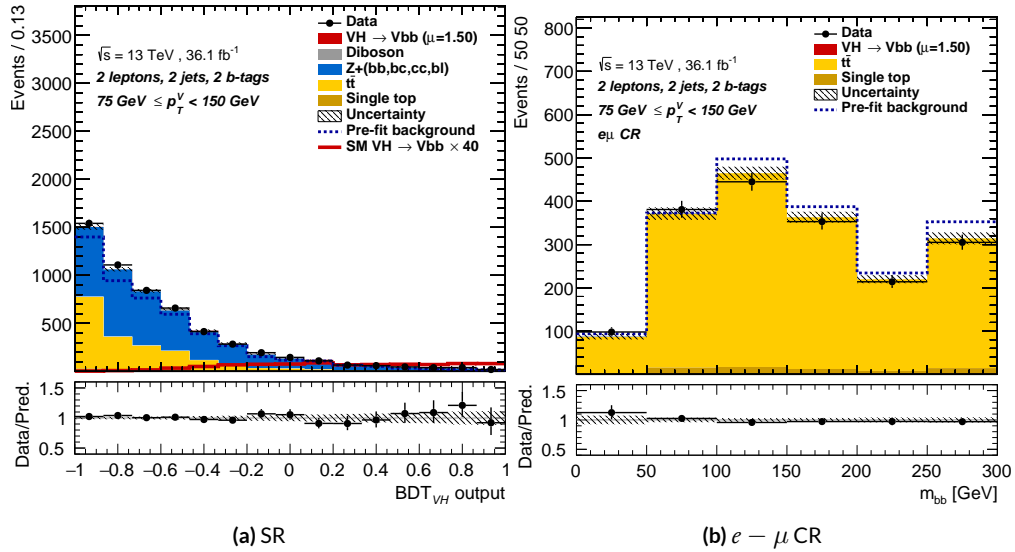


Figure 7.37: Postfit  $VH$  plots in the 2 jet, low pTV region for the RF variable set.

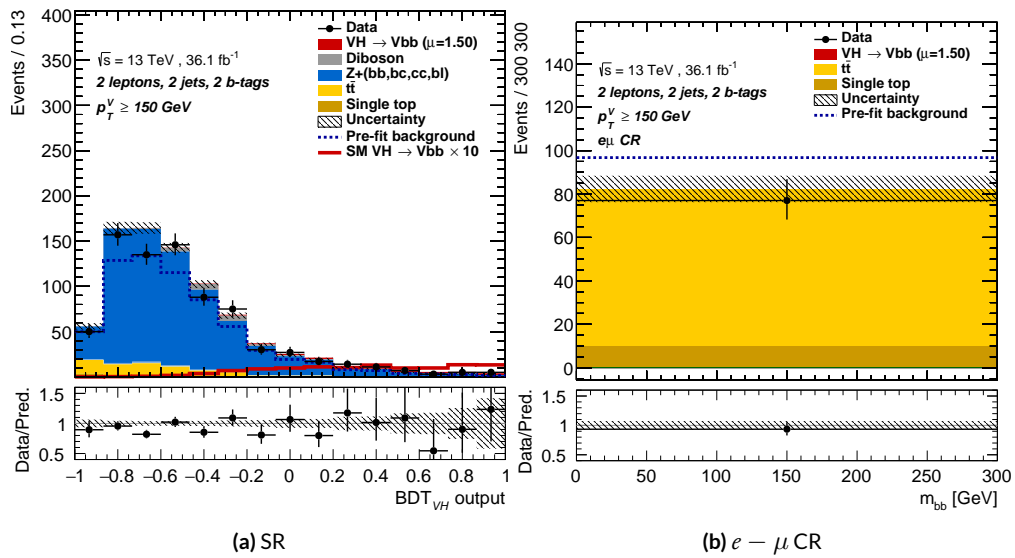
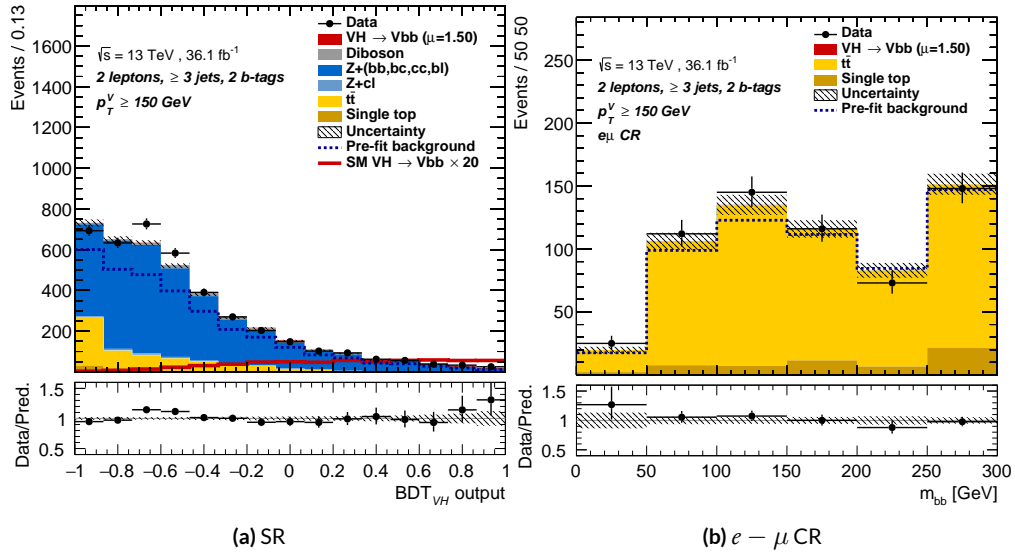
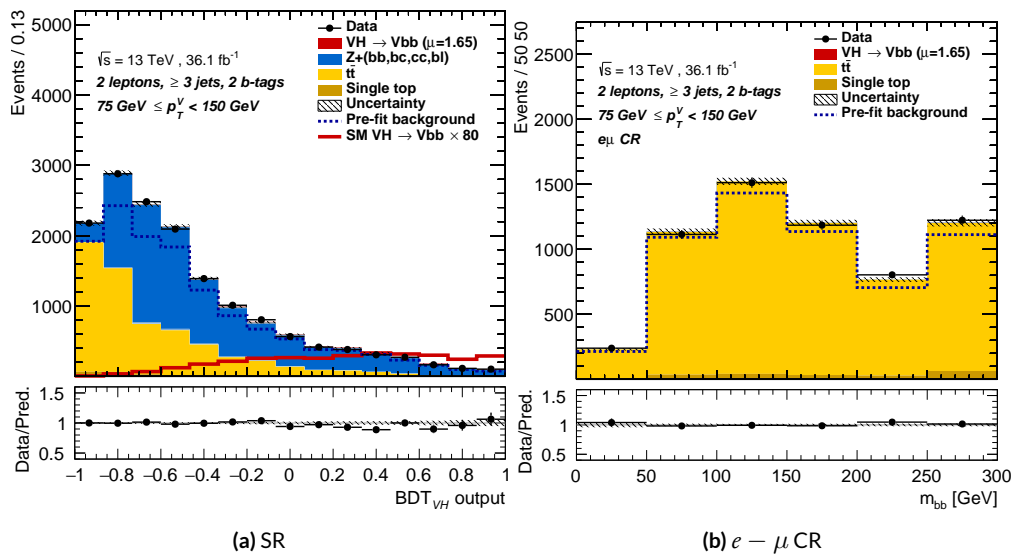


Figure 7.38: Postfit  $VH$  plots in the 2 jet, high pTV region for the RF variable set.



**Figure 7.39:** Postfit  $VH$  plots in the 3+ jet, high pTV region for the RF variable set.



**Figure 7.40:** Postfit  $VH$  plots in the 3+ jet, low pTV region for the LI variable set.

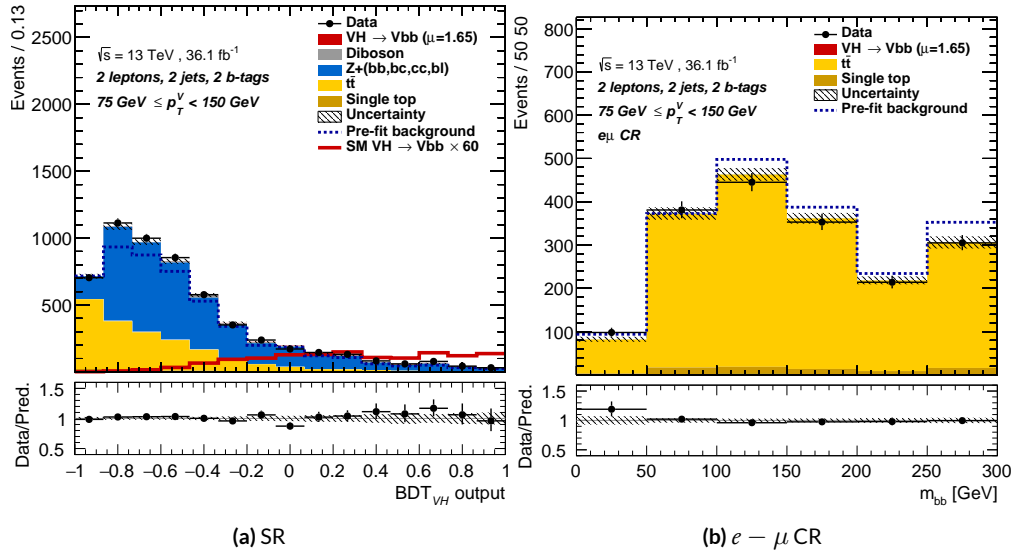


**Figure 7.41:** Postfit  $VH$  plots in the 2 jet, low pTV region for the LI variable set.

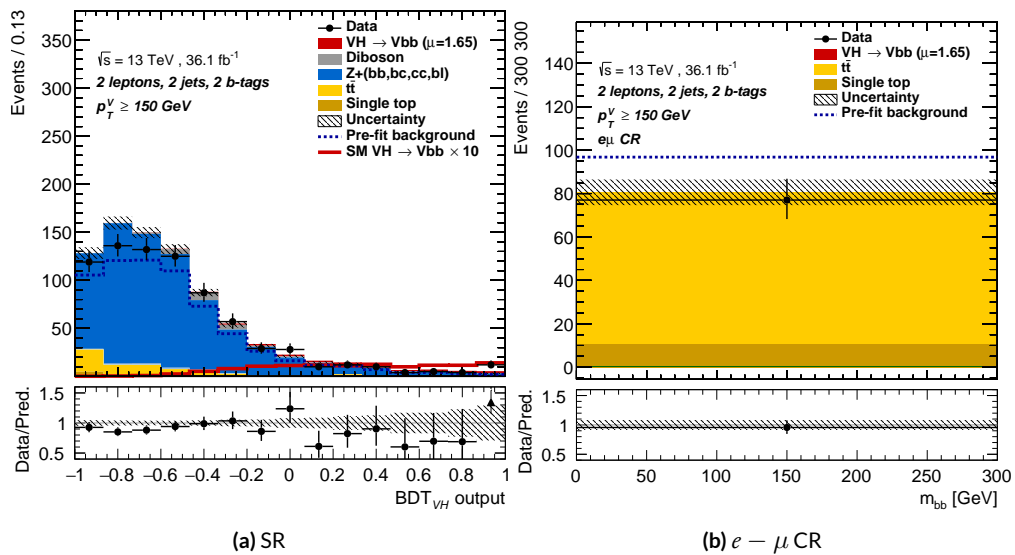


**Figure 7.42:** Postfit  $VH$  plots in the 2 jet, high pTV region for the LI variable set.

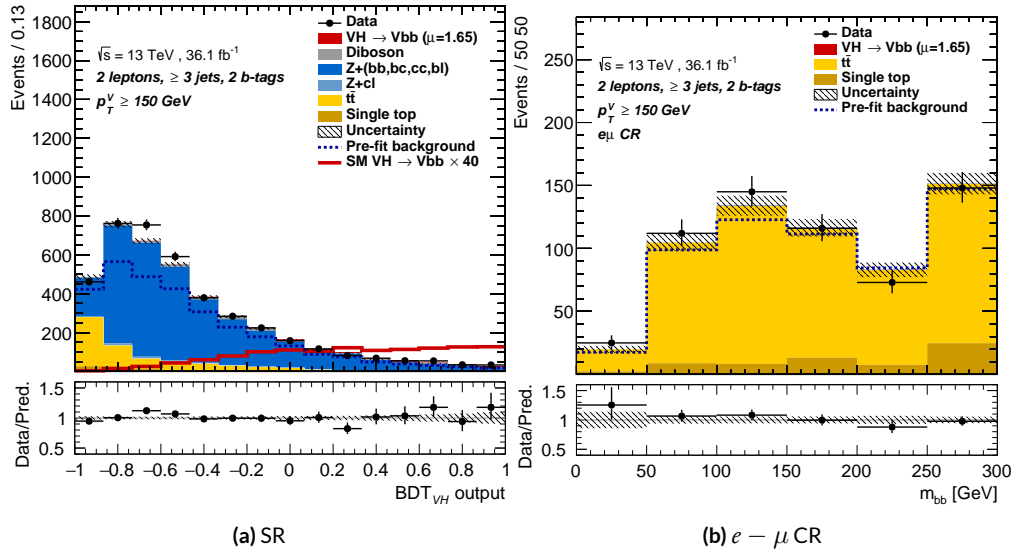


Figure 7.43: Postfit  $VH$  plots in the 3+ jet, high pTV region for the LI variable set.

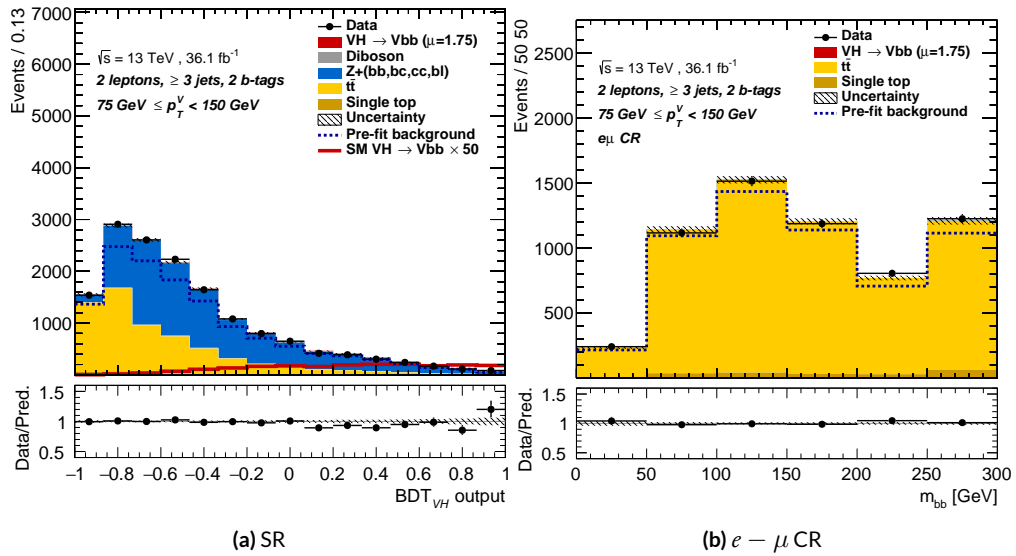
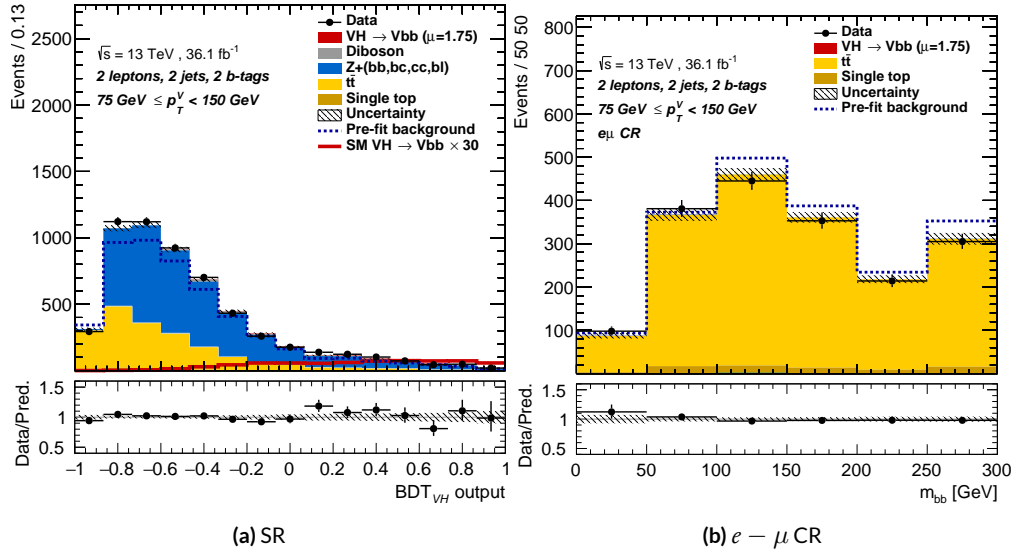
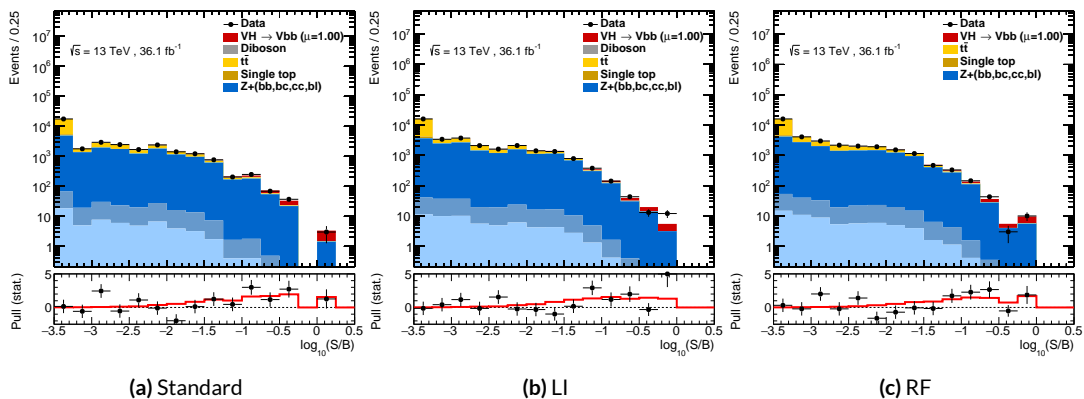


Figure 7.44: Postfit  $VH$  plots in the 3+ jet, low pTV region for the standard variable set.



**Figure 7.45:** Postfit  $VH$  plots in the 2 jet, low pTV region for the standard variable set.



**Figure 7.46:** Binned S/B plots for the standard (a), LI (b), and RF (c) variable sets. Signal is weighted to  $\mu = 1$  for comparison to the SM prediction.

*Kein Operationsplan reicht mit einiger Sicherheit  
über das erste Zusammentreffen mit der feindlichen  
Hauptmacht hinaus.*

Helmuth von Moltke

# 8

## Fit Results

THE RESULTS IN THIS CHAPTER were first reported in [60] and describe how the three different fit models detailed and validated Chapter 7, corresponding to the standard, RF, and LI variable sets described in Chapter 6 perform on actual  $VH$  fits. In particular sensitivities, nuisance parameter impacts, and signal strengths on expected fits to Asimov datasets and both expected and observed

fits on the actual  $36.1 \text{ fb}^{-1}$  dataset are compared.

Expected and observed sensitivities for the different variable sets may be found in Table 8.1. The RF fits feature the highest expected sensitivities, outperforming the standard set by 3.5% and 3.4% for fits to Asimov and observed datasets, respectively. The LI variable has a lower significance than both for expected fits to both Asimov and data with a 6.7% (1.7%) significance than the standard set for the Asimov (observed) dataset. While the fit using standard variables does have a higher observed significance than both the LI and RF fits, by 2.8% and 8.6%, respectively, these numbers should be viewed in the context of the best fit  $\hat{\mu}$  values, discussed below. That is, the standard set may yield the highest sensitivity for this particular dataset, but this is not necessarily (and likely is not) the case for any given dataset.

**Table 8.1:** Expected (for both data and Asimov) and observed significances for the standard, LI, and RF variable sets.

	Standard	LI	RF
Expected (Asimov)	2.06	1.92	2.13
Expected (data)	1.76	1.73	1.80
Observed (data)	2.87	2.79	2.62

A summary of fitted signal strengths and errors for both the Asimov (a) and observed (b) datasets are shown in Figure 8.1.\* A summary of error breakdowns is given in Tables 8.2 (Asimov) and 8.3 (observed) for total error, data statistics contributions, total systematic error contributions, and categories for which the total impact is  $\geq 0.1$  for the standard fit. As is to be expected for both the Asimov and observed dataset fits, the contribution to the total error on  $\mu$  arising from data statistics

---

\*For reference, the standalone 2-lepton fit from the fiducial analysis is  $2.11^{+0.50}_{-0.48}(\text{stat.})^{+0.64}_{-0.47}(\text{syst.})$

is nearly identical, since each set of fits uses the same selections and data.<sup>†</sup>

**Table 8.2:** Summary of error impacts on total  $\mu$  error for principal categories in the Asimov standard, LI, and RF fits.

	Std-KF	LI+MET	RF
Total	+0.608 / -0.511	+0.632 / -0.539	+0.600 / -0.494
DataStat	+0.420 / -0.401	+0.453 / -0.434	+0.424 / -0.404
FullSyst	+0.440 / -0.318	+0.441 / -0.319	+0.425 / -0.284
Signal Systematics	+0.262 / -0.087	+0.272 / -0.082	+0.290 / -0.088
MET	+0.173 / -0.091	+0.140 / -0.074	+0.117 / -0.063
Flavor Tagging	+0.138 / -0.136	+0.069 / -0.071	+0.076 / -0.078
Model Zjets	+0.119 / -0.117	+0.124 / -0.127	+0.095 / -0.086

**Table 8.3:** Summary of error impacts on total  $\hat{\mu}$  error for principal categories in the observed standard, LI, and RF fits.

	Std-KF	LI+MET	RF
Total	+0.811 / -0.662	+0.778 / -0.641	+0.731 / -0.612
DataStat	+0.502 / -0.484	+0.507 / -0.489	+0.500 / -0.481
FullSyst	+0.637 / -0.451	+0.591 / -0.415	+0.533 / -0.378
Signal Systematics	+0.434 / -0.183	+0.418 / -0.190	+0.364 / -0.152
MET	+0.209 / -0.130	+0.190 / -0.102	+0.152 / -0.077
Flavor Tagging	+0.162 / -0.166	+0.093 / -0.070	+0.115 / -0.099
Model Zjets	+0.164 / -0.152	+0.141 / -0.143	+0.101 / -0.105

The contribution from systematic uncertainties, however, does vary considerably across the variable sets. The Asimov fits are a best case scenario in the sense that, by construction, all NP's are equal to their predicted values (and so no "penalty" is paid for pulls on Gaussian NP's). The systematics error from the LI fit is slightly higher (subpercent) than that from the standard fit, and 4.6% higher er-

<sup>†</sup>Though not exactly identical. Since the BDT's are different for the different variable sets, the binning (as determined by transformation D) and bin contents in each set are generally different, leading to slightly different data statistics errors.

ror overall due to differences in data stats. The RF Asimov fit, however, has a 6.5% lower total error from systematics than the standard Asimov fit (and a 2.2% lower error overall). Moreover, for both the LI and RF sets, errors are markedly smaller for the MET and Flavor Tagging categories, with the RF fit also featuring a smaller errors on  $Z$ +jets modeling; the only notable exception to this trend in Asimov fits are the signal systematics.

These trends are more pronounced in the observed fits. As can be seen in Table 8.3, both the LI and RF fits have smaller errors from systematic uncertainties, both overall and in all principal categories, with the LI and RF fits having 7.5% (3.7%) and 16% (8.8%) lower systematics (total) error on  $\hat{\mu}$ , respectively.

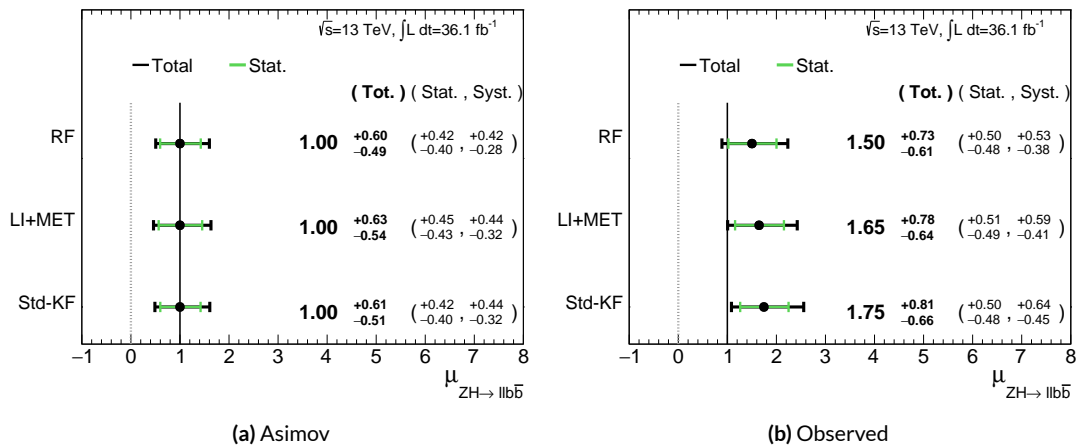


**Figure 8.1:**  $\mu$  summary plots for the standard, LI, and RF variable sets. The Asimov case (with  $\mu = 1$  by construction) is in (a), and  $\hat{\mu}$  best fit values and error summary are in (b).

Studying the performance of the Lorentz Invariant and RestFrames variable sets at both a data statistics only context and with the full fit model in the  $ZH \rightarrow \ell\ell b\bar{b}$  channel of the  $VH (b\bar{b})$  analysis suggests that these variables may offer a potential method for better constraining systematic un-

certainties in  $VH(b\bar{b})$  searches as more orthogonal bases in describing the information in collision events.

The marginally worse performance of the LI and RF variables (7.9% and 6.9%, respectively) with respect to the standard variable at a stats only level illustrates that neither variable set has greater intrinsic descriptive power in the absence of systematics in this closed final state. Hence, any gains from either of these variable sets in a full fit come from improved treatment of systematic uncertainties.

With full systematics, the LI variable set narrows the sensitivity gap somewhat, with lower significances by 6.7% (1.7%) on expected fits to Asimov (data) and by 2.8% on observed significances. The RF variable set outperforms the standard set in expected fits with 3.5% (3.4%) higher significance on Asimov (data), but has an 8.6% lower observed significance, though the observed significances should be viewed in the context of observed  $\hat{\mu}$  values.

Moreover, the LI and RF variable sets generally perform better in the context of the error on  $\mu$ . The LI fit is comparable to the standard set on Asimov data and has a 7.5% lower total systematics error on  $\hat{\mu}$  on observed data, while the RF fit is lower in both cases, with systematics error being 6.5% (16%) lower on Asimov (observed) data.

These figures of merit suggest that both the LI and RF variables are more orthogonal than the standard variable set used in the fiducial analysis. Moreover, the RF variable set does seem to consistently perform better than the LI set. Furthermore, both variable sets have straightforward extensions to the other lepton channels in the  $VH(b\bar{b})$  analysis. The magnitude of any gain from the more sophisticated treatment of  $E_T^{miss}$  in these extensions is beyond the scope of these studies, but

the performance in this closed final state do suggest that there is some value to be had in these non-standard descriptions independent of these considerations.

*If I have seen further, it is by standing on ye shoulders of  
giants.*

Isaac Newton

# 9

## Measurement Combinations

WHILE THE DISCUSSION thus far has focused on improvements looking towards future in just the  $ZH \rightarrow \ell\ell b\bar{b}$  channel, any actual result for SM  $VH(b\bar{b})$  combines all channels and all available datasets. Using additional channels at a given center of mass energy is straightforward since the fit model is designed with this combination in mind. This will be described in the context of the 36.1

$\text{fb}^{-1}$  13 TeV result in Section 9.1.

Combining dataset results (known as “workspaces”) from different center of mass energies is not so simple an exercise since both the underlying physics (and its associated modeling) and the treatment of key experimental considerations, like flavor tagging, and their associated systematics change from dataset to dataset. A combined fit model must take these considerations into account, and the formulation of the fit model combining the Run 1 ( $\sqrt{s} = 7$  TeV with  $4.7 \text{ fb}^{-1}$  of data, and  $\sqrt{s} = 8$  TeV with  $20.3 \text{ fb}^{-1}$  of data) and Run 2 ( $\sqrt{s} = 13$  TeV with  $36.1 \text{ fb}^{-1}$ ) SM  $VH(b\bar{b})$  results is the topic of Section 9.2. Its results, as reported in [13], are given in 9.3.

## 9.1 LEPTON CHANNEL COMBINATIONS

Preparation of results for the 0- and 1-lepton channels is functionally very similar to above discussions in Chapters 4, 5, 6, and 7. From a modeling standpoint, each channel comes in with different dominating background processes and dedicated simulation, described at length in [24], though there is a lot of overlap. In particular,  $t\bar{t}$ , , and diboson production is important for all three channels. The only important process not discussed here is contribution from multijet background, which is a small but important background in the 1-lepton case.

With respect to object definitions, no new objects are defined in the 0- and 1-lepton analyses, though the treatment of  $\vec{E}_T^{\text{miss}}$  is of greater concern in these channels, as  $\vec{E}_T^{\text{miss}}$  is a part of the signal final states in these channels. Triggers and event selection requirements are optimized by channel. A full list of requirements is given in Tables 9.1–9.3 from [14].

The mechanics of MVA training and implementation is very much the same across analysis chan-

**Table 9.1:** Summary of common signal event selections and the 2-lepton analysis.

Common Selections	
Jets	$\geq 2$ central jets
$b$ -jets	$2 b$ -tagged signal jets
Leading jet $p_T$	$> 45 \text{ GeV}$
$ \Delta R(\text{jet1}, \text{jet2}) $ (cut-based only)	$\leq 1.8 (p_T^V < 200 \text{ GeV}), \leq 1.2 (p_T^V > 200 \text{ GeV})$
2 Lepton	
Trigger	un-prescaled single lepton Tables 5 and 6 of Ref. [10]
Leptons	2 VH-loose leptons ( $\geq 1$ ZH-signal lepton) Same flavor, opposite-charge for $\mu\mu$
$m_{\ell\ell}$	$81 < m_{\ell\ell} < 101 \text{ GeV}$
$\vec{E}_T^{\text{miss}}$ significance (cut-based)	$\vec{E}_T^{\text{miss}}/\sqrt{H_T} < 3.5\sqrt{\text{GeV}}$
$p_T^V$ regions (BDT)	$[75, 150], [150, \infty] \text{ GeV}$
$p_T^V$ regions (cut-based)	$[75, 150], [150, 200], [200, \infty] \text{ GeV}$

**Table 9.2:** Summary of event selections in the 0-lepton analyses.

0 Lepton	
Trigger	HLT_xe70, xe90_mht, and xe110_mht
Leptons	o VH-loose lepton
$\vec{E}_T^{\text{miss}}$	$> 150 \text{ GeV}$
$S_T$	$> 120$ (2 jets), $> 150$ GeV (3 jets)
$ \min \Delta\phi(\vec{E}_T^{\text{miss}}, \text{jet}) $	$> 20^\circ$ (2jet), $> 30^\circ$ (3jet)
$ \Delta\phi(\vec{E}_T^{\text{miss}}, b) $	$> 120^\circ$
$ \Delta\phi(\text{jet1}, \text{jet2}) $	$< 140^\circ$
$ \Delta\phi(\vec{E}_T^{\text{miss}}, E_{T, \text{trk}}^{\text{miss}}) $	$< 90^\circ$
$p_T^V$ regions (BDT)	$> 150 \text{ GeV}$
$p_T^V$ regions (cut-based)	$[150, 200] \text{ GeV}, [200, \infty] \text{ GeV}$

**Table 9.3:** Summary of event selections in the 1-lepton analyses.

1 Lepton	
Trigger	$e$ channel: un-prescaled single electron Tables 5 and 6 of Ref. [10] $\mu$ channel: see 0-lepton triggers
Leptons	1 WH-signal lepton $> 1$ VH-loose lepton veto
$\vec{E}_T^{\text{miss}}$	$> 30$ GeV ( $e$ channel)
$m_{top}$	$< 225$ GeV or $m_{bb} > 75$ GeV
$m_T^W$ (cut-based only)	$< 120$ GeV
$p_T^V$ regions (BDT)	$> 150$ GeV
$p_T^V$ regions (cut-based)	$[150, 200]$ GeV, $[200, \infty]$ GeV

nels, with the major difference being the selection of input variables to the BDT discriminants. For a discussion of how the different final states affect variable selection see the discussion in Section 1.7 and in particular Table for the input variables used in the final analysis.

As previously mentioned, the fit model is flexible enough to seamlessly integrate combined results for the three separate lepton channels for a given dataset. Most nuisance parameters are treated as common across all fit regions. Some regions will have greater bearing on certain nuisance parameters—2-lepton regions, virtually free of  $W$ +jets events, will have virtually no effect on  $W$ +jets modeling systematics, for example. One notable exception are NP’s with `_L[012]` suffixes, which are predominantly the double ratio systematics discussed in Section 4.2.2 and function similar to the 2 vs. greater than 3 jet event double ratio systematics.

Adding different channels has great potential to constrain certain systematic uncertainties. Looking at the breakdown of systematic uncertainties in 2-lepton fits in Table 7.8, for example, multijet

and  $W$ +jets NP's contribute virtually no uncertainty, while  $\vec{E}_T^{\text{miss}}$  and  $Z$ +jets have very high impacts on the uncertainty on  $\hat{\mu}$ . 1-lepton events will bring up the multijet and  $W$ +jets uncertainties (and justify their inclusion in the combined fit model; their inclusion in the 2-lepton fit is for portability and a sanity check). Since the 2-lepton final state is by construction  $\vec{E}_T^{\text{miss}}$  free, it is not surprising that uncertainty due to  $\vec{E}_T^{\text{miss}}$  is high. Single channel standalone fits are never final results in this analysis, so the result relies on the other channels to better and more accurately constrain this uncertainty since these other final states do have  $\vec{E}_T^{\text{miss}}$  in their final states and are the channels for which the  $\vec{E}_T^{\text{miss}}$  treatment in the analysis has been optimized. Furthermore, something like  $Z$ +hf modeling is difficult to do given how constrained the analysis signal region is. Combining the information in the 0- and 2-lepton results (and introducing double ratio NP's to recognize that these channels do have important differences) also helps to constrain this difficult systematic uncertainty.

Once the fit inputs in each channel have been prepared and validated, a combined workspace can be directly constructed using the combined fit model. Significances are given in Table 9.4, and  $\hat{\mu}$  summaries for 2 and 3 POI fits are given in Figure 9.1. This combined workspace with observed signal strength of  $1.20^{+0.24}_{-0.23}(\text{stat.})^{+0.34}_{-0.28}(\text{syst.})$  is the Run 2 input for the Run 1 + Run 2 combination discussed below.

**Table 9.4:** Observed significance from an unconditional fit to the data corresponding to  $36.1 \text{ fb}^{-1}$  and expected significances from a fit to an Asimov dataset and from a fit to the data. Expected significances from individual regions are estimated separately.

Channel	Exp. sig. (Asimov)	Exp. sig. (data)	Obs. sig.
o-lepton (SR)	1.99	1.73	0.53
1-lepton (SR+CR)	1.81	1.81	2.30
2-lepton (SR+CR)	1.95	1.86	3.55
o,1,2-lepton (SR+CR)	3.19	3.03	3.54

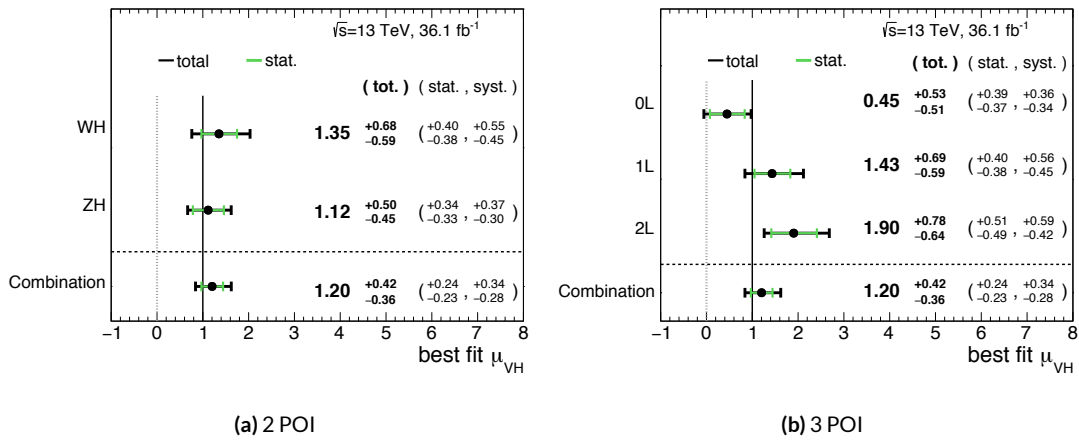


**Figure 9.1:** Run 2 signal strength summary plots for 2 (WH/ZH, (a)) and 3 (0, 1, and 2 lepton, (b)) POI fits.

## 9.2 THE COMBINED FIT MODEL

It is clear the signal strength parameter of interest should be fully correlated among the different datasets. Some signal modeling systematics were left unchanged from Run 1 through Run 2 and/or were designed to be explicitly correlated. Beyond these two special cases, it is not immediately clear what level of correlation should be imposed. The general methodology for settling upon a correlation scheme is as follows:

1. Identify which NP categories have significant impacts on  $\mu$
2. Of these NP's, identify which have one-to-one correspondences or established correlation schemes among  $\sqrt{s}$  values
3. Test whether correlation has a sizable impact on expected fit quantities

The only two sizable experimental NP categories are jet energy scale (JES) and flavor tagging systematics. Correlation schemes of varying degrees of completeness exist for these categories, so explicit NP correlations can be tested for these two categories. As these studies were conducted before unblinding, “sizable impact” was judged by comparing fit results (sensitivities, pull comparisons, and breakdowns) on combined workspaces using the unblinded and public  $\mu = 0.51$  result for Run 1 and Asimov data for the Run 2 result. These are treated in Sections 9.2.1 and 9.2.2. Modeling systematics require a slightly different treatment, and are explored in 9.2.3.

As noted in Chapter 7 when looking at pull comparison plots for combined workspaces, the error bars in these plots are calculated using a simultaneous HESSE matrix inversion, which can fail to give sensible values for high dimensional models (the combined workspaces have well over 500 NP's). This is not true of the nuisance parameter ranking plots, which use a MINOS based approach to test

the effect of each NP individually. This is much slower but much more rigorous, which is why only ranking plots appear outside of supporting material and pull comparisons are considered “diagnostic” plots.

### 9.2.1 JET ENERGY SCALE SYSTEMATICS

Fortunately for the case of jet energy scale systematics, the JetEtMiss group provides two recommended “strong” and “weak” correlation schemes between Run 1 and Run 2. These were used as a point of departure for the JES combination correlation scheme. However, the JES NP’s in both the Run 1 and Run 2 workspaces are a reduced set of NP’s, with some 56 (75) NP’s reduced to 6 (8) for Run 1 (2). In order to restore the full set of JES NP’s, the effective NP’s in each workspace are unfolded using maps detailing the linear combinations of unfolded NP’s that form the effective NP’s.

The linear combinations used to unfold the effective JES NP’s were calculated as follows:

$$NP_{i,eff} = \frac{\sum_j A_{ij} |NP_{j,unf}| NP_{j,unf}}{\sqrt{\sum_j A_{ij}^2 |NP_{j,unf}|^2}} \quad (9.1)$$

where *eff* and *unf* are for effective and unfolded NP’s, respectively, the  $A_{ij}$ ’s are scalar coefficients taken from raw maps, and  $|NP_{j,unf}|$  are the amplitudes of the unfolded NP’s. The raw  $A_{ij}$  and scaled maps for Run 1 and Run 2 may be found in Figure 9.2

Unfolding was found to have very little effect on both expected sensitivities and errors, as can be seen in Tables 9.5– 9.8.

It was also found that fit sensitivities and breakdowns were similarly indifferent to the use of ei-

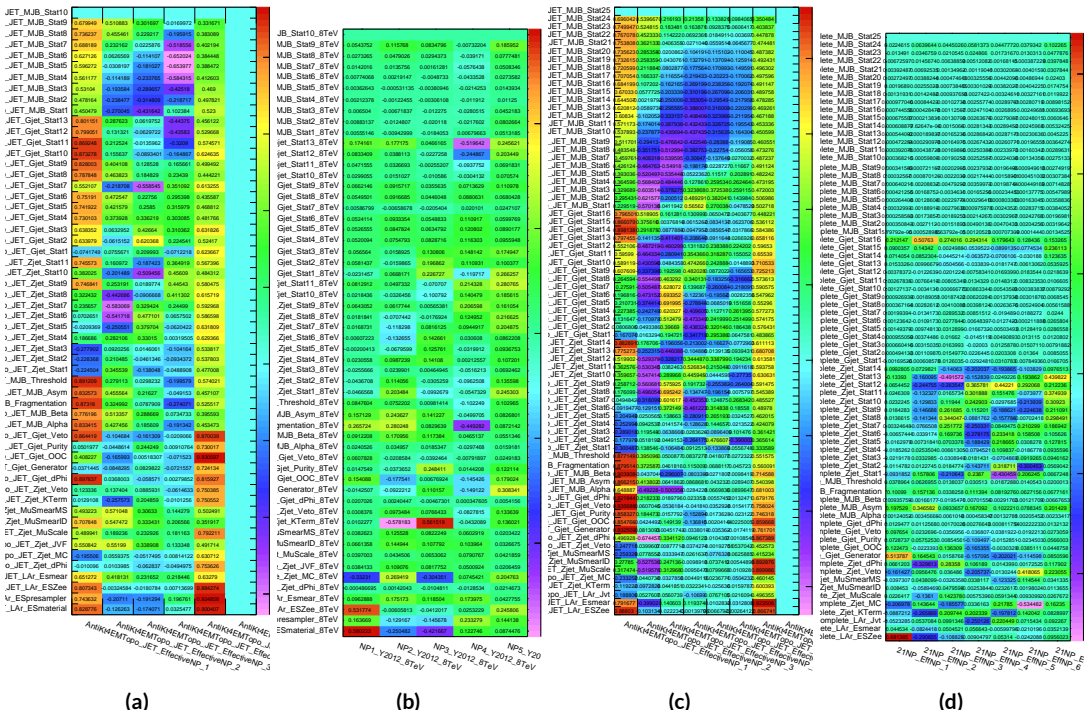


**Table 9.5:** Expected and observed sensitivities for Run 1, Run 2, and combined workspaces with effective and unfolded JES NP's.

	R <sub>1</sub> Unf	R <sub>1</sub> Eff	R <sub>2</sub> Unf	R <sub>2</sub> Eff	Comb Unf	Comb Eff
Exp. Sig.	2.604	2.606	3.014	3.014	4.005	3.998
Obs. Sig.	1.369	1.374	3.53	3.53	3.581	3.571
Exp. Limit	0.76 <sup>+0.30</sup> <sub>-0.21</sub>	0.76 <sup>+0.30</sup> <sub>-0.21</sub>	0.73 <sup>+0.29</sup> <sub>-0.21</sub>	0.73 <sup>+0.29</sup> <sub>-0.21</sub>	0.51 <sup>+0.20</sup> <sub>-0.14</sub>	0.51 <sup>+0.20</sup> <sub>-0.14</sub>
Obs. Limit	1.21	1.21	1.94	1.94	1.36	1.37

**Table 9.6:** Error on signal strength breakdowns for Run 1 workspaces with effective and unfolded JES NP's.

	R <sub>1</sub> Unfold	R <sub>1</sub> Eff
$ \Delta\hat{\mu} $		0.0018
$\hat{\mu}$	0.5064	0.5082
Total	+0.400 / -0.373	+0.401 / -0.373
DataStat	+0.312 / -0.301	+0.312 / -0.301
FullSyst	+0.250 / -0.220	+0.251 / -0.220
Jets	+0.060 / -0.051	+0.060 / -0.052
BTag	+0.094 / -0.079	+0.095 / -0.079

**Table 9.7:** Error on signal strength breakdowns for Run 2 workspaces with effective and unfolded JES NP's.

	R <sub>2</sub> Unfold	R <sub>2</sub> Eff
$ \Delta\hat{\mu} $		0.0
$\hat{\mu}$	1.2051	1.2052
Total	+0.421 / -0.366	+0.421 / -0.366
DataStat	+0.239 / -0.234	+0.239 / -0.234
FullSyst	+0.346 / -0.282	+0.346 / -0.282
Jets	+0.066 / -0.047	+0.066 / -0.047
BTag	+0.119 / -0.106	+0.119 / -0.106

**Table 9.8:** Error on signal strength breakdowns for combined workspaces with effective and unfolded JES NP's.

	Comb Unfold	Comb Eff
$ \Delta\hat{\mu} $		0.0006
$\hat{\mu}$	0.8992	0.8985
Total	+0.278 / -0.261	+0.278 / -0.261
DataStat	+0.185 / -0.181	+0.185 / -0.181
FullSyst	+0.208 / -0.187	+0.208 / -0.188
Jets	+0.040 / -0.044	+0.041 / -0.036
BTag	+0.076 / -0.076	+0.077 / -0.076

ther the strong or weak JES correlation schemes, as shown in Tables 9.9 and 9.10.

**Table 9.9:** Expected sensitivities for both effective and unfolded combined workspaces using the strong and weak JES correlation schemes.

	JES Weak Unfold	JES Weak Eff	JES Strong Unfold	JES Strong Eff
Exp. Sig.	3.57	3.57	3.59	3.59
Exp. Limit	$0.493^{+0.193}_{-0.138}$	$0.494^{+0.193}_{-0.138}$	$0.493^{+0.193}_{-0.138}$	$0.493^{+0.193}_{-0.138}$

**Table 9.10:** Error on signal strength breakdowns for both effective and unfolded combined workspaces using the strong and weak JES correlation schemes.

	Comb Unfold	Comb Eff	Strong Unfold	Strong Eff
$\Delta\hat{\mu}$	0.0009		0.0025	
Total	+0.269 -0.254	+0.27 -0.255	+0.27 -0.255	+0.27 -0.255
DataStat	+0.181 -0.177	+0.181 -0.177	+0.181 -0.177	+0.181 -0.178
FullSyst	+0.199 -0.183	+0.2 -0.183	+0.2 -0.183	+0.201 -0.183
Jets	+0.0387 -0.032	+0.041 -0.0337	+0.0425 -0.0329	+0.0432 -0.0338
BTag	+0.0975 -0.0933	+0.098 -0.0936	+0.0979 -0.0935	+0.098 -0.0936

Comparisons of top ranked nuisance parameters in Figures 9.3–9.5 and for the complete JES pull comparisons in Figures 9.6–9.9 also show very little difference with respect to correlation scheme (except obviously for the number of JES NP’s). Constrained pulls in pull comparisons should once again be taken as a shortcoming of **HESSE** and not the fit model.

As a result of these studies, the weak JES correlation scheme with uncorrelated effective JES NP’s (i.e. just the  $b$ -jet energy scale NP) has been chosen as the treatment of JES in the Run 1 + Run 2 combined fit.

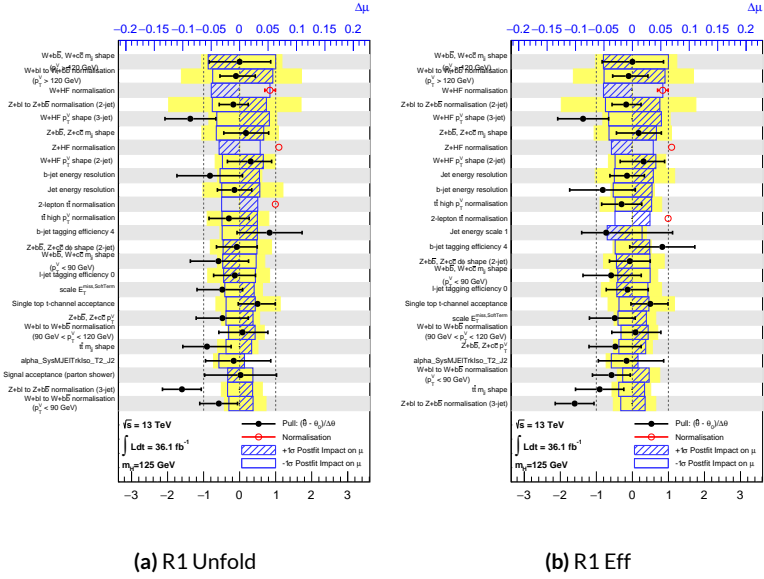


**Figure 9.3:** Ranks for the effective and unfolded JES NP Run1 combined workspaces.

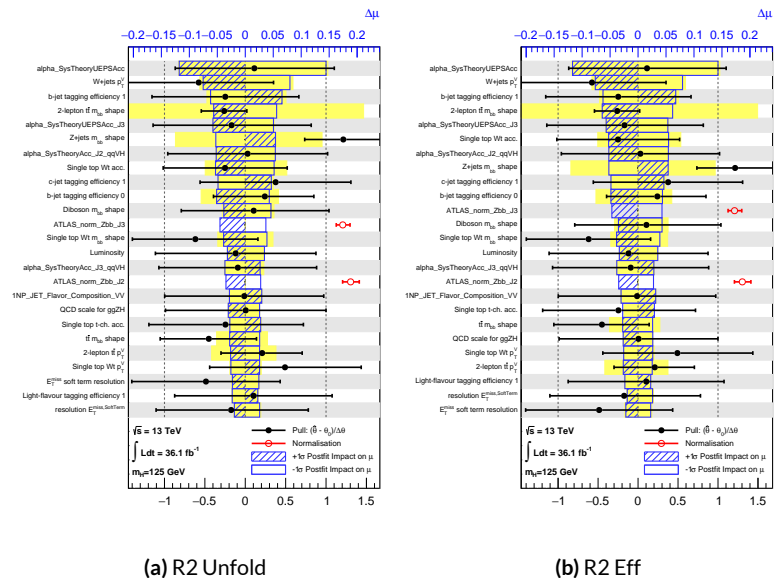


**Figure 9.4:** Ranks for the effective and unfolded JES NP Run2 combined workspaces.

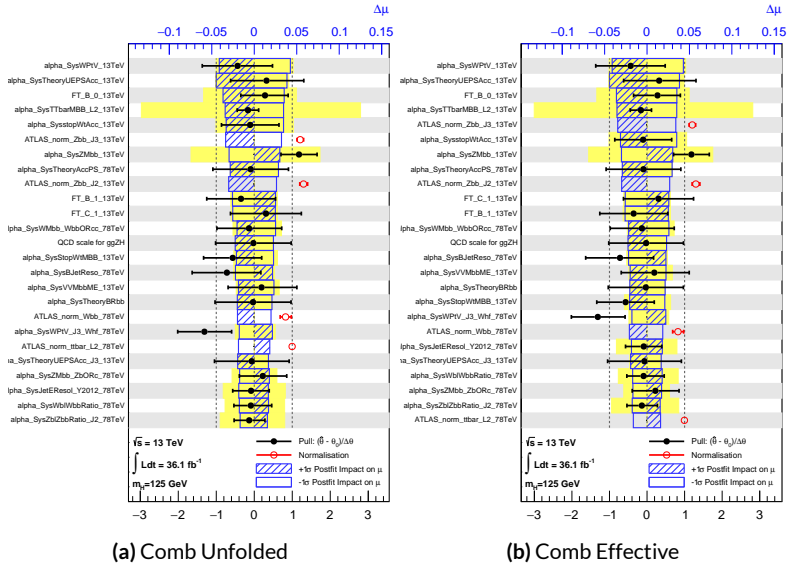


Figure 9.5: Ranks for the effective and unfolded JES NP Run1+Run2 combined workspaces.

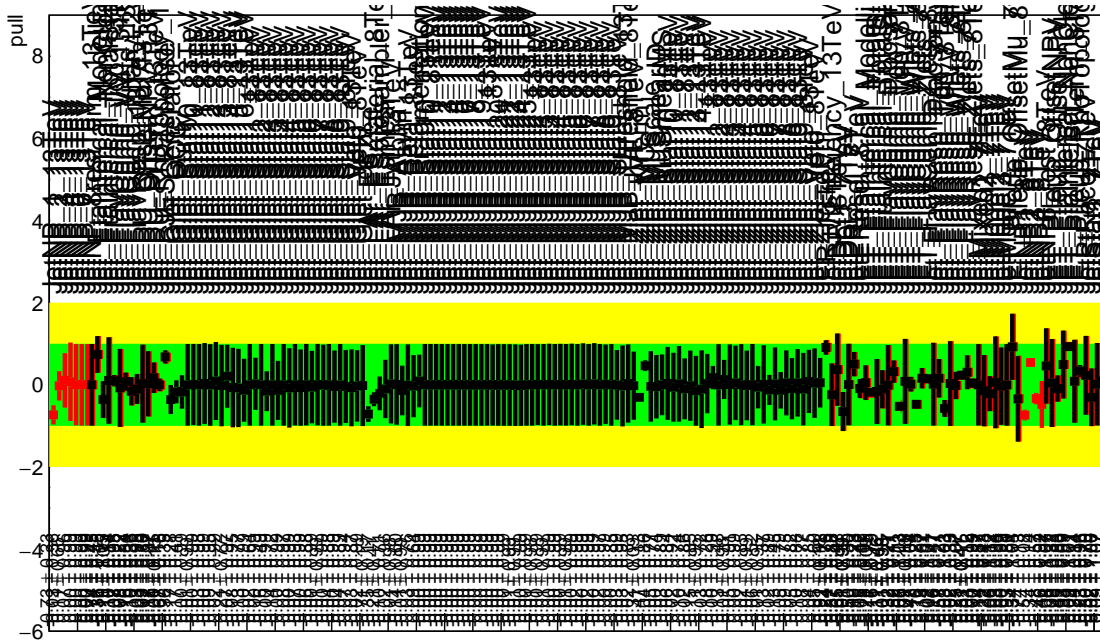


Figure 9.6: Pull Comparisons: jesu---Jet Comb Unfold, Comb Eff, Strong Unfold, Strong Eff

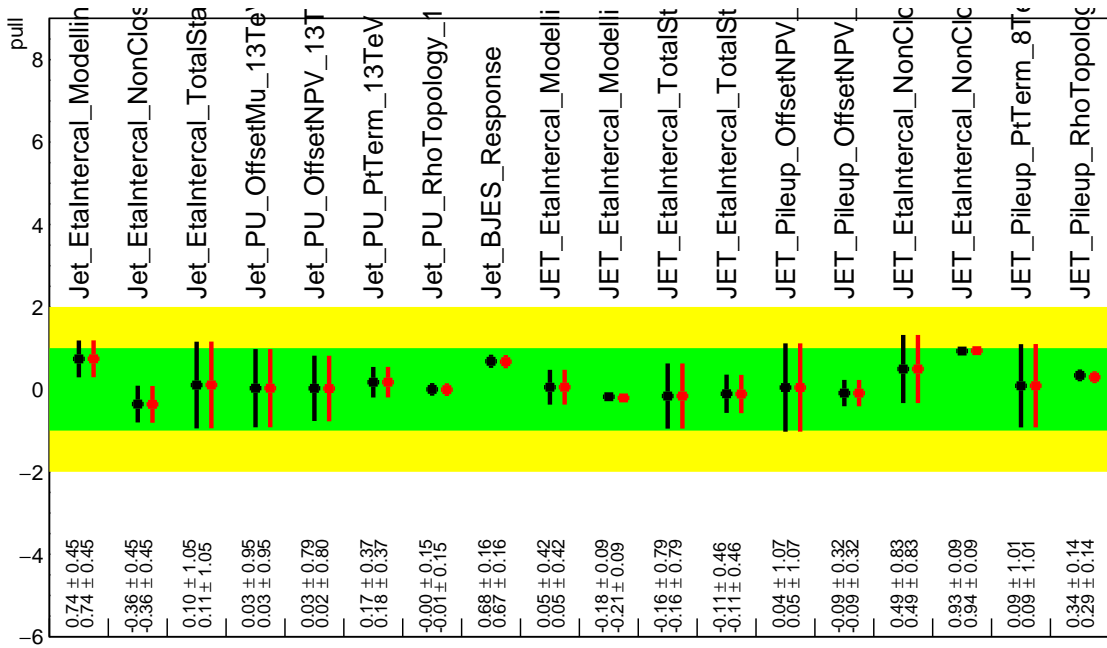


Figure 9.7: Pull Comparisons: jesu---JetMatched Comb Unfold, **Comb Eff**, **Strong Unfold**, **Strong Eff**

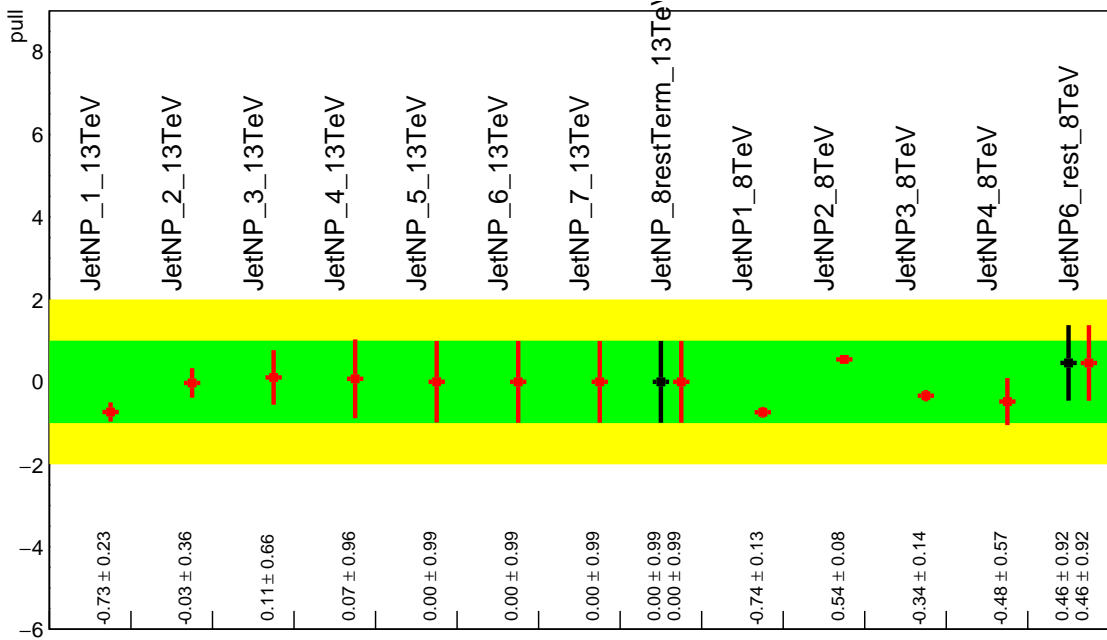
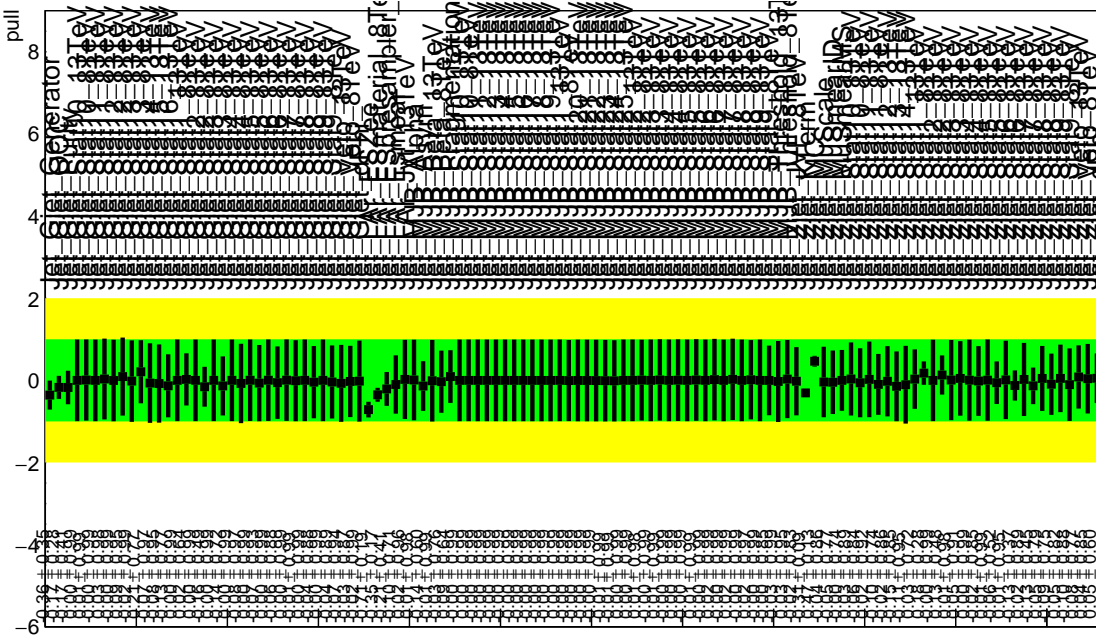


Figure 9.8: Pull Comparisons: jesu---JetEff Comb Unfold, **Comb Eff**, **Strong Unfold**, **Strong Eff**



**Figure 9.9:** Pull Comparisons: jesu---JetUnfold Comb Unfold, **Comb Eff**, Strong Unfold, **Strong Eff**

### 9.2.2 FLAVOR TAGGING

Unfortunately, the ATLAS Flavor Tagging group did not provide any recommendations for correlating Run 1 and Run 2 NP's, though given the high ranking of these NP's in the Run 2, result, performing at least some studies was deemed crucial. Nevertheless, great improvements and changes to the treatment of flavor tagging between Run 1 and Run 2 does weaken the argument for any strong flavor tagging correlation scheme.

Given that  $c$ -tagging changed significantly between Run 1 and Run 2 and that light tagging NP's are very lowly ranked, these sets of NP's are left uncorrelated. Moreover, the change in the physical meaning of the effective  $b$ -tagging NP's means a full correlation of such NP's (insomuch as they exist in each result) is one of limited utility. Hence, it was decided to leave flavor tagging NP's uncorre-

lated. However, since the meaning of the leading  $b$ -tagging NP's is approximately constant across years and since Run 2  $b$ -tagging NP's are very highly ranked in both the Run 2 only and combined fits, tests correlating these NP's were conducted, the results of which can be seen below. It should be noted that the leading B NP at 8 TeV, `SysBTagB0Effic_Y2012_8TeV`, has an opposite effect on  $t\bar{t}$  normalization than the 7 and 13 TeV NP's, and so must be flipped using a similar strategy as for JES unfolding. Initial studies of flavor tagging correlations did not flip this NP, and so results for this scheme (labeled “Bo 8TeV Not Flipped”) have also been included for comparison.

**Table 9.11:** Expected and observed sensitivities for a combination featuring the weak JES scheme, combination with the weak JES scheme + leading  $b$  NP's correlated, and the  $b$  correlation with the 8 TeV NP with sign unflipped.

	Comb Eff	BTag Bo	Bo 8TeV Not Flipped
Exp. Sig.	3.998	4.127	3.921
Obs. Sig.	3.571	3.859	3.418
Exp. Limit	$0.51^{+0.2}_{-0.143}$	$0.5^{+0.196}_{-0.14}$	$0.517^{+0.202}_{-0.144}$
Obs. Limit	1.37	1.41	1.35

**Table 9.12:** Run 1 + Run 2 W+jets modeling correlation projections

	Comb Eff	BTag Bo	Bo 8TeV Not Flipped
$ \Delta\hat{\mu} $	—	0.0446	0.0268
$\hat{\mu}$	0.8985	0.9431	0.8717
Total	+0.278 / -0.261	+0.275 / -0.256	+0.282 / -0.263
DataStat	+0.185 / -0.181	+0.180 / -0.177	+0.189 / -0.186
FullSyst	+0.208 / -0.188	+0.207 / -0.186	+0.209 / -0.186
BTag	+0.077 / -0.076	+0.071 / -0.068	+0.079 / -0.075
BTag b	+0.062 / -0.059	+0.055 / -0.049	+0.064 / -0.060

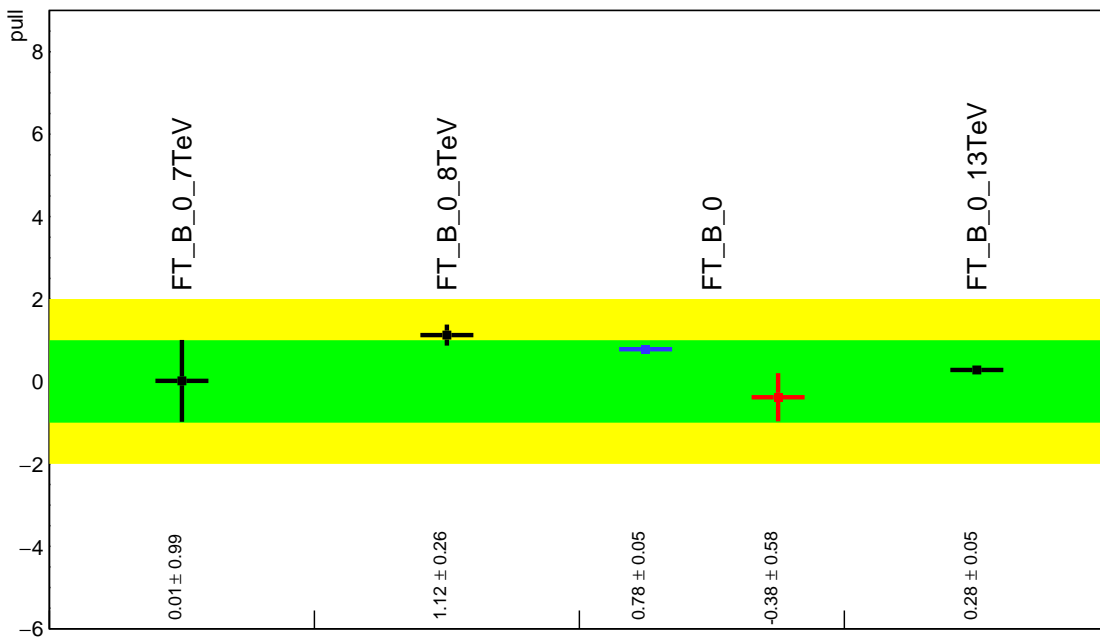


Figure 9.10: Pull Comparisons: btag-b---BTagB0 Comb Eff, BTag BO

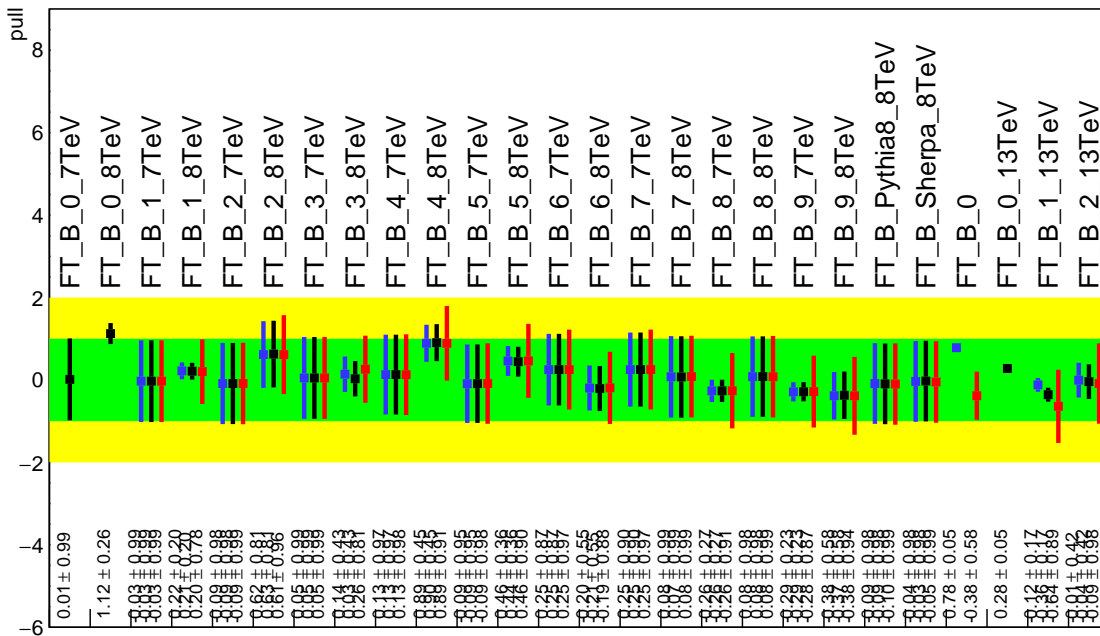
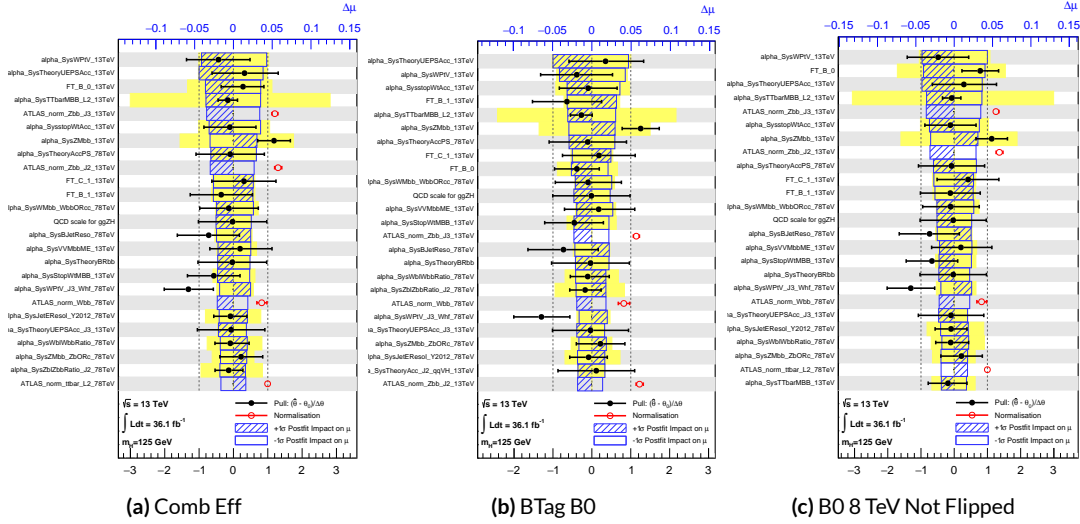


Figure 9.11: Pull Comparisons: btag-b---BTagB Comb Eff, BTag BO



**Figure 9.12:** NP rankings for a combination featuring the weak JES scheme and a combination with the weak JES scheme + leading  $b$  NP's correlated.

It is clear from these results that correlating the leading effective Eigen NP associated with  $b$ 's can have a noticeable effect on final fit results and that the 8 TeV Bo NP is the most important component of a combined Bo NP. It is also not so surprising that the 8 TeV result should drive the combined nuisance parameter since it is the only result to make use of both pseudocontinuous tagging-based and  $b$ -tag regions into the final fit, implicitly yielding much more information about  $b$ 's. The 13 TeV fit has neither of these regions. What is less clear is whether there are sufficient grounds for implementing this correlation (i.e. does the correspondence of these NP's across years warrant a full correlation). While there are no current plans to do so, this matter warrants careful scrutiny if Run 1 is to be combined with future results.

### 9.2.3 MODELING SYSTEMATICS

Another principal systematic category is modeling uncertainties. The effect of correlating groups of systematics was estimated using the same strategy employed by the ATLAS/CMS SM  $VH$  ( $b\bar{b}$ ) combination for Run 1. This extrapolation can be used to estimate the impact of correlations on the estimated signal strength, the total error on the signal strength, and the  $\chi^2$  of the result. The impact of such correlations is no more than a few percent effect, as the following tables demonstrate, beginning with the category with the greatest shift, W+jets modeling, in Table 9.13.

**Table 9.13:**  $\chi^2$  extrapolation correlation tests for W+jets modeling and various levels of assumed correlation between Run 1 and Run 2.

	$ \Delta\mu $	$\sigma$	$ \Delta\sigma $	$\chi^2$
$\rho=-1$	0.0024	0.2448	0.011 (4.3%)	0.95
$\rho=-0.6$	0.0015	0.2493	0.00654 (2.55%)	0.9804
$\rho=-0.3$	0.0008	0.2526	0.00325 (1.27%)	1.0045
$\rho=0$	—	0.2558	—	1.0298
$\rho=0.3$	0.0008	0.259	0.0032 (1.25%)	1.0564
$\rho=0.6$	0.0017	0.2622	0.00636 (2.49%)	1.0844
$\rho=1$	0.0029	0.2664	0.0105 (4.11%)	1.1242

### 9.2.4 FINAL CORRELATION SCHEME

The final Run 1 + Run 2 correlation scheme is shown in Table 9.14. As detailed above, neither JES nor modeling systematics had any demonstrable effect on combined fit results. Hence, only signal NP's and the  $b$ -jet energy scale are correlated (the weak JES scheme without unfolding). While the effect of flavor tagging correlations is less clear, the result physical arguments for correlation are less

strong; the size of effect was discovered rather late in the analysis process; and no nuisance parameter unfolding maps exist for flavor tagging as they do for JES, so it was decided to leave these uncorrelated as well.

**Table 9.14:** The final Run 1+Run 2 NP correlation scheme.

$7\text{ TeV NP}$	$8\text{ TeV NP}$	$13\text{ TeV NP}$
	ATLAS_BR_bb	SysTheoryBRbb
	SysTheoryQCDscale_ggZH	SysTheoryQCDscale_ggZH
	SysTheoryQCDscale_qqVH	SysTheoryQCDscale_qqVH
—	SysTheoryPDF_ggZH_8TeV	SysTheoryPDF_ggZH
—	SysTheoryPDF_qqVH_8TeV	SysTheoryPDF_qqVH
—	SysTheoryVHPt_8TeV	SysVHNLOEWK
SysJetFlavB_7TeV	SysJetFlavB_8TeV	SysJET_21NP_JET_BJES_Response

### 9.3 COMBINED FIT RESULTS

#### 9.3.1 COMBINED FIT MODEL VALIDATION

Before moving onto the final results, we present the rest of the validations for the Run 1 + Run 2 combined fits, beginning with impacts of ranked individual nuisance parameters in Figure 9.13 and for all nuisance parameter categories in Table 9.15. Both of these sets of results point to the most important nuisance parameters being signal systematics,  $b$ -tagging, and  $V$ +jets modeling systematics, with Run 2 NP's generally being higher ranked. That some NP's are strongly pulled is not unusual as the fit model has so many NP's;  $V$ +jets modeling in particular has been historically difficult.

In addition to looking at the behaviors of nuisance parameters to gauge fit model performance and stability, fits are conducted using multiple parameters of interest. Typical divisions are Run 1 vs. Run 2, lepton channels, and  $WH$  vs  $ZH$ . As mentioned in Chapter 7, the profile likelihood test

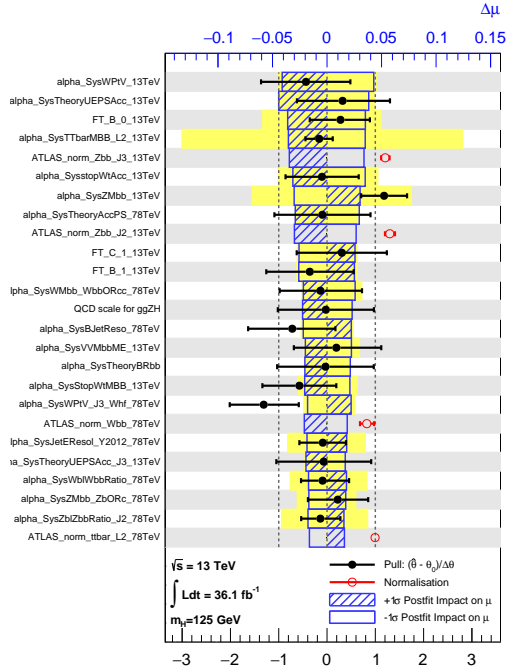


**Figure 9.13:** Ranked nuisance parameters for the Run1+Run2 combination.

statistic given in Equation 7.2 is, in the limit of large sample statistics, a  $\chi^2$  distribution with degrees of freedom equal to the number of parameters of interest plus number of nuisance parameters.

Thus, changing the number of interest parameters and leaving the rest of the fit model unchanged means that the difference between the nominal fit and a fit with more parameters of interest ought to also be distributed as a  $\chi^2$  distribution with degrees of freedom equivalent to the number of extra parameters of interest. This difference can then be interpreted as a compatibility between the two results using the standard tables for this distribution, giving another gauge of fit performance. These are shown in Table 9.16.

The low compatibilities associated with treating the lepton channels as separate parameters of interest are a symptom of the low signal strengths associated with the Run 1 o-lepton channel, in par-

**Table 9.15:** Summary of the impact of different nuisance parameter categories on the total error on  $\hat{\mu}$  for the combined Run1+Run2 fit.

Total	+0.278 / -0.261
DataStat	+0.185 / -0.181
FullSyst	+0.208 / -0.188
All normalizations	+0.068 / -0.069
Jets, MET	+0.046 / -0.040
BTag	+0.077 / -0.076
Luminosity	+0.026 / -0.014
Diboson	+0.030 / -0.027
Model Zjets	+0.049 / -0.050
Model Wjets	+0.082 / -0.083
Model ttbar	+0.047 / -0.046
Model Single Top	+0.047 / -0.045
Model Multi Jet	+0.027 / -0.038
Signal Systematics	+0.098 / -0.052
MC stat	+0.080 / -0.084

**Table 9.16:** Summary of multiple POI compatibilities. The well-known Run 1 7 TeV 0-lepton deficit is responsible for the low compatibility with the 6 and 3 POI fits.

Fit	Compatibility
Leptons (3 POI)	1.49%
$WH/ZH$ (2 POI)	34.2%
Run 1/Run 2 (2 POI)	20.8%
Run 1/Run 2 $\times$ Leptons (6 POI)	7.10%
Run 1/Run 2 $\times$ $WH/ZH$ (4 POI)	34.6%

ticular the 7 TeV result. Given the relatively small amount of data associated with the 7 TeV result, this should not be a cause for alarm. Signal strength summary plots for the fits treating Run 1 and Run 2 separately are shown in Figures 9.14-9.16, where the effect of the Run 1 parameters can be seen graphically.

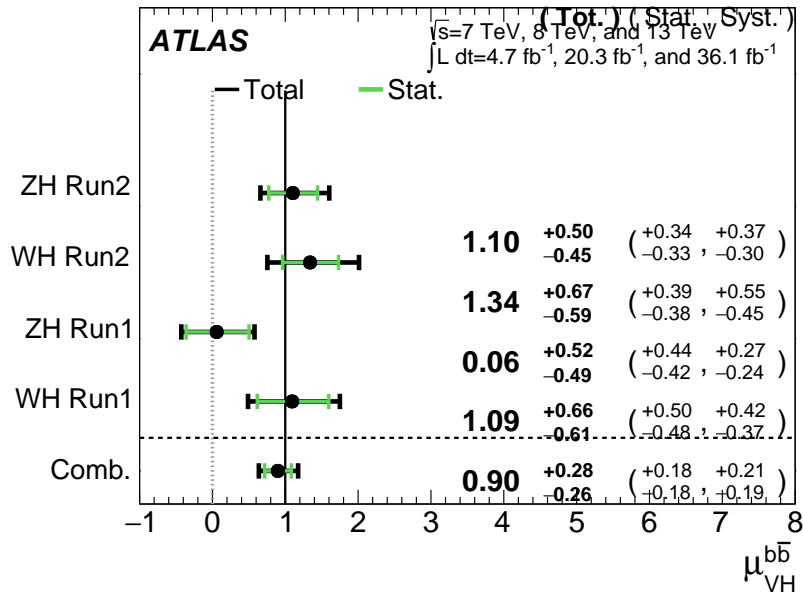


Figure 9.14:  $\hat{\mu}$  summary plot for a four parameter of interest fit.

### 9.3.2 FINAL RESULTS

The combined results yields an observed (expected) significance of 3.57 (4.00) and an observed (expected) limit of  $1.37 (0.510^{+0.200}_{-0.143})$ , with a signal strength of  $\hat{\mu} = 0.898^{+0.278}_{-0.261}$ .

The two and three parameter of interest signal strength summary plots, as well as a summary of the historical values of the 7, 8, and 13 TeV results may be found in Figures 9.17-9.19. The main

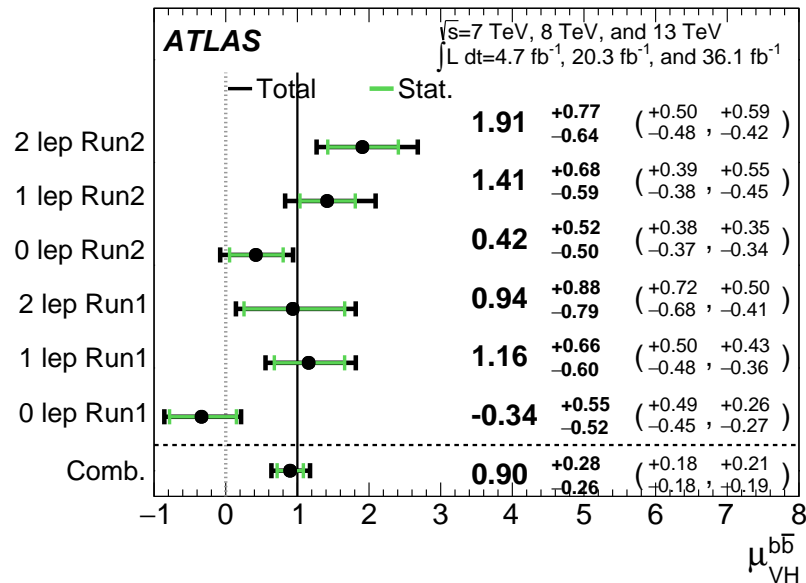


Figure 9.15:  $\hat{\mu}$  summary plot for a six parameter of interest fit.

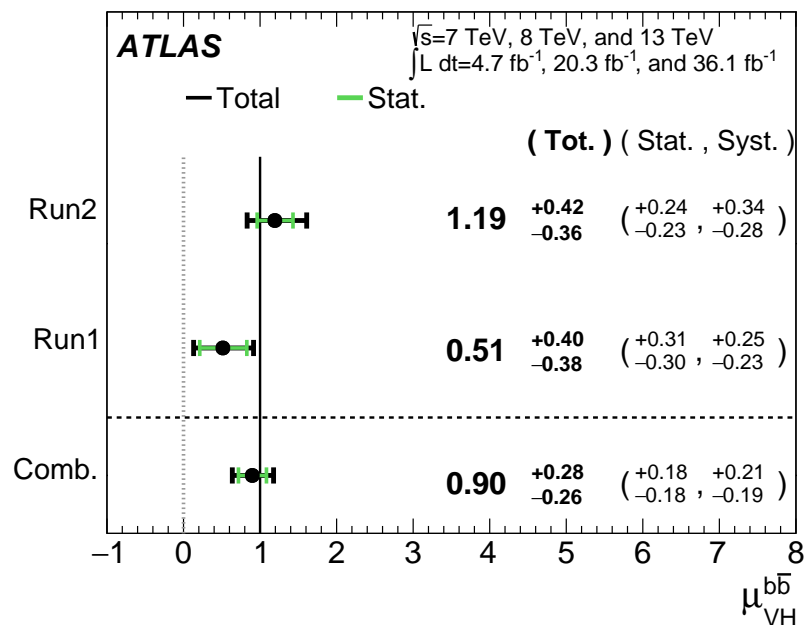
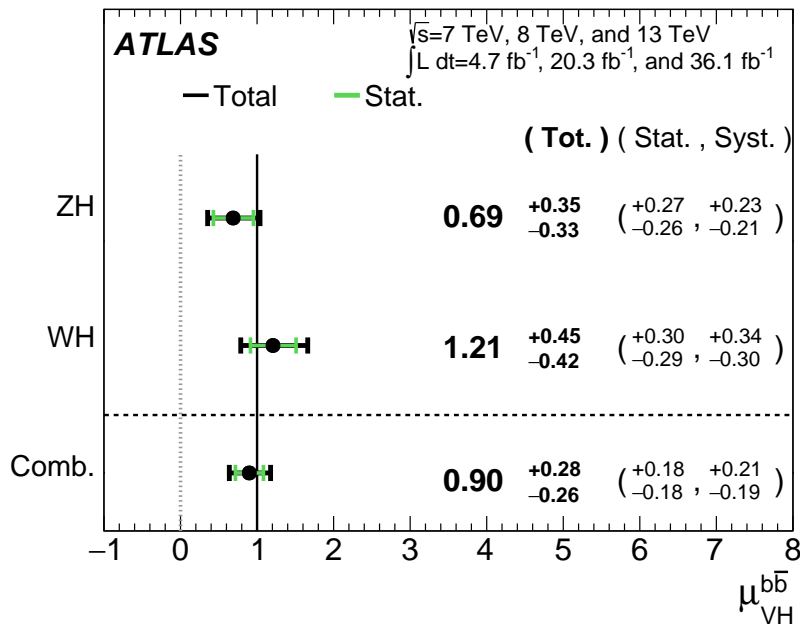


Figure 9.16:  $\hat{\mu}$  summary plot for a two parameter of interest (Run 1 and Run 2) values.

results for Run 1, Run 2, and the combination may be found in Table 9.17. These results were collectively noted as the first ever experimental evidence for SM  $VH(b\bar{b})$  in [13].

**Table 9.17:** A summary of main results for the Run 1, Run 2, and combined fits.

Dataset	$\hat{\mu}$	Total Error in $\hat{\mu}$	Obs. (Exp.)	Significance
Run 1	0.51	+0.40 / -0.37		1.4 (2.6)
Run 2	1.20	+0.42 / -0.36		3.54 (3.03)
Combined	0.90	+0.28 / -0.26		3.57 (4.00)



**Figure 9.17:**  $\hat{\mu}$  summary plot for a two parameter of interest fit.

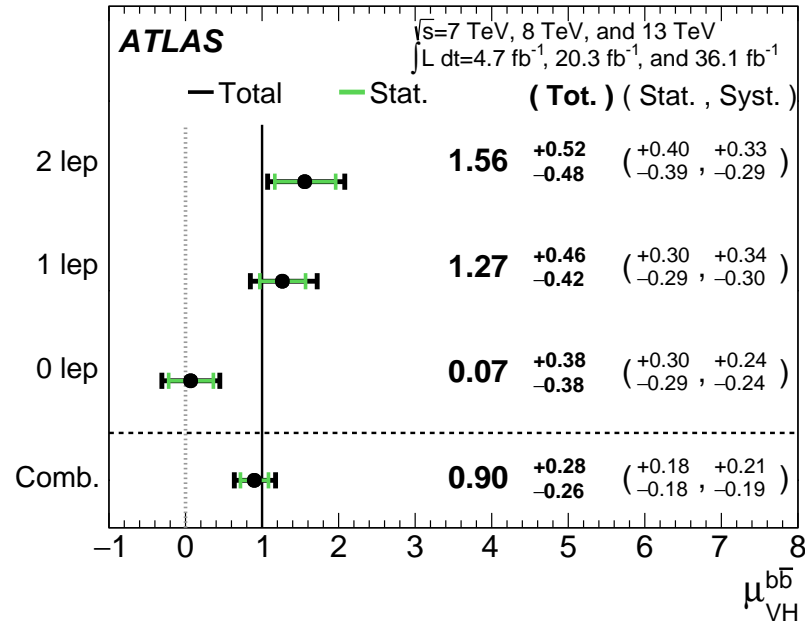


Figure 9.18:  $\hat{\mu}$  summary plot for a three parameter of interest fit.

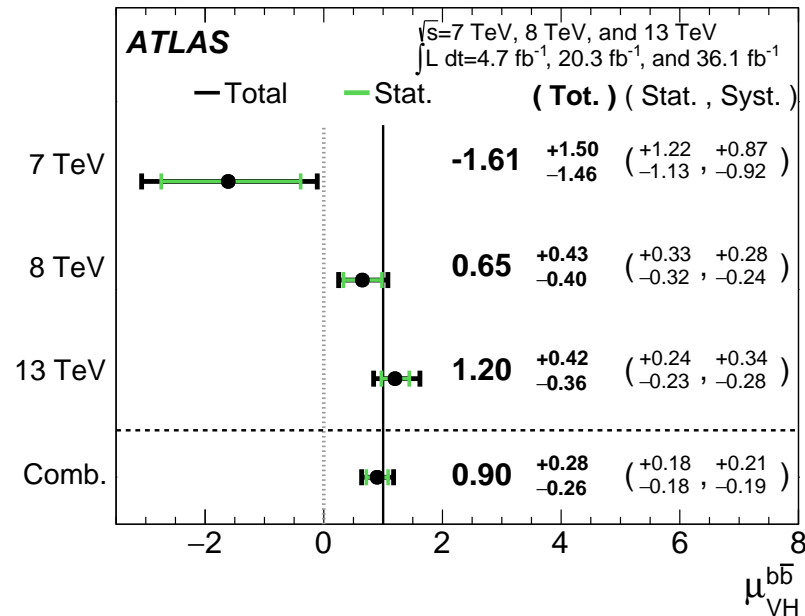


Figure 9.19:  $\hat{\mu}$  summary plot for different  $\sqrt{s}$  values.

*Vanitas vanitatum, omnis vanitas*

Ecclesiastes 1:2

# 10

## Closing Thoughts

SINCE BOTH THE LHC and ATLAS are performing very well, it is only a matter of time before the evidence for SM  $VH(b\bar{b})$  passes the 5 Gaussian standard deviation threshold necessary for discovery.

Official discovery may come less than a year after reports of first evidence and may not even require a combination with the Run 1 result, depending on the latter two years of ATLAS Run 2 data (2017

and 2018).

It is entirely natural to ask, then, how essential the techniques and results described in this thesis will prove to be moving forward. Neither the LI/RF multivariate techniques nor combination with Run 1 datasets and their accompanying low signal strength values are necessary for discovery, and the latter may not even be essential to timely<sup>\*</sup> discovery of SM  $VH(b\bar{b})$ . Nevertheless, both sets of results hold great potential as key parts of a concerted ensemble of efforts towards precision Higgs physics.

With the perhaps final major center of mass energy increase at the energy frontier ever complete, analyses must rely on increased integrated luminosity. Hence, it is becoming increasingly likely that any new fundamental physics at colliders will require the use of results of systematics limited analyses. This is the regime where the techniques described in this thesis will be most useful.

As the LHC and its experiments undergo successive stages of upgrades and operate in evermore extreme environments, the statistical fit models used to describe LHC data will continue to evolve in complexity and diverge from their predecessors. The techniques described in Chapter 9 will become increasingly more vital to producing the best physics results possible. The improvement in precision from  $\hat{\mu}_{VH} = 1.20^{+0.24}_{-0.23}(\text{stat.})^{+0.34}_{-0.28}(\text{syst.})$  to  $\hat{\mu}_{VH} = 0.90^{+0.18}_{-0.18}(\text{stat.})^{+0.21}_{-0.19}(\text{syst.})$  is just the beginning.

The best methods for reduction of systematic uncertainties will naturally depend in part on the state of the art for both fundamental physics process and detector modeling, but techniques that can reduce systematic uncertainties independent of fit model, dataset, and physics process provide

---

<sup>\*</sup>i.e. before or coincident with CMS

a promising avenue forward. The improvements in systematic uncertainties using the Lorentz Invariant and RestFrames variable techniques in the  $ZH \rightarrow \ell\ell b\bar{b}$  analysis, summarized in Table 10.1, show that a smarter and more orthogonal decomposition of information in a collision event provides benefits independent of any clever treatment of  $\vec{E}_T^{\text{miss}}$  (which both schemes also provide). Both techniques are readily extendable to other analysis channels, with the RestFrames concept demonstrating stronger performance and greater flexibility to nearly completely generic final states.

**Table 10.1:** Summary of performance figures for the standard, LI, and RF variable sets. Uncertainties on  $\hat{\mu}$  are quoted stat., syst. In the case of the latter two, % differences are given where relevant. Differences in errors on  $\mu$  are on full systematics and total error, respectively.

	Standard	LI	RF
$\hat{\mu}$	$1.75^{+0.50,0.64}_{-0.48,0.45}$	$1.65^{+0.51,0.59}_{-0.49,0.41}$	$1.50^{+0.50,0.53}_{-0.48,0.36}$
Asi. $\Delta err(\mu)$	—	< 1%, +4.6%	-6.5%, -2.2%
Obs. $\Delta err(\hat{\mu})$	—	-7.5%, -3.7%	-16%, -8.8%
Stat only sig.	4.78	4.39 (-7.9%)	4.44 (-6.9%)
Exp. (Asi.) sig.	2.06	1.92 (-6.7%)	2.13 (+3.5%)
Exp. (data) sig.	1.76	1.73 (-1.7%)	1.80 (+3.4%)
Obs. (data) sig.	2.87	2.79 (-2.8%)	2.62 (-8.6%)

Critical work remains to be done refining and extending the treatment of both the LI and RF techniques in  $VH(b\bar{b})$  analyses and their fit models, and completely independent techniques, like the use of multiple event interpretations addressed in Appendix B promise further improvements still.

No one can say for certain what the future of the energy frontier of experimental particle physics may hold, but more nuanced treatments of the information in collision events born of meaningful physical insight are sure to light the way.

*If it's stupid but it works, it isn't stupid.*

Conventional Wisdom

A

# Micromegas Trigger Processor Simulation

IN ORDER TO PRESERVE key physics functionality by maintaining the ability to trigger on low  $p_T$  muons, the Phase I Upgrade to ATLAS includes a New Small Wheel (NSW) that will supply muon track segments to the Level 1 trigger. These NSW trigger segments will combine segments from the sTGC and Micromegas (MM) trigger processors (TP). This note will focus in particular on the al-

gorithm for the MMTP, described in detail with initial studies in [61]. The goal of this note is to describe the MMTP algorithm performance under a variety of algorithm settings with both nominal and misaligned chamber positions, as well as addressing a number of performance issues.

This note is organized as follows: the algorithm and its outputs are briefly described in Section ??; Monte Carlo samples used are in Section B.1; nominal algorithm performance and certain quantities of interest are described in Section A.3; algorithm performance under misalignment, misalignment corrections, and corrected performance are shown in Section A.9; and conclusions are presented in Section A.24.

## A.1 ALGORITHM OVERVIEW

The algorithm begins by reading in hits, which are converted to slopes. These slopes are calculated under the assumption that the hit originates from the IP; slopes calculated under this assumption are denoted by a superscript  $g$  for global in order to distinguish them from local slopes calculated using only hits in the wedge. In the algorithm simulation, events are screened at truth level to make sure they pass certain requirements. The track’s truth-level coordinates must place it with the wedge since some generated tracks do not reach the wedge. These hits are stored in a buffer two bunch crossings (BCs) in time deep that separates the wedge into so-called “slope-roads.” If any given slope-road has sufficient hits to pass what is known as a coincidence threshold, a fit proceeds. A coincidence threshold is a requirement for an event expressed as  $aX+bUV$ , which means that an slope-road must have at least  $a$  hits in horizontal (X) planes and at least  $b$  hits in stereo (U or V (corresponding to positive and negative stereo rotations)) planes. For coincidence thresholds with a  $zX$  hit require-

ment there is the extra requirement that, in the case of only  $2X$  hits, one be on each quadruplet in order to ensure an adequate lever arm for the  $\Delta\theta$  calculation. Note that less stringent (lower hit) coincidence thresholds are inclusive; i.e. a slope-road passing a  $4X+4UV$  cut automatically passes  $2X+1UV$ . The coincidence threshold, size of the slope-roads (denoted  $b$ ), and the number of slope-roads into which each horizontal and stereo hits get written centered upon their nominal value are configurable parameters of the algorithm.

An individual hit's slope is calculated as shown in Equation A.1, where  $y_{base}$  is the local  $y$  coordinate (orthogonal to the beamline and direction of the horizontal strips) of a station's base,  $w_{str}$  is the strip pitch,  $n_{str}$  is the hit's strip number, and  $z_{plane}$  is the location of the hit's plane along the beamline.

$$M_{hit} = \frac{y}{z} = \frac{y_{base}}{z_{plane}} + \frac{w_{str}}{z_{plane}} \times n_{str} \quad (\text{A.1})$$

In the fit, individual hit slopes in a slope-road are used to calculate global slopes associated with each plane type, which are averages (e.g.  $M_X^{\ell}$  for the average slope of horizontal planes). These in turn are used to calculate the three composite slopes: slopes associated with the horizontal ( $m_x$ ) and vertical coordinates ( $m_y$ ) and the local slope of hits in the horizontal planes ( $M_X^l$ ), all of which are shown in Equation A.4. Note that the expression for  $M_X^l$  differs but is equivalent to the expression given in [61]. This is due to a procedural change in the algorithm. The local X slope is expressed in [61] as:

$$M_X^{local} = A_k \sum_i y_i z_i - B_k \sum_i y_i, \quad B_k = \frac{1}{n} \sum_i z_i A_k = \bar{z} A_k \quad (\text{A.2})$$

Procedurally, this entails doing the sums over  $y_i$  and  $y_i z_i$ , multiplying the sums by  $A_k$ ,  $B_k$ , and then subtracting both of these numbers,  $\mathcal{O}(10^3)$ , to get local slopes,  $\mathcal{O}(10^{-1})$ , while requiring precision on these numbers on the order of  $\mathcal{O}(10^{-3})$ . This requires precision in the sums  $\mathcal{O}(10^{-7})$ , and with 32 bit fixed point numbers, there are deviations with respect to the floating point calculations at the level of  $\mathcal{O}(10^{-5})$ , which is enough to introduce a significant bias in the  $\Delta\theta$  calculation.

In order to prevent these errors, we do the subtraction first

$$M_X^{local} = A_k \sum_i y_i z_i - B_k \sum_i y_i = A_k \sum_i (y_i z_i - y_i \bar{z}) = B_k \sum_i y_i \left( \frac{z_i}{\bar{z}} - 1 \right) \quad (\text{A.3})$$

Thus, we change the order of operations and store  $1/\bar{z}$  instead of  $A_k$  in addition to  $B_k$ . We also change the units of  $y_i$  and  $z_i$  in the calculation by dividing the millimeter lengths by 8192.\* With these changes, a 32 bit fixed point based algorithm has essentially identical performance to that of an algorithm based on the usual C++ 32 floating point numbers. Future work includes converting the 32 bit fixed point arithmetic to 16 bit where possible in the algorithm. While introducing 16 bit numbers uniformly might seem preferable, since simple 16-bit operations in the firmware can be done in a single clock tick, and a larger number of bits increases the algorithm latency, some numbers in the algorithm will require a larger number of bits, in particular in the local slope calculation, which is the single calculation in the algorithm requiring the largest numeric range.

In Equation A.4,  $\theta_{st}$  is the stereo angle of 1.5 degrees; the sums are over relevant planes;  $\bar{z}$  is the average position in  $z$  of the horizontal planes; and  $y_i$  and  $z_i$  in the local slope expression refer to the  $y$

---

\*Chosen since it is a perfect power of 2 and of order the length scale of  $z$  in millimeters

and  $z$  coordinates of hits in X planes.

$$m_x = \frac{1}{2} \cot \theta_{st} (\mathcal{M}_U^g - \mathcal{M}_V^g), \quad m_y = \mathcal{M}_X^g, \quad \mathcal{M}_X^l = \frac{\bar{z}}{\sum_i z_i^2 - 1/n (\sum_i z_i)^2} \sum_i y_i \left( \frac{z_i}{\bar{z}} - 1 \right) \quad (\text{A.4})$$

From these composite slopes, the familiar expressions for the fit quantities  $\theta$  (the zenith),  $\phi$  (the azimuth<sup>†</sup>), and  $\Delta\theta$  (the difference in  $\theta$  between the direction of the segment extrapolated back to the interaction point and its direction when entering the detector region; the following is an approximation) may be calculated, as noted in [61]:

$$\theta = \arctan \left( \sqrt{m_x^2 + m_y^2} \right), \quad \phi = \arctan \left( \frac{m_x}{m_y} \right), \quad \Delta\theta = \frac{\mathcal{M}_X^l - \mathcal{M}_X^g}{1 + \mathcal{M}_X^l \mathcal{M}_X^g} \quad (\text{A.5})$$

Looking at Equations A.4 and A.5, the dependence of fit quantities on input hit information becomes clear.  $\Delta\theta$  relies exclusively on information from the horizontal (X) planes. Both  $\theta$  and  $\phi$  rely on both horizontal and stereo slope information. However, the sum in quadrature of  $m_x$  and  $m_y$  in the arctangent for  $\theta$  means that  $\theta$  is less sensitive to errors in stereo hit information than  $\phi$ . Given that  $\theta_{st}$  is small,  $\cot \theta_{st}$  is large ( $\sim 38$ ), so  $m_x$  multiplies small differences in  $\mathcal{M}_U$  and  $\mathcal{M}_V$ , where  $m_y$  is simply an average over slopes. This means that while errors in horizontal hit information will affect all three fit quantities, comparable errors in stereo hits will have a proportionately larger effect on  $\theta$  and particularly on  $\phi$ . The  $\Delta\theta$  cut after step J in Figure ?? has been implemented, requiring all fits to have  $|\Delta\theta| < 16$  mrad. This requirement ensures good quality fits but also slightly reduces

---

<sup>†</sup>Defined with respect to the center ( $y$ ) axis and *not* the axis of the strips ( $x$ ) as is sometimes typical, so a hit along the center of the wedge has  $\phi = 0$

algorithm efficiency.

## A.2 MONTE CARLO SAMPLES

The Monte Carlo (MC) samples used for these studies were generated in Athena release 20.1.0.2 using simulation layout ATLAS-R2-2015-01-01-00 with muon GeoModel override version Muon-Spectrometer-R.07.00-NSW and modifications to have two modules per multiplet and xxuvuvxx geometry with a stereo angle of 1.5 degrees. Muons of a single  $p_T$  were generated around the nominal IP with a smearing of 50 mm along the beam line and 0.015 mm orthogonal to it; these muons were pointed toward a single, large sector of the NSW. Each event consists of one muon fired towards the single NSW wedge separated by effectively infinite time from other events.

## A.3 NOMINAL PERFORMANCE

In order to evaluate algorithm performance, a number of quantities are evaluated, including the fit quantities  $\theta$ ,  $\phi$ , and  $\Delta\theta$  as well as algorithm efficiency. Unless otherwise stated, that algorithm is run with a 4X+4UV coincidence threshold, slope-road size of 0.0009, an X tolerance of two slope-roads (i.e. hits in horizontal planes are written into the two slope-roads closest to the hits' value), a UV tolerance of four slope-roads<sup>†</sup>, and a charge threshold requirement on hits of 1 (measured in units of electron charge) for a sample of 30 000 events with a muon  $p_T$  of 100 GeV. Samples were also generated for  $p_T$  values of 10 GeV, 20 GeV, 30 GeV, 50 GeV, and 200 GeV, which were used in

---

<sup>†</sup>The larger tolerance on stereo hits takes into account the particulars of the  $m_x$  calculation mentioned in Section ??.

some of the following studies.

#### A.4 FIT QUANTITIES

In order to evaluate the performance of the algorithm’s fit quantities  $\theta$ ,  $\phi$ , and  $\Delta\theta$ , fit values are compared to truth-level MC values. The residual of the three fit quantities,  $\theta_{fit} - \theta_{tru}$ ,  $\phi_{fit} - \phi_{tru}$ , and  $\Delta\theta_{fit} - \Delta\theta_{tru}$ , are recorded for every fitted track. The distributions of these quantities, in particular their biases and standard deviations, are then used to evaluate performance. In most cases, following [61], the mean and standard deviation of a  $3\sigma$  Gaussian fit are quoted, as they capture the main features of the algorithm and generally behave like the raw mean and rms. Nevertheless, discussion of the raw quantities will be included when their behavior deviates markedly from that of the  $3\sigma$  fit quantities.

The truth-level quantities used in residual distribution are taken from information in the MC. These come directly from the MC for  $\theta$ ,  $\phi$ , and  $\Delta\theta$ . These quantities, along with the geometry of the (large) wedge, are then in turn used to calculate truth-level values for any intermediate quantities used in the algorithm.  $m_{x,tru}$ , for instance, is given by  $\tan \theta_{tru} \sin \phi_{tru}$ .

Residual distributions for fit quantities under the previously described default settings of the algorithm are shown in Figure A.1. Both the  $\theta_{fit} - \theta_{tru}$  and  $\Delta\theta_{fit} - \Delta\theta_{tru}$  distributions feature a mostly Gaussian shape with more pronounced tails. The mean bias for these distributions is negligible at under one tenth of a milliradian, and the fitted (raw) rms values are 0.349 (0.614) mrad for  $\theta$  and 1.03 (2.55) mrad for  $\Delta\theta$ . The case of the  $\phi_{fit} - \phi_{tru}$  distribution is less straightforward, with both the shape and bias arising from the xxuvuvxx geometry and relatively large extent of one of the two

$\eta$ -stations, as explained in Appendix B of [62]. The fitted (raw) rms for the  $\phi$  distribution is 8.67 (16.6) mrad.

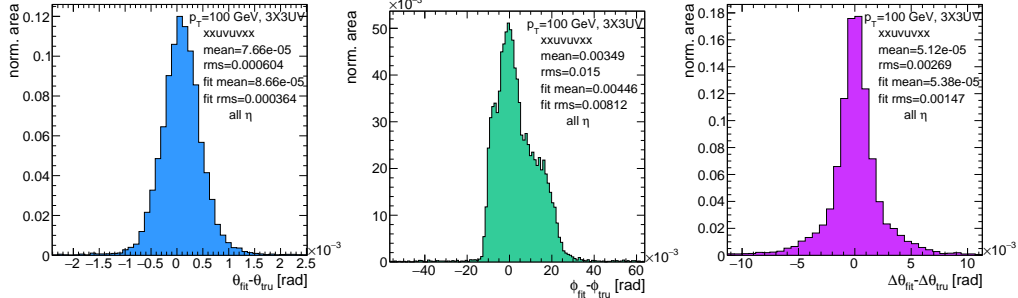


**Figure A.1:** Nominal residual plots;  $\theta, \phi, \Delta\theta$  for  $p_T = 100 \text{ GeV}$  muons

Both increasing muon  $p_T$  and increasing muon  $\eta$  for a fixed  $p_T$  imply increasing muon energy. As muons become more energetic, two effects compete in affecting the quality of fit. On the one hand, higher energy muons are deflected less by the ATLAS magnetic field, which should tend to improve the quality of the fit, since the fitted  $\theta$  (upon which  $\Delta\theta$  also relies) and  $\phi$  values are calculated under the infinite momentum muon (straight track) assumption. However, as muon energy increases, the likelihood that the muon will create additional secondaries increases, which creates extra hits that degrade the quality of the fit. While the geometry of the multiplet is such that there is very good resolution in the direction orthogonal to the horizontal strip direction, the shallow stereo angle of 1.5 degrees means that early hits caused by secondaries can have an outsize impact on  $m_x$ .  $\Delta\theta$ , which does not rely upon stereo information should feel the effect of secondaries the least and benefit from straighter tracks the most and hence benefit from higher muon energies;  $\phi$ , relying upon stereo information the most, would be most susceptible to secondaries and benefit the least from straighter

tracks and hence least likely to benefit from higher muon energy;  $\theta$  relies upon both horizontal and vertical slope information, though small errors are less likely to seriously affect the calculation, so the two effects are most likely to be in conflict for this fit quantity.

The interplay of these effects on the residual standard deviations can be seen in their dependences on  $\eta$  (Figure A.2; note that the final point in each of these plots is the rms of the distribution overall  $\eta$ ) and  $p_T$  (Figure A.3). For  $p_T = 100$  GeV muons,  $\Delta\theta$  performance increases with  $\eta$  (energy), and  $\phi$  performance decreases, as expected;<sup>§</sup> for  $\theta$ , the two effects appear to compete, with performance first increasing with  $\eta$  until the effects of secondaries begins to dominate. Integrated over all  $\eta$ , the effects are less clearly delineated. Both  $\Delta\theta$  and  $\theta$  performance increases with increasing  $p_T$ , suggesting straighter tracks with increasing energy are the dominant effect for these quantities, while  $\phi$  performance appears to improve and then deteriorate (the slight improvement at high  $p_T$  is due to the addition of the  $\Delta\theta$  cut into the algorithm, which filters out very poor quality fits).

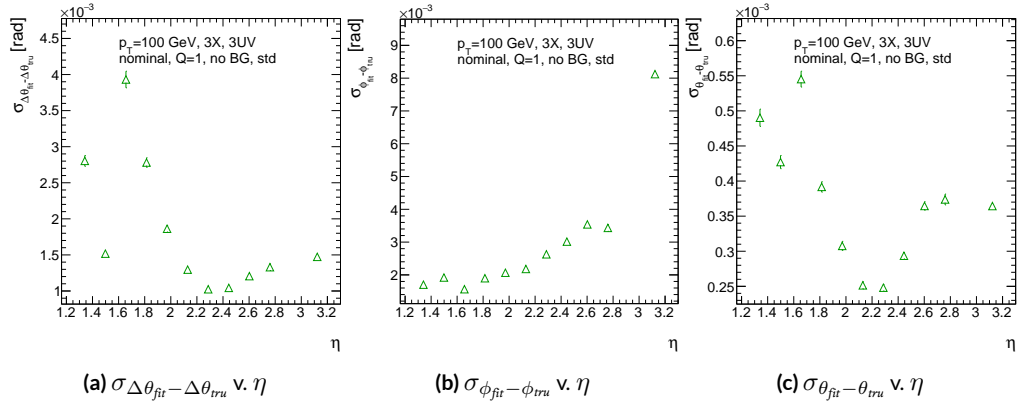


**Figure A.2:** The rms distributions of  $\Delta\theta$ ,  $\phi$ , and  $\theta$  as a function of  $\eta$  for  $p_T = 100$  GeV; the final point in each plot is the rms obtained from a fit to the full distribution including all  $\eta$  bins.

<sup>§</sup>The much worse overall performance for  $\phi$  is due to the  $\eta$  dependent bias and other effects

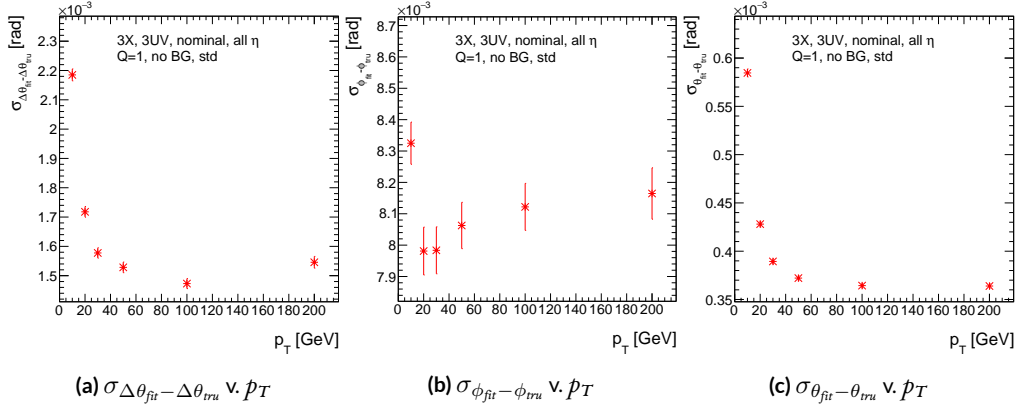


**Figure A.3:** The rms distributions of  $\Delta\theta$ ,  $\phi$ , and  $\theta$  as a function of  $p_T$ .

The rms of the three benchmark quantities as a function of algorithm set (i.e. slope-road) coincidence threshold are shown in Figure A.4 using Gaussian fits and in Figure A.5 for the raw quantities. The fitted  $\sigma$ 's for  $\theta$  and  $\phi$  are fairly stable across coincidence threshold.  $\Delta\theta$ , on the other hand, performs better particularly for the most stringent coincidence threshold; this is a result of the fact that additional information for more hits greatly improves the quality of the local slope fit calculation. The raw rms is a different story. Naïvely, one would expect the performance to get better with more stringent coincidence threshold, but this is not the case in Figure A.5. As the coincidence threshold gets more stringent, fewer and fewer tracks are allowed to be fit. When moving from 2X hits to 3X hits, the tracks that get vetoed populate the tails of the distribution outside the  $3\sigma$  fit range but are not in the very extremes of the distribution. While tracks with 2X hits are of lower quality than those with 3 and 4 X hits, tracks with the very worst fit values pass even the most stringent coincidence threshold requirements (e.g. as a result of many hits arising from a shower of secondaries). This is best illustrated when comparing the 2X+1UV  $\Delta\theta$  residual distribution with the 4X+4UV

distribution in Figure A.6. As both the overlayed normalized curves and ratio distribution show, while the most central regions are fairly similar, the  $\omega X + 1$  UV distribution is much more prominent in the tails but not the extreme tails, which means that, though the overall  $\omega X + 1$  UV raw rms goes down, the overall quality of algorithm fits is worse.

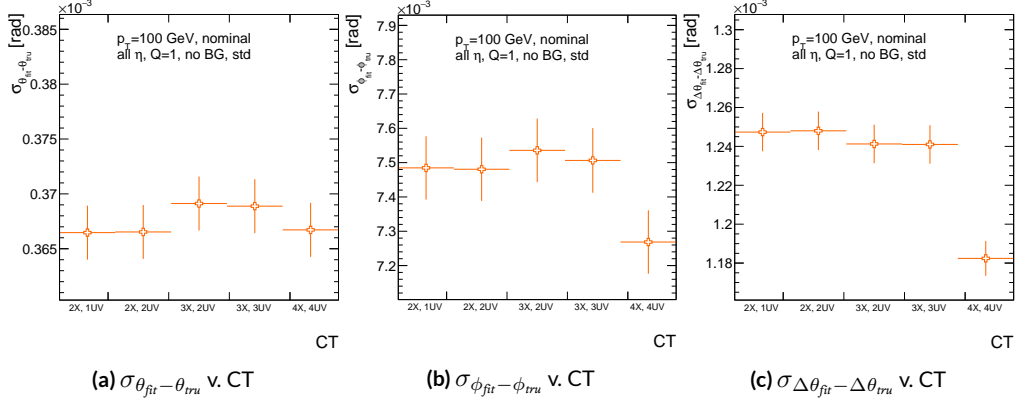


**Figure A.4:** The fitted rms of residual distributions for  $\theta$ ,  $\phi$ , and  $\Delta\theta$  as a function of coincidence threshold for  $p_T = 100$  GeV.

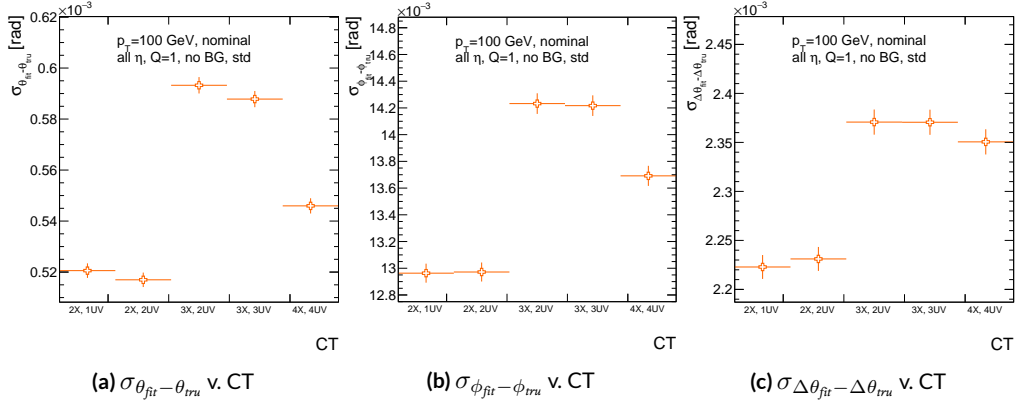


**Figure A.5:** The raw rms of residual distributions for  $\theta$ ,  $\phi$ , and  $\Delta\theta$  as a function of coincidence threshold for  $p_T = 100$  GeV.

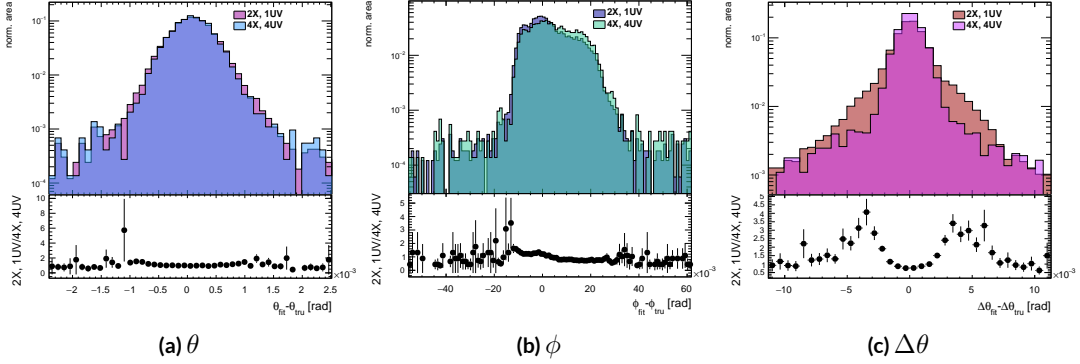


**Figure A.6:** Nominal  $\Delta\theta$  residual distribution for  $p_T = 100$  GeV muons with coincidence thresholds 2X+1UV and 4X+4UV normalized to the same area and plotted together (top) as well as the ratio of the 2X+1UV distribution and the 4X+4UV per bin.

## A.5 EFFICIENCIES

Two general efficiencies have been formulated to study the performance of the MMTP algorithm.

The first, denoted  $\varepsilon_{alg}$ , is the fraction of tracks that pass some (slope-road) coincidence threshold configuration that are successfully fit. An event that passes a slope-road coincidence but does not fit fails because some of the hits included are of sufficiently poor quality to throw off the fit. This efficiency answers the question of how often the algorithm performs fits when technically possible, giving a measure of overall algorithm performance for a given configuration. For example,  $\varepsilon = 95\%$  for 3X+2UV means that 95% of tracks that produce at least 3X hits and 2UV hits in at least one slope-road will be successfully fitted 95% of the time. The performance of this efficiency as a function of coincidence threshold,  $\eta$  (with the final point once again being the efficiency integrated over all  $\eta$ ), and  $p_T$  is shown in Figure A.7.  $\varepsilon_{alg}$  is fairly constant in  $\eta$  and decreases with increased  $p_T$ , which can be attributed to the increased likelihood of secondaries introducing lower quality hits that cause the

fit to fail.

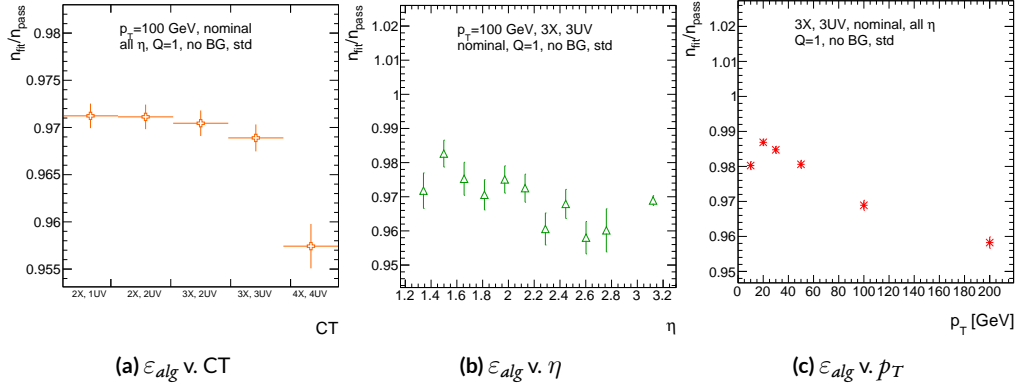


**Figure A.7:**  $\varepsilon_{alg}$  and as a function of coincidence threshold,  $\eta$  (final point is  $\varepsilon_{alg}$  integrated over all  $\eta$ ), and  $p_T$ .

The second efficiency type, denoted  $\varepsilon_{fit}$ , is the fraction of tracks that enter the wedge whose fits (if any) satisfy a given coincidence threshold. This efficiency can be used to help establish an optimal coincidence threshold setting in the algorithm, balancing the improved overall fit quality of higher thresholds with the greater number of fits for lower thresholds. Hence, an  $\varepsilon_{fit}$  of 95% at 3X+2UV means that 95% of tracks entering the wedge are fit and that these fits include at least 3X and 2UV hits.  $\varepsilon_{fit}$  as a function of coincidence threshold is shown in Figure A.8 (a), which shows that the majority of fits having at most 3X+3UV hits. That there is a marked drop to 4X+4UV is not surprising, as there is a substantial population outside the 4X+4UV bin in Figure A.9. The behavior of  $\varepsilon_{fit}$  with  $\eta$  in Figure A.8 (b) (with the final point once again being the efficiency integrated over all  $\eta$ ) is much more varied, with geometric effects of detector acceptance coming into play. The performance of  $\varepsilon_{fit}$  as a function of  $p_T$ , shown in Figure A.8 (c), is similar to that of  $\varepsilon_{alg}$  coincidence threshold, again consistent with the effects of secondaries at higher energies.

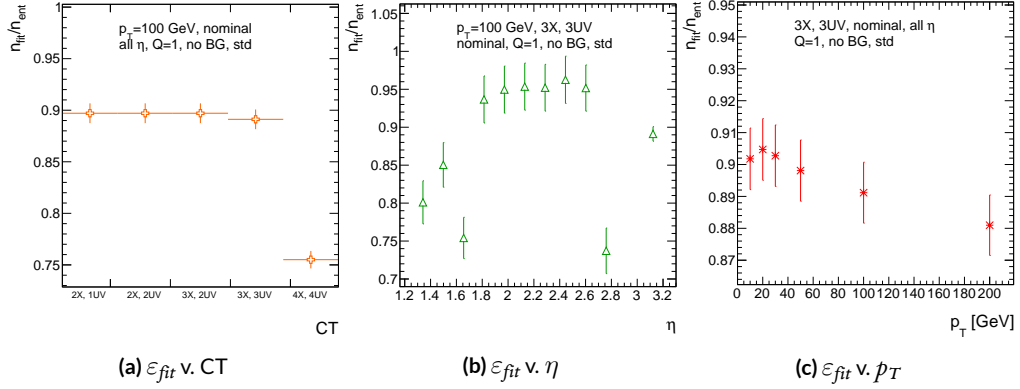


**Figure A.8:**  $\varepsilon_{\text{fit}}$  and as a function of coincidence threshold,  $\eta$  (final point is  $\varepsilon_{\text{fit}}$  integrated over all  $\eta$ ), and  $p_T$ .

In order to better understand efficiency behavior with coincidence threshold, the distribution of highest slope-road coincidence thresholds in events is shown in Figure A.9, with the o,o bin containing events that did not meet requirements for the minimum 2X+1UV coincidence threshold for a fit to occur. That the efficiency is lower at higher coincidence threshold suggests that most of the fits that fail have high hit multiplicity (i.e. a similar number fails in each of the coincidence threshold bins in Figure A.7 (a)), which is consistent with the interpretation that the primary source of fit failures is bad hits originating from secondaries created by higher energy muons.

## A.6 INCOHERENT BACKGROUND

The default slope-road size and tolerances associated with horizontal and stereo hits used in the above studies were configured to optimize algorithm performance, similar to studies in [61]. In order to evaluate algorithm performance under conditions with more limited resources, as might be expected at run-time, additional studies were conducted with the slope-road size and hit tolerances

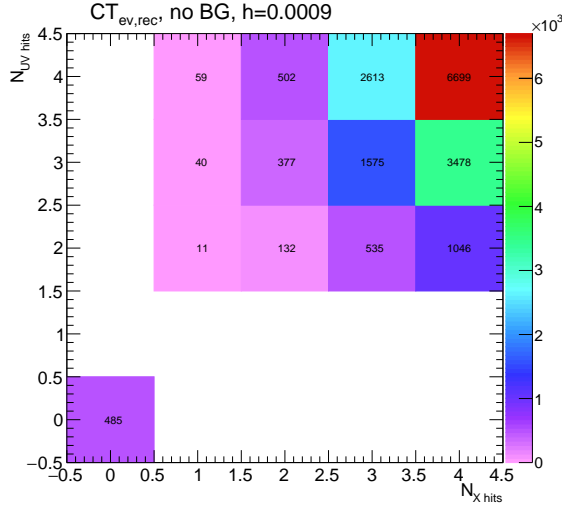


**Figure A.9:** The distribution of highest slope-road coincidence thresholds in events; the 0,0 bin is the number of events passing selection requirements that fail to form the minimum  $2X + 1\text{UV}$  coincidence threshold necessary for a fit.

set equivalent to the sensitive area of a single VMM chip<sup>¶</sup> both with and without generation of incoherent background.

Incoherent background is generated based on the assumption that the intensity only varies as a function of the distance from a point to the beamline,  $r$ . The number of hits per unit area per unit time as a function of  $r$  is given in Equation A.6 and taken from [61].

$$I = I_0 (r/r_0)^{-2.125} \quad (\text{A.6})$$

where  $r_0 = 1000$  mm and  $I_0 = 0.141$  kHz/mm<sup>2</sup>

Background generation happens per event as follows:

- i. Determine the total number of hits to be generated in this event according to a Poisson distri-

---

<sup>¶</sup>One VMM is assumed to cover 64 MM strips at 0.445 mm each.

bution

2. Assign a time to hits uniformly in  $[t_{start} - t_{VMM}, t_{end}]$  where start and end are for the event clock and  $t_{VMM}$  is the VMM chip deadtime (100 ns)
3. Assign a plane to hits uniformly
4. Assign a  $\phi$  value to hits uniformly
5. Assign an  $r$  to hits according to Equation A.6
6. Calculate hit information according to these values.

The expectation value for the Poisson distribution is determined by integrating Equation A.6 over the surface area of the wedge to get the total hit rate for the wedge,  $\Gamma$ , and then multiplying this by the length of the time window over which hits may be generated. With  $H = 982$  mm,  $b_1 = 3665$  mm, and  $\theta_w = 33\pi/180$ , we find<sup>||</sup>:

$$\Gamma = 2I_0 r_0^{2.125} \int_0^{\theta_w/2} d\phi \int_{H \sec \phi}^{(H+b_1) \sec \phi} r dr r^{-2.125} = 98.6657 \text{ MHz} \quad (\text{A.7})$$

In this case, we have taken the nominal values of the MM sector geometry for  $H$  (wedge base),  $b_1$  (the wedge height), and  $\theta_w$  (the wedge opening angle).

The effects of incoherent background and larger slope road size are summarized in Figure A.10 for efficiencies and in Figure A.12 and Table A.1 for residual of fit quantities.

Figure A.10 show the effect of both wider slope-roads and the introduction of background on efficiencies. The introduction of wider slope-roads increases the chance that an early errant hit (either

---

<sup>||</sup>Using Mathematica and the extra factor of  $r$  from the volume element

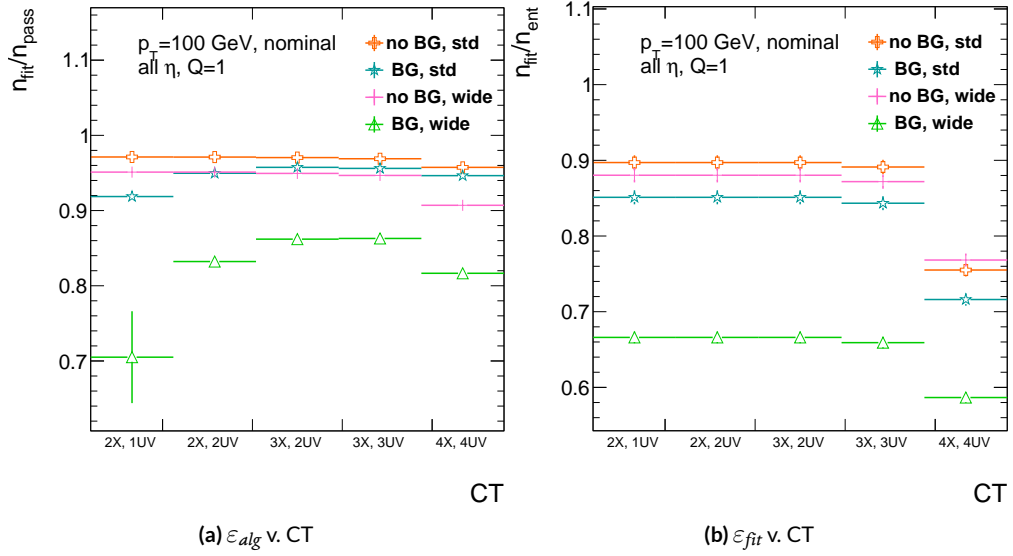


**Figure A.10:** The algorithm and total efficiencies as a function of coincidence threshold for different background settings and slope-road sizes (standard and wide (one slope road as 1 VMM chip)).

from secondaries/ionization or background) will be introduced into the fit, and the presence of incoherent background greatly increases the number of such errant hits. Both wider slope-roads and background drive down the number of fits (numerator) in both efficiencies, and background can artificially inflate the denominator of  $\varepsilon_{alg}$ , a reco-level, slope-road coincidence threshold. The shape of the  $\varepsilon_{fit}$  versus coincidence threshold distributions remains fairly constant with each complicating factor (standard, wider slope-roads, background, both wider slope-roads and background), suggesting many muons will simply not be fit with any number of hits;  $\varepsilon_{fit}$  does not take into account the coincidence threshold of tracks that are not fit, so the effect appears uniform across coincidence threshold. The effects seen for  $\varepsilon_{alg}$ , which are not uniform across coincidence threshold can be better understood when examining the distribution of event highest coincidence thresholds, shown for wide slope-roads both without and with background in Figure A.11. Take, for example the  $zX+1UV$

case. The  $2X+1UV$  bin in particular has a marked increase when background is introduced. No new, good tracks are introduced between the no background and background cases, so the increase is entirely due to bad, background hits; hence, these events do not (and should not) fit, causing the particularly pronounced drop in this bin between these two cases in Figure A.10.

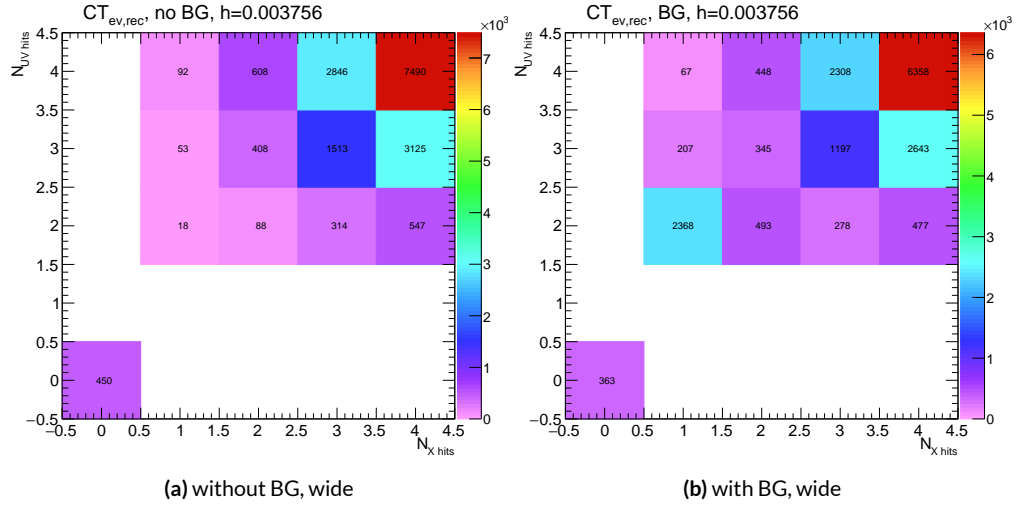


**Figure A.11:** The distribution of highest slope-road coincidence thresholds in events for the algorithm with wide slope-roads (width of 1 VMM) both without (a) and with (b) incoherent background; the 0,0 bin is the number of events passing selection requirements that fail to form the minimum  $2X+1UV$  coincidence threshold necessary for a fit.

The effect of increasing slope-road size and incoherent background on fit quantity residual rms values as a function of  $p_T$  is shown in Figure A.12. As the figure shows, the fitted rms values are fairly robust against increased slope-road size and background. This does not hold for all of the raw rms values, however, as shown in Table A.1. Just as with the efficiencies, the introduction of background has a larger effect than that of increased slope-road size, which does not seem to have an overly large impact on any of the fit quantities on its own. While  $\Delta\theta$  remains robust to both increased slope-road size and background (likely due to the  $\Delta\theta$  cut of 16 mrad built into the algorithm),  $\theta$  shows

some degradation in performance, and the  $\phi$  residual raw rms shows a very large increase upon the introduction of background. Nevertheless, the contrasting behavior of the fitted and raw rms values suggests that tracks that drive up the raw rms values already had very poor fit quality even before the introduction of background, so the impact on fit quantities should remain fairly limited.

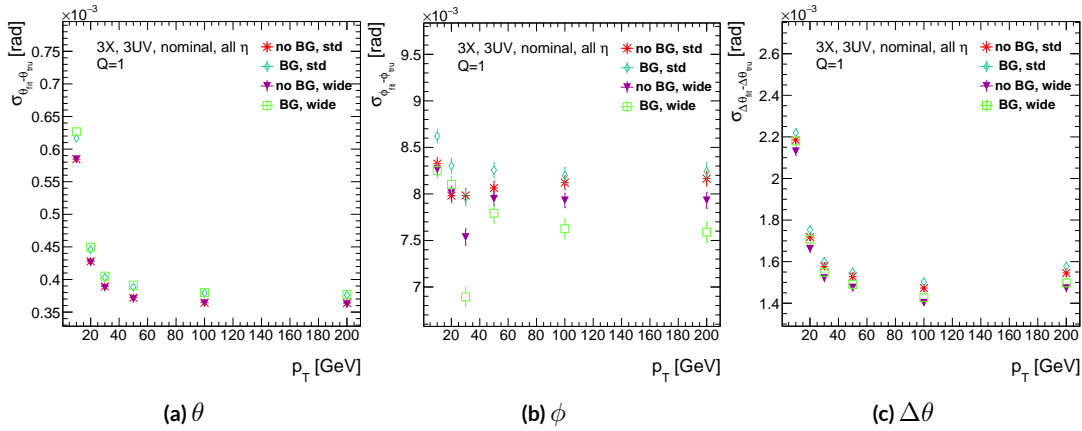


**Figure A.12:** The three fit quantity residual rms values as a function of  $p_T$  for different background settings and slope-road sizes (standard and wide (one slope road as 1 VMM chip)).

**Table A.1:** The fitted (absolute)  $\sigma$  of fit quantity residuals in mrad under different algorithm settings.

	No BG, std	No BG, wide	BG, std	BG, wide
$\theta$	0.364 (0.604)	0.363 (0.542)	0.379 (0.886)	0.380 (1.07)
$\phi$	8.12 (15.0)	7.93 (13.2)	8.20 (24.6)	7.63 (24.8)
$\Delta\theta$	1.47 (2.69)	1.40 (2.66)	1.50 (2.89)	1.43 (2.90)

As Table A.1 shows, rms values appear to be robust to an increase in slope-road size. Nevertheless, though the fitted  $\sigma$  residual values are also fairly robust to the introduction of background, the raw rms values are not. While the raw  $\Delta\theta$  rms stays stable, both  $\theta$  and  $\phi$  suffer noticeable degra-

dation, which suggests that the introduction of background has a detrimental effect on horizontal slope residual (i.e. on stereo strips in particular). This level of degradation is likely acceptable for  $\theta$ , though further steps may need to be taken to address  $\phi$ .

### A.7 BCID

A fitted track's BCID is determined by the most common BCID associated with its hits. Concerns were raised that this might cause incorrect BCID association for fitted tracks. In order to address this, the rate of successful BCID association for fitted tracks was recorded. Figure A.13 shows the dependence of this success rate as a function of  $p_T$  and coincidence threshold in the different background and resource conditions used in the previous section. The successful BCID identification rate is always over 99.5%, demonstrating that this issue is not a concern with the state-of-the-art detector simulation.

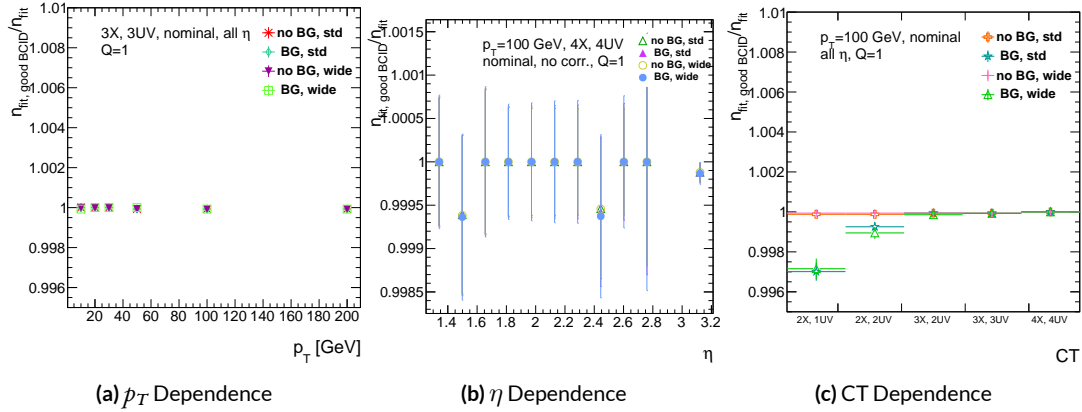


**Figure A.13:** The rate of good BCID association based majority hit BCID as a function of  $p_T$  and coincidence threshold.

## A.8 CHARGE THRESHOLD

The MMTP uses the first hits registered passing a charge threshold requirement given in units of electron charge. In principle, it would be beneficial to be able to use any hits that are registered regardless of deposited charge, but in the high rate environment envisioned for the NSW, this requirement might need to be raised. Nominal algorithm settings have this charge threshold requirement set to 1, and studies were conducted on algorithm performance for charge threshold values of 0, 1, and 2. Efficiencies as a function of coincidence threshold for different charge thresholds are shown in Figure A.14. Increasing the charge threshold lowers both efficiencies, particularly at high coincidence threshold, which suggests that energetic muons with secondaries create both very many hits and hits with higher charge. While the shapes of the fit quantity distributions as a function of  $p_T$  in Figure A.15 are fairly constant across charge threshold, performance is not.  $\theta$  and  $\Delta\theta$  show some improvement with higher charge threshold, particularly at low  $p_T$ , suggesting that resolution improves in the vertical direction, but  $\phi$  shows degradation at higher charge threshold, which is a symptom of more highly charged particles experiencing greater bending in the ATLAS magnetic field in the  $\phi$  direction.

## A.9 MISALIGNMENTS AND CORRECTIONS

The performance of the trigger algorithm under misalignment has been studied for each of the six alignment quantities (three translations and three rotations all along the principal axes) described in [?] and [?], whose convention we will follow here. For the simulated wedge studied here the

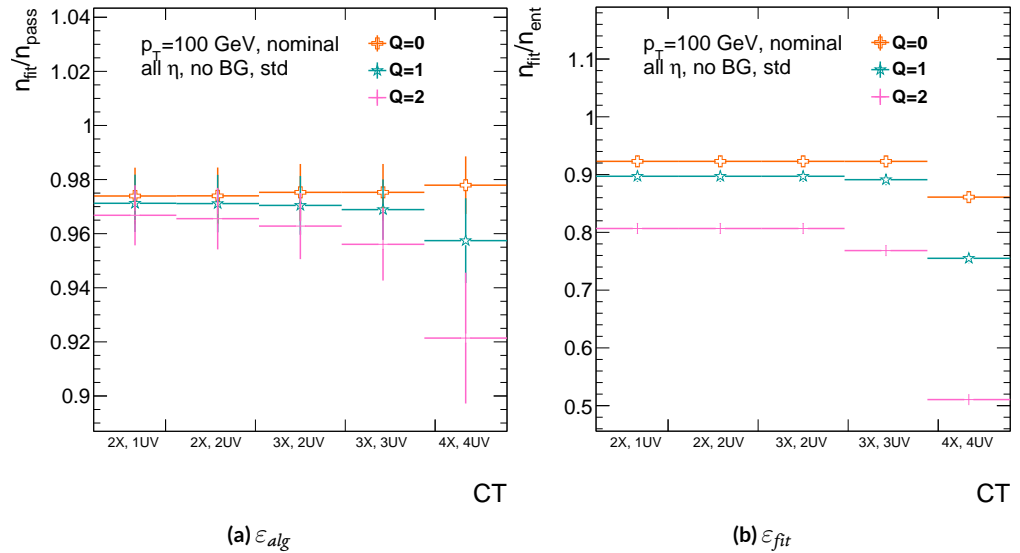


**Figure A.14:** The efficiencies as a function of coincidence threshold for charge thresholds of 0, 1, and 2.

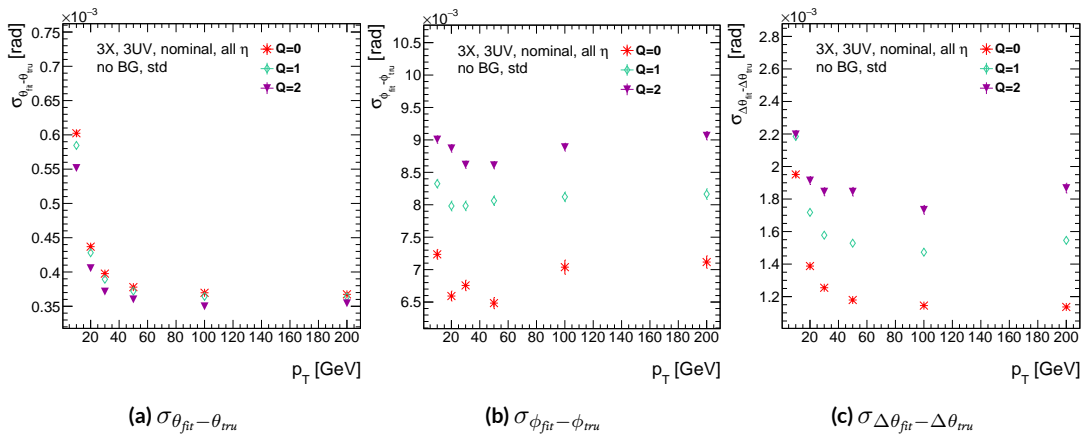


**Figure A.15:** The fit quantity residual rms values as a function of  $p_T$  for charge thresholds of 0, 1, and 2.

local coordinates described in [? ] are taken to be centered at the center of the base of the wedge<sup>\*\*</sup>, the local  $t$  axis corresponds to the axis of the beam line, the local  $z$  axis corresponds to the direction orthogonal to both the beam line and the horizontal strips, and the local  $s$  axis completes the right-handed coordinate system. The rotation angles  $\alpha$ ,  $\beta$ , and  $\gamma$  correspond to rotations around the local  $t$ ,  $z$ , and  $s$  axes, respectively. Note that the local  $s$ ,  $z$ , and  $-t$ , axes correspond to the usual global  $x$ ,  $y$ , and  $z$  axes. Misalignments were studied in twenty evenly spaced increments from nominal positions to misalignments of 1.5 mrad for the rotations (-1.5 mrad to +1.5 mrad for the  $\gamma$  case), and of 5 mm (a roughly corresponding linear shift) for the translations. In all cases, the front quadruplet is misaligned while the rear quadruplet remains in its nominal position. While only the front quadruplet of a single wedge is misaligned, the framework for misalignment presented below could be used to study generic local and global misalignments. The six misalignments are schematically represented in Figure A.16.

Chamber misalignments manifest themselves as altered strips in algorithm input. In order to simulate the effects of misalignment, the change in the local  $y$  coordinate—the distance from the bottom wedge center in the direction perpendicular to both the beamline and the strip direction—is calculated for a track coming straight from the interaction point defined by the truth-level  $\theta$  and  $\phi$  angles for generic misalignment. This displacement in  $y$  is then added to input hit information and the algorithm is then run normally.

To understand how this displacement is calculated, some notation first needs to be described.

---

<sup>\*\*</sup>Not, as is sometimes the case, the centroid position for simplicity's sake, as the agreed upon geometry of the detector changed several times while studies were in progress; any transformation in a centroid-origin coordinate system can of course be formed by a combination of the six transformations examined.

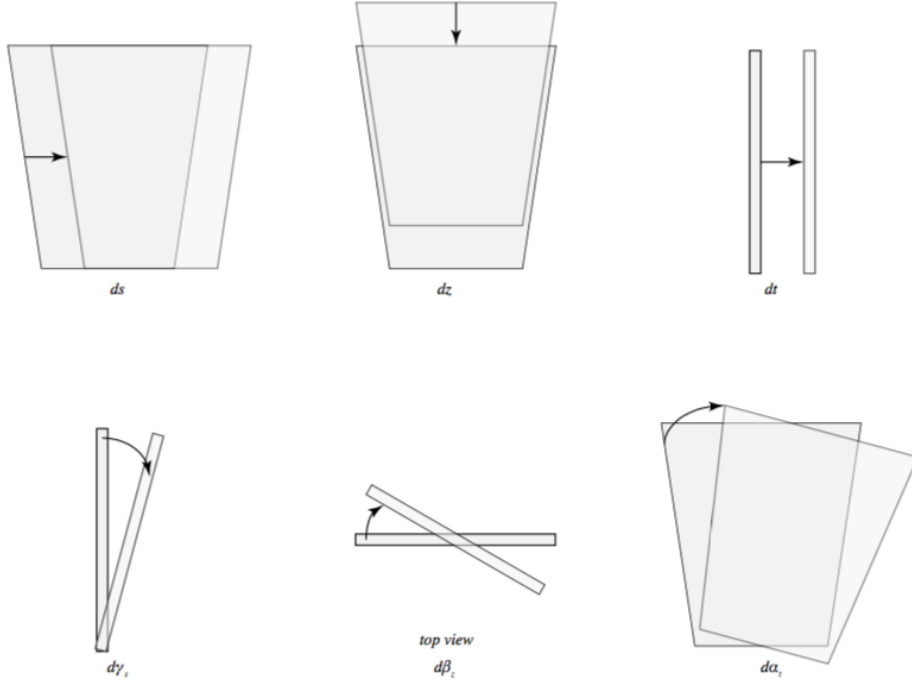


**Figure A.16:** The different misalignment cases as defined in the AMDB manual.

**Table A.2:** A summary of notation used in this section: note that non-AMDB notation is used in this section.

Symbol	Definition
$s_x, s_y, s_z, \vec{s}$	Position of the muon hit in ATLAS global coordinates; the infinite momentum muon track
$\hat{n}$	Vector normal to the plane; taken to be $\hat{z}$ (the beamline) in the nominal case
$\mathcal{O}_{IP}^{g,l}$	Position of the interaction point in ATLAS global ( $g$ ) or wedge local ( $l$ ) coordinates
$\mathcal{O}_{base}^{g,l}$	Position of the plane base in ATLAS global ( $g$ ) or wedge local ( $l$ ) coordinates; $(0, y_{base}, z_{pl})$ ( $(0, 0, 0)$ ) for the nominal case in global (local) coordinates
$\vec{\zeta}$	$\vec{s} - \vec{\mathcal{O}}_{base}$
$(quant)'$	quantities after misalignment

Generically speaking, a hit is the intersection of a line (the muon track) with a plane (the individual plane in the multiplet). We assume the muon moves in a straight line defined by the origin and the truth-level  $\theta_{pos}$  and  $\phi_{pos}$  (i.e. the infinite momentum limit) and that the MM plane is rigid and defined by a point, which we take to be the center of the bottom edge of the plane, and a normal vector, which we take to be the  $z$  axis in the nominal case.

The coordinate axes  $x, y, z$  axes used here correspond to the usual AMDB  $s, z, -t$  axes. Since the direction does not really matter when studying misalignment or corrections thereof, the major difference is the choice of origin.

The muon track we denote<sup>††</sup>  $\vec{s}$ , the bottom point of the plane  $\vec{\mathcal{O}}_{base}$ , and the normal vector  $\hat{n}$ .

The muon track will always be given as (the wedge gets moved, not the muon):

$$\vec{s} = \mathcal{O}_{IP} + k\hat{s} \quad (\text{A.8})$$

$$\hat{s} = \sin \theta_{pos} \sin \phi_{pos} \hat{x} + \sin \theta_{pos} \cos \phi_{pos} \hat{y} + \cos \theta_{pos} \hat{z} \quad (\text{A.9})$$

$$\vec{s} = k\hat{s} = \frac{z_{pl}}{\cos \theta_{pos}} \hat{s} = z_{pl} (\tan \theta \sin \phi \hat{x} + \tan \theta \cos \phi \hat{y} + 1) \quad (\text{A.10})$$

where  $k \in \mathbb{R}$ , along with the unit vector  $\hat{s}$ , defines the point where the track intersects the wedge.

Rotations are done before translations, according to the order prescribed in the AMDB guide for chamber alignment, so the axes the principal axes of the plane are rotated according to the following

---

<sup>††</sup>Recall  $\phi_{pos}$  is defined with respect to the  $y$  axis instead of the  $x$  axis, as might otherwise be typical.

matrix (where  $s$ ,  $c$ , and  $t$  are the obvious trigonometric substitutions)

$$\begin{aligned}
 & \left( \begin{array}{ccc} 1 & 0 & 0 \\ 0 & c\gamma & -s\gamma \\ 0 & s\gamma & c\gamma \end{array} \right) \left( \begin{array}{ccc} c\beta & 0 & s\beta \\ 0 & 1 & 0 \\ -s\beta & 0 & c\beta \end{array} \right) \left( \begin{array}{ccc} c\alpha & -s\alpha & 0 \\ s\alpha & c\alpha & 0 \\ 0 & 0 & 1 \end{array} \right) \\
 & = \boxed{\left( \begin{array}{ccc} c\alpha c\beta & -s\alpha c\beta & s\beta \\ s\alpha c\gamma + c\alpha s\beta s\gamma & c\alpha c\gamma - s\alpha s\beta s\gamma & -c\beta s\gamma \\ s\alpha s\gamma - c\alpha s\beta c\gamma & c\alpha s\gamma + s\alpha s\beta c\gamma & c\beta c\gamma \end{array} \right)} = \mathcal{A} \tag{A.ii}
 \end{aligned}$$

The thing that matters is what the new strip hit is—i.e. what the new  $y$  value is since this, along with a plane number, is all that is fed into the algorithm. To find this, we must solve for the new point of intersection with the rotated plane and then apply the effects of translations. The path connecting the base of the wedge with the intersection of the muon track will always be orthogonal to the normal vector of the plane. Our quantities after misalignment, denoted by primed quantities, will look like

$$\mathcal{O}_{base} \rightarrow \mathcal{O}_{base} + ds\hat{x} + dz\hat{y} + dt\hat{z} = \mathcal{O}'_{base}, \quad \hat{n} \rightarrow A\hat{n} = A\hat{z} = \hat{z}', \quad \vec{s} \rightarrow k'\hat{s} + \mathcal{O}_{IP} = \vec{s}' \tag{A.12}$$

so, moving to explicit, global coordinates in the last line so we can do the computation (relying on the fact that any vector in the wedge, namely  $\vec{\zeta} = \vec{s} - \mathcal{O}$  the local coordinates of the interaction

point, is necessarily orthogonal to  $\hat{n}$ ):

$$0 = \hat{n} \cdot (\vec{\mathcal{O}}_{base} - \vec{s}) \rightarrow 0 = A\vec{z}' \cdot (\vec{\mathcal{O}}'_{base} - (k'\hat{s} + \vec{\mathcal{O}}'_{IP})) \quad (A.13)$$

$$\rightarrow k' = \frac{s\beta\vec{\mathcal{O}}'_{base-IP,x} - c\beta s\gamma\vec{\mathcal{O}}'_{base-IP,y} + c\beta c\gamma\vec{\mathcal{O}}'_{base-IP,z}}{\hat{s} \cdot \vec{z}'} \quad (A.14)$$

$$= \frac{s\beta ds - c\beta s\gamma(y_{base} + dz) + c\beta c\gamma(z_{pl} + dt)}{s\beta s\theta s\phi - c\beta s\gamma s\theta c\phi + c\beta c\gamma c\theta} \quad (A.15)$$

To find our new  $y$  coordinate, we need to evaluate  $s'_y = \hat{y}' \cdot k'\vec{s}$  to find the final correction of:

$$\Delta y = \vec{\zeta}' \cdot \hat{y}' - \vec{\zeta} \cdot \hat{y} = (k'\hat{s} - \vec{\mathcal{O}}'_{base}) \cdot \hat{y}' - (s_y - y_{base}) \quad (A.16)$$

The correction will be plane dependent since (denoting the stereo angle  $\omega$ ):

$$\hat{y}_x = \hat{y} \rightarrow \hat{y}'_x = -s\alpha c\beta \hat{x} + (c\alpha c\gamma - s\alpha s\beta s\gamma) \hat{y} + (c\alpha s\gamma + s\alpha s\beta c\gamma) \hat{z} \quad (A.17)$$

and

$$\begin{aligned} \hat{y}_{U,V} &= \pm s\omega \hat{x}' + c\omega \hat{y}'_{U,V} = [\pm c\alpha c\beta s\omega - s\alpha c\beta c\omega] \hat{x} + [\pm (s\alpha c\gamma + c\alpha s\beta s\gamma) s\omega \\ &\quad + (c\alpha c\gamma - s\alpha s\beta s\gamma) c\omega] \hat{y} + [\pm (s\alpha s\gamma - c\alpha s\beta c\gamma) s\omega + (c\alpha s\gamma + s\alpha s\beta c\gamma) c\omega] \hat{z} \end{aligned} \quad (A.18)$$

## A.10 INDIVIDUAL CASES

Currently we only study the cases where one misalignment parameter is not zero. We examine these in detail below, calculating the most pertinent quantities in the misalignment calculation,  $k'/k$  and

the new horizontal and stereo  $y$  axes. Before setting out, we simplify the expressions for the transformed  $\hat{y}'$ 's, removing any terms with the product of two sines of misalignment angles, which will be zero.<sup>‡‡</sup>

$$\hat{y}'_x = -s\alpha c\beta \hat{x} + c\alpha c\gamma \hat{y} + c\alpha s\gamma \hat{z} \quad (\text{A.19})$$

and

$$\hat{y}'_{U,V} = [\pm c\alpha c\beta s\omega - s\alpha c\beta c\omega] \hat{x} + [\pm s\alpha c\gamma s\omega + c\alpha c\gamma c\omega] \hat{y} + [\mp c\alpha s\beta c\gamma s\omega + c\alpha s\gamma c\omega] \hat{z} \quad (\text{A.20})$$

If the translations are zero,

$$k' = \frac{-c\beta s\gamma y_{base} + c\beta c\gamma z_{pl}}{s\beta s\theta s\phi - c\beta s\gamma s\theta c\phi + c\beta c\gamma c\theta}, \quad k'/k = \frac{-c\beta s\gamma y_{base}/z_{pl} + c\beta c\gamma}{s\beta t\theta s\phi - c\beta s\gamma t\theta c\phi + c\beta c\gamma} \quad (\text{A.21})$$

A.II  $ds \neq 0$

$k'/k = 1$  (the point of intersection does not move closer or further from the IP), and only the stereo planes are affected. Note that only relevant term in Equation A.16, for the stereo strip  $\hat{y}$  for  $\vec{\mathcal{O}}'_{base} = ds\hat{x}$  is:

$$\pm \sin \omega ds \approx \pm 0.0261 ds \quad (\text{A.22})$$

meaning that a displacement in  $x$  of 17 mm, more than three times the range of misalignments studied, would be necessary for a shift in the stereo planes corresponding to one strip width.

---

<sup>‡‡</sup>If only one misalignment parameter is non-zero, then two or more sines will contain at least one term will contain  $\sin 0 = 0$ .

A.12  $dz \neq 0$

$k'/k = 1$  (the point of intersection does not move closer or further from the IP). This case is the trivial one (cf. Equation A.16 with  $\vec{\mathcal{O}}_{base}' = dz\hat{y}$ ).  $y$  just gets moved in the opposite direction as the wedge. Correction is an additive constant.

A.13  $dt \neq 0$

$k'/k = (z_{pl} + dt) / z_{pl}$ .  $y$  gets modified by a simple scale factor. Correct by storing changing definitions of plane positions in algorithm to match the misaligned values.

A.14  $\alpha \neq 0$

$k'/k = 1$  and

$$\hat{y}'_x = -s\alpha\hat{x} + c\alpha\hat{y} \quad (\text{A.23})$$

$$\hat{y}'_{u,v} = [\pm c\alpha s\omega - s\alpha c\omega]\hat{x} + [\pm s\alpha s\omega + c\omega]\hat{y} \quad (\text{A.24})$$

A.15  $\beta \neq 0$

We have  $k'/k = (1 + \tan \beta \tan \theta \sin \phi)^{-1}$ , and

$$\hat{y}'_x = \hat{y} \quad (\text{A.25})$$

$$\hat{y}'_{u,v} = \hat{y} \pm (c\beta\hat{x} - s\beta\hat{z})s\omega \quad (\text{A.26})$$

**Table A.3:** A summary of corrections with additional constants/operations (written as  $n_{const}/n_{ops}$ ;  $n_X$  is the number of X hits in a fit) necessary for analytic corrections. Yes means a correction exists but might not entirely remove misalignment effects, while yes+ means a quality of correction is only limited by knowledge of misalignment and memory

	$\Delta s$	$\Delta z$	$\Delta t$	$\gamma_s$	$\beta_z$	$\alpha_t$
Analytic Resources	yes+ 11c/2op	yes+ oc/oop	yes+ oc/oop	yes 56c/1op	no —	yes 400c/2 $n_X$ op, 32c/12 $n_X$ op
Simulation	yes+	no	no	no	yes+	yes+

A.16  $\gamma \neq 0$

$$k'/k = \frac{1 - \tan \gamma \frac{y_{base}}{z_{pl}}}{1 - \tan \gamma \tan \theta \cos \phi} \quad (\text{A.27})$$

$$\hat{y}'_x = c\gamma \hat{y} + s\gamma \hat{z} \quad (\text{A.28})$$

$$\hat{y}'_{U,V} = \pm s\omega \hat{x} + \omega \hat{y} - s\gamma \omega \hat{z} \quad (\text{A.29})$$

In order to evaluate algorithm performance under misalignment and corrections for misalignment, the absolute means and relative resolutions of the fit quantities  $\theta$ ,  $\phi$ , and  $\Delta\theta$  are measured as a function of misalignment. In the following, results will only be shown for which the effects of misalignment are significant. “Significant,” for misalignments of 1 mm (0.3 mrad) for translations (rotations) means more than a 5% degradation in rms and/or bias shifts in  $\theta$ ,  $\phi$ , and  $\Delta\theta$  of 0.01 mrad, 1 mrad, and 0.1 mrad, respectively.

While corrections are typically done on a case-by-base basis, they fall under two general cate-

gories, analytic and simulation based. Analytic corrections rely upon specific knowledge of the misalignment, with each case being handled separately; as such, the additional resources required, both extra constants and operations, if any, vary accordingly. Simulation based corrections are all done in the same manner. The algorithm is run over a training MC sample (same setup but with  $p_T = 200$  GeV instead of the normal 100 GeV sample so as not to overtrain the corrections), and the mean biases for  $\theta$ ,  $\phi$ , and  $\Delta\theta$  are saved for different, equally spaced regions in the  $\eta - \phi$  plane over the wedge based on the fitted  $\theta$  and  $\phi$  values. Currently, these values are saved for 10  $\eta$  and 10  $\phi$  bins (100  $\eta, \phi$  bins total), with the number of bins in each direction being a configurable parameter. When the algorithm runs with simulation based correction, this table of constant corrections is saved in a LUT before runtime, and corrections are added to final fit quantities based on the (uncorrected)  $\theta$  and  $\phi$  fit values. With the settings mentioned, this is 300 extra constants ( $10\eta\text{-bins} \times 10\phi\text{-bins} \times 3$  fit quantities) and two extra operations (a lookup and addition for each quantity done in parallel). The simulation correction can, in principle, also be applied to the algorithm in nominal conditions with non-trivial improvements, as detailed below in Section A.17. Depending on the misalignment case in question, different approaches work better. A summary of correction methods, including resources necessary for the individual analytic cases, is shown in Table A.3.

### A.17 SIMULATION CORRECTION OF THE ALGORITHM UNDER NOMINAL CONDITIONS

In addition to using simulation based correction to counter the effects of several classes of misalignment, the correction can be applied at to the algorithm under nominal conditions. The main effect of this correction is to mitigate the effects of the bias in stereo strips. As such, the correction has a

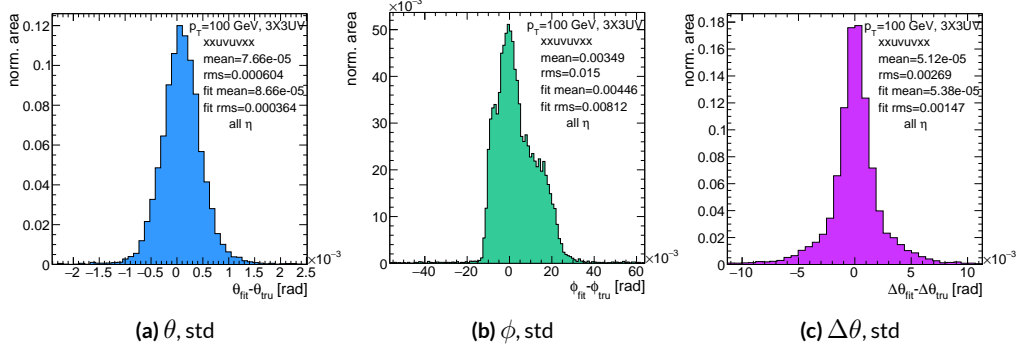


Figure A.17: Nominal residual plots for the uncorrected cases;  $\theta, \phi, \Delta\theta$  for  $p_T = 100 \text{ GeV}$  muons

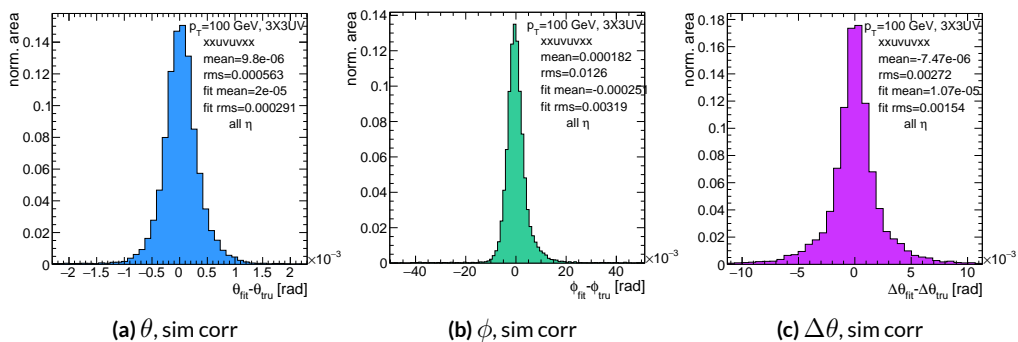
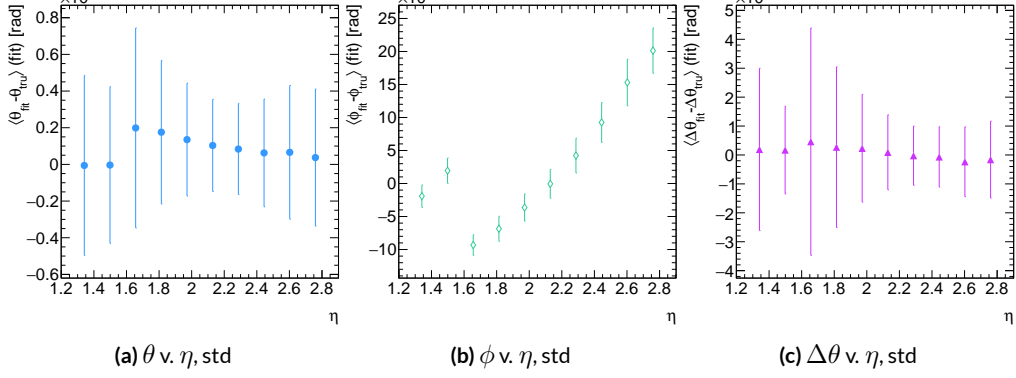


Figure A.18: Nominal residual plots for the simulation corrected cases;  $\theta, \phi, \Delta\theta$  for  $p_T = 100 \text{ GeV}$  muons

larger effect on quantities that rely on the aggregate slope  $m_y$ , as can be seen in Figures A.17 and A.18, improving  $\sigma_{\theta_{fit} - \theta_{true}}$  resolution by about 25%, and reducing  $\sigma_{\phi_{fit} - \phi_{true}}$  by over 50% and restoring a largely Gaussian shape. The slight, apparent degradation in  $\Delta\theta$  is due to a more mild version of the effect seen in Figure A.6.

As can be seen in Figures A.19 and A.20, the simulation based correction also removes the  $\eta$  dependence to fit quantity resolution distributions, as expected. One consequence of this is that simulation-based corrections applied to the misalignment cases below will restore performance to the “sim” distributions of Figure A.18 and not the “std” distributions of Figure A.17. Hence, when making comparisons between simulation corrected curves and the nominal performance point, simulation-corrected distributions of benchmark quantities versus misalignment will often look generally better.



**Figure A.19:** Nominal residual plots as a function of  $\eta$  with points as means and error bars as rms values in each  $\eta$  bin for the angles  $\theta, \phi, \Delta\theta$  for  $p_T = 100$  GeV muons in the uncorrected case.

That the improvements from a simulation-based correction improve performance of the algorithm in nominal conditions most for the quantities that depend most on stereo information ( $\phi$  and

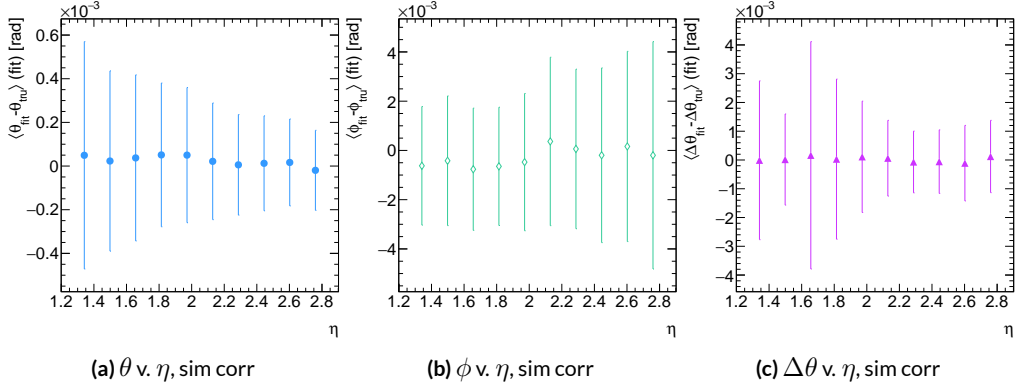


**Figure A.20:** Nominal residual plots as a function of  $\eta$  with points as means and error bars as rms values in each  $\eta$  bin for the angles  $\theta, \phi, \Delta\theta$  for  $p_T = 100$  GeV muons in the corrected case.

$\theta$ ) and remove the  $\eta$  dependence of fit quantity resolutions suggests that there could, in principle, be analytic corrections that could be applied to the nominal algorithm. One possible solution is to introduce an additional set of constants, having the  $y_{base}$  depend on the strip number, similar to the  $\gamma_s$  correction for  $z_{plane}$  described in Section A.21, which would add a lookup per hit and  $8 \times n_{bins,y}$  extra constants that would be optimized as the  $\gamma_s$  correction was.

$$M_{hit} = \frac{y}{z} = \frac{y_{base}}{z_{plane}} (n_{str}) + \frac{w_{str}}{z_{plane}} n_{str} \quad (\text{A.30})$$

The simulation correction residual rms values suggest a limit on the quality of such a correction and could perhaps be implemented generically on their own regardless of misalignment for rms values on fit quantities of 0.291 mrad for  $\theta$ , 3.19 mrad for  $\phi$ , and 1.54 for  $\Delta\theta$ , which represent a 20% improvement for  $\theta$ , a 62% improvement for  $\phi$ , and a slight degradation in  $\Delta\theta$  of 4.7%, again owing to an effect similar to the one in A.6.

### A.18 TRANSLATION MISALIGNMENTS ALONG THE HORIZONTAL STRIP DIRECTION ( $\Delta s$ )

A translation in  $s$  (i.e. along the direction of a horizontal strip) only affects the stereo strips, and, since the stereo angle is small, a very large misalignment is necessary for effects to be noticeable (a misalignment of roughly 17 mm corresponds to one strip's misalignment in the stereo planes). The only quantity to show any meaningful deviation with misalignments with translations in  $s$  is the  $\phi$  residual bias (a change of 0.4 mrad at  $\Delta s = 1$  mm), as can be seen in the uncorrected curve of Figure A.21.

A translation in  $s$  induces a constant shift in the calculated horizontal slope,  $m_x$  in Equation A.4. This constant shift should only depend on which stereo planes included in a fit are misaligned and how misaligned they are. Hence, the correction to  $m_x$ , for a sum over misaligned stereo planes  $i$ , with their individual misalignments in  $s$  and plane positions in  $z$  is:

$$\Delta m_x = \frac{1}{N_{\text{stereo}}} \sum_{i, \text{misal stereo}} \frac{\Delta s_i}{z_{i, \text{plane}}} \quad (\text{A.31})$$

Given prior knowledge of misalignment, these corrections to  $m_x$  can be performed ahead of time and saved in a lookup table (LUT), similar to the LUT used for constants in the X local slope ( $M_x^l$ ) calculation. The added overhead of this analytic correction is hence eleven constants in memory, a lookup, and one addition. The correction perfectly corrects the effects of misalignment, as can be seen in Figure A.21. The simulation based correction described above can also be used to correct for  $\Delta s$  misalignments, with the results of that correction also shown in Figure A.21. The apparent dis-

crepancy between the simulated and analytic correction is a natural consequence of the fact that the simulation correction, as previously mentioned, restores the  $\phi$  residual distribution to an overall more Gaussian shape.

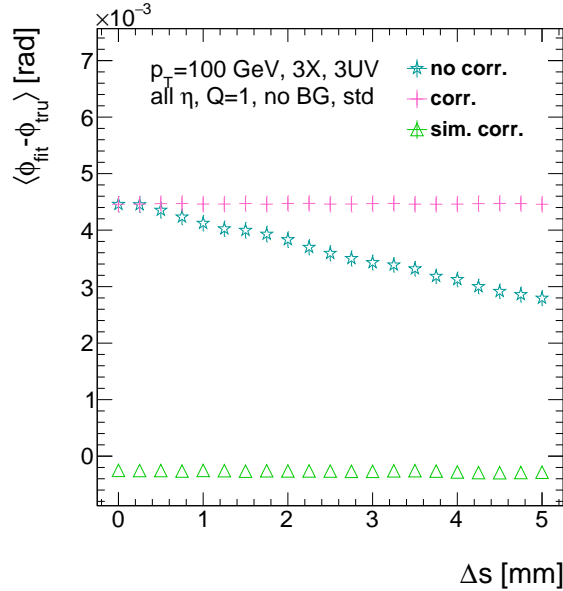


**Figure A.21:** The mean of the  $\phi$  residual as a function of misalignment for the uncorrected case and the analytic and simulation correction cases.

### A.19 TRANSLATION MISALIGNMENTS ORTHOGONAL TO THE BEAMLINE AND HORIZONTAL STRIP DIRECTION ( $\Delta z$ )

A translation in AMDB  $z$ , the direction orthogonal to both the beamline and the horizontal strip direction, corresponds to a translation in the  $y$  of Equation A.1, affecting all slope calculations. This has a large impact on the  $\theta$  residual bias and both the bias and rms of  $\Delta\theta$  residual, as can be seen in Figures A.22 (a)–(c). The marked degradation and non-linear behavior in performance at very high

levels of misalignments is a result of low statistics; there are fewer fits at high level of misalignments since for  $\Delta z \gtrsim 3$  mm, most fits will fail the  $\Delta\theta$  cut. The  $\theta$  bias shifts by about 0.075 mrad at  $\Delta z = 1$  mm, and  $\Delta\theta$  shifts by about 5 mrad for the same level of misalignment. While the fitted rms of the  $\Delta\theta$  residual remains fairly stable for  $\Delta z < 1$  mm or so, between  $\Delta z = 2$  mm and  $\Delta z = 3$  mm, the rms increases by 15% before the  $\Delta\theta$  cut issue mentioned above intervenes.

Fortunately, these misalignments are straightforward to correct with knowledge of the misalignment. The only modification necessary for this correction is to change the definitions of  $y_{base}$  in Equation A.1 for the individual hit slope addressing. This is done before runtime and adds no overhead to the algorithm, and the correction quality is only limited by knowledge of the misalignment. The results of this correction are also shown in Figures A.22 (a)–(c) and restore nominal performance.

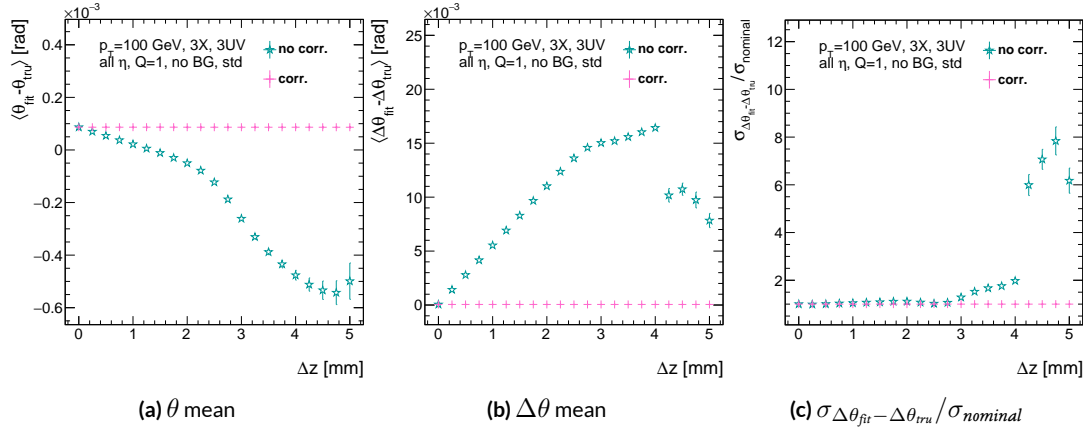


**Figure A.22:** The affected quantities of  $\Delta z$  misalignments:  $\theta$  bias,  $\Delta\theta$  bias, and  $\sigma_{\Delta\theta_{fit} - \Delta\theta_{true}} / \sigma_{\text{nominal}}$  for both the misaligned and corrected cases.

---

Since  $\Delta\theta = \frac{M_X^t - M_X^s}{1 + M_X^t M_X^s}$  and  $M_X^t = B_k \sum y_i (z/\bar{z} - 1)$ , a shift  $\Delta y$  translates (with typical slope values of  $\sim 0.3$ ) to  $5B_k (z_1 + z_2)/\bar{z}$  (with  $B_k$  in units of inverse mm); set equal to 16 mrad ( $\Delta\theta$  is centered at zero), this corresponds to  $\Delta y = 2.7$  mm

## A.20 TRANSLATION MISALIGNMENTS PARALLEL TO THE BEAMLINE ( $\Delta t$ )

The effects of misalignment due to translations in  $t$  are very similar to those due to translations in  $z$  without the complication of the  $\Delta\theta$  cut, affecting the  $z$  instead of the  $y$  coordinate that enters into hit slope calculations. Again,  $\theta$  bias,  $\Delta\theta$  bias, and  $\sigma_{\Delta\theta_{fit}-\Delta\theta_{tru}}$  are the primarily affected quantities. For  $\Delta t = 1$  mm,  $\theta$  bias shifts by about 0.02 mrad,  $\Delta\theta$  bias shifts by just under 2 mrad, and  $\sigma_{\Delta\theta_{fit}-\Delta\theta_{tru}}$  degrades by about 20%. The correction for this misalignment once again costs no overhead and consists of changing stored constants in the algorithm, in this case the positions along the beamline of the misaligned planes, with results similarly limited by knowledge of the misalignment.

The slight improvement with correction to  $\Delta\theta$  rms is due to the real effect of a larger lever arm.

Both the misaligned and corrected distributions of affected quantities of interest are shown in Figure A.23.

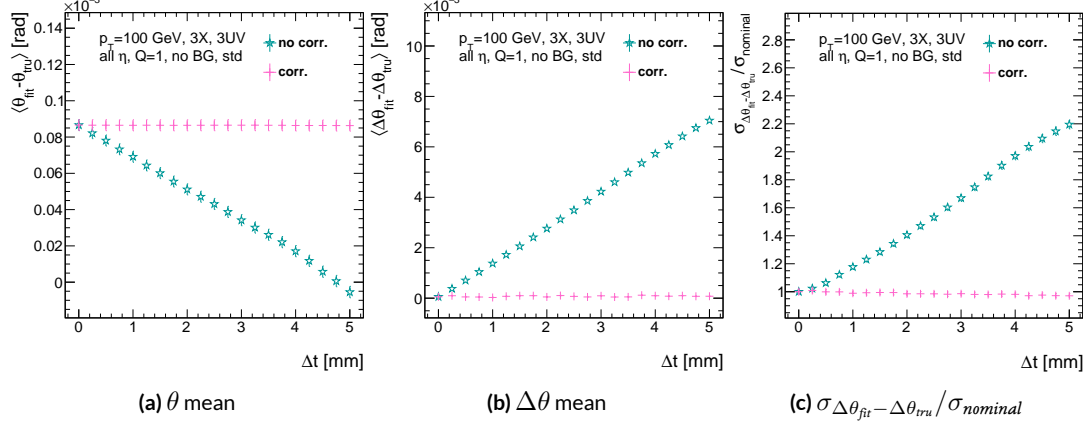


**Figure A.23:** The affected quantities of  $\Delta t$  misalignments:  $\theta$  bias,  $\Delta\theta$  bias, and  $\sigma_{\Delta\theta_{fit}-\Delta\theta_{tru}}/\sigma_{nominal}$  for both the misaligned and corrected cases.

## A.21 CHAMBER TILTS TOWARDS AND AWAY FROM THE IP ( $\gamma_s$ ROTATION)

Chamber misalignment due to rotations around the  $s$  axis act effectively like a translation in  $t$  that depends on strip number. These rotations tilt misaligned chambers away from (towards) the IP for positive (negative) values of  $\gamma_s$ . Since, unlike for the other two rotation cases that will be studied, positive and negative rotation values are not symmetric, this misalignment is studied for both positive and negative  $\gamma_s$  values. The divergent effect at the tails is a result of a large population of fits not having fit quantities within the cores, and so not appearing in the fit rms. Once again, affected quantities of interest  $\theta$  bias,  $\Delta\theta$  bias, and  $\sigma_{\Delta\theta_{fit}-\Delta\theta_{tru}}$ . The effects of misalignment can be seen in Figures A.24 (a)–(c). The relationship between biases and  $\gamma_s$  is roughly linear with  $\Delta\gamma_s = 0.3$  mrad (the angular scale corresponding to linear shifts of  $\sim 1$  mm) corresponding to 0.005 mrad (0.12 mrad) for  $\theta$  ( $\Delta\theta$ ). For  $\sigma_{\Delta\theta_{fit}-\Delta\theta_{tru}}$ , degradation is not symmetric. For negative (positive)  $\gamma_s$ , with the quadruplet tilted towards (away from) the IP, slope-roads are artificially expanded (shrunk), decreasing (increasing) the granularity of the trigger, explaining the asymmetry in Figure A.24 (c), with the degradation being a 10% (25%) effect for  $\gamma_s$  of  $+(-)0.3$  mrad.

Corrections are less simple in this case. In principle, corrections of the same accuracy of the translations could be calculated per strip, but the overhead of one correction per strip (many thousands of constants) is prohibitive. Instead, each plane was divided into eight equal segments with a  $t$  value ( $z$  in the slope calculation) assigned to strips in each region to correct for the misalignment. This amounts to 56 extra constants and a 2D instead of a 1D LUT for  $z$  positions while the algorithm runs. The corrected distributions can also be seen in Figures A.24 (a)–(c). The corrections, while

not as effective as for the simple translation cases, are still very effective with the quoted misalignment values for bias shifts down to 0.001 mrad (0.25 mrad) for  $\theta$  ( $\Delta\theta$ ) and no more than a 2% degradation in  $\sigma_{\Delta\theta_{fit}-\Delta\theta_{tru}}$  for  $|\gamma_s| = 0.3$  mrad.

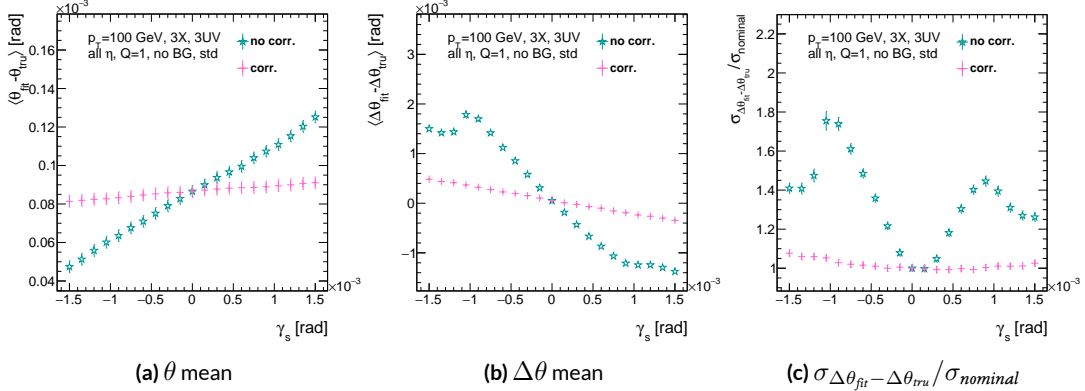


**Figure A.24:** The noticeable effects of rotations in the  $s$  axis and the behavior of these quantities ( $\theta$  and  $\Delta\theta$  bias shifts and  $\sigma_{\Delta\theta_{fit}-\Delta\theta_{tru}}/\sigma_{nominal}$ ) with and without misalignment correction.

## A.22 ROTATION MISALIGNMENTS AROUND THE WEDGE VERTICAL AXIS ( $\beta_z$ )

While misalignments coming from rotations around the  $z$  axis (the direction orthogonal to both the beamline and the horizontal strip direction) foreshorten the strips as seen from the IP and add a deviation in  $t$ , the long lever arm largely washes out any effects of this misalignment. Only the  $\sigma_{\Delta\theta_{fit}-\Delta\theta_{tru}}$  is noticeably affected, though only at severe misalignments, with only about a 1% degradation in performance at  $\beta_z = 0.3$  mrad (corresponding to a linear shift of  $\sim 1$  mm). A simulation based correction works well to cancel out the effects of this misalignment, and the  $\sigma_{\Delta\theta_{fit}-\Delta\theta_{tru}}$  as a function of misalignment with and without corrections are shown in Figure A.25. The apparent 2% effect in the simulation corrected curve is a result of a more mild version of the effect shown in

Figure A.6.

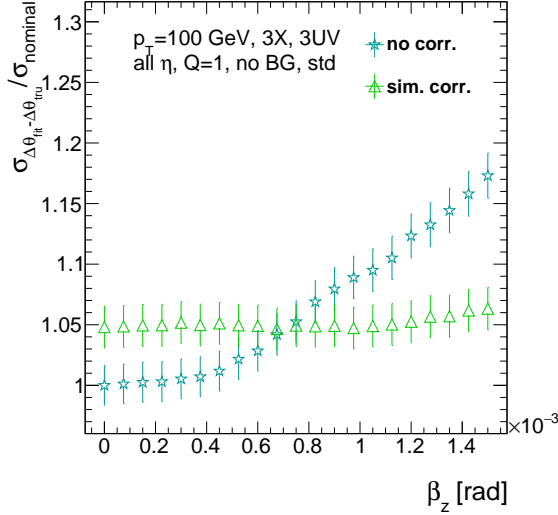


**Figure A.25:** The effects of rotations in the  $z$  axis on  $\sigma_{\Delta\theta_{fit} - \Delta\theta_{tru}} / \sigma_{nominal}$  a function of  $\beta_z$  both with and without misalignment corrections.

### A.23 ROTATION MISALIGNMENTS AROUND THE AXIS PARALLEL TO THE BEAMLINE ( $\alpha_t$ )

Misalignments arising from rotations around the  $t$  axis (parallel to the beamline at the center of the base of the wedge) are essentially rotations in the  $\phi$  direction. The quantities of interest most affected are the  $\phi$  bias and  $\sigma_{\Delta\theta_{fit} - \Delta\theta_{tru}}$ , as shown in Figures A.26 (a) and (b), respectively, and correspond to a shift in  $\phi$  bias of 0.2 mrad and a 10% degradation in  $\sigma_{\Delta\theta_{fit} - \Delta\theta_{tru}}$  for  $\alpha_t = 0.3$  mrad (corresponding to a linear shift of  $\sim 1$  mm). The raw instead of fitted mean  $\phi$  biases is used in Figure A.26 (a) to better illustrate the effect of misalignment.

Since the effect of misalignment is dependent on horizontal (along the strip direction,  $\hat{s}$ ) in addition to vertical information, corrections cannot be applied before a fit takes place. The  $\phi$  bias shift is uniform over the entire wedge, so a constant additive correction to  $\phi$  based on the level of misalign-

ment can be applied to all fits depending on how many misaligned stereo planes enter in the fit.  $\Delta\theta$  is less straightforward, but corrections to the  $y$  and  $z$  information used in the local slope calculation in Equation A.4 can be applied once  $\theta_{fit}$  and  $\phi_{fit}$  are known. These corrections are calculated ahead of time in bins of uniform  $\eta$  and  $\phi$  as with the simulation corrections using the same framework as the misalignment calculation. The results of both types of correction can be seen in Figure A.23. The apparent discrepancy between the simulation and analytic corrections in the  $\phi$  bias happens for the same reason as in the  $\Delta s$  misalignment correction cases, as simulation correction restores a more Gaussian shape to the  $\phi$  residual distribution opposed to the uncorrected nominal case, as discussed in Section A.17.

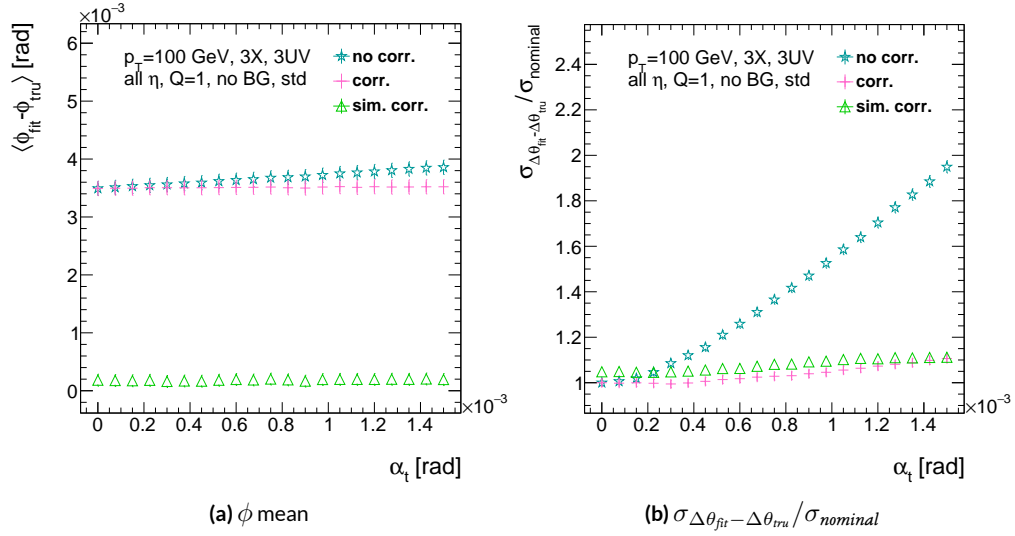


**Figure A.26:** The effects of rotation misalignments around the  $t$  axis for  $\phi$  bias and  $\sigma_{\Delta\theta_{fit}-\Delta\theta_{tru}}/\sigma_{nominal}$  as a function of misalignment. The uncorrected and both the analytic and simulation correction cases are shown.

## A.24 CONCLUSION

The algorithm for Micromegas detectors in the NSW Trigger Processor performs well in a variety of conditions and has proven robust to a number of effects to deliver measurements on muon tracks of the three angles  $\theta$ ,  $\phi$ ,  $\Delta\theta$ . Under nominal conditions, the rms values for the residuals of these quantities are 0.364 mrad for  $\theta$ , 8.12 mrad for  $\phi$ , and 1.47 mrad for  $\Delta\theta$ . Algorithm performance was found to be largely independent of the charge threshold setting, and a hit majority BCID association was found to provide proper timing information over 99.7% even in the most relaxed settings (2X+1UV coincidence threshold requirement+wide slope-road+background). The introduction of wide slope-roads to better mimic potentially limited algorithm resources at run time and the introduction of incoherent background was found to have a manageable effect on fit quantity residual rms values and on total algorithm efficiency for sufficiently stringent coincidence threshold. The effects of the three translation and three rotation misalignments specified by AMDB convention were studied, and correction methods for each of the six cases was developed. Simulation-based corrections were found to improve nominal algorithm performance to residual rms value of 0.291 mrad for  $\theta$ , 3.19 mrad for  $\phi$ , and 1.54 for  $\Delta\theta$ , which represent improvements of 20%, 62%, and -4.7%, respectively. Misalignment corrections were found to restore nominal performance for all but the rotation around the  $s$  axis, and a summary of tolerances may be found in Table A.4.

**Table A.4:** A summary of levels of misalignment corresponding to a 10% degradation in any residual rms or, for biases shifts of, 0.01 mrad for  $\theta$ , 1 mrad for  $\phi$ , and 0.25 mrad for  $\Delta\theta$  for both the uncorrected and corrected cases;  $> 5$  mm and  $> 1.5$  mrad mean that such a degradation does not occur for the range of misalignment studied. Most affected quantity in parentheses.

	No Correction	Correction
$\Delta s$	4 mm ( $\phi$ bias)	$> 5$ mm
$\Delta z$	0.25 mm ( $\Delta\theta$ )	$> 5$ mm
$\Delta t$	0.25 mm ( $\Delta\theta$ )	$> 5$ mm
$\gamma_s$	0.15 mrad ( $\Delta\theta$ bias)	0.75 mrad
$\beta_z$	0.9 mrad ( $\Delta\theta$ rms)	$> 1.5$ mrad
$\alpha_t$	0.375 mrad ( $\Delta\theta$ rms)	$> 1.5$ mrad

*Tod-Not-Brot*

Old German Proverb

# B

## Telescoping Jets

ANOTHER APPROACH TO IMPROVING  $ZH \rightarrow \ell\ell b\bar{b}$  is the use of telescoping jets [63], which harnesses the power of multiple event interpretations. The use of multiple event interpretations was originally developed with non-deterministic jet algorithms like the Q-jets (“quantum” jets) algorithm [64]. When a traditional or “classical” algorithm, such as the Cambridge-Aachen[65] and

anti- $k_t$ [66] algorithms, is applied to an event, it produces one set of jets for that event, i.e. a single interpretation of that event. With multiple event interpretations, each event is instead given an ensemble of interpretations. In the case of Q-jets, this ensemble is created through a non-deterministic clustering process for an anti- $k_t$  jet algorithm. With telescoping jets, multiple jet cone radii (the characteristic size parameter,  $R$ ) around a set of points in the pseudorapidity-azimuth ( $\eta - \phi$ ) plane are used to generate a series of jet collections. Instead of an event passing or not-passing a given set of cuts, a fraction (called the cut-weight,  $z$ ) of interpretations will pass these cuts. This cut-weight allows for enhanced background suppression and increased significance of observed quantities for a given data set, as detailed in Ref. [67]. The telescoping jets algorithm provides the benefits of multiple event interpretations without the significant computational overhead of a non-deterministic algorithm like the Q-jets algorithm, and its multiple cone sizes are particularly suited to studying processes like associated production, which suffers from a pronounced low tail in the dijet invariant mass distribution due to final state radiation (FSR) “leaking” outside the relatively narrow jets used for object reconstruction.

### B.I MONTE CARLO SIMULATION

The MC simulated samples used in this study are the same as in Ref. [? ]. The signal sample used is generated in PYTHIA8 [68] with the CTEQ6L1 parton distributions functions (PDFs) and AU2 tune[69, 70, 71] for the  $ZH$  process with  $m_H = 125$  GeV (henceforth,  $ZH125$ ). The primary background processes examined in this study were  $Z$ +jets with massive  $b$  and  $c$  quarks. These samples are generated with version 1.4.1 of the SHERPA generator [72].

## B.2 JET RECONSTRUCTION AND CALIBRATION

In order to construct telescoping jets, jet axes must first be found around which to “telescope.” In the reconstructed-level analysis, the anti- $k_t$  algorithm with  $R = 0.4$  is used to reconstruct jets from topological clusters in the calorimeters. The four vectors of these anti- $k_t$  algorithm with  $R = 0.4$  jets are calibrated to match truth information obtained from simulation and validated in data. To take into account the effect of pile-up interactions, jet energies are corrected using a jet-area based technique [73], and each jet with  $p_T < 50$  GeV and  $|\eta| < 2.4$  is subject to a requirement that at least 50% of the scalar sum of the  $p_T$  of tracks matched to this jet be composed of tracks also associated with the primary vertex. Jet energies are also calibrated using  $p_T$  and  $\eta$ -dependent correction factors [74]. Furthermore, at least two jets must have  $|\eta| < 2.5$  in order to be  $b$ -tagged. The MV1 algorithm [75? ? ?] is used for  $b$ -tagging. Once jets are reconstructed and  $b$ -tag weights have been calculated, the two hardest,  $b$ -tagged jets are used as the telescoping jet axes. Additional details can be found in Ref. [76].

After the telescoping jet axes have been established, telescoping jets are constructed using topological clusters in the calorimeters at a variety of jet cone sizes. Including the original anti- $k_t$  jets used for the  $R = 0.4$  case, twelve total sets of jets of cone sizes ranging from  $R = 0.4\text{--}1.5$  are constructed, with each successive size having a radius 0.1 larger than the preceding set. For each jet axis, telescoping jets consist of any topological cluster lying within  $R$  of the axis. In the event of overlap, clusters are assigned to the closer jet axis. If a given cluster is equidistant from the two jet axes, the cluster is assigned to whichever jet axis is associated with the anti- $k_t$  jet with higher  $p_T$ . Calibra-

tion for the telescoping jets is conducted using corrections for anti- $k_t$  calorimeter topological cluster jets; the  $R = 0.4$  corrections are used for telescoping  $R = 0.5$ , and the  $R = 0.6$  corrections are used for telescoping  $R \geq 0.6$  (cf. Sec. B.4). The telescoping cone jets ( $R \geq 0.5$ ) at reconstructed level are trimmed using Cambridge-Aachen jets with  $R = 0.3$  and  $f_{cut} = 0.05$  with respect to the untrimmed jet  $p_T$  [77]. Since these jets are trimmed, the active area correction is not applied. In the event a  $Z$  candidate electron falls within  $R$  of the axis of a telescoping jet, its 4-momentum is subtracted from that of the jet vectorially.

A similar process is used to construct telescoping jets in the truth-level analysis below. Instead of the two hardest  $b$ -tagged anti- $k_t$  with  $R = 0.4$  jets reconstructed with calorimeter topological clusters, the two hardest truth  $b$ -jets in an event are used. Instead of making a cut on  $b$ -tagging weight to  $b$ -tag, truth jets are examined to see whether a  $b$ -hadron with  $p_T > 5$  GeV is contained within  $\Delta R < 0.4$  of the jet axis; the presence of a  $b$ -hadron is used to  $b$ -tag truth-level jets. These two jets again provide the jets for the  $R = 0.4$  case and the axes around which telescoping takes place. Stable truth particles, not including muons and neutrinos, are used in place of calorimeter topological clusters.  $Z$  candidate electron-telescoping jet overlap removal is performed at truth level, too. Missing  $E_T$  is calculated using the vector sum of the four momenta of stable truth-level neutrinos. Since there are no pileup particles stored at truth level, truth-level telescoping jets are not trimmed.

### B.3 EVENT RECONSTRUCTION AND SELECTION

Events are selected on the basis of a combination of leptonic, jet, and missing  $E_T$  requirements, which are outlined in Table B.1. Leptons are categorized by three sets of increasingly stringent qual-

ity requirements, which include lower limits on  $E_T$ , upper limits on  $|\eta|$ , impact-parameter requirements, and track-based isolation criteria. The requirements differ for electrons [78] and muons [79]. Events are selected with a combination of single lepton, dielectron, and dimuon requirements. Each event must contain at least one lepton passing medium requirements and at least one other lepton passing loose requirements. These leptons are used to create a dilepton invariant mass cut to ensure the presence of a  $Z$  boson and suppress multijet backgrounds.

Event selection requirements are also imposed on the anti- $k_t$  with  $R = 0.4$  jets. There must be at least two  $b$ -tagged jets in a given event. The  $p_T$  of the harder  $b$ -tagged jet must be at least 45 GeV, and the second  $b$ -tagged jet must have  $p_T$  of at least 20 GeV. There are further topological cuts on the separation of the two jets  $\Delta R(b, \bar{b})$ , the distance between the two jets in the  $(\eta, \phi)$  plane, according to the transverse momentum of the  $Z$  boson,  $p_T^Z$ . These are shown in Table B.2.

The truth-level analysis has the same missing  $E_T$ , jet  $p_T$ ,  $m_{ll}$ , and additional topological selection criteria, but the use of truth-level information simplifies the other requirements. Instead of lepton quality requirements,  $Z$  boson candidate leptons' statuses and MC record barcodes are checked to ensure the leptons are stable.

In the jet calibration validation, the reconstructed level analysis lepton and  $m_{ll}$  requirements are imposed, but neither the missing  $E_T$  nor the jet selection requirements are applied so as not to bias the validation.

**Table B.1:** A summary of basic event selection requirements. Truth-level  $b$ -tagging is done with truth-level information.

Requirement	Reconstructed	Truth	Validation
Leptons	1 med. + 1 loose	2 produced by $Z$ boson	1 med. + 1 loose
$b$ -jet	2 $b$ -tags	2 $b$ -jets	—
$p_T$ jet 1 (jet 2)		$> 45 \text{ GeV} (> 20) \text{ GeV}$	—
Missing $E_T$		$E_T^{\text{miss}} < 60 \text{ GeV}$	—
$Z$ boson		$83 < m_{ll} < 99 \text{ GeV}$	

**Table B.2:** Topological requirements of the event selection.

$p_T^Z [\text{GeV}]$	$\Delta R(b, b)$
0–90	0.7–3.4
90–120	0.7–3.0
120–160	0.7–2.3
160–200	0.7–1.8
> 200	< 1.4

## B.4 VALIDATION OF JET CALIBRATION

In order to validate the jet energy scale and resolution of jets constructed with this telescoping-jets algorithm, values of  $p_T^{rec}/p_T^{tru}$  are studied for each value of  $R$  for the  $Z+jets$  MC sample. In a given event, all jets, not just the two hardest  $b$ -tagged jets, are telescoped. These jets are constructed in the same way as in the reconstructed and truth-level analyses; reconstructed-level jets are made from calorimeter topological clusters within  $R$  of the anti- $k_t$  with  $R = 0.4$  jet axes and then trimmed, and truth-level jets are made from stable truth particles within  $R$  of the anti- $k_t$  with  $R = 0.4$  jet axes. The reconstructed and truth-level telescoping jet ensembles are matched according to the separation in the  $(\eta, \phi)$  plane of their corresponding anti- $k_t$  with  $R = 0.4$  jets used as seeds. Only jets with  $|\eta| < 1.2$  are examined here, and the results of studies on the  $ZH125$ ,  $ZZ$ , and  $t\bar{t}$  samples, as well as over other  $|\eta|$  ranges, are outlined in [63]. Any reconstructed jets not within  $\Delta R = 0.3$  of a truth jet are discarded. In the event that multiple reconstructed jets are the same distance away from a given truth jet, the reconstructed jet with the highest  $p_T$  gets matched. Matching is retained for all  $R$  values (i.e. telescoping seeds are matched, and telescoping jets are assumed to match if the anti- $k_t$  jets from which their seeds are derived match).

Once anti- $k_t$  with  $R = 0.4$  reconstructed and truth jets are matched, response functions are created by generating a series of distributions of  $p_T^{rec}/p_T^{tru}$  in 20 GeV bins of  $p_T^{tru}$  from 20–200 GeV, one bin for 200–300 GeV, and one bin for 300–500 GeV for each  $R$ , with bins chosen for purposes of statistics. Ensembles with  $p_T^{tru} < 20$  GeV are ignored since no calibration exists for jets with transverse momentum below this value. The values of  $\langle p_T^{rec}/p_T^{tru} \rangle$  in each  $p_T^{tru}$  bin are calculated by doing

a two sigma gaussian fit on the distribution of  $p_T^{rec}/p_T^{tru}$  in that bin and taking the mean of that fit, and the error on the mean is taken from the error of this parameter in the fit. The resolutions are the values of the square root of the variance on this fit. As the total response distributions in Figure B.1 show, performance is best for low  $R$  values and high values of  $p_T^{tru}$ . Figure B.1 shows the  $R = 0.4$  (antik $k_t$ ) case to show a baseline for performance,  $R = 0.6$  to show the deviations with “correct” calibrations, and  $R = 1.0, 1.5$  to show how big those deviations get with larger  $R$  jets. The resolutions,  $\sigma_{p_T^{rec}/p_T^{tru}}$ , as a function of  $p_T^{tru}$  are shown in Figure B.1(b). For  $p_T^{tru} > 60$  GeV, response is fairly consistent over various  $R$  values. Resolution, as might naively be expected, is worse for increasingly larger values of  $R$ . For  $p_T^{tru} < 60$  GeV, resolution degrades, and response degrades in particular for increasing  $R$ ; this is likely a result from residual pileup effects.

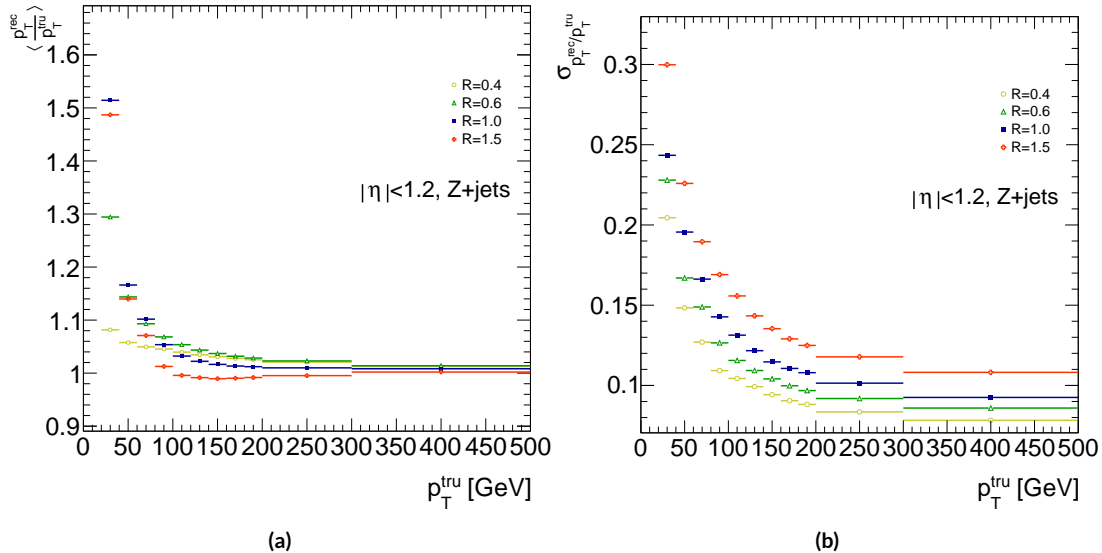


**Figure B.1:** The mean and resolution of  $p_T^{rec}/p_T^{tru}$  for the background  $Z+jets$  sample for  $|\eta| < 1.2$  and for  $R = 0.4, 0.6, 1.0$ , and  $1.5$  in 20 GeV bins of  $p_T^{tru}$  for 20-200 GeV, one bin for 200-300 GeV, and one bin for 300-500 GeV, with bins chosen for purposes of statistics.

## B.5 TRUTH-LEVEL ANALYSIS

To understand the limits and sources of any potential improvements, a truth-level analysis was conducted on MC samples with a  $ZH_{125}$  signal sample and a  $Z+jets$  background sample. Distributions for the dijet invariant mass,  $m_{bb}$ , were made for each telescoping radius. Both signal and background samples develop more pronounced tails in the high  $m_{bb}$  region as  $R$  increases, as shown in Figure B.2.  $N_{events}$  is normalized to expected values in data.

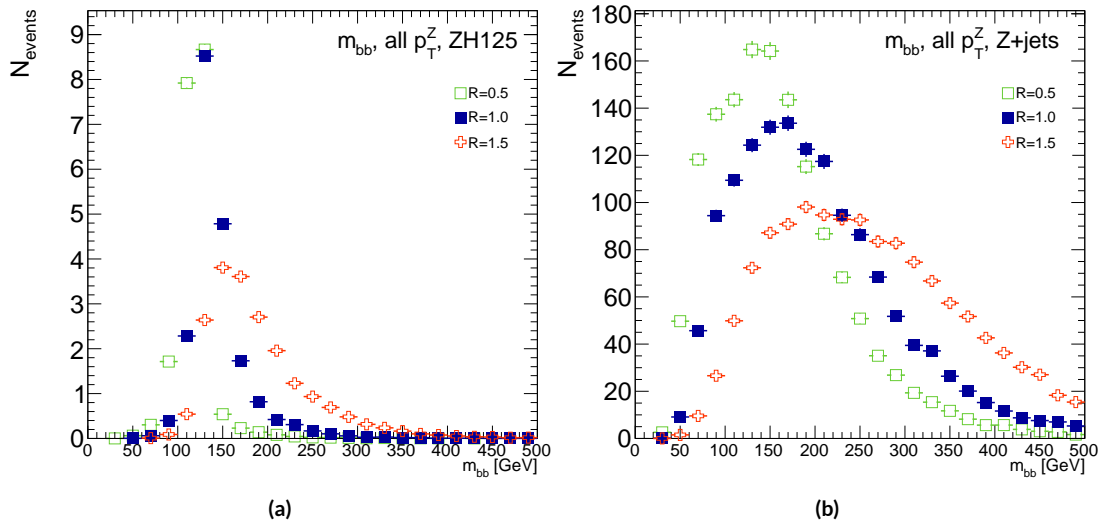


**Figure B.2:** The  $m_{bb}$  distribution for the telescoping jets with  $R = 0.5, 1.0$ , and  $1.5$  truth-level jets is shown for the signal and background samples in (a) and (b), respectively.

One way to take advantage of this information is to make a cut on  $m_{bb}$  for two different radii. This is graphically depicted in Figure B.3 for the optimized combination of  $m_{bb,R=0.9}$  (telescoping cone jets constructed as outlined in Sec. B.2) vs.  $m_{bb,R=0.4}$  (anti- $k_t$  jets). At truth-level, the majority of events in the signal  $ZH_{125}$  sample are concentrated in relatively narrow region of parameter space,

where this is certainly not the case for the more diffuse  $Z+jets$  background sample.

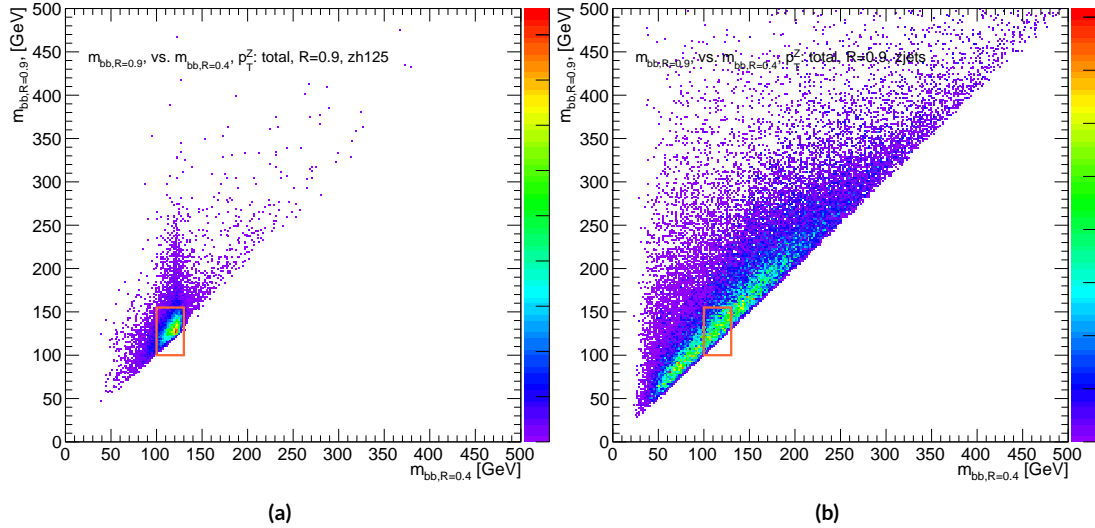


**Figure B.3:** The 2D distribution of  $m_{bb,R=0.9}$  vs.  $m_{bb,R=0.4}$  is shown for signal and background truth-level samples in (a) and (b), respectively. The region chosen for the double  $m_{bb}$  cut is outlined in orange.

Another way to take advantage of multiple event interpretations is to make use of an event's cut-weight, denoted  $z$  and defined as the fraction of interpretations in a given event that pass a certain set of cuts (in this note, a cut on  $m_{bb}$ ). The distribution of cut-weights for a sample of events is denoted  $\rho(z)$ . To enhance the significance of a cut-based analysis, events can be weighted by the cut-weight or any function  $t(z)$  of the cut-weight. Weighting events by  $t(z)$  modifies the usual  $S/\delta B$  formula used to calculate significances. In this note,  $\delta B$  is based on Poissonian statistics and is taken as  $0.5 + \sqrt{0.25 + N_B}$ , where  $N_B$  is the number of background events.

## B.6 ERRORS ON TELESCOPING SIGNIFICANCES

Significances of measurements are quoted in units of expected background fluctuations, schematically,  $S/\delta B$ . For counting experiments with high numbers of events, we can use Gaussian statistics and express this as  $S/\sqrt{B}$ , which we here denote as  $\mathcal{S}$ . However, with lower statistics, it becomes more appropriate to use Poissonian statistics, and

$$\mathcal{S}_{gaus} = \frac{S}{\sqrt{B}} \rightarrow \mathcal{S}_{pois} = \frac{S}{0.5 + \sqrt{0.25 + B}} \quad (\text{B.1})$$

where  $0.5 + \sqrt{0.25 + B}$  is the characteristic upward fluctuation expected in a Poissonian data set using the Pearson chi-square test[80].

## B.7 COUNTING

The significance is given as above, where  $S = N_S$  and  $B = N_B$ . That is, the signal and background are just the number of events in signal and background that pass some cuts. The error for the Gaussian case is the standard:

$$\Delta \mathcal{S}_{gaus} = \frac{1}{\sqrt{B}} \Delta S \oplus \frac{S}{2B^{3/2}} \Delta B \quad (\text{B.2})$$

The error for the Poissonian case is:

$$\Delta \mathcal{S}_{pois} = \frac{1}{0.5 + \sqrt{0.25 + B}} \Delta S \oplus \frac{S}{2(0.5 + \sqrt{0.25 + B})^2 \sqrt{0.25 + B}} \Delta B \quad (\text{B.3})$$

where  $\oplus$  denotes addition in quadrature, and  $\Delta S(B)$  is the error on signal (background).

## B.8 MULTIPLE EVENT INTERPRETATIONS

Using multiple event interpretations changes the formulae used in with simple counting. That is,  $S$  is not necessarily merely  $N_S$ , the number of events passing some signal cuts, and similarly for  $B$  and  $N_B$ . Using an event weighting by some function of the cut-weight,  $z$ , denoted  $t(z)$ ,  $S = N_S \langle t \rangle_{\rho_S}$  and  $B = N_B \langle t^2 \rangle_{\rho_B}$ . So

$$\mathcal{S}_{t,gaus} = \frac{N_S \langle t \rangle_{\rho_S}}{\sqrt{N_B \langle t^2 \rangle_{\rho_B}}} \rightarrow \mathcal{S}_{t,pois} = \frac{N_S \int_0^1 dz t(z) \rho_S(z)}{0.5 + \sqrt{0.25 + N_B \int_0^1 dz t^2(z) \rho_B(z)}} \quad (\text{B.4})$$

For histograms, everything is done bin-wise. The notation used below is as follows:  $\rho_i$  is the value of  $\rho(z)$  at bin  $i$  (where the bins run from 0 to  $n_{tel}$ , where  $n_{tel}$  is the total number of telescoping radii).  $t_i = t_i(\rho_{S,i}, \rho_{B,i}, i/n_{tel})$  is the value of  $t(z)$  at bin  $i$ , which can depend, in principle, on  $\rho_{S,i}$ ,  $\rho_{B,i}$ , and  $i/n_{tel}$  (the last of which is  $z$  in bin  $i$ ). Explicitly,

$$N = \sum_{i=0}^{n_{tel}} \rho_i, \quad \int_0^1 dz t(z) \rho_S(z) = \sum_{i=0}^{n_{tel}} t_i \rho_{S,i}, \quad \int_0^1 dz t^2(z) \rho_B(z) = \sum_{i=0}^{n_{tel}} t_i^2 \rho_{B,i}$$

For the calculations that follow, let  $\xi = \sum_{i=0}^{n_{tel}} t_i \rho_{S,i}$ ,  $\psi = 0.5 + \sqrt{0.25 + N_B \sum_{i=0}^{n_{tel}} t_i^2 \rho_{B,i}}$ ,  $\partial_S = \frac{\partial}{\partial \rho_{S,i}}$  (and similarly for  $B$ ), so  $\mathcal{S}_t = N_S \xi / \psi$

Some partial derivatives:

$$\begin{aligned}
\partial_S N_S &= 1, & \partial_{B,i} N_B &= 1 \\
\partial_S \xi &= t_i + (\partial_S t_i) \rho_{S,i}, & \partial_B \xi &= (\partial_B t_i) \rho_{B,i} \\
\partial_S \psi &= \frac{N_B t_i (\partial_S t_i) \rho_{B,i}}{\sqrt{0.25 + N_B \sum_{i=0}^{n_{tel}} t_i^2 \rho_{B,i}}}, & \partial_B \psi &= \frac{\sum_{i=0}^{n_{tel}} t_i^2 \rho_{B,i} + N_B (t_i^2 + 2t_i (\partial_B t_i) \rho_{B,i})}{2\sqrt{0.25 + N_B \sum_{i=0}^{n_{tel}} t_i^2 \rho_{B,i}}} \\
\partial_S \mathcal{S}_t &= \frac{\xi}{\psi} + \frac{N_S}{\psi} \partial_S \xi - \frac{N_S \xi}{\psi^2} \partial_S \psi, & \partial_B \mathcal{S}_t &= N_S \left( \frac{1}{\psi} \partial_B \xi - \frac{\xi}{\psi^2} \partial_B \psi \right)
\end{aligned}$$

Thus,

$$\Delta \mathcal{S}_{t,i} = \left[ \frac{\xi}{\psi} + \frac{N_S}{\psi} \partial_S \xi - \frac{N_S \xi}{\psi^2} \partial_S \psi \right] \Delta \rho_{S,i} \oplus N_S \left[ \frac{1}{\psi} \partial_B \xi - \frac{\xi}{\psi^2} \partial_B \psi \right] \Delta \rho_{B,i} \quad (\text{B.5})$$

and the total error is given by the sum in quadrature over all bins  $i$  of  $\Delta \mathcal{S}_{t,i}$ .

$$\text{B.9} \quad t(z) = z$$

With  $t(z) = z$ ,  $t_i = i/n_{tel}$ , so  $\partial_S t_i = \partial_B t_i = 0$ . So:

$$\begin{aligned}
\partial_S \psi &= \partial_B \xi = 0 \\
\partial_S \xi &= \frac{i}{n_{tel}} \\
\partial_B \psi &= \frac{\sum_i i^2 \rho_{B,i} + N_B t^2}{n_{tel} \sqrt{n_{tel}^2 + N_B \sum_i i^2 \rho_{B,i}}}
\end{aligned}$$

so  $\Delta\mathcal{S}_{z,i}$  reduces to

$$\Delta\mathcal{S}_{t,i} = \left[ \frac{\xi + N_S t_i}{\psi} \right] \Delta\rho_{S,i} \oplus \left[ \frac{N_S \xi}{\psi^2} \partial_B \psi \right] \Delta\rho_{B,i} \quad (\text{B.6})$$

$$\text{B.10} \quad t(z) = \rho_S(z) / \rho_B(z)$$

With the likelihood optimized\*  $t^*(z) = \rho_S(z) / \rho_B(z)$ ,  $t_i = \rho_{S,i} / \rho_{B,i}$ , so  $\partial_S t_i = 1 / \rho_{B,i}$  and  $\partial_B t_i = -\rho_{S,i} / \rho_{B,i}^2$ . So:

$$\begin{aligned} \partial_S \xi &= 2 \frac{\rho_{S,i}}{\rho_{B,i}} = 2t_i \\ \partial_B \xi &= -\frac{\rho_{S,i}}{\rho_{B,i}} = -t_i \\ \partial_S \psi &= \frac{N_B t_i}{\sqrt{0.25 + N_B \sum_i \rho_{S,i}^2 / \rho_{B,i}}} \\ \partial_B \psi &= \frac{\sum_i \rho_{S,i}^2 / \rho_{B,i} - N_B (\rho_{S,i} / \rho_{B,i})^2}{\sqrt{1 + 4N_B \sum_i \rho_{S,i}^2 / \rho_{B,i}}} \end{aligned}$$

simplifying somewhat the terms in the per bin error in Equation B.6.

The new significance figure using multiple event interpretations becomes, with  $\rho_S$  and  $\rho_B$  denoting the cut-weight distributions in signal and background, respectively

$$\frac{S}{\delta B} = \frac{N_S \langle t \rangle_{\rho_S}}{0.5 + \sqrt{0.25 + N_B \langle t^2 \rangle_{\rho_B}}} \quad (\text{B.7})$$

---

\*for the Gaussian statistics case

Of particular interest is the likelihood optimized  $t(z)$ ,<sup>†</sup>  $t^*(z) = \rho_S(z)/\rho_B(z)$ .  $m_{bb}$  windows are chosen separately for each scheme studied to maximize total significances and are summarized in

Table B.3.

$$\left(\frac{S}{\delta B}\right)_z = \frac{N_S \epsilon_S}{0.5 + \sqrt{0.25 + N_B (\epsilon_B^2 + \sigma_B^2)}} \quad (B.8)$$

$$\left(\frac{S}{\delta B}\right)_{t^*(z)} = \frac{N_S \int_0^1 dz \frac{\rho_S^2(z)}{\rho_B(z)}}{0.5 + \sqrt{0.25 + N_B \int_0^1 dz \frac{\rho_S^2(z)}{\rho_B(z)}}} \quad (B.9)$$

where  $\epsilon_{S,B}$  are the means of  $\rho_{S,B}(z)$  and  $\sigma_B^2$  is the variance of  $\rho_B(z)$ . Further details can be found in Refs. [63, 67] and Appendix B.6.

**Table B.3:**  $m_{bb}$  windows studied. These windows were chosen to optimize significances over all  $p_T^Z$ .

Analysis Type	$S/\delta B$ Type	Optimal $m_{bb}$ Window
Reconstructed	$\text{anti-}k_t, R = 0.4$ $t(z) = z$ $t(z) = \rho_S(z)/\rho_B(z)$ $\text{anti-}k_t, R = 0.4, \text{telescoping } R = 0.6$	$90-140 \text{ GeV}$ $110-155 \text{ GeV}$ $110-155 \text{ GeV}$ $95-140 \text{ GeV} (R = 0.4),$ $105-160 \text{ GeV} (R = 0.6)$
Truth	$\text{anti-}k_t, R = 0.4$ $t(z) = z$ $t(z) = \rho_S(z)/\rho_B(z)$ $\text{anti-}k_t, R = 0.4, \text{telescoping } R = 0.9$	$100-130 \text{ GeV}$ $115-140 \text{ GeV}$ $120-135 \text{ GeV}$ $100-130 \text{ GeV} (R = 0.4),$ $100-155 \text{ GeV} (R = 0.9)$

The truth-level distributions  $\rho_S(z)$ ,  $\rho_B(z)$ , and  $\rho_S(z)/\rho_B(z)$  are shown for the  $m_{bb}$  window that optimizes  $(S/\delta B)_{t^*(z)}$  in Figure B.4, and significance improvements as a function of  $p_T^Z$  are

---

<sup>†</sup>Derived under the assumption of Gaussian statistics in Ref [67]

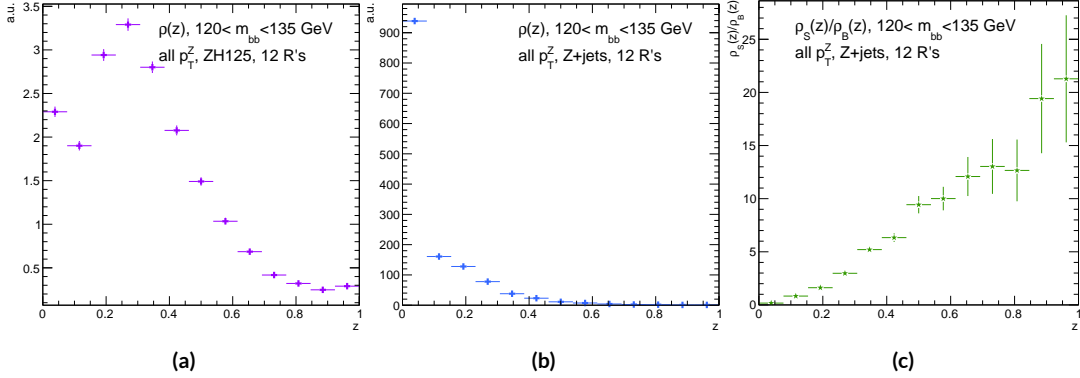


**Figure B.4:** Truth-level  $\rho(z)$  distributions for the  $m_{bb}$  window optimizing  $(S/\delta B)_{t^*(z)} \cdot \rho_S(z)$  for the signal  $ZH125$  sample is shown in (a), and  $\rho_B(z)$  for the background  $Z+jets$  sample is shown in (b). The distribution of  $\rho_S(z)/\rho_B(z)$  for these samples is shown in (c).

summarized in Figure B.5. Uncertainties in Figures B.5 and B.9 are statistical uncertainties. JES systematics will need to be evaluated for different  $R$ 's, as modeling uncertainties is an outstanding issue, but these systematics will likely be strongly correlated for the different  $R$ 's and are not anticipated to be a very large contribution to total uncertainties. While the two dimensional  $m_{bb}$  cut and  $t(z) = z$  schemes only showed marginal improvement at truth level at 2.87%<sup>‡</sup> and 1.45%, respectively, the likelihood optimized  $t^*(z)$  showed a more substantial 40.7% improvement overall, with a steady increase in improvement with increasing  $p_T^Z$ . Figure B.5 (d) summarizes the improvements with respect to  $p_T^Z$  for the  $t^*(z)$  event weight for five, seven, and twelve telescoping radii (interpretations) per event. Improvements increase with a greater number of interpretations and are more pronounced at higher  $p_T^Z$  for this scheme. The optimal  $120 < m_{bb} < 135$  GeV window for  $t^*(z)$  case is among the smallest studied. The benefits of this window's narrowness are suggested in Figure B.4.

<sup>‡</sup>The limited improvement is provably due to the simplified treatment of the 2D case; better performance with a more sophisticated treatment has been observed in Ref. [81].

While the background cut-weight distribution,  $\rho_B(z)$  in Figure B.4 (b) behaves as one might with a marked peak at  $z = 0$ , the signal  $\rho_S(z)$  distribution peaks at a relatively modest  $z = 0.3$ , which indicates that much of the gain at truth level comes from background rejection. This is possible at truth level since there is both truth-level information available and no smearing and since  $\rho_S/\rho_B$  is the relevant quantity (as shown in Figure B.4 (c)).

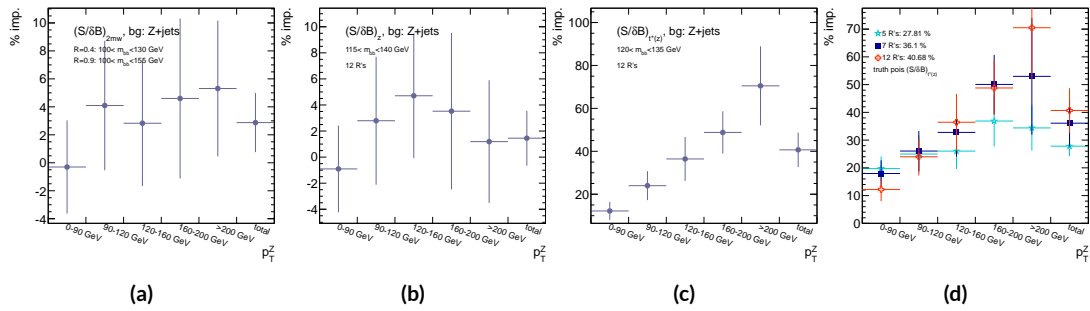


**Figure B.5:** A summary of the improvements for different truth-level telescoping jet cuts and weights is shown in bins of  $p_T^Z$ . The final bin is the total improvement over all  $p_T^Z$ . Shown are improvements for the 2D  $m_{bb}$  cut (a),  $t(z) = z$  (b),  $t(z) = t^*(z)$  with 12 radii (c), and  $t(z) = t^*(z)$  for various radii (d).

## B.II RECONSTRUCTED-LEVEL ANALYSIS

At reconstructed level, the same overall effect of introducing a high tail in  $m_{bb}$  distributions with increasing  $R$  is evident in comparing Figures B.2 and B.6. The optimal  $m_{bb}$  windows, however, grow larger, due to the lack of truth-level information.

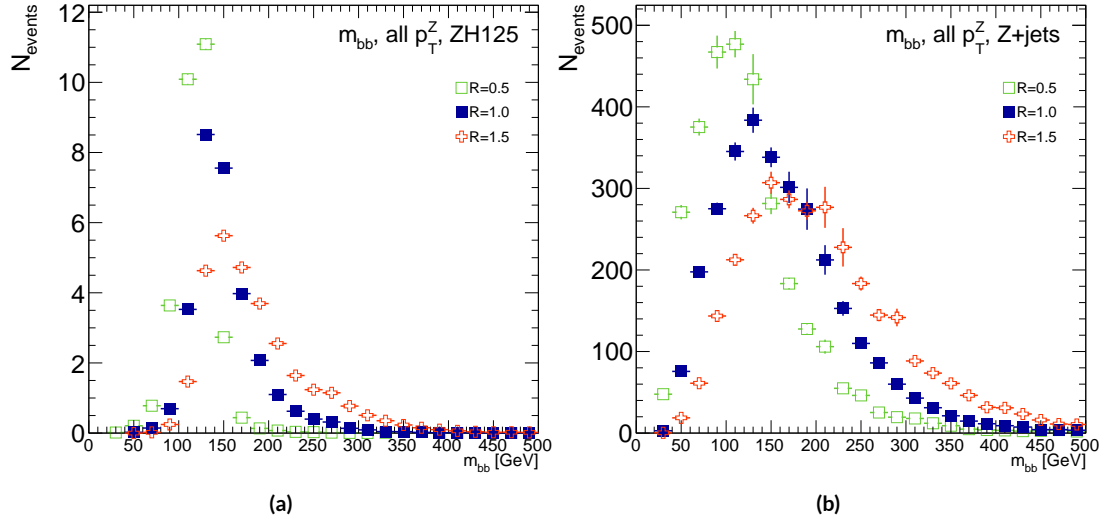


**Figure B.6:** The  $m_{bb}$  distribution for the telescoping jets with  $R = 0.5$ ,  $R = 1.0$ , and  $R = 1.5$  reconstructed-level jets is shown for the signal and background samples in (a) and (b), respectively.

Total significance gains at reconstructed level for the two dimensional  $m_{bb}$  cut and the  $t(z) = z$  case are similar, at 2.87% and 1.45%, respectively. The optimal two-dimensional  $m_{bb}$  cut at reconstructed level is  $95 < m_{bb,R=0.4} < 140$  GeV,  $105 < m_{bb,R=0.6} < 160$  GeV. Just as at truth level, the  $R = 0.4$   $m_{bb}$  cut is comparable to the optimal single  $R = 0.4$   $m_{bb}$  cut, and the second  $m_{bb}$  cut is at similar values (cf. Table B.3 and Figures B.3 and B.7). However, the optimal second telescoping radius is markedly smaller at  $R = 0.6$  versus the optimal truth-level second radius of  $R = 0.9$ , which

suggests that effects like pileup at reconstructed level obscure correlations between the  $R = 0.4$  interpretations and limit the usefulness of larger  $R$  interpretations in this particular scheme. The  $t(z) = z$  case has a wider optimal window and yields about half the improvement it does at truth level.

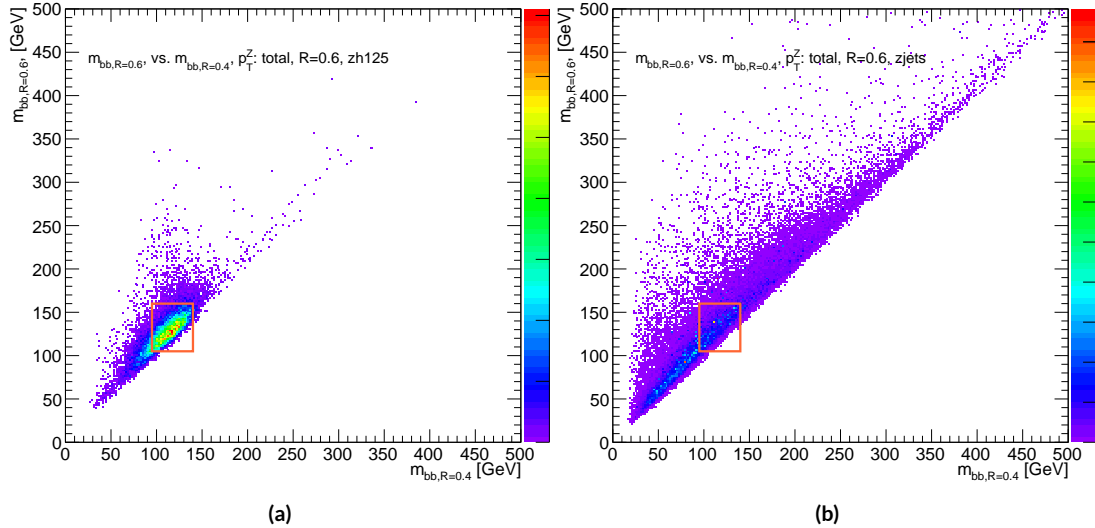


**Figure B.7:** The 2D distribution of  $m_{bb,R=0.8}$  vs.  $m_{bb,R=0.4}$  is shown for signal and background reconstructed-level samples in (a) and (b), respectively. The region chosen for the double  $m_{bb}$  cut is outlined in orange.

The optimal  $m_{bb}$  window for the  $t^*(z)$  case is also markedly wider at reconstructed level, at  $110 < m_{bb} < 155$  GeV in comparison to the truth-level optimal  $120 < m_{bb} < 135$  GeV. The  $\rho(z)$  distributions for the signal  $ZH125$  and background  $Z+jets$  as well as the  $\rho_S(z)/\rho_B(z)$  in this window are shown in Figure B.8. Compared with the truth-level distributions in Figure B.4, both the signal and background optimal  $\rho(z)$  distributions have higher values at higher  $z$ . The peak in  $\rho_S(z)$  at  $z = 1$  suggests that at reconstructed level, maximizing the number of more “signal-like” events is the key to optimizing significances, as opposed to the optimal, background suppressing  $\rho(z)$  distri-

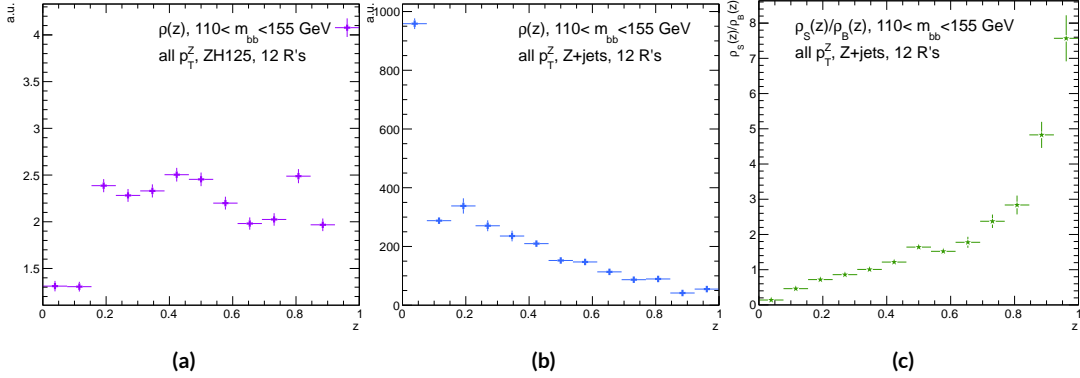


**Figure B.8:** Reconstructed-level  $\rho(z)$  distributions for the  $m_{bb}$  window optimizing  $(S/\delta B)_{t^*(z)} \cdot \rho_S(z)$  for the signal  $ZH125$  sample is shown in (a), and  $\rho_B(z)$  for the background  $Z+jets$  sample is shown in (b). The distribution of  $\rho_S(z)/\rho_B(z)$  for these samples is shown in (c).

butions at truth level. The use of a greater number of interpretations per event (telescoping radii) does appear to result in overall greater improvement as at truth level, as twelve radii performed better than five, but this is less clear at reconstructed level, as shown in Figure B.9 (d). The improvement at reconstructed level using an event weight of  $t^*(z)$  is 20.5%, just over half the improvement at truth level but still quite significant. Summaries of improvements as a function of  $p_T^Z$  for all three cases studied and for the  $t^*(z)$  case for different numbers of telescoping radii are shown in Figure B.9.

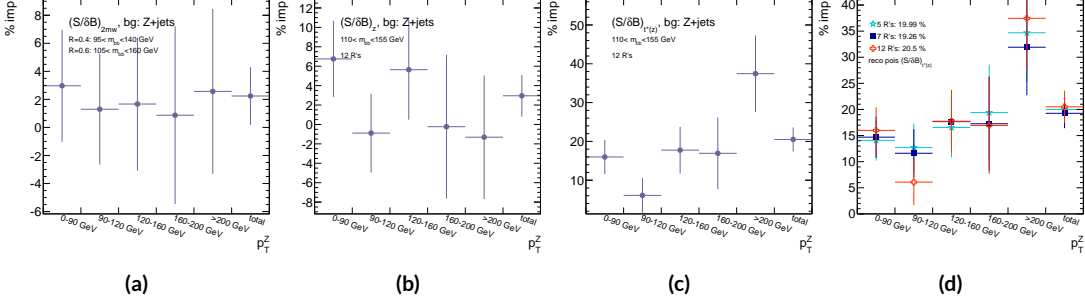


**Figure B.9:** A summary of the improvements for different reconstructed-level telescoping jet cuts and weights is shown in bins of  $p_T^Z$ . The final bin is the total improvement over all  $p_T^Z$ . Shown are improvements for the 2D  $m_{bb}$  cut (a),  $t(z) = z$  (b),  $t(z) = t^*(z)$  with 12 radii (c), and  $t(z) = t^*(z)$  for various radii (d).

**Table B.4:** A summary of significances for different weighting schemes and cuts and for reconstructed and truth jets for a luminosity of  $20.3 \text{ fb}^{-1}$ .  $\text{akt4}$  refers to the standard cut-based analysis using anti- $k_t$  with  $R = 0.4$  jets. Column titles are  $p_T^Z$  regions in GeV.

Type	0–90	90–120	120–160	160–200	> 200	total
$\text{akt4}_{\text{rec}}$	0.47492	0.28214	0.28339	0.25748	0.37337	0.76887
$\text{akt4}_{\text{tru}}$	0.57414	0.30655	0.37309	0.35042	0.53569	0.98619
$2 m_{bb, \text{rec}}$	0.48903	0.2858	0.28812	0.25972	0.38297	0.78611
$2 m_{bb, \text{tru}}$	0.5724	0.3191	0.38364	0.36655	0.56414	1.0145
$z_{\text{rec}}$	0.50698	0.27962	0.29937	0.25688	0.36846	0.79158
$z_{\text{tru}}$	0.56894	0.31511	0.39065	0.36277	0.54206	1.0005
$t^*(z)_{\text{rec}}$	0.55085	0.29931	0.33367	0.30107	0.51321	0.92649
$t^*(z)_{\text{tru}}$	0.64425	0.38008	0.50904	0.5214	0.91337	1.3873

## B.12 CONCLUSIONS AND PROSPECTS

The use of telescoping jets to provide multiple event interpretations shows promise as an avenue to increase significances in the  $H \rightarrow b\bar{b}$  search in ATLAS and make an observation in the systematics-limited environment of early Run 2. A preliminary study using the telescoping jets algorithm with 12 telescoping radii to build 12 event interpretations on 2012 Monte Carlo based on the full, cut-based Run 1 analysis yielded a 20.5% improvement in  $S/\delta B$  over using anti- $k_t$  with  $R = 0.4$  alone at reconstructed level using a likelihood maximized event weighting to study the  $ZH \rightarrow llb\bar{b}$  process. The jets used in this note at reconstructed level were trimmed in order to guarantee reasonable resolution in the large- $R$  interpretations. The algorithm, in particular, showed discriminating power at high  $p_T^Z$ , so better performance can be expected in Run 2 with a higher  $\sqrt{s}$  and higher numbers of events with large  $p_T^Z$ . Additionally, the many simplifying assumptions regarding jet calibration and the relatively basic use of information<sup>§</sup> from multiple invariant masses in this note suggest that even further improvements than those quoted are possible. While this note did not explore the correlations between multiple event interpretations and the variables used in the BDT of the latest multivariate version of the  $H \rightarrow b\bar{b}$  analysis[23], new phenomenological studies suggest that such correlations are not strong[81]. The corresponding reconstructed-level study, using a BDT, is left for future work. Also left for future work are better understanding the effects of jet trimming and which interpretations are the most useful.

---

<sup>§</sup>For examples of more sophisticated treatments compared to the treatment in this note, see Ref [81].

*Ah, peut on être heureux?*

*Quand on forme des autres voeux?*

J. P. Rameau, *Les Indes Galantes*

# C

## Historical Aside

INTERNATIONAL COLLABORATIONS with thousands of scientists like those at CERN's (the European Organisation for Nuclear Research) 27 km circumference Large Hadron Collider (LHC) are fast becoming the norm in many fields of science, making the past seven decades of discovery in particle physics seem a natural part of history's long march of progress. Seemingly arcane terms like dark

matter and the Higgs boson (the infamous “God particle”) even pop up in blockbuster movies and primetime television. All of this, however, would have been impossible without the fascist and then communist existential threats to the American world order throughout the 20th century.

The Manhattan Project and its atomic arsenal were a direct response to the threat of global fascism in World War II. They both secured the United States’ position as a world power at the end of the war and laid the foundations for many particle physics developments for the following three decades. High ranking American officials were well aware that this would have been impossible without the contributions of particle physicists. Some of these physicists, like Enrico Fermi and Arthur Compton, were already Nobel laureates and luminaries in the field. Others, like Richard Feynman and Owen Chamberlain, would go on to make their marks in the decades following the war. Though a few of these physicists, most notably Edward Teller, would continue their work on nuclear weapons, most of these physicists would return to basic science research as the nation turned towards the uneasy peace time of the Cold War.

Particle physicists’ service and connections made during the war would serve them well in the decades to come as the military-controlled Manhattan Project transitioned to the civilian-led Atomic Energy Commission (AEC). The AEC was founded in 1946 to oversee the nuclear arsenal, the development of atomic power, and related fundamental research in the United States. Many of those on AEC board were former Manhattan Project particle physicists, including Glenn Seaborg, the AEC chairman from 1961-1971. Congressional oversight for AEC funding consisted of a single committee, the Joint Committee on Atomic Energy (JCAE), whose deliberations often took place behind closed doors owing to the AEC’s sensitive national security mission. Elementary particle physics research

was clearly central to the AEC mission at its founding, as nuclear fission was the bleeding edge of particle physics at the beginning of World War II and represented the culmination of decades of highly specialized research that had no immediately obvious practical application. Furthermore, particle accelerator technology, the main workhorse then as now for basic science research in particle physics and the most expensive item on any particle physicist's wish list, had been crucial to many of these discoveries. The anticipation of future windfalls as momentous as the power of the atom and the exemplary performance of particle physicists during the war ensured that experimental particle physics and particle accelerators would remain the crown jewel of AEC research throughout the organization's existence.

The AEC's sizable budget (thanks to its crucial mission of securing the nation's nuclear arsenal) and lavish support were the biggest contributing factors to the development of particle physics in the mid 20th century through its funding of accelerator facilities. Particle accelerators use powerful electromagnetic fields to take beams of subatomic particles, usually protons or electrons, as close to the speed of light as possible before colliding them into either fixed targets or other beams to produce high energy collisions. Physicists use these collisions to test models of the universe that predict behavior in these extreme regimes. Without more energetic collisions, progress becomes functionally impossible. While the first such accelerator was smaller than the average human hand, studying more complete models of the universe called for more energetic collisions and hence bigger, more powerful, and more expensive accelerators.

Soon, these experiments became too big and expensive for individual universities to operate on their own. Progress in American particle physics became entirely dependent on the AEC, and hence

on the continued threat of nuclear annihilation. National laboratories, all under AEC stewardship, became regional centers of research for particle physicists. By the late 1960's, Brookhaven National Laboratory, Lawrence Berkeley National Laboratory, and the Stanford Linear Accelerator Center hosted the majority of cutting edge accelerator facilities in the country alongside a dwindling number of single university accelerators. By the decade's end Cornell hosted the only such university operated facility. The competitive rivalry among these different institutions fostered American success and dominance in experimental particle physics through the 1970's. The culmination of AEC patronage was the National Accelerator Laboratory (now Fermilab), which began operations in 1967. Fermilab's construction was not a foregone conclusion given the economically challenging backdrop of the Vietnam War, but an emphasis on cost effective plans for both the laboratory and accelerator backed by the full support of the AEC secured Fermilab's funding. Fermilab would ultimately become home to the Tevatron, the final particle accelerator in the United States to claim the title of the world's most powerful.

Particle physics only became more dependent on the existence of a Soviet threat with the end of the AEC. Due to budgetary pressures, the AEC was abolished in 1975, and its duties were eventually reorganized into the Department of Energy (DOE). Under DOE administration, proposed particle physics experiments now had to compete against research projects from the entire range of fields germane to American energy instead of only other nuclear and particle physics projects. Moreover, DOE leadership had far fewer officials with track records of supporting particle physics research projects above all others. Nevertheless, there remained one last, great effort to promote collider physics in the United States, the Superconducting Supercollider (SSC). The SSC was an incredibly

ambitious design: a 50 mile ring under the Waxahachie desert with superconducting magnets to accelerate protons and antiprotons to energies more than three times higher than the LHC's current world record. The project was conceived during the Reagan administration and billed as a megaproject to reassert American dominance as the president took a more aggressive approach to the Soviet threat. Unfortunately, the project was perhaps too ambitious and suffered from management problems. It is not surprising, then, that the end of the Cold War spelled the end of the SSC. With no external threat to American global dominance, there was little impetus to continue funding such an expensive and over-budget project. There has not been a single initiative since for the United States to recapture its once commanding lead over efforts in Western Europe.

Western Europe was the only other serious center of 20th century particle physics, and successes there also depended upon five decades of existential threat to the United States, though in a less direct fashion. Most obviously, American institutions and physicists have been essential to the development of European particle physics, just as European physicists were crucial to the success of the Manhattan Project. Seven of the ten Cold War era CERN Directors General were either educated or did research at American universities, and every major particle physics discovery since the end of World War II has relied on both American and European talent and infrastructure. Furthermore, the European approach to experimental particle physics, epitomized by CERN, emphasized consensus and cooperation and was emblematic of larger geopolitical currents on the European continent in the latter half of the 20th century. Such a culture and its success would have been impossible without the same threats that facilitated American success in particle physics. While limited resources of member states were no doubt contributing factors in CERN's genesis, the collaborative culture of

CERN and other pan-European organizations was a reaction to centuries of competition for continental dominance. After the total destruction of the world wars, enough was enough. The relatively peaceful prosperity on the Western side of the Iron Curtain made European cooperation possible, while the threat at Western Europe's doorstep only heightened the urgency of pan-European desires. Hence, the symbolic importance of European unity during the Cold War is hard to underestimate, and CERN-facilitated European cooperation made it a forerunner to organizations like the European Union and a model to the world. Every major achievement in particle physics after 1940 therefore relies on facilities and institutions on both sides of the Atlantic that would never have been formed without the back to back threats of global fascism and Soviet Communism.

With the cancellation of the SSC in 1993 and the closing of Fermilab's Tevatron in 2011, CERN and its LHC remain the lone laboratory and experiment at the energy frontier. The United States is now a mere "observer state" at CERN: American talent and funding are essential to CERN and its mission, but the United States does not have a seat on CERN's governing council. It remains to be seen whether a legacy of over six decades of international cooperation will provide sufficient motivation for particle physics to continue at CERN after the LHC without guarantee of any discovery at the next experiment. Current nuclear threats, while attention grabbing, are far from existential and unlikely to reignite any initiative for distinctly American science megaprojects. The only other prospect for a future collider at the energy frontier is China, whose nationalistic desire for superpower status may prove a sufficiently powerful and lasting motivator for the next generation of collider.

# References

- [1] Symmetry Magazine. The Standard Model of Particle Physics, 2015. URL <http://www.symmetrymagazine.org/standard-model/>.
- [2] Fabienne Marcastel. CERN’s Accelerator Complex. La chaîne des accélérateurs du CERN. Oct 2013. URL <https://cds.cern.ch/record/1621583>. General Photo.
- [3] CERN. LHC first beam: a day to remember, 2008. URL <http://cerncourier.com/cws/article/cern/36296>.
- [4] Giulio Stancari, Valentina Previtali, Alexander Valishev, Roderik Bruce, Stefano Redaelli, Adriana Rossi, and Belen Salvachua Ferrando. Conceptual design of hollow electron lenses for beam halo control in the Large Hadron Collider. Technical Report FERMILAB-TM-2572-APC. FERMILAB-TM-2572-APC, CERN, Geneva, Oct 2014. URL <https://cds.cern.ch/record/1700455>. Comments: 23 pages, 1 table, 10 figures.
- [5] The ATLAS Collaboration, G Aad, E Abat, J Abdallah, and et al. A A Abdelalim. The atlas experiment at the cern large hadron collider. *Journal of Instrumentation*, 3(08):S08003, 2008. URL <http://stacks.iop.org/1748-0221/3/i=08/a=S08003>.
- [6] ATLAS Collaboration. Study of the material of the atlas inner detector for run 2 of the lhc, 2017.
- [7] M Capeans, G Darbo, K Einsweiller, M Elsing, T Flick, M Garcia-Sciveres, C Gemme, H Pernegger, O Rohne, and R Vuillermet. ATLAS Insertable B-Layer Technical Design Report. Technical Report CERN-LHCC-2010-013. ATLAS-TDR-19, Sep 2010. URL <https://cds.cern.ch/record/1291633>.
- [8] Gavin P. Salam. Towards jetography. 2009. doi: 10.1140/epjc/s10052-010-1314-6.
- [9] B Heinemann, F Hirsch, and S Strandberg. Performance of the ATLAS Secondary Vertex b-tagging Algorithm in 7 TeV Collision Data. Technical Report ATLAS-COM-CONF-2010-042, CERN, Geneva, May 2010. URL <https://cds.cern.ch/record/1266283>. (Was originally ’ATL-COM-PHYS-2010-274’).

- [10] Adrian Buzatu and Wei Wang. Object selections for SM Higgs boson produced in association with a vector boson in which  $H \rightarrow b\bar{b}$  and  $V$  decays leptonically with Run-2 data: Object support note for VH(bb) 2015+2016 dataset publication. Technical Report ATL-COM-PHYS-2016-1674, CERN, Geneva, Nov 2016. URL <https://cds.cern.ch/record/2233686>. This is a support note for the VH(bb) SM publication using the 2015+2016 datasets.
- [11] Observation of a new particle in the search for the Standard Model Higgs boson with the ATLAS detector at the LHC. *Phys.Lett.*, B716:1–29, 2012. doi: 10.1016/j.physletb.2012.08.020.
- [12] Observation of a new boson at a mass of 125 GeV with the CMS experiment at the LHC. *Phys.Lett.*, B716:30–61, 2012. doi: 10.1016/j.physletb.2012.08.021.
- [13] ATLAS Collaboration. Evidence for the  $b \rightarrow b\bar{b}$  decay with the atlas detector, 2017.
- [14] Tatsuya Masubuchi, Jose Benitez, Andrew Stuart Bell, Spyridon Argyropoulos, Hannah Arnold, Yara Amaral Coutinho, Arturo Rodolfo Sanchez Pineda, Adrian Buzatu, Giovanni Calderini, and et al. Chan, Stephen Kam-wah. Search for a Standard Model Higgs boson produced in association with a vector boson and decaying to a pair of  $b$ -quarks. Technical Report ATL-COM-PHYS-2016-1724, CERN, Geneva, Nov 2016. URL <https://cds.cern.ch/record/2235437>.
- [15] C. Patrignani et al. Review of Particle Physics. *Chin. Phys.*, C40(10):100001, 2016. doi: 10.1088/1674-1137/40/10/100001.
- [16] Stephan Hagebock. Lorentz Invariant Observables for Measurements of Hbb Decays with ATLS, CERN, Geneva, 2017. URL [https://indico.cern.ch/event/611919/contributions/2471459/attachments/1425444/2205142/17.03.28\\_DPG.pdf](https://indico.cern.ch/event/611919/contributions/2471459/attachments/1425444/2205142/17.03.28_DPG.pdf).
- [17] Paul Jackson and Christopher Rogan. Recursive jigsaw reconstruction: Hep event analysis in the presence of kinematic and combinatoric ambiguities. 2017.
- [18] The Proton Synchrotron Booster. Jul 2012. URL <http://cds.cern.ch/record/1997372>.
- [19] The Proton Synchrotron. Jan 2012. URL <http://cds.cern.ch/record/1997189>.
- [20] The Super Proton Synchrotron. Jan 2012. URL <http://cds.cern.ch/record/1997188>.

- [21] Lyndon Evans and Philip Bryant. Lhc machine. *Journal of Instrumentation*, 3(08):S08001, 2008. URL <http://stacks.iop.org/1748-0221/3/i=08/a=S08001>.
- [22] Christopher C Tully. *Elementary particle physics in a nutshell*. Princeton Univ. Press, Princeton, NJ, 2011. URL <https://cds.cern.ch/record/1417476>.
- [23] F Ahmadov, L Alio, BMM Allbrooke, T Bristow, D Buescher, A Buzatu, Y Coadou, C Debenedetti, Y Enari, G Facini, W Fisher, P Francavilla, G Gaycken, J Gentil, R Goncalo, G Gonzalez Parra, JF Grivaz, C Gwilliam, S Hageboeck, G Halladjian, M Jackson, D Jamin, R Jansky, K Kiuchi, V Kostyukhin, K Lohwasser, and et al. Lopez Mateos, D. Supporting Document for the Search for the bb decay of the Standard Model Higgs boson in associated (W/Z)H production with the ATLAS detector. Technical Report ATL-COM-PHYS-2014-051, CERN, Geneva, Jan 2014. URL <https://cds.cern.ch/record/1645654>.
- [24] Aidan Robson, Giacinto Piacquadio, and Elisabeth Schopf. Signal and Background Modelling Studies for the Standard Model  $VH$ ,  $H \rightarrow b\bar{b}$  and Related Searches: Modelling support note for VH(bb) 2015+2016 dataset publication. Technical Report ATL-COM-PHYS-2016-1747, CERN, Geneva, Dec 2016. URL <https://cds.cern.ch/record/2235887>. This is a support note for the VH(bb) SM publication using the 2015+2016 datasets.
- [25] S. Alioli et al. NLO Higgs boson production via gluon fusion matched with shower in POWHEG. *JHEP*, 0904:002, 2009.
- [26] Torbjorn Sjostrand, Stephen Mrenna, and Peter Z. Skands. A Brief Introduction to PYTHIA 8.1. *Comput.Phys.Commun.*, 178:852–867, 2008. doi: 10.1016/j.cpc.2008.01.036.
- [27] Georges Aad et al. Measurement of the  $Z/\gamma^*$  boson transverse momentum distribution in  $pp$  collisions at  $\sqrt{s} = 7$  TeV with the ATLAS detector. *JHEP*, 09:145, 2014. doi: 10.1007/JHEP09(2014)145.
- [28] Richard D. Ball et al. Parton distributions for the LHC Run II. *JHEP*, 04:040, 2015. doi: 10.1007/JHEP04(2015)040.
- [29] Johan Alwall, Michel Herquet, Fabio Maltoni, Olivier Mattelaer, and Tim Stelzer. Madgraph 5 : Going beyond. 2011. doi: 10.1007/JHEP06(2011)128.
- [30] LHC Higgs Cross Section Working Group, S. Dittmaier, C. Mariotti, G. Passarino, and R. Tanaka (Eds.). Handbook of LHC Higgs Cross Sections: 1. Inclusive Observables. *CERN-2011-002*, CERN, Geneva, 2011.

- [31] M.L. Ciccolini, S. Dittmaier, and M. Kramer. Electroweak radiative corrections to associated WH and ZH production at hadron colliders. *Phys. Rev.*, D68:073003, 2003. doi: 10.1103/PhysRevD.68.073003.
- [32] Michał Czakon, Paul Fiedler, and Alexander Mitov. Total Top-Quark Pair-Production Cross Section at Hadron Colliders Through  $\alpha(\frac{4}{\delta})$ . *Phys. Rev. Lett.*, 110:252004, 2013. doi: 10.1103/PhysRevLett.110.252004.
- [33] M. Aliev, H. Lacker, U. Langenfeld, S. Moch, P. Uwer, et al. HATHOR: Hadronic Top and Heavy quarks cross section calculator. *Comput. Phys. Commun.*, 182:1034–1046, 2011. doi: 10.1016/j.cpc.2010.12.040.
- [34] P. Kant, O.M. Kind, T. Kintscher, T. Lohse, T. Martini, S. Molbitz, P. Rieck, and P. Uwer. Hathor for single top-quark production: Updated predictions and uncertainty estimates for single top-quark production in hadronic collisions. *Computer Physics Communications*, 191: 74 – 89, 2015. ISSN 0010-4655. doi: <http://dx.doi.org/10.1016/j.cpc.2015.02.001>. URL <http://www.sciencedirect.com/science/article/pii/S0010465515000454>.
- [35] John M. Campbell and R. K. Ellis. MCFM for the Tevatron and the LHC. *Nucl. Phys. Proc. Suppl.*, 205-206:10–15, 2010. doi: 10.1016/j.nuclphysbps.2010.08.011.
- [36] Matthew D. Schwartz. *Quantum Field Theory and the Standard Model*. Cambridge University Press, 2014. ISBN 1107034736, 9781107034730. URL <http://www.cambridge.org/us/academic/subjects/physics/theoretical-physics-and-mathematical-physics/quantum-field-theory-and-standard-model>.
- [37] T. Gleisberg et al. Event generation with SHERPA 1.1. *JHEP*, 02:007, 2009. doi: 10.1088/1126-6708/2009/02/007.
- [38] Andy Buckley, Jonathan Butterworth, David Grellscheid, Hendrik Hoeth, Leif Lonnblad, James Monk, Holger Schulz, and Frank Siegert. Rivet user manual, 2010.
- [39] Iain W. Stewart and Frank J. Tackmann. Theory uncertainties for higgs and other searches using jet bins. 2011. doi: 10.1103/PhysRevD.85.034011.
- [40] Gionata Luisoni, Paolo Nason, Carlo Oleari, and Francesco Tramontano. Hw ±/hz + o and 1 jet at nlo with the powheg box interfaced to gosam and their merging within minlo. *Journal*

*of High Energy Physics*, 2013(10):83, 2013. ISSN 1029-8479. doi: 10.1007/JHEP10(2013)083.  
URL [http://dx.doi.org/10.1007/JHEP10\(2013\)083](http://dx.doi.org/10.1007/JHEP10(2013)083).

- [41] Richard D. Ball et al. Parton distributions with LHC data. *Nucl. Phys.*, B867:244–289, 2013. doi: 10.1016/j.nuclphysb.2012.10.003.
- [42] J. Alwall, R. Frederix, S. Frixione, V. Hirschi, F. Maltoni, O. Mattelaer, H. S. Shao, T. Stelzer, P. Torrielli, and M. Zaro. The automated computation of tree-level and next-to-leading order differential cross sections, and their matching to parton shower simulations. *JHEP*, 07:079, 2014. doi: 10.1007/JHEP07(2014)079.
- [43] ATLAS Run 1 Pythia8 tunes. Technical Report ATL-PHYS-PUB-2014-021, CERN, Geneva, Nov 2014. URL <https://cds.cern.ch/record/1966419>.
- [44] Michiel Botje et al. The PDF4LHC Working Group Interim Recommendations. 2011.
- [45] T. Gleisberg, S. Höche, F. Krauss, M. Schönherr, S. Schumann, F. Siegert, and J. Winter. Event generation with sherpa 1.1. *Journal of High Energy Physics*, 2009(02):007, 2009. URL <http://stacks.iop.org/1126-6708/2009/i=02/a=007>.
- [46] Nils Lavesson and Leif Lonnblad. W+jets matrix elements and the dipole cascade. 2005. doi: 10.1088/1126-6708/2005/07/054.
- [47] M Delmastro, S Gleyzer, C Hengler, M Jimenez, T Koffas, M Kuna, K Liu, Y Liu, G Marchiori, E Petit, M Pitt, E Soldatov, and K Tackmann. Photon identification efficiency measurements with the ATLAS detector using LHC Run 1 data. Technical Report ATL-COM-PHYS-2014-949, CERN, Geneva, Aug 2014. URL <https://cds.cern.ch/record/1747242>.
- [48] Electron efficiency measurements with the ATLAS detector using the 2012 LHC proton-proton collision data. Technical Report ATLAS-CONF-2014-032, CERN, Geneva, Jun 2014. URL <https://cds.cern.ch/record/1706245>.
- [49] ATLAS Collaboration. MCPAnalysisGuidelinesMC15, 2015. URL <https://twiki.cern.ch/twiki/bin/view/AtlasProtected/MCPAnalysisGuidelinesMC15>.
- [50] Muon reconstruction performance in early  $\sqrt{s}=13$  TeV data. Technical Report ATL-PHYS-PUB-2015-037, CERN, Geneva, Aug 2015. URL <https://cds.cern.ch/record/2047831>.

- [51] ATLAS Collaboration. Performance of missing transverse momentum reconstruction for the ATLAS detector in the first proton-proton collisions at at  $\sqrt{s} = 13$  TeV. Technical Report ATL-PHYS-PUB-2015-027, CERN, Geneva, Jul 2015. URL <https://cds.cern.ch/record/2037904>.
- [52] W Lampl, S Laplace, D Lelas, P Loch, H Ma, S Menke, S Rajagopalan, D Rousseau, S Snyder, and G Unal. Calorimeter Clustering Algorithms: Description and Performance. Technical Report ATL-LARG-PUB-2008-002. ATL-COM-LARG-2008-003, CERN, Geneva, Apr 2008. URL <https://cds.cern.ch/record/1099735>.
- [53] Loch, Peter and Lefebvre, Michel . Introduction to Hadronic Calibration in ATLAS, 2007. URL <https://indico.cern.ch/event/13514/contributions/138580/subcontributions/12940/attachments/107156/152645/IntroLectureDraft2-8.pdf>.
- [54] Jet Calibration and Systematic Uncertainties for Jets Reconstructed in the ATLAS Detector at  $\sqrt{s} = 13$  TeV. Technical Report ATL-PHYS-PUB-2015-015, CERN, Geneva, Jul 2015. URL <https://cds.cern.ch/record/2037613>.
- [55] ATLAS Collaboration. Tagging and suppression of pileup jets with the ATLAS detector. Technical Report ATLAS-CONF-2014-018, CERN, Geneva, May 2014. URL <https://cds.cern.ch/record/1700870>.
- [56] Expected performance of the ATLAS  $b$ -tagging algorithms in Run-2. Technical Report ATL-PHYS-PUB-2015-022, CERN, Geneva, Jul 2015. URL <https://cds.cern.ch/record/2037697>.
- [57] Gordon Watts, Frank Filthaut, and Giacinto Piacquadio. Extrapolating Errors for  $b$ -tagging. Technical Report ATL-COM-PHYS-2015-7II, CERN, Geneva, Jul 2015. URL <https://cds.cern.ch/record/2034234>. This is for internal information only, no approval to ever be seen outside of ATLAS.
- [58] Glen Cowan, Kyle Cranmer, Eilam Gross, and Ofer Vitells. Asymptotic formulae for likelihood-based tests of new physics. *Eur. Phys. J. C*, 71:1554, 2011. doi: 10.1140/epjc/s10052-011-1554-0.
- [59] A. L. Read. Presentation of search results: the  $CL_s$  technique. *J. Phys. G*, 28:2693–2704, 2002.

- [60] Stephen Kam-wah Chan and John Huth. Variations on MVA Variables in the SM  $ZH \rightarrow llb\bar{b}$  Search. Technical Report ATL-COM-PHYS-2017-1318, CERN, Geneva, Aug 2017. URL <https://cds.cern.ch/record/2281412>.
- [61] B Clark, D Lopez Mateos, N Felt, J Huth, and J Oliver. An Algorithm for Micromegas Segment Reconstruction in the Level-1 Trigger of the New Small Wheel. Technical Report ATL-UPGRADE-INT-2014-001, CERN, Geneva, Sep 2014. URL <https://cds.cern.ch/record/1753329>.
- [62] Stephen Kam-wah Chan, David Lopez Mateos, and John Huth. Micromegas Trigger Processor Algorithm Performance in Nominal, Misaligned, and Corrected Misalignment Conditions. Technical Report ATL-COM-UPGRADE-2015-033, CERN, Geneva, Dec 2015. URL <https://cds.cern.ch/record/2113121>.
- [63] S Chan, J Huth, D Lopez Mateos, and K Mercurio.  $ZH \rightarrow llb\bar{b}$  Analysis with Telescoping Jets. Technical Report ATL-PHYS-INT-2015-002, CERN, Geneva, Jan 2015. URL <https://cds.cern.ch/record/1982439>.
- [64] A. Hornig T. S. Roy D. Krohn S. D. Ellis, S. D. Ellis and M. D. Schwartz. Qjets: A non-deterministic approach to tree-based jet substructure. *Phys. Rev. Lett.*, 108, 2012. URL <http://arxiv.org/abs/1201.1914>.
- [65] G. D. Leder S. Moretti Y. L. Dokshitzer, Y. L. Dokshitzer and B. R. Webber. Better jet clustering algorithms. *JHEP*, 9708, 1997. URL <http://arxiv.org/abs/hep-ph/9707323>.
- [66] G. P. Salam M. Cacciari, M. Cacciari and G. Soyez. The anti- $k_t$  jet clustering algorithm. *JHEP*, 0804, 2008. URL <http://arxiv.org/abs/0802.1189>.
- [67] D. Krohn D. Kahawala, D. Kahawala and M. D. Schwartz. Jet sampling: Improving event reconstruction through multiple interpretations. 2013. URL <http://arxiv.org/abs/1304.2394>.
- [68] S. Mrenna T. Sjöstrand, T. Sjöstrand and P. Z. Sands. A brief introduction to pythia 8.1. *Comput. Phys. Commun.*, 178, 2008. URL <http://arxiv.org/abs/0710.3820>.
- [69] D. Stump J. Huston H. Lai P.M. Nadolsky et al. J. Pumplin, J. Pumplin. New generation of parton distributions with uncertainties from global qcd analysis. *JEGP*, 0207, 2002. URL <http://arxiv.org/abs/hep-ph/0201195>.

- [70] ATLAS tunes of PYTHIA 6 and Pythia 8 for MCII. Technical Report ATL-PHYS-PUB-2011-009, CERN, Geneva, Jul 2011. URL <http://cds.cern.ch/record/1363300>.
- [71] New ATLAS event generator tunes to 2010 data. Technical Report ATL-PHYS-PUB-2011-008, CERN, Geneva, Apr 2011. URL <https://cds.cern.ch/record/1345343>.
- [72] T. Gleisberg et al. T. Gleisberg et al. Event generation with sherpa 1.1. *JHEP*, 02, 2009. URL <http://arxiv.org/abs/0811.4622>.
- [73] M. Cacciari, M. Cacciari G. P. Salam, and G. P. Salam. Pileup subtraction using jet areas. *Phys. Lett.*, B659, 2008. URL <http://arxiv.org/abs/0707.1378>.
- [74] Jet energy measurement with the atlas detector in proton-proton collisions at  $\sqrt{s} = 7$  TeV *Eur. Phys. J.*, C73, 2013. URL <http://arxiv.org/abs/1112.6426>.
- [75]  $b$ -jet tagging calibration on  $c$ -jets containing  $D^{*+}$  mesons. Technical Report ATLAS-CONF-2012-039, CERN, Geneva, Mar 2012. URL <https://cds.cern.ch/record/1435193>.
- [76] Search for the  $bb$  decay of the Standard Model Higgs boson in associated W/ZH production with the ATLAS detector. Technical Report ATLAS-CONF-2013-079, CERN, Geneva, Jul 2013. URL <https://cds.cern.ch/record/1563235>.
- [77] J. Thaler L. Wang D. Krohn, D. Krohn. Jet trimming. 2009. URL <http://arxiv.org/abs/0912.1342>.
- [78] Electron performance measurements with the atlas detector using the 2010 lhc proton-proton collision data. *Eur. Phys. J.*, C72, 2012. URL <http://arxiv.org/abs/1110.3174v2>.
- [79] Measurement of the  $w \rightarrow l\nu$  and  $z/\gamma^* \rightarrow ll$  production cross sections in proton-proton collisions at  $\sqrt{s} = 7$  TeV with the atlas detector. *JHEP*, 1012, 2010. URL <http://arxiv.org/abs/1010.2130>.
- [80] W. Verkerke and D. Kirkby. The RooFit toolkit for data modeling. In *2003 Computing in High Energy and Nuclear Physics, CHEP03*, 2003.
- [81] Yang-Ting Chien, David Farhi, David Krohn, Andrew Marantani, David Lopez Mateos, and Matthew Schwartz. Quantifying the power of multiple event interpretations. 2014. doi: 10.1007/JHEP12(2014)140.